Fakultät für Medizin

Oncogenic drivers, epithelial-to-mesenchymal transition, and E-cadherin function shape the tumor microenvironment of pancreatic cancer

Tânia Custódio Santos

Vollständiger Abdruck der von der Fakultät für Medizin der Technischen Universität München zur Erlangung des akademischen Grades eines

Doctor of Philosophy (Ph.D.)

genehmigten Dissertation.

Vorsitzende: Prof. Dr. Alessandra Moretti

Betreuer: Prof. Dr. Dieter Saur

Prüfer der Dissertation:

1. Prof. Dr. Marc Schmidt-Supprian

2. Priv.-Doz. Dr. Jan Böttcher

Die Dissertation wurde am 04.03.2022 bei der Fakultät für Medizin der Technischen Universität München eingereicht und durch die Fakultät für Medizin am 01.08.2022 angenommen.

Index

Figure Index

Table Index

Abbreviations

%	Percentage
×g	Times gravity
°C	Degree Celsius
µg	Microgram
µL	Microliter
µM	Micromolar
4-OHT	4-hydroxytamoxifen
ACTA2	Actin alpha 2
ADEX	Aberrantly differentiated endocrine exocrine
ADM	Acinar-to-ductal metaplasia
AF	Alexa Fluor®/Alexa Fluor™
AFN	Atipamezole, flumazenil, naloxone
AIC	Adaptive immune cell
AJ	Adherens junction
AKT	Serine-threonine kinase
ANOVA	Analysis of variance
APC	Adenomatous polyposis coli
APC/C	Anaphase-promoting/cyclosome
apCAF	Antigen-presenting cancer-associated fibroblast
APS	Ammonium persulfate
ARID2	AT-rich interactive domain-containing protein 2
ATL	Atypical flat lesion
ATM	Ataxia telangiectasia mutated serine-protein kinase
BACH1	BTB and CNC homology 1
bp	Base pairs
BRAF	Rapidly accelerated fibrosarcoma isoform B
BSA	Bovine serum albumin
CAF	Cancer-associated fibroblast
CAR3	Carbonic anhydrase 3
CCL	Chemokine (C-C motif) ligand
CD	Cluster of differentiation
cDC	Conventional dendritic cell
CDKN2A	Cyclin-dependent kinase inhibitor 2A

Ck	Cytokeratin
CK18	Keratin 18
CL	Cell line
cm^2	Square centimeter
CODEX	CO detection by indEXing
COL1A1	Collage type I alpha 1 chain
COX2	Cyclooxygenase 2
CSF1R	Colony stimulating factor 1 receptor
CTC	Circulating tumor cell
CTL	Cytotoxic T lymphocyte
CXCL	Chemokine (C-X-C motif) ligand
CXCR	Chemokine (C-X-C motif) receptor
Cy	Cyanine
CyTOF	Time-of-flight mass cytometry
DAB	3,3'-Diaminobenzidine
DC	Dendritic cell
ddH_2O	Bidistilled water
dH_2O	Distilled water
DMEM	Dulbecco’s modified Eagle’s medium
DMSO	Dimethyl sulfoxide
DNA	Deoxyribonucleic acid
dNTP	Deoxynucleotide triphosphate
DPBS	Dulbecco’s phosphate-buffered saline
DR	Death receptor
DTT	1,4-Dithiothreitol
EC	Endothelial cell
E-cadherin/E-cadh/*Cdh1*	Epithelial cadherin
ECM	Extracellular matrix
EDTA	Ethylenediaminetetraacetic acid
EGF	Epidermal growth factor
eGFP	Enhanced green fluorescent protein
EMT	Epithelial-to-mesenchymal transition
EPC1	Enhancer of polycomb homolog 1
ERK	Extracellular signal-regulated kinase

EtOH	Ethanol
FABP4	Fatty acid binding protein 4
FACS	Fluorescence-activated cell sorting
FAP	Fibroblast activation protein
FcεRI	High affinity IgE receptor
FFPE	Formalin-fixed paraffin-embedded
FGF	Fibroblast growth factor
FoV	Field of view
FSF	*frt-STOP-frt*
g	gram
GAP	GTPase-activating protein
GAPDH	Glyceraldehyde 3-phosphate dehydrogenase
GATA3	GATA binding protein 3
GDP	Guanosine diphosphate
GEF	Guanine nucleotide exchange factor
GEMM	Genetically engineered mouse model
GFAP	Glial fibrillary acidic protein
GJ	Gap junction
GM-CSF	Granulocyte/monocyte colony stimulating factor
gMDSC	Granulocytic myeloid-derived suppressor cell
GSK3β	Glycogen synthase kinase 3 beta
GTP	Guanosine triphosphate
H&E	Hematoxylin and eosin
H2-Ab1	Histocompatibility 2 class II antigen A beta 1
HGF	Hepatocyte growth factor
i.p.	Intraperitoneal
iCAF	Inflammatory cancer-associated fibroblast
ICAM1	Intercellular adhesion molecule 1
ICC	Immunocytochemistry
IF	Immunofluorescence
IFN	Interferon
Ig	Immunoglobulin
IGF1	Insulin-like growth factor 1
IGFBP5	Insulin-like growth factor binding protein 5

IHC	Immunohistochemistry
IIC	Innate immune cell
IL	Interleukin
IL6R	Interleukin 6 receptor
inf-moDC	Monocyte-derived inflammatory dendritic cell
iNOS	Inducible nitric oxide synthase
IPMN	Intraductal papillary mucinous neoplasia
IRF	Interferon regulatory factor
ITGAM	Integrin subunit alpha M
ITPN	Intraductal tubular papillary neoplasm
kDa	Kilodalton
KEGG	Kyoto Encyclopedia of Genes and Genomes
KO	Knockout
KRAS	Kirsten rat sarcoma virus
LSL	*Lox-STOP-Lox*
LY6C1	Lymphocyte antigen 6 complex locus C1
M	Molar
mA	Milliampere
MCN	Mucinous cystic neoplasm
M-CSF	Macrophage colony stimulating factor
MDSC	Myeloid-derived suppressor cell
MEK	Mitogen activated protein kinase
MET	Mesenchymal-to-epithelial transition
mg	Milligram
MHC	Major histocompatibility complex
mIHC	Multiplex immunohistochemistry
min	Minute
mL	Milliliter
mM	Millimolar
mm^3	Cubic millimeter
MMF	Midazolam, medetomidine, fentanyl
MMP	Matrix metalloprotein
moMDSC	Monocytic myeloid-derived suppressor cell
MSigDB	Molecular Signature Database

mTOR	Mechanistic target of rapamycin kinase
mTORC	Mechanistic target of rapamycin complex
MTT	3-(4,5-dimethylthiazol-2-yl)-2,5-diphenyltetrazolium bromide
myCAF	Myofibroblastic cancer-associated fibroblast
n/a	Not applicable
NA	Numerical aperture
N-cadherin/N-cadh	Neuronal cadherin
NCR1	Natural cytotoxicity triggering receptor 1
NFκB	Nuclear factor κB
NK	Natural killer
NKain4	Na^+/K^+-transporting ATPase subunit beta-1-interacting protein 4
nm	Nanometer
nM	Nanomolar
PanIN	Pancreatic intraepithelial neoplasia
PBR	*Pdx1-CreER^{T2}*; *BRAF^{V600E}/LSL-Braf^{V637E}*
PBS	Phosphate-buffered saline
PCC	Pancreatic cancer cell
PCR	Polymerase chain reaction
PD-1	Program death receptor 1
PDAC	Pancreatic ductal adenocarcinoma
pDC	Plasmacytoid dendritic cell
PDGF	Platelet-derived growth factor
PDGFRB	Platelet-derived growth factor receptor beta
PDK1	3-phosphoinositide–dependent protein kinase 1
PD-L	Programmed death ligand
PDPN	Podoplanin
PDX1	Pancreatic and duodenal homeobox 1
PFA	Paraformaldehyde
PI3K	Phosphoinositide 3-kinase
PIK3CA	Phosphatidylinositol-4,5-bisphosphate 3-kinase catalytic subunit alpha
PIP_2	Phosphatidylinositol-4,5-bisphosphate
PIP_3	Phosphatidylinositol-3,4,5-bisphosphate
PK	*Pdx1-Cre/Ptf1a-p48^{Cre}/Pdx1-Flp*; *LSL-/FSF-Kras^{G12D}*
PKE	*Pdx1-Cre; LSL-Kras^{G12D}; Cdh1^{fl}*

PKP	*Pdx1-Cre*; *LSL-Kras^{G12D}*; *Trp53^{lox}/LSL-Trp53^{R172H}*
PKPE	*Pdx1-Cre; LSL-Kras^{G12D}; LSL-Trp53^{R172H}*; *Cdh1^{fl}*
PPI3K	*Pdx1-Cre/Ptf1a-p48^{Cre}*; *LSL-Pik3ca^{H1047R}*
PPT	Primary pancreatic tumor
Prrx1	Paired-related homeodomain transcription factor 1
PSC	Pancreatic stellate cell
PTEN	Phosphatase and tensin homolog deleted on chromosome 10
Ptf1a-p48	Pancreas transcription factor 1a
Qdot	Quantum dot
QM	Quasimesenchymal
R26	Rosa26
RNA	Ribonucleic acid
RNA-seq	RNA sequencing
rpm	Revolutions per minute
RT	Room temperature
S100P	S100 calcium binding protein P
scRNA-seq	Single cell RNA sequencing
SD	Standard deviation
SDS	Sodium dodecyl sulfate
SDS-PAGE	Sodium dodecyl sulfate polyacrylamide gel electrophoresis
sec	Second
SEM	Standard error of mean
SHH	Sonic hedgehog
SLPI	Secretory leukocyte peptidase inhibitor
SMAD4	Mothers against decapentaplegic homologue 4
ssGSEA	Single sample gene set enrichment analysis
STAT3	Signal transducer and activator of transcription 3
TAE	Tris-acetate-EDTA
tdTomato	Tandem dimer Tomato
TEM	Transendothelial migration
TEMED	N,N,N',N'-tetramethylethylenediamine
TGFβ	Transforming growth factor-beta
Th	T helper lymphocyte
TIL	Tumor-infiltrating lymphocyte

TJ	Tight junction
TKR	Tyrosine kinase receptor
TLR	Toll-like receptor
TME	Tumor microenvironment
TNF	Tumor necrosis factor
Treg	T regulatory lymphocyte
TRP53/Trp53	Transformation-related protein 53
UV	Ultraviolet
V	Volt/Voltage
v/v	volume per volume
VCAM1	Vascular cell adhesion molecule 1
VEGF	Vascular endothelial growth factor
Vim	Vimentin
W	Watt
w/v	weight per volume
WT	Wild-type
αSMA	Smooth muscle actin alpha

1. Abstract

Immune-profiling is an important tool for characterizing the tumor microenvironment (TME) and identifying predictive markers for response to immunotherapy. Pancreatic ductal adenocarcinoma (PDAC) is characterized by a highly immunosuppressive environment, however how different oncogenic drivers and tumor differentiation status shape the TME is unclear. Our first goal in this study was to comprehensively characterize the TME of murine pancreatic tissues using histocytometry, multiplex immunohistochemistry (mIHC), and RNA sequencing (RNA-seq). Hence, we investigated the impact of *Kras*, *Pik3ca*, and *Braf* mutations and of the differentiation status on the TME composition and found that Pik3ca-driven tumors possess higher stromal and immune contents compared to both differentiated and undifferentiated Kras-driven tissues, suggesting that the driver mutation may have a stronger impact on TME abundance than the tumor differentiation status. Pik3ca-driven tumors also present the highest infiltration of adaptive immune cells, and B lymphocytes were in close proximity to cancer cells harboring *Pik3ca* mutation. To assess the performance of RNA-seq from bulk tumor samples as a high-throughput technique to study the TME, correlation matrixes based on sequencing data were used to infer communication between TME and tumor cell pairs and then compared to the interactions observed in the imaging data. While RNA-seq data was able to confirm interactions that were detected with the imaging analysis (e.g., tumor cells and macrophages), it also provided new correlations (e.g., Pik3ca-driven cancer cells and cytotoxic T cells). Thus, mIHC methodology can be an invaluable tool for immune-profiling in tumor tissues and may be complemented with sequencing techniques for a more in-depth analysis of the cellular composition and interactions within the TME.

Epithelial-to-mesenchymal transition (EMT) is a hallmark of PDAC and linked to poor prognosis. Although *Cdh1* is considered to be a major gatekeeper of the epithelial differentiation status, it remains unclear if cancers undergo morphological changes due to *Cdh1* loss and what may be the functional impact of this loss for tumor initiation and progression and for the interaction with the TME. The second goal of this study was to probe the function of E-cadherin (*Cdh1*) on PDAC tumorigenesis and progression, and to investigate if *Cdh1* deletion confers an advantage to cancer cells to survive in metastatic microenvironments. *Cdh1* was genetically deleted at various stages of mice development, leading to a significantly reduced survival time and an increased incidence of cystic tumors. When *Cdh1* was depleted during pancreatic intraepithelial neoplasia (PanIN) development, the animals present a lower incidence of hepatic metastases than control mice. In addition, *Cdh1*-knockout cells do not exhibit a more mesenchymal morphology, and, by single sample gene set enrichment analysis, we found that *Cdh1* loss in malignant cells induces downregulation of EMT- and inflammation-related signalings. Due to the lack of complete *Cdh1* recombination upon 4-hydroxytamoxifen-treatment of $Cdh1^{fl/fl}$ cell lines, *Cdh1*-proficient and -deficient clones were generated. Orthotopic implantation of *Cdh1*-deficient clones into mouse pancreata revealed a high incidence of ascites formation compared to *Cdh1*-

proficient clones. Altogether, our results suggest that *Cdh1* loss alone does not drive EMT, but it may influence the metastatic dissemination in PDAC.

2. Zusammenfassung

Immune profiling ist ein wichtiges Instrument zur Charakterisierung der Tumormikroumgebung (TME) und zur Identifizierung prädiktiver Marker für das Ansprechen auf eine Immuntherapie. Das duktale Adenokarzinom des Pankreas (PDAC) ist durch eine stark immunsuppressive Umgebung gekennzeichnet. Es ist jedoch unklar, wie die verschiedenen onkogenen Treiber und der Differenzierungsstatus der Krebszellen das TME beeinflussen. Unser erstes Ziel in dieser Studie war die umfassende Charakterisierung des TME von murinen Pankreasgeweben unter Verwendung von Histozytometrie, Multiplex-Immunhistochemie (mIHC) und RNA-Sequenzierung (RNA-Seq). Wir haben hierfür die Auswirkungen von *Kras*-, *Pik3ca*- und *Braf*-Mutationen sowie des Differenzierungsstatuses auf die Zusammensetzung des Immun-TME untersucht. Die Histozytometrie zeigte, dass Pik3ca-getriebene Tumoren im Vergleich zu differenzierten und undifferenzierten Kras-getriebenen Tumoren einen höheren Stroma- und Immunzellgehalt besitzen, was darauf hindeutet, dass die Treibermutation einen stärkeren Einfluss auf die TME hat als der Tumor-Differenzierungsstatus. mIHC-Panels mit Markern für angeborene und adaptive Leukozyten zeigten, dass Pik3ca-getriebene Tumoren die höchste Infiltration adaptiver Immunzellen aufweisen und B-Lymphozyten näher an Krebszellen lokalisiert waren. Um RNA-Seq aus Bulk-Tumorproben als Hochdurchsatztechnik zur Untersuchung des TME zu bewerten, wurden Korrelationsmatrizen basierend auf Sequenzierungsdaten verwendet, um auf die Kommunikation zwischen TME und Tumorzellen zu schließen, und dann mit den zuvor beobachteten Wechselwirkungen in den Bilddaten verglichen. Während die RNA-Seq-Daten Wechselwirkungen bestätigen konnten, die mit der Bildgebungsanalyse nachgewiesen wurden (z. B. Tumorzellen und Makrophagen), lieferten sie auch neue Korrelationen (z. B. Pik3ca-getriebene Krebszellen und zytotoxische T-Zellen). Daher kann die mIHC-Methodik ein wertvolles Werkzeug für das *Immune profiling* in Tumorgeweben sein und durch Sequenzierungstechniken für eine systematische Analyse der Zellzusammensetzung und der Wechselwirkungen innerhalb der TME ergänzt werden.

Die Epithelial-Mesenchymale Transition (EMT) ist ein Markenzeichen von PDAC und mit einer schlechten Prognose verbunden. Obwohl *Cdh1* als wichtiger Gatekeeper für den epithelialen Differenzierungsstatus gilt, bleibt unklar, ob Krebserkrankungen aufgrund des Verlusts von *Cdh1* morphologische Veränderungen erfahren und welche funktionellen Auswirkungen dieser Verlust auf die Tumorentstehung und -progression sowie auf die Interaktion mit dem TME haben könnte. Das zweite Ziel dieser Studie war es, die Funktion von E-Cadherin (*Cdh1*) bei der PDAC-Tumorentstehung und -progression zu untersuchen und herauszufinden, ob die Deletion von *Cdh1* den Krebszellen einen Vorteil beim Überleben in metastatischen Mikroumgebungen verschafft. *Cdh1* wurde dazu in verschiedenen Entwicklungsstadien von Mäusen genetisch entfernt. Dies führte zu einer signifikant verkürzten Überlebenszeit und einer erhöhten Inzidenz von zystischen Tumoren. Wenn *Cdh1* während der pankreatischen intra-epithelialen Neoplasie (PanIN)-Progression deletiert wurde, zeigten diese Tiere eine geringere Inzidenz von Lebermetastasen als die Kontrollmäuse. Darüber hinaus konnten *Cdh1*-Knockout-

Zellen keine mesenchymale Morphologie aufweisen, und durch eine *single sample gene set enrichment* Analyse fanden wir heraus, dass der *Cdh1*-Verlust in malignen Zellen zu einer Herunterregulierung von EMT- und Entzündungs-assoziierten Signalen führt. Aufgrund der unvollständigen *Cdh1*-Rekombination in induzierbaren *Cdh1*$^{fl/fl}$-Zelllinien wurden *Cdh1*-positive und -defiziente Klone erzeugt. Die orthotope Implantation von *Cdh1*-defizienten Klonen in Pankreata von Mäusen im Vergleich zu *Cdh1*-positive Klonen ergab eine hohe Inzidenz an Aszitesbildung. Zusammengefasst legen unsere Ergebnisse nahe, dass der Verlust von *Cdh1* allein die EMT nicht antreibt, aber die metastatische Verbreitung beim Pankreaskarzinom beeinflussen kann.

3. Introduction

3.1. Pancreatic ductal adenocarcinoma

Pancreatic ductal adenocarcinoma (PDAC) comprises the most predominant disease of the pancreas and remains one of the most lethal of solid malignancies, with a 5-year overall survival of 9%, and an estimated 432,242 deaths worldwide in 2018 (Rawla et al., 2019). Moreover, contrarily to other tumor entities such as breast, prostate and colorectal cancer, predictions indicate that the incidence of PDAC is expected to rise in the next decade, becoming the second leading cause of cancer-related death by 2030 (Rahib et al., 2014). While risk factors including age, family history or predisposing syndromes are unavoidable, there are several established risk factors related to lifestyle and metabolism such as smoking, alcoholism, and diabetes mellitus, that can be modified or at least controlled in order to prevent this disease (Boursi et al., 2017; Raimondi et al., 2007; Tramacere et al., 2010). Due to the lack of non-invasive and low-cost screening tools, the screening is restricted to individuals with an increased PDAC risk, and it is not feasible on a population level. Two additional reasons for the extremely poor prognosis of PDAC are the lack of appropriate early diagnosis and the lack of a definitive curative treatment for advanced stage or metastatic disease. Since most PDAC patients are asymptomatic or have non-specific symptoms, this malignancy is often diagnosed at a late stage of the disease. Moreover, surgical resection followed by adjuvant therapy (gemcitabine or 5-fluorouracil) is the only curative therapy available, however only up to 20% of all PDAC patients present a resectable tumor stage (Kleeff et al., 2016; Werner et al., 2013). Other treatment options include conventional chemotherapy, radiotherapy, and molecularly target therapy, which continue to be used to extend the survival time of patients. The high levels of acquired resistance to these treatments and the challenges to develop new therapies have been associated with the highly heterogeneity at the cellular and molecular levels and to the dense and complex microenvironment of PDAC tumors (Bailey et al., 2016; Principe et al., 2020; Puleo et al., 2018; Witkiewicz et al., 2015). Therefore, increasing knowledge about pancreatic cancer initiation and progression as well as the role of its tumor microenvironment (TME) in tumorigenesis is essential for the identification of new potential therapeutic targets and development of novel clinical approaches.

3.1.1. Tumorigenesis and Molecular landscape

Pancreas is an endoderm-derived organ with both endocrine and exocrine functions, being composed by endocrine cells (α, β, and δ) as well as acinar and ductal cells that maintain glucose homeostasis and regulate dietary macromolecules digestion (Grant et al., 2016; Röder et al., 2016). Pancreatic cancer arises from dysfunction of these cells and by their outgrowth. Tumor evolution is a sequential process that begins with the formation of pre-malignant precursor lesions identified as having origin in intraductal papillary mucinous neoplasm (IPMN), pancreatic mucinous cystic neoplasm (MCN), intraductal tubular papillary neoplasm (ITPN), atypical flat lesion (ATL), or pancreatic intraepithelial neoplasia (PanIN) (Ferreira et al., 2017; Haeberle &

Esposito, 2019). PanINs are the most common precursor lesions and have origin in acinar cells, which in turn respond to oncogenic hits by undergoing acinar-to-ductal metaplasia (ADM). These lesions are divided into three different stages based on their morphology (increase of architectural and nuclear atypia), ranging from PanIN-1A/PanIN-1B (low grade) to PanIN-3 (high grade) progressing then to invasive adenocarcinoma (Hruban et al., 2008), as depicted in Fig. 1. Throughout this transformation process, pancreatic cells are more susceptible to pro-oncogenic hits, such as activating mutations in the pro-oncogene from *Kirsten rat sarcoma virus* (*KRAS*), considered to be the trigger for pancreatic tumor initiation and posterior development (Witkiewicz et al., 2015). In fact, *KRAS* mutations are detected in >90% of low and high grade PanINs as well as in invasive PDAC (Biankin et al., 2012; Kanda et al., 2012); in a small subset of cases, oncogenic *rapidly accelerated fibrosarcoma isoform B* (*BRAF*) and *phosphatidylinositol-4,5-bisphosphate 3-kinase catalytic subunit alpha* (*PIK3CA*) mutations have also shown to be sufficient to induce pancreatic tumorigenesis (Payne et al., 2015; Witkiewicz et al., 2015). Mutations in *KRAS* are followed by alterations and/or inactivating mutations in *cyclin-dependent kinase inhibitor 2A* (*CDKN2A*), which can be detected in PanIN-1/2 lesions (Kanda et al., 2012). With progression of tumor formation, inactivation of tumor suppressor genes, including *mothers*

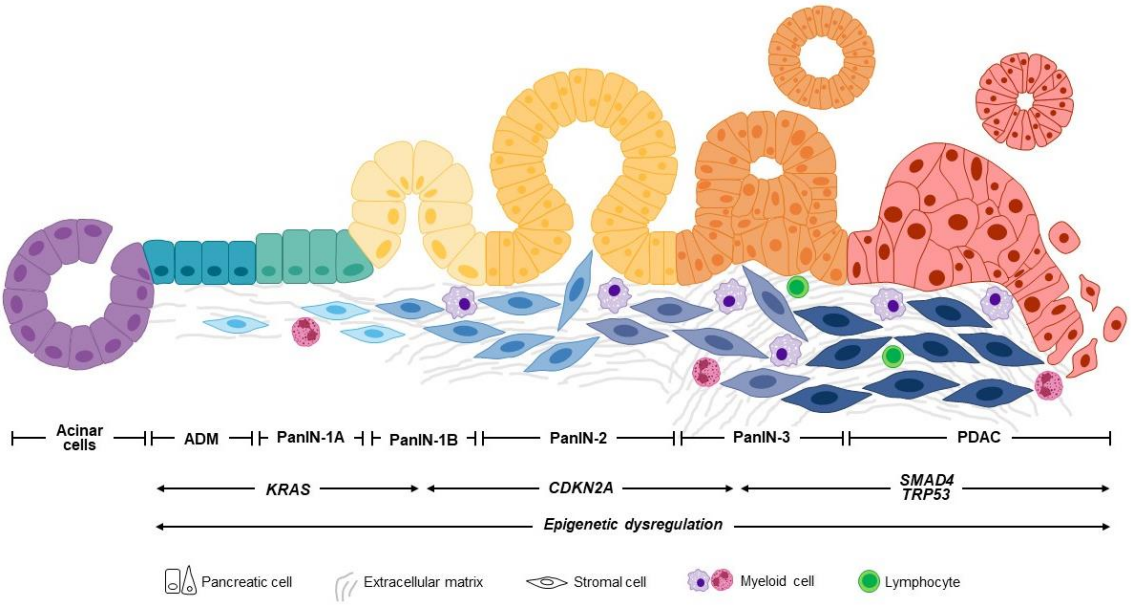

Fig. 1. Pancreatic ductal adenocarcinoma progression.
Acinar cells undergo acinar-to-ductal metaplasia (ADM) due to activation of *Kirsten rat sarcoma virus* (*KRAS*) mutation. Cells progress to low grade pancreatic intraepithelial neoplasia (PanIN)-1A and PanIN-1B lesions, when other alterations start to accumulate, such as inactivating mutations in *cyclin-dependent kinase inhibitor 2A* (*CDKN2A*), also observed in PanIN-2 lesions. The progression to higher grade PanIN-3 lesions and finally pancreatic ductal adenocarcinoma (PDAC) is marked by additional inactivating mutations of tumor suppressor genes *mothers against decapentaplegic homologue 4* (*SMAD4*) and *transformation-related protein 53* (*TRP53*). All the multi-step progress of tumor evolution is accompanied by epigenetic dysregulation and alterations in the surrounding microenvironment, with progressive increase of desmoplastic reaction and changes on the immune cell content.
ADM denotes the acinar-to-ductal metaplasia, *CDKN2A* the *cyclin-dependent kinase inhibitor 2A*, *KRAS* the *Kirsten rat sarcoma virus*, PanIN the pancreatic intraepithelial neoplasia, PDAC the pancreatic ductal adenocarcinoma, *SMAD4* the *mothers against decapentaplegic homologue 4*, *TRP53* the *transformation-related protein 53*.

against decapentaplegic homologue 4 (*SMAD4*) and *transformation-related protein 53* (*TRP53*), are also identified in PDAC. In addition, in the last years, numerous studies involving omics analysis (genomics, epigenomics, transcriptomics) allowed the examination of the mutational and transcriptional landscape of PDAC (Bailey et al., 2016; Biankin et al., 2012; Collisson et al., 2011; Witkiewicz et al., 2015). Altogether, these studies added to the well-established driver mutated genes several more uncommon alterations, such as the chromatin modifiers *enhancer of polycomb homolog 1* (*EPC1*) and *AT-rich interactive domain-containing protein 2* (*ARID2*) as well as the DNA repair gene *ataxia telangiectasia mutated serine-protein kinase* (*ATM*), providing new candidate targets for the development of therapies for PDAC. Besides the genetic alterations, epigenetic regulation of chromatin-based mechanisms, such as DNA methylation and histone post-translational modification, and regulation by non-coding RNAs are also highly altered throughout the progression of PDAC (Cheng et al., 2015; Nones et al., 2014). Furthermore, these epigenetic alterations play important roles in cell growth, survival, and migration. Overall, accumulated evidence points to the high molecular heterogeneity within tumors, which in part influences the response of each PDAC patient to the treatment. So, it remains an urgent need to identify efficient biomarkers for the detection of early stages of this cancer.

Sequencing of the human genome also brought novel classification systems according to the molecular profiles with the aim of improving patient stratification towards personalized treatment strategies (Bailey et al., 2016; Collisson et al., 2011; Moffitt et al., 2015) (Table 1). The work by Collisson and colleagues demarcated the following subtypes: 1) classical subtype characterized by high expression of adhesion-associated and epithelial-like genes; 2) quasimesenchymal (QM) subtype described by having a more mesenchymal-associated gene expression and the poorest prognosis; and 3) exocrine-like subtype showed high expression of tumor cell-derived digestive enzyme genes (Collisson et al., 2011). Moreover, Moffitt *et al*. extended on the previous work by defining two tumor-specific subtypes (classical and basal-like), while adding stromal classifications (normal and activated) (Moffitt et al., 2015). The basal-like subtype is comprised of tissue with high content of laminins and keratins also observed in other cancer basal-like entities such as breast or bladder. When comparing with the other two subtypes described by Collisson, Moffitt stated that the QM is partially driven by a mixture of basal-like and stromal genes and the exocrine-like subtype by the normal pancreas. The novelty of this work is the definition of stromal subtypes: normal stroma was characterized by high expression of pancreatic stellate cell (PSC) markers (*actin alpha 2*, *ACTA2*; *vimentin* and *desmin*), while the activated stromal subtype presented a more diverse set of genes not only associated with macrophages (*integrin subunit alpha M*, *ITGAM*; and chemokine (C-C motif) ligands *CCL13* and *CCL18*), but also related to tumor promotion such as Wnt family members *WNT2* and *WNT5A*, and matrix metalloproteins (MMPs) *MMP9* and *MMP11*. This last stromal subtype was also characterized by the presence of *fibroblast activation protein* (*FAP*) and, as previous reports have demonstrated, it may be partially responsible for the worse prognosis of patients with activated stroma profile. Most recently, Bailey *et al*. defined four subtypes based on differential expression

Table 1. Distinct molecular subtypes of pancreatic ductal adenocarcinoma. Adapted from (Torres & Grippo, 2018).

Work ref	Source	Classification	Survival (months)	Methodology	Comments
Collisson *et al.*, 2011	27 microdissected human PDAC samples; 19 human and 15 mouse PDAC cell lines.	**Classical:** adhesion-associated and epithelial-like genes;	23	Global gene expression analysis.	Classical subtype cell lines more sensitive to erlotinib; QM subtype cell lines more sensitive to gemcitabine.
		Quasimesenchymal (QM): mesenchymal-associated genes;	6.6		
		Exocrine-like: tumor cell-derived digestive enzyme genes.	19.7		
Moffitt *et al.*, 2015	145 primary and 61 metastatic PDAC tumors; 17 PDAC cell lines; 46 pancreas and 88 distant site adjacent normal human samples.	**Tumor-specific subtypes**		Global gene expression analysis. RNA sequencing for validation of findings.	"Classical" subtype from Collisson's work overlapped with Classical subtype. QM subtype appeared to be a mixture of genes from basal-like and stromal subtypes.
		Classical: high adhesion-associated and epithelial-like gene expression;	19		
		Basal-like: laminins and keratins expression.			
		Stroma-specific subtypes			
		Normal: markers for pancreatic stellate cells;	24		
		Activated: genes associated with macrophages and with fibroblasts, genes involved in tumor promotion.	15		
Bailey *et al.*, 2016	456 primary tumors; 41 patient-derived cell lines; mouse-derived PDAC cell lines.	**Squamous:** enriched for *TRP53* mutations, activated integrin signaling and activated epidermal growth factor (EGF) signaling. Hypermethylation of genes involved in pancreatic endodermal cell fate determination;	13.3	Integrated genomic analysis (whole-genome and deep-exome sequencing, with gene copy number analysis) and RNA sequencing.	Overlapping with Collisson's and Moffitt's work: Squamous with "QM" and "basal-like"; Pancreatic progenitor with both "Classical" subtypes; and ADEX with "exocrine-like" subtype. Only Immunogenic subtype did not overlap with previous subtypes.
		Pancreatic progenitor: expression of genes involved in early pancreatic development;	23.7		
		Immunogenic: immune infiltrate with B cell signaling pathways, antigen presentation, $CD4^+$ and $CD8^+$ cell signaling pathways;	30		
		Aberrantly differentiated endocrine exocrine (ADEX): transcriptional networks in later stages of pancreatic development and differentiation.	23.6		

ADEX, aberrantly differentiated endocrine exocrine; CD, cluster of differentiation; EGF, epidermal growth factor; PDAC, pancreatic ductal adenocarcinoma; QM, quasimesenchymal; *TRP53*, *transformation-related protein 53*.

of transcription factors and downstream targets: 1) squamous was enriched for *TRP53* mutations and had a poor prognosis; 2) pancreatic progenitor presented preferential expression of genes involved in early pancreatic development (such as, *pancreatic and duodenal homeobox 1*, *PDX1*); 3) immunogenic, which was characterized by upregulation of immune pathways; and 4) aberrantly differentiated endocrine exocrine (ADEX) displayed upregulation of genes involved in *KRAS* activation and exocrine and endocrine differentiation (Bailey et al., 2016). All the mentioned studies show that an unlimited number of characteristics can be selected as features to classify patients and their subtype-based stratification has the potential for genomics-driven precision medicine (Aung et al., 2018). Even though in these genomic studies, the usage of human samples was crucial, yet the mouse samples also provided important information about human PDAC.

3.1.2. Modeling the biology of pancreatic ductal adenocarcinoma in mice

Among the tumor entities, pancreatic cancer is the least accessible, due to the retroperitoneal location of pancreas rendering this an issue for routine tissue sampling. As such, genetically engineered mouse models (GEMMs) of PDAC loom several benefits to study human diseases since they faithfully recapitulate the genetic and biological evolution of the human cancer. This allows not only to address basic tumor biological questions, but also to develop strategies for early detection, improve clinical drug testing and assessment of therapeutic responses. However, caution remains in assuming that information generated by animal models can be directly translatable to human cancer.

During the 80s, tissue-specific transgene expression and transgenic tumor induction in mouse pancreas were achieved (Quaife et al., 1987; Swift et al., 1984). With the expansion of knowledge in genetic basis of PDAC and the consensus regarding PanINs being direct non-invasive neoplastic precursor lesions to human pancreatic cancer, significant progress was made in pancreatic developmental biology, especially with the identification of transcription factors and signaling pathways underlying pancreatic morphogenesis and cell differentiation (Ahlgren et al., 1996; Krapp et al., 1998). *Pdx1* and *pancreas transcription factor 1a* (*Ptf1a-p48*) are among the factors identified as critical regulators of early embryonic pancreatic development and both are expressed at the pancreas epithelial progenitor stage. For this reason, these factors have been widely used as promoters in transgenic mouse models to study PDAC (Schönhuber et al., 2014; Seidler et al., 2008). As *Kras* mutations are not sufficient to induce PDAC, a conditionally expressed allele needed to be constructed to target the expression of this oncogene in pancreatic progenitor cells (Hingorani et al., 2003). Hingorani *et al.* developed a GEMM with conditional *Cre/loxP*-based activation of an endogenous *Kras* allele in pancreatic progenitor cells, either by a *Pdx1* promoter-driven transgene or by *Cre* knockin at the *Ptf1a-p48* locus (Hingorani et al., 2003). Cre recombinase excises the stop codon flanked between the *loxP* sites in the *Lox-STOP-Lox* (*LSL*) $Kras^{G12D}$ transcript and subsequent recombination allows the expression of the mutant allele engineered to contain a glycine (G) → aspartic acid (D) substitution in codon 12, one of the most common mutations found in human PDAC. With this GEMM, also referred as PK mouse model, it was possible to develop pancreatic tumors in mice that faithfully recapitulated human

disease with PanIN lesion development and progression to invasive and metastatic PDAC. Liver, lung, and lymph node are the typical organs metastasized by pancreatic cancer cells (PCCs) (Hingorani et al., 2003). In addition, to mimic with more accuracy what is observed in the human PDAC, *Kras*^{G12D} mice have been crossed with loss-of-function or mutant alleles, such as *Cdkn2a*, *Trp53* and/or *Smad4* (Bardeesy, Aguirre, et al., 2006; Bardeesy, Cheng, et al., 2006). The presence of inactivated tumor suppressors increased the tumor development up to 100% and significantly shortened their latency compared to the PK model.

As mentioned above, mutational activation of *BRAF* or *PIK3CA* only occurs in rare cases of human PDAC. Yet, the generation of GEMMs with these mutations may provide relevant information regarding essential signaling pathways involved in the development and progression of PDAC. While developing the *Braf* model (also referred as PBR), Collisson and colleagues realized that, upon Cre activation, the expression of *BRAF*^{V600E} mutation (the equivalent mouse mutation is *Braf*^{V637E}) resulted in embryonic lethality (Collisson et al., 2012). To circumvent this issue, the expression of *BRAF*^{V600E} mutation in pancreas was controlled by a tamoxifen-inducible Cre recombinase under *Pdx1* promoter (*Pdx1-CreER*^{T2}). Similarly to PK model, this PBR model led to PanIN lesion formation; however these PanINs did not progress to PDAC tumors at least within one year (Collisson et al., 2012). To examine other mutations that may be able to initiate PDAC independently of *Kras*, GEMMs harboring *Pik3ca* mutations were also generated. Eser and colleagues developed a GEMM where the *Pik3ca*^{H1047R} hotspot mutation, the most common mutation of the *PIK3CA* among solid tumors, was expressed in the pancreas by *Ptf1a-p48*^{Cre} (Eser et al., 2013). Histopathologically, *Pik3ca*^{H1047R}-induced tumors were indistinguishable from the ones induced by *Kras*^{G12D} mutation, ranging from well-differentiated to undifferentiated PDAC and presenting metastases in the same organs as the PK model (Hingorani et al., 2003; Payne et al., 2015). Posteriorly, using the same mutation in *Pik3ca*, Payne and colleagues investigated the effects of a constitutively active phosphoinositide 3-kinase (PI3K) in the pancreas by expressing the H1047R mutation under the *Pdx1* promoter (Payne et al., 2015). This model, also referred as PPI3K, showed that the activation of this signaling pathway leads to development of pre-malignant lesions and invasive PDAC in 80% of the mice as well as high infiltration of stromal cells. So, by using the mentioned GEMMs, the role of the signaling pathways in PDAC development and progression as well as its impact in the microenvironment can be studied.

3.1.3. KRAS, BRAF, and PIK3CA and their signaling pathways

Mutationally activated *KRAS* gene comprises the most frequently mutated gene in human cancer, including PDAC, and it belongs to the *RAS* family together with *NRAS* and *HRAS* (Liu et al., 2019). The RAS proteins are small GTPases that function as binary ON-OFF molecular switches, cycling between guanosine diphosphate (GDP)-bound (inactive) and guanosine triphosphate (GTP)-bound (active) (Menyhárd et al., 2020). The regulation of RAS signaling consists in a balance between activation by guanine nucleotide exchange factors (GEFs) and inactivation by GTPase-activating proteins (GAPs) (Maurer et al., 2012; Trahey & McCormick, 1987). Upon the binding of a ligand to an upstream receptor such as a tyrosine kinase receptor,

KRAS is activated and transmits signals from the cell membrane to the nucleus, leading to activation of transcription factors involved in the regulation of several intracellular signaling networks. Among the crucial roles of RAS proteins are the regulation of cell proliferation and survival acting upon signaling pathways such as RAF/mitogen activated protein kinase (MEK)/extracellular signal-regulated kinase (ERK) and PI3K/serine-threonine kinase (AKT)/mechanistic target of rapamycin kinase (mTOR) (Kennedy et al., 2011; Ozkan-Dagliyan et al., 2020). All the essential steps from the extracellular stimuli that activates RAS to the cascades of RAF and PI3K are illustrated in Fig. 2. When mutated, KRAS remains constitutively active, being thereby persistently “ON”, which in turn enhances its downstream signaling associated with tumorigenesis (Smith et al., 2013). Despite decades of extensive attempts to develop an effective therapy against RAS, no therapeutic agent has successfully target this GTPase, so no drug has been clinically approved. For this reason, RAS has been historically considered “undruggable”. However, a recent study developed by Kessler and colleagues showed that, using a structure-based nanomolar inhibitor, it is possible to inhibit KRAS by blocking the interaction between GDP-KRAS and GEFs as well as inhibiting the interactions between GTP-KRAS with its effectors (RAF and PI3K) (Kessler et al., 2019). These inhibitions reduced the phospho-ERK and phospho-AKT levels and consequently led to an anti-proliferative effect. The success in the identification of direct RAS-binding compounds rendered that perhaps RAS is indeed “druggable” after all.

Among the downstream effectors of RAS network are RAF and PI3K signaling pathways, two pathways that have been studied most extensively in PDAC and their blockage has been exploited for cancer therapies. The RAF family (ARAF, BRAF, and CRAF) is composed by serine-threonine protein kinases that have critical roles in mediating many cellular functions such as growth, apoptosis, migration, and differentiation (Matallanas et al., 2011). Under physiological conditions, after activation of RAS, there is an increased accumulation of RAF proteins at the plasma membrane where they are phosphorylated and activated. Consequently, RAF phosphorylates and activates MEK isoforms (MEK1 and MEK2), which in turn phosphorylate and activate the ERK isoforms (ERK1 and ERK2). Furthermore, ERK isoforms can then activate cytosolic targets or be translocated to the nucleus (Matallanas et al., 2011). Given the important roles of RAF/MEK/ERK signaling, its activation is tightly regulated, having several negative feedback controls that limit its activity. However, these negative feedback signals are often bypassed upon genetic alterations of RAS and RAF proteins that destabilize their inactive conformation and promote the active state, which lead to hyperactivation of RAF/MEK/ERK cascade (Wan et al., 2004). In order to target this signaling pathway for cancer therapy, RAF inhibitors (e.g., ponatinib), MEK inhibitors (e.g., AZD-6244 and GDC-0623), and ERK inhibitors (e.g., SCH772984) have been developed and applied to therapy (Alagesan et al., 2015; Baumann et al., 2020; Bryant et al., 2019; Cotto-Rios et al., 2020). Recently, Baumann and colleagues showed synergistic anti-tumor efficacy resulted from the combination of MEK inhibitor GDC-0623 with agonist antibodies targeting the immunostimulatory cluster of differentiation (CD)40 receptor, a transmembrane protein expressed in antigen-presenting cells, such as dendritic cells (DCs),

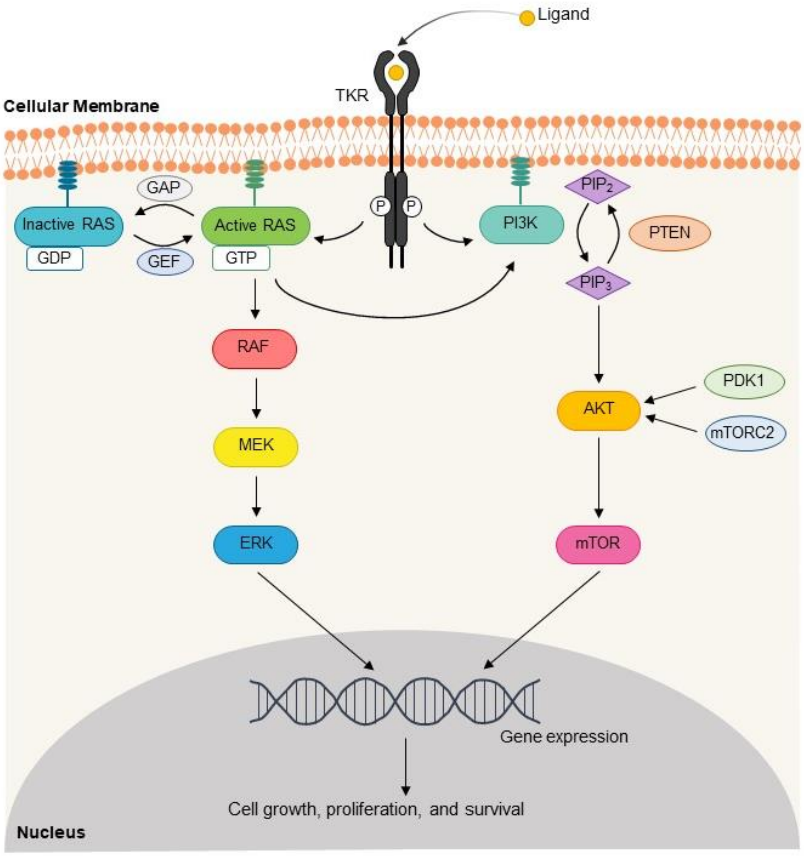

Fig. 2. Rat sarcoma virus (RAS), Rapidly accelerated fibrosarcoma (RAF), and Phosphoinositide 3-kinase (PI3K) signaling cascades.
Ligand binds to the extracellular domain of the tyrosine kinase receptor (TKR) and results in phosphorylation of the intracellular domains. Activated TKR leads to activation of rat sarcoma virus (RAS) through guanosine triphosphate (GTP)-bound (active RAS) or activation of phosphoinositide 3-kinase (PI3K). Regarding the RAS cascade, the balance between active and inactive (guanosine diphosphate (GDP)-bound) conformations is controlled by GTPase-activating proteins (GAPs) and guanine nucleotide exchange factors (GEFs). Activation of RAS can promote the activation of rapidly accelerated fibrosarcoma (RAF), mitogen activated protein kinase (MEK), and extracellular signal-regulated kinase (ERK). Besides the RAF cascade, active RAS can also promote the PI3K cascade. PI3K phosphorylates phosphatidylinositol-4,5-bisphosphate (PIP_2) to phosphatidylinositol-3,4,5-bisphosphate (PIP_3); this phosphorylation is negatively regulated by phosphatase and tensin homolog deleted on chromosome 10 (PTEN). In turn, PIP_3 activates serine-threonine kinase (AKT); this kinase is fully activated following phosphorylation either by 3-phosphoinositide-dependent protein kinase 1 (PDK1) or by the mechanistic target of rapamycin kinase complex 2 (mTORC2). Once activated, AKT phosphorylates mTOR that, together with ERK, triggers expression of genes involved in cell growth, proliferation, and survival.
AKT denotes the serine-threonine kinase, ERK the extracellular signal-regulated kinase, GAP the GTPase-activating protein, GDP the guanosine diphosphate, GEF the guanine nucleotide exchange factor, GTP the guanosine triphosphate, MEK the mitogen activated protein kinase, mTORC2 the mechanistic target of rapamycin kinase complex 2, PKD1 the 3-phosphoinositide-dependent protein kinase 1, PIP_2 the phosphatidylinositol-4,5-bisphosphate, PIP_3 the phosphatidylinositol-3,4,5-bisphosphate, PI3K the phosphoinositide 3-kinase, PTEN the phosphatase and tensin homolog deleted on chromosome 10, RAF the rapidly accelerated fibrosarcoma protein, RAS the rat sarcoma virus protein, TKR the tyrosine kinase receptor.

and B lymphocytes (Baumann et al., 2020). The MEK inhibitor exerted a strong anti-tumor cytotoxicity along with pro-immunogenic effects on tumor and TME. On one hand, there was an enhancement of major histocompatibility complex (MHC)-restricted antigen presentation and suppression of myeloid-derived suppressor cells (MDSCs), M2-type tumor-associated

macrophages and regulatory $CD4^+$ T cells (Tregs) (Baumann et al., 2020). While, on the other hand, agonist anti-CD40 complemented the drug action through the increase of antigen presentation and stimulation of Tregs and cytotoxic $CD8^+$ T lymphocytes (CTLs). Another family of kinases is the PI3Ks, a family of lipid enzymes whose main function is catalyze the phosphorylation of phosphoinositides (Jean & Kiger, 2014). Depending on their primary structure, substrate specificity and regulation, PI3Ks are divided into three main classes (class I, II, and III). p100α is one of the catalytic subunits that belongs to the class I PI3Ks and it is encoded by the *PIK3CA* gene. In response to extracellular stimuli, catalytic subunits of class I PI3Ks (p110α, p110β, and p110δ) are recruited to activated membrane receptors (Jean & Kiger, 2014). PI3Ks phosphorylate phosphatidylinositol-4,5-bisphosphate (PIP_2), promoting the formation of plasma membrane–associated phosphatidylinositol-3,4,5-bisphosphate (PIP_3) (Chalhoub & Baker, 2009). PIP_3 can then recruit AKT informs (AKT1, AKT2, and AKT3) that are fully activated upon phosphorylation either by 3-phosphoinositide–dependent protein kinase 1 (PDK1) or by the mTOR complex 2 (mTORC2). AKT activation eventually triggers mTOR and other downstream pathways involved in cell growth, proliferation, and survival. As every crucial pathway, PI3K signaling is highly regulated by negative regulators that dephosphorylate PIP_3 into PIP_2, being the phosphatase and tensin homolog deleted on chromosome 10 (PTEN) the major endogenous PI3K inhibitor (Chalhoub & Baker, 2009). The loss of balance of PIP_3 levels may lead to dramatic consequences, such as aberrant cell growth and proliferation, which subsequently can lead to cancer development. Several drugs have been developed to target the PI3K pathway, including PI3K inhibitors (e.g., BKM-120 and GDC-0941), PI3K/mTOR inhibitors (e.g., BEZ235), mTOR inhibitors (e.g., metformin), or AKT inhibitors (e.g., MK-2206), which have been tested individually or in combination with other agents (Alagesan et al., 2015; Hu et al., 2015; Sinnett-Smith et al., 2013; Venkannagari et al., 2012). Despite the success of many of these drugs to increase apoptosis, block tumor growth, prevent metastasization and extend survival, drug-related dosage-dependent toxicity and development of drug resistance are major challenges to the therapy. Altogether, these studies not only argue for the exploration of combinatory therapy that targets signaling pathways and the surrounding TME, but also point to the importance of understanding the underlying cellular and molecular mechanisms governing the interactions between PCCs and cells within the TME that can be used as a novel strategy to fight cancer.

3.2. Tumor Microenvironment

A key histopathological feature that starts to evolve early around PanIN lesions and accompanies the PDAC development is the surrounding microenvironment, also known as desmoplastic (stromal) reaction. Among the different tumor entities, pancreatic cancer is the one characterized by having the highest stromal-to-tumoral ratio, accounting a stroma formation of up to 90% of the tumor volume (Neesse et al., 2011). Several studies have shown that the stromal response influences tumor growth, progression, migration, invasion, angiogenesis, metastasis

formation, and chemoresistance (Hwang et al., 2019; Nielsen et al., 2016; Orozco et al., 2018). The desmoplastic reaction is composed by an abundance of extracellular matrix (ECM) proteins (mainly collagen, fibronectin, and proteoglycans) and a diverse population of cells including PSCs, cancer-associated fibroblasts (CAFs), immune cells, and endothelial cells (ECs) (Orozco et al., 2018). In an initial phase of the tumor formation, the production of stroma is stimulated by PCC-derived growth factors such as transforming growth factor-beta (TGFβ), epidermal growth factor (EGF), fibroblast growth factor (FGF), and insulin-like growth factor 1 (IGF1) (Neesse et al., 2011). This creates a unique network that orchestrate a complex tumor-stromal cross-talk and it is still widely debated whether the surrounding desmoplastic cells support or restrain cancer progression and contribute to therapeutic resistance in PDAC. Recently, Elyada and colleagues showed that, in established tumors, the major TME population (~87%) is composed by myeloid cells, consisting of macrophages, neutrophils, and a small subset DCs, whereas the CAF fraction is reduced to around 2% of all cells, depicting a predominant strong immunosuppressive microenvironment in PDAC (Elyada et al., 2019). For decades, it was believed that the desmoplastic reaction functioned as defensive response of pancreas aimed to confine tumor growth and spread to distant organs. However, numerous studies emerged providing evidence that the TME elements promote tumorigenesis and are correlated to poor prognosis, showing the duality of roles that the various components of the TME may play (Mahajan et al., 2018; Tian et al., 2019). Furthermore, the tumor stroma has been also recognized as an attractive therapeutic target in PDAC, especially because, contrarily to PCCs, cells within the TME are genetically stable and less susceptible to develop resistance (Bhome et al., 2016; Murciano-Goroff et al., 2020). Thus, the improvement of our knowledge regarding pancreatic carcinogenesis as well as the role of the surrounding stromal cells throughout tumor progression is believed to open the way towards the development of novel clinical therapeutic treatments.

3.2.1. Pancreatic stellate cells and Cancer-associated fibroblasts

Stratification systems based on tumor and microenvironment features reflect the importance of the desmoplastic reaction in human PDAC. An “activated” stroma-specific subtype is characterized by activated inflammatory stromal response and high levels of fibroblast-related genes and correlated to worse prognosis for patients. Thus, it seems to exist a complex interplay between CAFs and malignant cells that leads to tumor-promoting or tumor-suppressing functions. CAFs are recognized as a key cell population and an active component of pancreatic TME, which undergo morphological and functional changes when compared to normal fibroblasts. During pancreatic tumorigenesis and progression, activated PSCs are generally considered to be the most predominant source of CAFs within the pancreas and are responsible for most of the desmoplastic reaction (Apte et al., 1999; Öhlund et al., 2017). In a healthy pancreas, PSCs comprise up to 4% of all the pancreatic cells and, under physiological conditions, they are predominantly in their quiescent state, exhibiting cytoplasmic lipid droplets and expressing both desmin and glial fibrillary acidic protein (GFAP) (Apte et al., 1998; Apte et al., 1999; Öhlund et al., 2017). Upon activation, a PSC transforms from a quiescent vitamin A-storing cell to a highly

activated myofibroblast-like cell with additionally expression of the cytoskeletal protein smooth muscle actin alpha (αSMA) (Apte et al., 1998; Apte et al., 1999). Several growth factors and cytokines including TGFβ, platelet-derived growth factor (PDGF), tumor necrosis factor alpha (TNFα), and interleukin 8 (IL8), as well as inflammatory and oncogenic signals can stimulate the activation of PSCs (Schneider et al., 2001; Wang et al., 2019). In PDAC, it has been demonstrated that activated PSCs accompany PCCs to distant metastatic sites where they promote colonization, survival, and proliferation, stimulate angiogenesis within the tumor and have the capacity to intravasate/extravasate through blood vessels (Xu et al., 2010). Thus, this suggests a pro-tumorigenic interplay between stromal and tumor cells. PSCs and CAFs share several overlapping features, from the expressed markers and the produced ECM proteins to the ability to reverse back to their quiescent states. Firstly, CAFs express markers also present in mesenchymal cells such as αSMA and vimentin, as well as common fibroblast markers including PDGF receptor (PDGFR), FAP alpha (FAPα), collage type I alpha 1 chain (COL1A1) and podoplanin (PDPN), a surface protein identified by single cell RNA sequencing (scRNA-seq) as a pan-CAF marker (Elyada et al., 2019). Altogether, this indicates that a unique CAF biomarker cannot define the entire CAF population; instead, the heterogeneity of markers points towards the existence of distinct subpopulations characterized by specific combination of several markers. Secondly, similarly to PSCs, CAFs also play a role in the synthesis and deposition of ECM, being the main source of fibrotic matrisomal proteins, including collagens (e.g., collagen VI and collagen IX), glycoproteins (e.g., fibrillin and laminin), proteoglycans (e.g., proteoglycan 2 and lumican), and ECM regulators (e.g., trypsin-2 and cathepsin G) (Tian et al., 2019). Thirdly, both PSCs and CAFs can revert to a quiescent and non-proliferative phenotype upon termination or blockage of the activation stimuli (Dauer et al., 2018; Lachowski et al., 2017). Usage of drugs that would inactive CAFs can be considered as an appealing therapeutic strategy, as this would disrupt the tumor-stroma cross-talk and potentially halt tumor progression.

According to specific markers expressed by CAFs and their functions, these fibroblasts of PDAC TME can be divided into subtypes: 1) myofibroblastic CAFs (myCAFs); 2) inflammatory CAFs (iCAFs); 3) antigen-presenting CAFs (apCAFs); and 4) lipofibroblasts (Elyada et al., 2019). myCAFs showed a high expression of smooth muscle genes *ACTA2* and *transgelin*, *PDGFR beta* (*PDGFRB*) and *COL12A1* and they are associated with epithelial-to-mesenchymal transition (EMT), myogenesis, ECM receptor interaction and focal adhesion pathways (Elyada et al., 2019; Öhlund et al., 2017). Therefore, myCAFs may have a role in dissemination to distant organs and high amounts of this subtype of fibroblasts in the tumors might be correlated to poor drug response. iCAF subcluster is characterized by low expression of αSMA and high expression of chemokines and inflammatory mediators such as *IL6*, *chemokine (C-X-C motif) ligand 1* (*CXCL1*) and *lymphocyte antigen 6 complex locus C1* (*LY6C1*), and specific collagens (e.g., *COL14A1*), which suggest more pro-tumorigenic properties of iCAFs (Elyada et al., 2019; Öhlund et al., 2017). myCAFs and iCAFs are found in distinct spatial locations and they result from distinct interactions between quiescent PSCs and PCCs (Öhlund et al., 2017). On one hand, myCAFs are in the periglandular region, being most proximal to tumor cells and their formation requires juxtacrine

interactions between PSCs and PCCs. While, on the other hand, iCAFs are more distal to tumor cells, which secrete factors that induce PSCs to acquire an inflammatory phenotype through paracrine manner signaling. Regarding apCAFs, this subcluster is distinct from both myCAFs and iCAFs and is characterized by the expression of genes that belong to the class II MHC family (such as, *CD74* and *histocompatibility 2 class II antigen A beta 1*, *H2-Ab1*), which are usually restricted to antigen-presenting cells of the immune system (Elyada et al., 2019). In addition, these CAFs also express other inflammatory-related genes such as *secretory leukocyte peptidase inhibitor* (*SLPI*), *Na^+/K^+-transporting ATPase subunit beta-1-interacting protein 4* (*NKain4*) and *interferon regulatory factor 5* (*IRF5*). The authors hypothesize that apCAFs can interact with $CD4^+$ T cells as a decoy receptor to deactivate these immune cells through the induction of anergy or differentiation into Tregs and decrease the amount of CTLs (Elyada et al., 2019). Thus, apCAFs might contribute to an immunosuppressive environment in PDAC. myCAF, iCAF and apCAF populations have been confirmed to be present in human PDAC highlighting that GEMMs are a powerful tool to faithfully recapitulate human malignancies and their environments (Elyada et al., 2019; Öhlund et al., 2017). Notably, in mice tumors, myCAFs and iCAFs are equally distributed composing approximately 45% of the $PDPN^+$ population, while there was only about 10% of apCAFs within all CAFs. Lastly, a small cluster of fibroblasts was identified as lipofibroblasts, a lineage that, similarly to PSCs, presents lipid droplets and expresses lipid metabolism genes including *fatty acid binding protein 4* (*FABP4*) and *carbonic anhydrase 3* (*CAR3*) (Elyada et al., 2019). Regardless the subpopulation, CAFs are highly plastic, increasing the heterogeneity of already heterogeneous pancreatic tumors. This means that the fibroblasts are dynamic and can transdifferentiate into different phenotypes based on their spatial and TME cues. CAFs' plasticity presents an exciting opportunity to target specific subpopulations, for example, by converting myCAFs and iCAFs into apCAFs. Nevertheless, further research is essential to fully assess whether the fibroblasts are targetable cells and understand the effects of their therapeutic targeting. The advances in scRNA-seq and other technologies will allow to expand the knowledge regarding CAF populations present in the pancreatic TME and explore their functions and interactions with surrounding cells, with the ultimate aim of unveil if they are good candidates for targeted therapies.

3.2.2. Innate and Adaptive immune cells

Although the TME of PDAC is mainly composed by stromal cells, it is also replete with immune cells. The link between inflammation and PDAC tumorigenesis is well known, and it is related to the activation of inflammatory mediators involved in tumor growth, apoptosis, metastatic dissemination, and drug resistance, which are hallmarks of this disease (Delitto et al., 2015; Hanahan & Weinberg, 2011; Hausmann et al., 2014). Among the inflammatory signaling pathways associated with PDAC are nuclear factor κB (NFκB), the key modulator of inflammation-induced carcinogenesis; IL6/signal transducer and activator of transcription 3 (STAT3) and toll-like receptors (TLRs), both having an important role in acceleration of cancer development; and TGFβ that can play a dual role in tumorigenesis, being either tumor-suppressive or tumor-

promoting (Hausmann et al., 2014). Notably, the immune reaction to cancer harbors dual potential for suppressing or promoting its development and thus shaping its progression. This polarity of the immune response is partly due to the existence of innate and adaptive immunity (Chang & Beatty, 2020; Hastings, 2008), as illustrated in Fig. 3. While the innate immunity represents the first line of defense against cancer through the recognition of tumor cells as strange to the organism and proceeding to their elimination, being characterized by having a fast response, oppositely to the adaptive immunity that has a slower response since it requires antigen-specific responses. The innate immune cells (IICs) include macrophages (also referred as tumor-associated macrophages), DCs, natural killer (NK) cells, granulocytes, and MDSCs, and all these cells, apart from the NK cells, have a myeloid lineage progenitor. Whilst the adaptive immune cells (AICs) comprise the T and B lymphocytes and NK T cells, which have a lymphoid lineage progenitor. The immune cells are either tissue resident or they are recruited by cancer cells from the bone marrow or the spleen via aberrant overexpression of inflammatory cytokines, which either augment or inhibit the host immune response (Haas & Obenauf, 2019; Parente et al., 2018). The immune content changes throughout tumor progression: in early stages of the disease, lymphocytic infiltration is prominent, creating a TME suitable for the growth of early lesions, and in invasive stages, macrophages, MDSCs, DCs, and Treg cells help to establish an

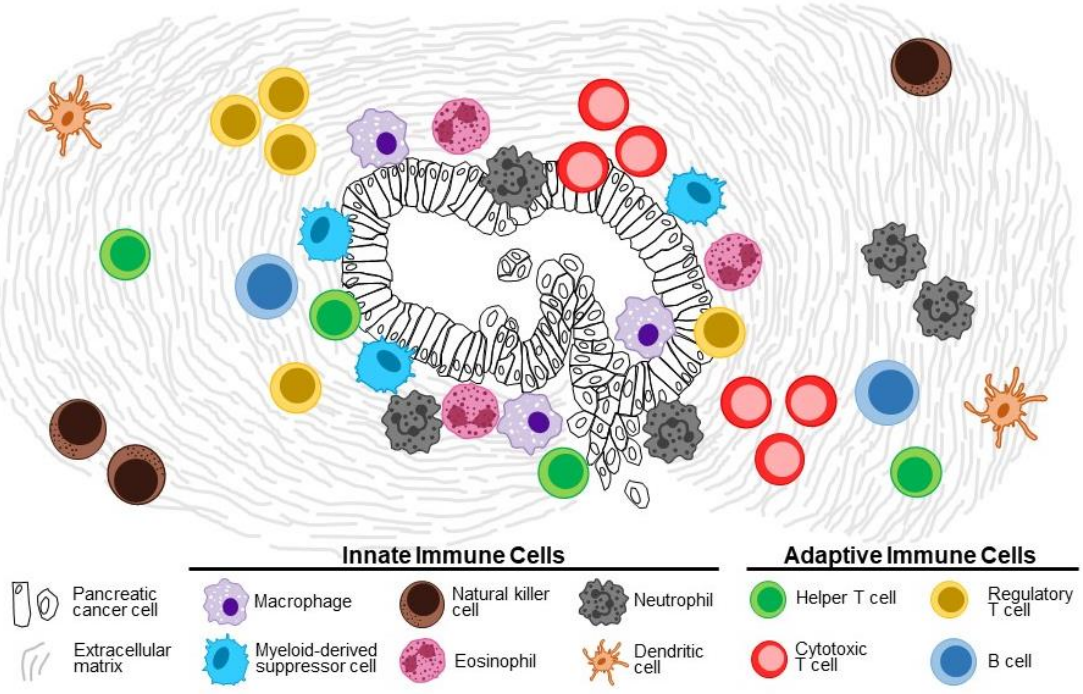

Fig. 3. Immune cells within the tumor microenvironment of pancreatic ductal adenocarcinoma. Besides the stromal cells that secrete an abundance of extracellular matrix proteins, the pancreatic tumor microenvironment is also composed by immune cells. The cells of the immune system can be divided into innate and adaptive immune cells. The innate immunity comprises the following cells: macrophages, natural killer cells, myeloid-derived suppressor cells, granulocytes (neutrophils and eosinophils), and dendritic cells. Whereas the adaptive immune cells are composed by T and B lymphocytes. The immune content, their spatial distribution, and their interactions with the malignant cells change throughout cancer progression, harboring dual potential for suppressing or promoting tumor development.

immunosuppressive TME, therefore escaping from the host immune surveillance (Clark et al., 2007; Lee et al., 2020). Interestingly, the interactome, i.e. the prediction of potential ligand-receptor interactions based on scRNA-seq, allows to assess potential relationships between PCCs and immune cells. Lee and colleagues observed that epithelial tumor cells have a close interaction with DCs and myeloid cells, but fewer connections with lymphocytes (Lee et al., 2020). Thus, the characterization of the complex and heterogeneous immune landscape of PDAC can provide valuable clues regarding the dynamic interplay between malignant and immune cells. In turn, this information can then be employed in the development of novel therapeutic strategies that aim to restore an immunoreactive microenvironment and, in doing so, create and maintain the immunogenicity of tumors to yield durable responses to immunotherapy.

Tumor-associated macrophages

Macrophages are tissue sentinels that maintain tissue integrity by eliminating damaged cells and repairing matrices (Italiani & Boraschi, 2014). These cells have origin in monocytes, which differentiate due to the influence of macrophage colony stimulating factor (M-CSF) and granulocyte/monocyte CSF (GM-CSF) produced by stromal cells. Macrophages are characterized by their cellular plasticity that enables them to obtain different phenotypic and functional states, being categorized in two extreme polarization states. On one hand, M-CSF promotes the polarization of macrophages into an anti-inflammatory or homeostatic M2-like phenotype; while, on the other hand, GM-CSF leads to a M1-like inflammatory phenotype (Italiani & Boraschi, 2014). CSF1 receptor (CSF1R; also referred as CD115) is one of the macrophage markers together with F4/80 and CD68 (Clark et al., 2007; Italiani & Boraschi, 2014; Steele et al., 2020). As in most solid tumors, tumor-associated macrophages represent the most abundant immune population within the TME of PDAC and their infiltration begins incredibly early in pre-invasive disease, being recruited by PCC-secreted factors and persisting throughout the tumor development (Clark et al., 2007; Panni et al., 2019; Steele et al., 2020). These immune cells preferentially accumulate around neoplastic ducts in PanIN lesions and in invasive carcinomas they are more evident in surrounding tumor stroma interacting with AICs, such as T helper (Th) cells, CTLs, and NK cells. In turn, macrophages secrete pro-tumorigenic factors such as IL6, M-CSF and MMPs, and immunosuppressive factors including TGFβ, having thus a dual role promoting tumor growth and dissemination due the induction of EMT as well as creating an immunosuppressive TME (Amit & Gil, 2013; Helm, Held-Feindt, et al., 2014; Tekin et al., 2020). Moreover, macrophages can also promote drug resistance. Amit and Gil showed that macrophages stimulate the upregulation of cytidine deaminase, an intracellular enzyme responsible for the inactivation of gemcitabine, by malignant cells (Amit & Gil, 2013). Interestingly, therapeutic usage of a CSF1R inhibitor in a PDAC mouse model decreased the total amount of macrophages, especially the pro-tumoral ones (Zhu et al., 2014). The CSF1R blockade overcame immune suppression, leading to an upregulation of CTL responses, T cell recruitment and interferon (IFN) responses. Considering all these facts, macrophages represent a potential

therapeutic target, whereby their activation, recruitment, and reeducation might have beneficial anti-tumorigenic effects on PDAC.

Dendritic cells

DCs are important players in the network of phagocytizing and antigen presentation to naïve T cells (Gardner & Ruffell, 2016). These mononuclear cells develop in the bone marrow from common DC precursors that give rise to plasmacytoid DC (pDC) and conventional DC (cDC) subsets and from classical monocytes that under inflammatory conditions can differentiate to generate the monocyte-derived inflammatory DC (inf-moDC) subset. The maturation process is initiated upon recognition of danger-associated molecular patterns via pattern recognition receptors (PRRs), which contribute for the specific functions of each DC subset (Gardner & Ruffell, 2016). As a result of maturation, DCs upregulate their antigen presentation machinery and costimulatory molecules, rendering them the capacity of differentiation and activation of T cells, and thus bridging innate and adaptive immunities. The cDCs express CD11c, CD68 and MHCII markers and these myeloid cells are divided into two classes: cDC1s, which specialize in CTL activation, and cDC2s, which specialize in Th cells. In PDAC, the production of G-CSF by PCCs downregulates IRF8 in cDC progenitors, which results in reduction of cDC1 development (Hegde et al., 2020; Meyer et al., 2018). The scarcity of cDCs compared with macrophages or neutrophils favors the expansion of tumor-promoting Th cells and correlates with poor patient outcome. Thus, overcoming deficiency of these myeloid cells in early stage PDAC leads to suppression of tumor growth, while restoration of cDC function in advanced stages restores tumor restraining immunity due to the enhancement of CTL and Th cell activities. Altogether, these findings expand our understanding of DCs' role in PDAC and open opportunities to combinatorial strategies to modulate these immune cells in combination with existing therapies.

Natural killer cells

As their name suggests, NK cells are "naturally" cytotoxic and, in contrast to AICs, they do not require prior antigen exposure to mediate their cytolytic functions (Abel et al., 2018). NK cells are identified by the presence of NK1.1, natural cytotoxicity triggering receptor 1 (NCR1; also referred as CD335), and CD49b. Activation of these cells is determined by the balance between activating and inhibitory receptor stimulation and, once activated, NK cells produce pro-inflammatory and immunosuppressive cytokines (Abel et al., 2018). These include IFNγ, TNFα, GM-CSF, CCL3 and IL8, which promote the recruitment and activation of T cells as well as innate immune mediators such as macrophages, DCs, and neutrophils. NK cells are present in high frequency in blood of PDAC patients, even though the migration of these cells into the tissue is rather low (<0.5%) (Lim et al., 2019). The scarcity of NK cells within the tumors is related to the following factors: 1) the lack of a proper chemokine signaling that could attract these IICs to the tumors; 2) poor engagement of activating receptors, which indicates impairment of killing tumor cells, promoting thus PDAC progression; and 3) upon reaching a hypoxic TME, circulating NK cells fail to survive or proliferate, contributing to a specific immune escape of malignant cells.

Thus, understanding the mechanisms behind the impairment of chemokine signaling between NK cells and PCCs and their reactivation via the activator receptors may give use to the “natural” functions of these cells and contribute to anti-tumor immunotherapy.

Granulocytes

Granulocytes are the most abundant population of leukocytes. Their heterogeneity and plasticity shape innate, rapid immune responses as well as adaptive ones via antigen presentation, leading even to the suggestion of referring these cells as atypical antigen-presenting cells (Lin & Lore, 2017). The granulocytic family comprises neutrophils, eosinophils, and basophils. Neutrophils are the most dominant population among granulocytes and, analogously to the polarization stages observed in macrophages, this subset of granulocytes also exhibits an anti-tumorigenic N1 phenotype and a pro-tumorigenic N2 profile influenced by TGFβ (Fridlender et al., 2009; Lin & Lore, 2017). Neutrophils are characterized by expression of CD11b and Ly6G and they are a major source of pro-inflammatory cytokines (such as, TNFα, INFγ, IL12, and GM-CSF), chemokines (including CXCL1, CXCL5, and CCL5), MMPs (such as, MMP1, MMP2, and MMP9), and neutrophil elastase, which all together promote tumor proliferation and dissemination as well as recruitment of both stromal and immune cells (Fridlender et al., 2009; Gaida et al., 2012; Miller-Ocuin et al., 2019). Therefore, considering the contribution of neutrophils for the high metastatic propensity of PDAC, targeting or reprogramming the activity of these granulocytes might be promising for therapy.

Eosinophils represent a minority of peripheral blood leukocytes and they may promote or inhibit tumor growth, although the specific role in PDAC is not well studied (Varricchi et al., 2018). Eosinophils are identified by the expression of markers including CD193 and Siglec-F (Gitto et al., 2020). These granulocytes produce mediators such as eosinophil cationic protein, eosinophil peroxide, and eosinophil-derived neurotoxin, cytokines, chemokines, angiogenic and lipid mediators. IL5 is a particularly important cytokine, since it has a role on growth, proliferation, differentiation, maturation, and activation of eosinophils (Gitto et al., 2020; Varricchi et al., 2018). In tumorigenesis of pancreas, eosinophils are recruited into the microenvironment due to the release of IL5 by damaged pancreatic acinar cells and the levels of this cytokine are diminished in advanced lesions. Eosinophils accumulate in fibrotic regions rather than infiltrate into the tumors, which promote Th2 cell-associated immune response and tumor development (Gitto et al., 2020; Lin & Lore, 2017). Further research is needed to fully understand the role of eosinophils in PDAC and their potential for immunotherapy.

Finally, basophils represent an exceedingly rare population (<1%) of circulating leukocytes, demonstrating to be able to induce polarized Th cell responses (Lin & Lore, 2017). These granulocytes are characterized by expression of high affinity IgE receptor FcεRI and CD123. The presence of basophils expressing IL4 in tumor draining lymph nodes contributes to the stabilization of Th2 cells, having thus a tumor-promoting role in PDAC (De Monte et al., 2016). Similarly to eosinophils, the understanding of basophils contribution to the immune response in

PDAC would help decipher their role in this disease, which in turn may also provide therapeutic strategies via manipulation or targeting of these granulocytes.

Myeloid-derived suppressor cells

MDSCs are functionally defined as immunosuppressive and they represent a heterogenous population of immature myeloid cells. Through TME-related factors, MDSCs can acquire phenotypic and morphological features of macrophages and neutrophils, being then called monocytic (moMDSC) and granulocytic (gMDSC) MDSCs, respectively (Siret et al., 2019). moMDSCs are characterized by high expression of Ly6C and negative expression of Ly6G, whilst gMDSCs express Ly6G and lower levels of Ly6C. Both intratumoral MDSC subsets contribute to a strongly immunosuppressive TME due to their ability to disrupt major mechanisms of immunosurveillance including suppression of CTL proliferation and induction of their death as well as activation of Treg cells (Siret et al., 2019). Since immune suppression plays a pivotal role in regulating cancer progression, metastasization, and reduction of immunotherapy efficacy, MDSCs can be an immunomodulatory therapy target to block or at least alleviate their immunosuppressive activities and pro-tumorigenic functions. Administration of RIG-I-like helicases ligands, promising immunostimulatory RNA that entered phase I/Ib clinical trials for the treatment of advanced solid tumors, induced a reduction of suppressive capacity of MDSCs via a type I IFN-driven response (Metzger et al., 2019). Moreover, a switch from a M2/G2-towards a M1/G1-polarized phenotype in MDSCs and increased recruitment and activation of T lymphocytes and DCs were also observed. This study provides evidence that targeting MDSCs can reprogram and remodel the TME of PDAC to bust the immune response against PCCs.

T lymphocytes

T (thymus-derived) lymphocytes or $CD3^+$ cells can additionally express either CD8 glycoprotein on their surface and be called $CD8^+$ T cells (cytotoxic, CTL) or CD4 glycoprotein and be then called $CD4^+$ T cells (Golubovskaya & Wu, 2016). In addition, naïve $CD4^+$ T cells differentiate into distinct subsets upon stimulation by specific cytokines: Th2 (helper) by IL4 and Treg (regulatory) by IL2 and TGFβ. In turn, these subsets release specific cytokines that can have either pro- or anti-inflammatory functions. Th2 releases IL4, which is important for B lymphocytes, while Treg secretes TGFβ and IL10, a cytokine with an immunosuppressive function (Golubovskaya & Wu, 2016). Additionally to CD3 and CD4 markers, Th2 can also be identified by the expression of the transcription factor GATA binding protein 3 (GATA3) and Treg by the expression of CD25 and the transcription factor FOXP3. Collectively, T lymphocytes play a central role in orchestrating adaptive immune responses, such as killing transformed cells by CTLs, modulating the function of B cells by Th2 cells, and regulating immunosuppressive responses by Tregs. However, tumor progression and metastasization are evidence that malignant cells have the ability to bypass and escape these suppressive inflammatory responses of T cells. The recruitment of tumor-infiltrating lymphocytes (TILs) is correlated with the differentiation status (grading) of the tumor, thus in undifferentiated/advanced stage tumors, a reduction of CTLs and

$CD4^+$ T cells is observed together with a higher abundance of Tregs compared to well-differentiated tumors (Goebel et al., 2015; Helm, Mennrich, et al., 2014). Among the TILs in PDAC, CTLs are in general less abundant (<1% of $CD3^+$ TILs) than $CD4^+$ T cells, with an average CD8:CD4 ratio of 0.75 (Sakellariou-Thompson et al., 2017). This implies that CTLs are either excluded in invasive tumors or show no ability to inhibit tumor progression. PCCs express programmed death-1-ligand 1 (PD-L1), a ligand which binds to the program death receptor 1 (PD-1) expressed on activated TILs, and the interaction between these molecules leads to suppression of T cell activation and proliferation and posterior cell death. A combined blockage of PD-L1 and IL6 receptor (IL6R) to deplete CTLs revealed higher percentage of circulating $CD4^+$ T cells and significant increase of TILs within the TME (Mace et al., 2018). Thus, inactivation or depletion of CTLs may lead to an immunosuppressive environment and recovery of their effector role represents one of the main therapeutic goals towards the elimination of malignant cells. Furthermore, Th2 cells can be polarized and attacked through the secretion of IL13-mediated DCs, which in turn are activated by CAFs (De Monte et al., 2011; Goebel et al., 2015). Recruitment of Th2 cells within the TME exerts tumor-promoting effector functions through the secretion of cytokines (such as, IL6 and TNFα) that thereby promote differentiation of M2 macrophages and induce EMT of PCCs. Regarding Tregs, their depletion alters the TME with loss of myCAFs and infiltration of both macrophages and MDSCs and accelerates pancreatic carcinogenesis due to Th2 responses (Y. Zhang, J. Lazarus, et al., 2020). All the mentioned studies point the multiple roles of TILs within pancreatic TME to support the progression of PDAC.

B lymphocytes

B (bone marrow-derived) lymphocytes are responsible for the production of antibodies and they express a diversity of cell surface immunoglobulin (Ig; IgM, IgD, IgG, IgA and IgE), receptors recognizing specific antigenic epitopes (LeBien & Tedder, 2008). Once activated by an antigen, B cells generate memory B cells and high-affinity antibody-secreting plasma cells. These AICs are identified by the expression of markers such as CD19, CD20, CD40 and B220. In PDAC, the spatial intratumoral distribution of B lymphocytes influences rather these cells exert pro-tumorigenic and immunosuppressive functions as scatteringly infiltrated B cells or have a tumor-suppressive and immunostimulatory functions when organized in lymphoid structures (Castino et al., 2016). Interestingly, depletion of tumor-infiltrating B cells using an anti-CD20 antibody resulted in an increase of components of anti-tumor immune response including significant increase in genes related to T and NK cell infiltration (*CD4*, *CD8*, and *NCR1*), activation (*IL12*, *IFNG*, and *TNFA*), and recruitment (*CXC receptor 3, CXCR3*). In addition, inhibition of bruton tyrosine kinase, a kinase that regulates suppression of B cell and macrophage-mediated T cell responses, with the FDA-approved inhibitor ibrutinib restores anti-tumor immune responses, which in turn restrains tumor growth and improves responsiveness to chemotherapy (Gunderson et al., 2016). Thus, it is evident that tumor-infiltrating B cells are involved in the progression of PDAC, being essential continuing to understand their role in this disease to facilitate the development of new effective therapies.

Taken together, tumor cells and different immune cells cooperate and communicate to form a tumor-friendly environment. At early stages of cancer development, the cells of the immune system may exert a negative pressure, which frequently is overcome by malignant cells, shifting the balance from an anti-tumorigenic to a pro-tumorigenic environment. Whereas in advanced cancer stages, the immune cells modulate features such as tumor growth, EMT, invasion, and posteriorly dissemination of PCCs to distant organs. As such, cancer and TME cells are seen as cellular compartments that co-evolute rather than separate entities, therefore genetic alterations in PCCs can modulate and influence both stromal and immune cells.

3.2.3. Influence of driver mutations in the tumor microenvironment

In comparison to other tumor entities, PDAC has minimal mutational load and neoepitopes burden, meaning that the PCCs have a reduced expression of epitopes, which makes these cells more challenging to be recognized by the immune system (Alexandrov et al., 2013; Evans et al., 2016). Despite having an intrinsic impact on the tumor cell, genetic alterations, such as *KRAS* mutation, can also influence the surrounding environment to promote and maintain cancer malignancy. Mutant *KRAS* signaling in PCCs increases the secretion of GM-CSF, cytokines, and the growth morphogen sonic hedgehog (SHH), which in turn regulates myCAF expansion (Tape et al., 2016). Cancer-derived SHH also changes the proteosome of myCAFs, promoting the synthesis of ECM components and regulating secreted growth factors important for the function of these stromal cells. Reciprocally, activated myCAFs regulate proliferation and survival of tumor cells via IGF1 receptor/AXL-AKT axis (Tape et al., 2016). Moreover, oncogenic *Kras* mutations in pancreatic acinar cells trigger an augmented attraction of M1 macrophages due to the upregulation of intercellular adhesion molecule 1 (ICAM1) expression (Liou et al., 2015). Counterintuitively, M1 macrophages cooperate with Kras activation to promote progression from ADM through secretion of pro-inflammatory cytokines and proteases, accelerating PDAC tumorigenesis. Altogether, these findings provide a glimpse of how KRAS is involved in remodeling the TME and a better understanding of the impact of its activation in the components of the surrounding microenvironment may reveal putative targets with clinical relevance.

In contrast to *KRAS*, much less is known about the impact of tumor-related *PIK3CA* and *BRAF* mutations in the TME, especially in a PDAC context. *Pik3ca* mutation was shown to lead to abundant stromal and immune infiltration, namely by T lymphocytes (Payne et al., 2015; Sivaram et al., 2019). Both $CD4^+$ and $CD8^+$ T cells cooperate with each other to promote the growth of PCCs harboring *Pik3ca* mutation. Thus, tumor-intrinsic *Pik3ca* represses tumor immunogenicity in PDAC. Regarding *BRAF*, the mutation of this oncogene promotes a stromal cell-mediated immunosuppressive mechanism via tumor-secreted IL1 in melanoma (Khalili et al., 2012). In turn, IL1 stimulates CAFs, which contribute to the inhibitory effects on CTLs, by upregulating the checkpoint ligand molecules PD-L1, PD-L2 and cyclooxygenase 2 (COX2). In addition, another immune escape mechanism induced by *BRAF* involves the increased expression of immunosuppressive mediators, such as IL6, IL10, and vascular endothelial growth

factor (VEGF) (Sumimoto et al., 2006). These cytokines can impair maturation of DCs, and suppress their capacity to produce IL12 and TNFα, leading to an immunosuppressive TME.

Altogether, these studies delineate a link between oncogene activation and resulting effects in the TME. In addition, they emphasize that tumor-promoting effects of oncogenic signaling pathways are not restricted to intrinsic processes of tumor cells but can also reprogram and modulate the cells within the TME for their own growth advantage. However, to better understand the impact of PDAC driver mutations, especially *Pik3ca* and *Braf*, on TME, the usage of GEMMs harboring solely an oncogenic aberration can unveil new personalized targets according to the genetic background of the tumor.

3.3. From the pancreas to the secondary organ

Pancreas is an epithelial organ, and its morphogenesis and architecture are ensured by cell-cell interactions. Epithelial cells establish interactions with adjacent cells through intercellular junctions including tight junctions (TJs; junctions that regulate paracellular routes between adjacent cells), gap junctions (GJs; channels that connect the cytoplasm of two adjacent cells) and adherens junctions (AJs; specialized junctions located at the basolateral plasma membrane) (Apte & Wilson, 2005). AJs have a central role in the epithelial adhesion, where the interaction between cadherins, especially epithelial cadherin (E-cadherin), and cytoplasmic catenin proteins (e.g., β-catenin) support the regulation of cell cytoskeletal dynamics and intracellular signaling (Apte & Wilson, 2005; Huber et al., 2001). Under physiological conditions, the regulation of the epithelial junctions ensures homeostasis of the epithelial tissue and their deregulation is associated with carcinogenesis in the presence of an oncogene and posterior metastases formation (Kaneta et al., 2020; Serrill et al., 2018). Reduction or loss of E-cadherin expression has been observed in up to 60% of human PDAC samples, especially in undifferentiated tumors, which is correlated to high metastatic potential (von Burstin et al., 2009). However, the exact role of *Cdh1*, the gene that encodes E-cadherin, loss in EMT induction and PDAC development remains to be determined. Thus, loss of cell-cell adhesion contributes to the acquisition of a more aggressive and invasive phenotype by tumor cells, allowing them to spread into blood vessels and finally form metastases in distant organs, such as the liver and lungs.

Metastasization is a multistep process ranging from motility of tumor cells into the surrounding tissue on the primary tumor site to their colonization in the specific ‘target organ’ (Fares et al., 2020). The metastatic cascade is described as including the following steps: EMT that facilitates invasion and dissemination of cancer cells and their intravasation through the vasculature endothelium, survival during the bloodstream journey, extravasation at the target site vasculature and finally colonization and proliferation within the secondary site, where the malignant cells reacquire their epithelial phenotype via mesenchymal-to-epithelial transition (MET). In PDAC, PCCs normally metastasize the liver, lung, and distant lymph nodes, being the liver the most colonized organ due to its highly permeable sinusoidal vessels (Fares et al., 2020;

Oweira et al., 2017). Patients with liver metastases have the poorest prognosis compared to individual with tumors in other secondary organs. Thus, identifying and understanding all the mechanisms behind the metastasization of PCCs may limit tumor progression, making all steps of the metastatic cascade potential targets for the therapeutic intervention.

3.3.1. Epithelial-to-mesenchymal transition and Local invasion

It is well accepted that EMT plays an important role in epithelial cancer development, dissemination, and metastases formation, but only a small number of cancer cells in the primary tumor undergo this morphological transition (Zhou et al., 2017). EMT is a reversible process whereby an epithelial cell loses its junctions and polarity to acquire a mesenchymal phenotype with spindle-like cell shape that gives the cell the ability to migrate, as depicted in Fig. 4. During this process, epithelial cells downregulate the expression of epithelial markers, such as E-cadherin and cytokeratin, followed by increased expression of mesenchymal proteins including neuronal cadherin (N-cadherin) and vimentin (Zhou et al., 2017). Curiously, mosaic

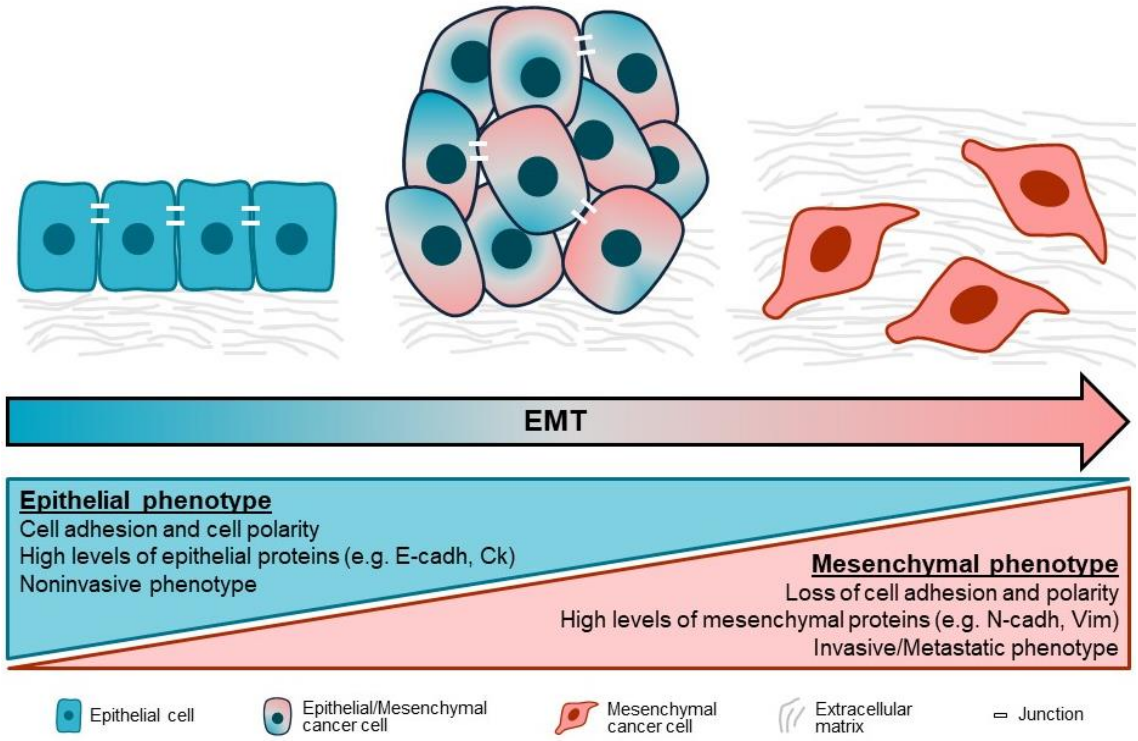

Fig. 4. Cancer cell undergoing epithelial-to-mesenchymal transition.
Epithelial-to-mesenchymal transition (EMT) is a process by which epithelial cancer cells acquire mesenchymal characteristics. Epithelial cells are connected through intercellular adhesion junctions, being polarized, and presenting a noninvasive phenotype. However, during EMT, epithelial cells lose cell adhesion and polarity, changing from a cuboidal/cylindrical shape to a spindle-like cell morphology that contributes for their invasive/metastatic phenotype. In addition, the levels of epithelial proteins, such as epithelial cadherin (E-cadh) and cytokeratin (Ck), decrease, whereas the levels of mesenchymal proteins, including neuronal cadherin (N-cadh) and vimentin (Vim), increase.
Ck denotes the cytokeratin, E-cadh the epithelial cadherin, EMT the epithelial-to-mesenchymal transition, N-cadh the neuronal cadherin, Vim the vimentin. Adapted from (Custódio-Santos et al., 2017).

downregulation of E-cadherin expression in the primary tumor reveals selective pressure to form E-cadherin-positive liver metastases and E-cadherin-negative lung metastases (Reichert et al., 2018). Furthermore, the loss of p120-catenin, a binding partner responsible for stabilizing E-cadherin, increases the number of metastases, predominantly in the lung (Reichert et al., 2018). The re-expression of p120-catenin in PCCs is sufficient to restore liver metastatic tropism. These findings might suggest that E-cadherin and p120-catenin expression is essential for metastases formation by PCCs within specific secondary sites, such as the liver, but not to the lung. EMT is dynamically orchestrated by a network of transcription factors. Recently, BTB and CNC homology 1 (BACH1), a transcription factor responsible for repressing the expression of genes involved in protection against oxidative stress, showed to be implicated in RAS-driven tumor formation by increasing cell migration and invasion via suppression of E-cadherin expression (Sato et al., 2020). Thus, BACH1 joins the list of 'EMT regulators' composed by other transcriptional factors including TWIST, SNAIL and ZEB, whose function is also repressing E-cadherin expression (Sato et al., 2020; Zhou et al., 2017). Furthermore, malignant cells undergoing EMT induce the secretion and enhance the activity of MMPs that degrade ECM (Grünwald et al., 2016). In turn, the ECM functions as a 'reservoir' of growth factors that can be proteolytically released and can locally induce cell proliferation and migration (Bonnans et al., 2014). So, although an intact ECM network maintains tissue architecture, regulates the organ morphogenesis, and supports homeostasis, this intrinsic barrier to invasiveness is not enough to stop the cascade that culminates in metastasization of the secondary site. Together with the morphological changes induced by EMT, the degradation of ECM allows the cancer cells to locally invade and opens the way to the vasculature, promoting their dissemination into the bloodstream.

Invasive strategies are closely related to EMT. Although EMT presents motility advantages to cells, not all the tumor cells complete this process, retaining certain epithelial characteristics (Aiello et al., 2018). This alternative program is referred as 'partial EMT' and the cells internalize epithelial proteins, such as E-cadherin, continuing to transcriptionally express epithelial genes simultaneously to the expression of mesenchymal ones. Partial EMT promotes collective tumor cell migration with the formation of multicellular clusters, in contrast with the single cell migration pattern associated with the 'complete EMT' process (Aiello et al., 2018). Collective migration of malignant cells with the hybrid epithelial and mesenchymal phenotype or polyclonal clusters formed by distinct tumor sub-clones may favor the survival within the circulation and therefore they are more likely to reach the vasculature of a distant organ and colonize it (Maddipati & Stanger, 2015). Moreover, the interactions between PCCs and cells within the pancreatic TME also contribute to determining invasion and metastasization (Hwang et al., 2019; Ye et al., 2018). Particularly, PSCs increase PCC invasion due to EMT induction, invadopodia formation and ECM remodeling as well as drug resistance via multiple secreted factors, including IL6, IGF1, and EGF (Hwang et al., 2019). In addition, macrophages also facilitate tumor progression due to paracrine induction of vascular cell adhesion molecule 1 (VCAM1), a molecule involved in cell cycle, proliferation, migration, and invasion, in PCCs (Ye et al., 2018). Considering that metastasization is a major cause of mortality in cancer patients, a detailed understanding of EMT and local

invasion and respective contribution of the TME could potentially lead to more effective therapeutic strategies for PDAC.

3.3.2. Intravasation, Circulation, and Extravasation

Cancer cells detach from the primary tumor mass by undergoing EMT and then invade the surrounding microenvironment, where they encounter stromal and immune cells, which in turn can facilitate the migration of the malignant cells towards the nearby vasculature. The penetration of the vessel wall and entry into the circulation is called intravasation (Fares et al., 2020). While tumor cell invasiveness has been correlated to increased intravasation, the interaction between malignant cells and ECs and posterior transendothelial migration (TEM) into circulation remains poorly characterized. Additionally, the fact that the TEM is a localized and transient process and the heterogeneous morphology of vascular ECs represent a challenge to model and study this step of the metastatic cascade *in vitro* (Reymond et al., 2013). Nevertheless, over the past few years, three-dimensional microfluidic models have been developed to study intravasation in more detail and understand and identify molecular components and signaling pathways involved in this process. An organotypic model containing juxtaposed tumor cells and endothelial lumens described by Nguyen and colleagues exhibited cell invasion through modulation of matrix and ablation of ECs by PCCs (Nguyen et al., 2019). In further detail, the invasion was collective, with epithelial cells remaining connected to each other, and, upon contact with the ECs, the PCCs wrapped around the blood vessel and spread along its length before intravasating into the endothelium. During intravasation, part of the blood vessel was occupied by PCCs promoting apoptosis of proximal ECs and deposition of collagen (Nguyen et al., 2019). The endothelial ablation mediated by cancer cells may be a potential mechanism to explain hypovascularity in PDAC. Besides the anatomical changes of the blood vessels, the PCC penetration through the tight intercellular space between two ECs also requires extensive tumor cell contractility and can lead to nuclear deformation (Denais et al., 2016). Intravasation of malignant cells leads to impairment of the integrity of the nuclear envelope and DNA content, which can promote DNA damage and genomic rearrangements and only an efficient repairment allows the cell to survive. Once within the circulatory system, invasive cancer cells migrate out of primary tumor site until reaching the vasculature of a secondary organ where they will form new tumors. However, malignant cells must survive the journey within the bloodstream.

The intravascular microenvironment and the wide distance between the pancreas and a distant secondary organ are hostile for most intravasating cancer cells, turning their survival into a great challenge. Firstly, circulation in the bloodstream occurs as single circulating tumor cells (CTCs) or as CTC clusters, having the clusters greater predisposition of forming distal metastasis compared to single cells (Amantini et al., 2019; Fares et al., 2020). Secondly, the interactions between CTCs and the microenvironmental components of circulation, such as immune cells, determine survival and the ability of CTCs to eventually extravasate into distant sites (Fares et al., 2020). In the blood of PDAC patients, besides single CTCs and CTC clusters, atypical CTCs were also detected. These last CTCs were characterized by the expression of tumor markers

such as Epcam and pan-cytokeratin as well as of the pan-immune cell marker CD45 (Amantini et al., 2019). The atypical clusters containing tumoral and immune components display an advantage in the survival of the CTC, with a progressive malignant behavior and tumorigenic abilities, contributing hence to the metastatic spread. The atypical CTCs can also be formed by the adhesion of platelets, another blood component, to the tumor cells, conferring them protection against immune surveillance and consequently facilitating metastatic spread (Ting et al., 2014). Interestingly, abundant expression of stroma-associated ECM genes, such as decorin and IGF binding protein 5 (IGFBP5), is a common feature of keratin-rich CTCs (Ting et al., 2014). This contrasts with the primary tumor, where these gene products are normally secreted by reactive stromal cells rather than by the epithelial cancer cells. The characterization of the CTCs might provide further insight into their origin within the primary tumor and the mechanisms by which they invade and survive within the bloodstream.

An important step in the metastatic process is the ability of CTCs to adhere and migrate through ECs to disseminate into a secondary organ. Similarly to intravasation, extravasation also requires TEM of tumor cells across the endothelium. CTCs, especially clusters, are rapidly entrapped within capillaries of distance organs. Indeed, given the relatively large diameters of PCCs (13–23 µm) and the diameter of a capillary (3–30 µm), it is likely that a vast majority of tumor cells becomes trapped in smaller capillaries (Nguyen et al., 2016; Sarveswaran et al., 2016). In addition, organs such as the liver and bone have highly permeable sinusoidal vessels, which increase the rate of metastasis formed in these organs, in contrast to other organs such as the brain that have tight and highly selective endothelial barriers (Fares et al., 2020). Extravasation is a complex process that involves the endothelial adhesion of the tumor cells mediated by specific surface molecules including ICAM1 and VCAM1 (Reymond et al., 2013). The expression of these surface molecules increases on the membranes of PCCs and ECs due to the cytokines secreted by both malignant cells and Tregs (Huang et al., 2017). ICAM1 facilitates endothelial adhesion and TEM via formation of an ICAM1-fibrinogen-ICAM1 bridge. Fibrinogen is one of the ICAM1 ligands and binds with high affinity to two ICAM1 molecules – one is present on the membrane of a PCC and the second molecule is expressed on the membrane of the EC – to promote a strong cell-cell adhesion (Huang et al., 2017). Therefore, all receptor-ligand bonds tightly attach the PCC to the vascular endothelium, and consequently facilitate the migration of the malignant cell. Interestingly, the targeting of the cytokines and/or adhesion molecules using blocking antibodies and small molecules can potentially be useful to prevent the adhesion of tumor cells to the endothelium and hence prevent the formation of metastases by PCCs. Upon adhesion to the ECs, malignant cells must transmigrate across the endothelium to complete the extravasation step. S100 calcium binding protein P (S100P) was identified as an important player in TEM of PCCs due to its interactions with different cytoskeletal filaments of the cancer cell such as myosin and tubulin (Barry et al., 2013; Du et al., 2020). The overexpressed S100P is located mainly in the nuclei and in microtubule organizing centers, where this protein binds to the cytoskeletal filaments leading to a redistribution of these filaments and consequently enhancing cell TEM. Overall, since the growth in the primary tumor site until the end of extravasation,

numerous obstacles and barriers have been already overcame by the cancer cell. Once inside the secondary organ, the malignant cell faces a new microenvironment that plays a crucial role in cell fate decision and subsequent formation of well-established metastases.

3.3.3. Colonization of the distant organ

The metastatic cascade culminates in dissemination of the tumor cell in the distant organ where it extravasated. The formation of undetectable micrometastases is followed by proliferation of malignant cells to form large macroscopic metastases. However, the PCCs need a favorable microenvironment to proliferate. The microenvironment as well as organ-related factors may favor the formation of a pro-metastatic niche, which consequently influences the organ-specific pattern of spread presented by cancer cells. Stephen Paget was the first one to postulate that the conditions that promote the formation of metastases are not exclusively anatomical, but also depend on favorable interactions of the cancer cell ('seed') with the permissive microenvironment in the secondary tissue ('soil') (Paget, 1889). More than one century later, a newer hypothesis emerged proposing that metastatic cells are able to bring their own soil from the primary tumor site, such as stromal components, to the secondary organ (Xu et al., 2010). Despite the existence of theories to explain the formation of the metastatic niche and posterior metastases, there are still numerous cellular and molecular aspects of the colonizing step that remain a mystery to unravel. One of the gaps on our knowledge is whether the formation of macrometastases is the result of successive cell divisions or rather the continued entry of malignant cells through compromised endothelium. The first hypothesis is the most likely since studies using multi-color lineage tracing technology in PDAC GEMMs demonstrated that polychromatic metastases arise from pre-existing clusters that outgrow and not from an independent seeding by distinct clones at the same location (Maddipati & Stanger, 2015). As mentioned above, metastatic progression is highly influenced by environmental factors that are unique to each metastatic site. Accordantly, peritoneal and diaphragmatic metastases were polyclonal, while lung and liver lesions drift towards monoclonality (Maddipati & Stanger, 2015). These observations may in part reflect differences in the different timings of dissemination (early versus late) as well as in selective pressures among the distinct organs that may favor a certain clonal progression. Lineage tracing technology represents a powerful tool to track migration, proliferation, and dissemination of specific cells *in vivo* that allows to explore aspects of cancer evolution, especially the history and chronology of events like metastasization. A more comprehensive understanding of the metastatic formation and its biological phenomena can provide new therapeutic avenues.

Once inside the secondary site, tumor cells have three possible fates: dormancy, proliferation, or cell death (Fares et al., 2020). Cancer cells that enter in a state of dormancy do not form metastases, because they are in a quiescence, non-proliferating cellular state (Sosa et al., 2014). Cellular dormancy is regulated by both cancer cell intrinsic and autocrine mechanisms, as well as signals mediated by the pre-metastatic niche. The induction of the dormant-to-proliferative switch is influenced by the balance of signaling pathways, such as RAF/MEK/ERK, PI3K/AKT/mTOR and TGFβ/SMAD, which inhibits cell death through pro-survival mechanisms

(Ischenko et al., 2015). The host microenvironment also plays a role in waking the cells from their dormant state upon formation of a pro-metastatic niche suitable for the outgrowth of the tumor cells into well-established metastases. The pro-metastatic niche is characterized by an increased presence of myeloid cells (e.g., macrophages and neutrophils), a decrease of lymphoid cells (T and B lymphocytes and NK cells) and an enhanced deposition of matrix proteins (e.g., collagens and periostin) (Nielsen et al., 2016). Macrophages induce the transformation of resident stellate cells into myofibroblast, which in turn create a more fibrotic metastatic microenvironment that favors the reactivation of the tumor cells and triggers their proliferation. Hence, elements of the pro-metastatic niche in distant organs may regulate the efficiency of the metastatic process.

As long as conditions are favorable in the secondary organ, cancer cells reacquire their epithelial phenotype via MET to form metastases (Fares et al., 2020). This phenotypic reverse process to the initial EMT can be completed by PCCs regardless of the program they underwent through EMT (complete or partial EMT) (Aiello et al., 2018). During MET, the malignant cells re-express E-cadherin in their membranes and downregulate the expression of mesenchymal genes, including *CDH11*, *COLA8A2*, *PDGFRB* and *SNAIL*. The MET promotes the adaption and survival of metastatic PCCs at the microenvironment of secondary organ. Although the induction and regulation of MET in malignant cells are not fully understood, the isoform of the paired-related homeodomain transcription factor 1a (Prrx1a) demonstrated to stimulate metastatic outgrowth of liver metastases along with tumor differentiation and MET (Takano et al., 2016). The regulation of the switching between Prrx1a and Prrx1b, isoform that promotes invasion, tumor dedifferentiation and EMT, is mediated in part by the upregulation of hepatocyte growth factor (HGF). Targeting HGF with a neutralizing antibody in combination with gemcitabine reduces primary tumor volume and metastases formation (Takano et al., 2016). Therefore, inhibition of MET may contribute to prevent the growth of secondary tumors in PDAC patients with metastatic disease.

Metastasis is a hallmark of cancer and represents the endpoint of the multistep metastatic process. Successful metastatic cancer cells have the ability to overcome all the obstacles that normally prevent the formation of secondary tumors. These cells pass through the growth and local invasion in the pancreas, migration towards a vessel, intravasation into the bloodstream, survival in circulation, extravasation across the endothelium of a secondary site, establishment of interactions with microenvironment components, and finally formation of metastasis. Despite significant advancements in our understanding about metastasization, there is still no clinically approved drug designed to specifically undermine the metastatic process. The failure to translate basic biology to the clinic may be explained by a diversity of factors including the complexity of the metastatic cascade, the distinct mechanisms used by cancer cells to metastasize, the organotropism presented by the tumor cells, challenges imposed by the different microenvironments encountered in the secondary organ. Therefore, more studies are necessary to elucidate the mechanisms behind PDAC metastases and to develop novel and efficient therapeutic approaches able to prevent the formation of these secondary tumors at distant organs.

3.4. Aims of this work

Cancer cell–intrinsic properties caused by oncogenic mutations have been well characterized; however, how specific oncogenes and the differentiation status of a tumor impact the TME is not well understood. To characterize the tumor immune microenvironment in subtypes of PDAC, we aimed at establishing multiplex immunohistochemistry (mIHC) panels. In addition, to better understand the influence of the driver mutations and of the differentiation status of the tumor on the immune TME, we characterized the tumor-associated cellular composition of tissues harvested from animals harboring *Kras*, *Pik3ca*, or *Braf* mutations by histocytometry, mIHC, and RNA-seq analyses. Histocytometry analysis allows the identification of cellular populations especially tumoral, stromal, and immune and determination of their ratios in the pancreatic tissues, and mIHC the characterization of specific immune cells and their interactions with tumor cells as well as with other inflammatory populations. Furthermore, the comparison between the imaging data and RNA-seq data from bulk tumor samples was performed to assess if the sequencing data could be used as a high-throughput technique to study the TME.

EMT is a hallmark in metastasis formation, being the loss of *Cdh1* one of the main initiation signals. However, it remains to clarify whether the downregulation of the E-cadherin expression is a major driver or a consequence of EMT. The aim of this study was to investigate the impact of *Cdh1* deletion on PDAC tumorigenesis and tumor progression, and to determine if the deletion of this epithelial gene confers an advantage to the cancer cells to survive and proliferate in metastatic microenvironments. Therefore, conditional and inducible *Cdh1* inactivation mouse models were generated as well as murine primary cancer cell lines from tumor animals. Characterization of the *Cdh1* GEMMs was performed, including assessment of the tumor types, histopathological evaluation, and determination of the metastatic potential and formation in liver and lungs. Furthermore, the effect of *Cdh1* deletion on viability, growth, and colony formation of mouse-derived PCCs was assessed. By single sample gene set enrichment analysis (ssGSEA), we further evaluate the signaling pathways altered by *Cdh1* loss in *Cdh1*-depleted cell lines. Finally, *Cdh1*-deficient and -proficient clones were generated from 4-hydroxytamoxifen (4-OHT)-treated $Cdh1^{fl/fl}$ cell lines. Upon functional analysis of these clones, they were orthotopically implanted and the tumor size and metastatic formation were assessed.

4. Materials

4.1. Technical equipment

Table 2. Technical equipment

Technical equipment	Source
Analytical balance ABJ-NM/ABS-N	Kern & Sohn GmbH, Balingen, DE
Aperio Versa 8 digital scanner	Leica Microsystems GmbH, Wetzlar, DE
Autoclave VX-150	Systec GmbH, Linden, DE
AxioCam MRc	Carl Zeiss AG, Oberkochen, DE
Bag sealer Folio FS 3602	Severin Elektrogeräte GmbH, Sundern, DE
Centrifuge 5415 D	Eppendorf AG, Hamburg, DE
Centrifuge 5427 R	Eppendorf AG, Hamburg, DE
Centrifuge Heraeus™ Multifuge™ X3 FR	Thermo Fisher Scientific Inc., Waltham, MA, USA
CO_2 incubator HERAcell™ VIOS 250i	Heraeus Holding GmbH, Hanau, DE
Confocal microscope TCS SP8	Leica Microsystems GmbH, Wetzlar, DE
Cryogenic sample storage	Worthington Industries, Inc., Columbus, OH, USA
Cryostat CM3050 S	Leica Microsystems GmbH, Wetzlar, DE
Digital orbital shaker	Heathrow Scientific, Vernon Hills, IL, USA
Electrophoresis power supply Consort EV243	AlphaMetrix Biotech GmbH, Rödermark, DE
Electrophoresis power supply EPS 601	Amersham Biosciences Corp., Little Chalfont, GB
Electrophoresis power supply PowerPac 1000	Bio-Rad Laboratories Inc., Hercules, CA, USA
Electrophoresis power supply PowerPac™ HC	Bio-Rad Laboratories Inc., Hercules, CA, USA
Freezer	Liebherr, Bulle, DE
Fridge	Siemens AG, Munich, DE
Gel documentation system UVP UVsolo touch	Analytik Jena GmbH, Jena, DE
Gel Electrophoresis System Biometra Compact L/XL	Analytik Jena GmbH, Jena, DE
Heated paraffin embedding module HistoCore Arcadia H	Leica Microsystems GmbH, Wetzlar, DE
HERA freeze™ HFU T Series	Thermo Fisher Scientific Inc., Waltham, MA, USA
Homogenizer SilentCrusher M with tool 6F	Heidolph Instruments GmbH & Co. KG, Schwabach, DE
Incubator 206	MELAG oHG, Berlin, DE
Incubator U26	Memmert, GmbH + Co.KG, Büchenbach, DE
Laminar flow	ARGE Labor- und Objekteinrichtungen GmbH, Wathlingen, DE
Magnetic stirrer, Ikamag® RCT	IKA® Werke GmbH & Co. KG, Staufen, DE
Microcentrifuge LLG-uniCFUGE 2	Faust Laborbedarf AG, Schaffhausen, CH
Microscope Axio Vert.A1	Carl Zeiss AG, Oberkochen, DE
Microscope DM IL LED	Leica Microsystems GmbH, Wetzlar, DE
Microscope ICC50 W	Leica Microsystems GmbH, Wetzlar, DE
Microtome Microm HM355S	Thermo Fisher Scientific Inc., Waltham, MA, USA
Microwave MAX	Whirlpool, Benton Harbor, MI, USA
Mini-PROTEAN® Tetra Cell	Bio-Rad Laboratories Inc., Hercules, CA, USA
Mixer RT-3D	Fröbel Labortechnik GmbH, Lindau, DE
Multimode microplate reader CLARIOstar	BMG Labtech, Ortenberg, DE
NanoPhotometer® N60	Implen GmbH, Munich, DE
Odyssey® Fc imaging system	Li-Cor Biosciences, Lincoln, NE, USA
Orbital shaker Rotamax 120	Heidolph, Instruments GmbH & Co. KG, Schwabach, DE
Paraffin tissue floating bath SB80	Microm, Walldorf, DE
pH meter pH 50+ DHS	XS Instruments, Carpi, IT
Precision balance PCB	Kern & Sohn GmbH, Balingen, DE
Qubit® 2.0 Fluorometer	Invitrogen GmbH, Karlsruhe, DE
Roller mixer RM5	Ingenierbüro CAT M. Zipperer GmbH, Ballrechten-Dottingen, DE
Scanner Perfection V370 Photo	Seiko Epson Corp., Suwa, JP
Stemi SV 11 stereomicroscope	Carl Zeiss AG, Oberkochen, DE
Thermal Cycler Biometra TOne	Analytik Jena GmbH, Jena, DE
Thermomixer comfort	Eppendorf AG, Hamburg, DE
Tissue processor ASP300S	Leica Microsystems GmbH, Wetzlar, DE
Vertical laminar flow cabinet ENVAIReco® Safe Comfort	ENVAIR Ltd., Haslingden, GB
Vortex-Genie™ 2	Scientific Industries Inc., Bohemia, NY, USA

Water bath 1083	GFL Gesellschaft für Labortechnik mbH, Burgwedel, DE

4.2. Consumables

Table 3. Consumables

Consumables	Source
25 mL pipetting reservoir	Argos Technologies, Vernon Hills, IL, USA
Aluminum foil	Carl Roth GmbH & Co. KG, Karlsruhe, DE
Black nail polish	dm-drogerie markt GmbH + Co. KG, Karlsruhe, DE
Blood glucose test strips	Abbott GmbH & Co. KG, Ludwigshafen, DE
Cell scrapers	Sarstedt Inc, Nümbrecht, DE
Combitips® advanced 0.2, 1 and 2.5 mL	Eppendorf AG, Hamburg, DE
Conical tubes 15 and 50 mL	Greiner Bio-One, Kremsmünster, AT
Cotton-tipped applicators	Lohmann & Rauscher GmbH & Co. KG, Neuwied, DE
Cover slips 18 x 18 mm	Paul Marienfield GmbH & Co. KG, Lauda-Königshofen, DE
Cover slips 24 x 50 mm	Thermo Fisher Scientific Inc., Waltham, MA, USA
CryoPure tubes	Sarstedt AG & Co., Nümbrecht, DE
Dewar carrying flask, type B	KGW-Isotherm, Karlsruhe, DE
Disposable scalpels	Feather Safety Razor Co. Ltd., Osaka, JP
Dry ice	Linde plc, Dublin, IE
Falcon® 6-, 12-, 24- and 96-well clear flat bottom cell culture microplates	Corning Inc., Corning, NY, USA
Glass staining dish and 20-slide unit	VWR International Ltd., Radnor, PA, USA
Hand Tally Counter	neoLab Migge GmbH, Heidelberg, DE
Ice block COOL PACK	Coolike Regnery GmbH, Bensheim, DE
ImmEdge™ hydrophibic barrier pen	Vector Laboratories Inc., Burlingame, CA, USA
Immersion oil Type F	Leica Microsystems GmbH, Wetzlar, DE
Lab glassware	Schott AG, Mainz, DE
Microscope slides Superfrost®	Thermo Fisher Scientific Inc., Waltham, MA, USA
Microtome blades S35 and C35	Feather Safety Razor Co. Ltd., Osaka, JP
Multilpy®-µStrip PCR reaction tubes	Sarstedt AG & Co., Nümbrecht, DE
Multipette® stream	Eppendorf AG, Hamburg, DE
Neubauer hemocytometer 0,100 mm Depth	Assistent, Sondheim vor der Rhön, DE
Nitrocellulose blotting membrane Amersham™ Protran™ 0.2 µm NC	GE Healthcare, Chicago, IL, USA
Paper role	Mobiloclean Handelsgruppe GmbH & Co. KG, Munich, DE
Parafilm™ M Laboratory Wrapping Film	Bemis Company Inc., Neenah, WI, USA
Pasteur pipettes	Hirschmann Laborgeräte GmbH & Co. KG, Eberstadt, DE
Petri dishes 10 and 15 cm	Sarstedt AG & Co., Nümbrecht, DE
Pipette tips 10, 100, 200 and 1000 µL	Sarstedt AG & Co., Nümbrecht, DE
Pipettes Reference®, Research®	Eppendorf AG, Hamburg, DE
Plastic ruler 30 cm	Möbius & Ruppert GmbH & Co. KG, Erlangen, DE
Plastic staining dish	Carl Roth GmbH & Co. KG, Karlsruhe, DE
Precision wipes	Kimberly-Clark Worldwide Inc., Irving, TX, USA
Reaction tubes 0.5, 1.5 and 2 mL	Sarstedt AG & Co., Nümbrecht, DE
Rotilabo®-folded filters type 113P	Carl Roth GmbH & Co. KG, Karlsruhe, DE
Rotilabo®-stirring magnets set I	Carl Roth GmbH & Co. KG, Karlsruhe, DE
Safe-lock tubes BioPur® 1.5 and 2 mL	Eppendorf AG, Hamburg, DE
Sample vials PE, Ø External 14 mm, volume 2,5 mL (for cryopreserved tissues)	Carl Roth GmbH & Co. KG, Karlsruhe, DE
SCIENCEWARE® Slide Staining and Storage System	VWR International Ltd., Radnor, PA, USA
Serological pipettes 5, 10, 25 and 50 mL	Greiner Bio-One, Kremsmünster, AT
Shrink wrap film	VEMATEC GmbH, Berlin, DE
Single use needles Sterican® 20, 26 and 27 G	B. Braun Melsungen AG, Melsungen, DE
Single use syringes Omnifix® 1 mL	B. Braun Melsungen AG, Melsungen, DE
Slide storage box 25 and 100 slides	Sigma-Aldrich, St. Louis, MO, USA

Staining chamber with metal plates	Thermo Fisher Scientific Inc., Waltham, MA, USA
Stripettor™ Ultra	Corning Inc., Corning, NY, USA
Surgical instruments	Thermo Fisher Scientific Inc., Waltham, MA, USA
Tissue culture flasks 25, 75 and 175 cm^2	Greiner Bio-One, Kremsmünster, AT
Tissue embedding cassettes Q Path® MacroStar VI and VIII	VWR International Ltd., Radnor, PA, USA
Tissue strong 100V	Lucart Professional, Villa Basilica, IT
Vertical staining jar with glass lid	VWR International Ltd., Radnor, PA, USA
Whatman™ cellulose Western blotting paper	GE Healthcare, Chicago, IL, USA

4.3. Chemicals and Reagents

Table 4. Chemicals and reagents

Chemical or Reagent	Source
1,4-Dithiothreitol (DTT)	Carl Roth GmbH & Co. KG, Karlsruhe, DE
100%, 96%, 80% and 70% Ethanol (EtOH)	Otto Fischar GmbH & Co. KG, Saarbrücken, DE
2-Mercaptoethanol, 98%	Sigma-Aldrich, St. Louis, MO, USA
2-Propanol (isopropanol)	Carl Roth GmbH & Co. KG, Karlsruhe, DE
3,3'-Diaminobenzidine (DAB) peroxidase substrate kit	Vector Laboratories Inc., Burlingame, CA, USA
4-Hydroxytamoxifen (4-OHT)	Sigma-Aldrich, St. Louis, MO, USA
Acetic acid glacial	Carl Roth GmbH & Co. KG, Karlsruhe, DE
Aceton	Otto Fischar GmbH & Co. KG, Saarbrücken, DE
Acrylamide Rotiphorese® gel 30	Carl Roth GmbH & Co. KG, Karlsruhe, DE
Agarose	Sigma-Aldrich, St. Louis, MO, USA
Ammonium persulfate (APS)	Sigma-Aldrich, St. Louis, MO, USA
Ammonium sulfate	Sigma-Aldrich, St. Louis, MO, USA
Antigen unmasking solution, citric acid based (pH 6.0)	Vector Laboratories Inc., Burlingame, CA, USA
Aqua sterile water	B. Braun Melsungen AG, Melsungen, DE
Avidin/Biotin blocking kit	Vector Laboratories Inc., Burlingame, CA, USA
Bovine serum albumin (BSA) fraction V	SERVA Electrophoresis GmbH, Heidelberg, DE
Bradford reagent	SERVA Electrophoresis GmbH, Heidelberg, DE
Bromophenol blue	Sigma-Aldrich, St. Louis, MO, USA
Collagenase type 2	Worthington Biochemical Corp., Lakewood, NJ, USA
Complete EDTA-free protease inhibitor cocktail tablets	Roche Deutschland Holding GmbH, Grenzach-Wyhlen, DE
Cresol red	AppliChem GmbH, Darmstadt, DE
D(+)-saccharose	Carl Roth GmbH & Co. KG, Karlsruhe, DE
Dimethyl sulfoxide (DMSO)	Carl Roth GmbH & Co. KG, Karlsruhe, DE
DMSO	AppliChem GmbH, Darmstadt, DE
dNTP mix, 10 mM each	Fermentas GmbH, St. Leon-Rot, DE
Dodecylsulfate Na-salt in pellets (SDS)	SERVA Electrophoresis GmbH, Heidelberg, DE
Donkey, Goat and Rat serums	LINARIS Biologische Produkte GmbH, Dossenheim, DE
Dulbecco's Modified Eagle's Medium (DMEM) – high glucose	Sigma-Aldrich, St. Louis, MO, USA
Dulbecco's phosphate buffered saline (PBS)	Sigma-Aldrich, St. Louis, MO, USA
Dulbecco's phosphate buffered saline (PBS) powder	Sigma-Aldrich, St. Louis, MO, USA
Eosin 2% w/v	HiMedia Laboratories Pvt. Ltd., Mumbai, IN
Ethanol absolute ≥ 99.8%	Sigma-Aldrich, St. Louis, MO, USA
Ethidium bromide	Sigma-Aldrich, St. Louis, MO, USA
Ethylenediaminetetraacetic acid (EDTA)	Sigma-Aldrich, St. Louis, MO, USA
Fetal bovine serum (FBS) Superior	Sigma-Aldrich, St. Louis, MO, USA
Forene® isoflurane	Abbott GmbH & Co. KG, Ludwigshafen, DE
Frozen section medium Richard-Allan Scientific NEG-50	Thermo Fisher Scientific Inc., Waltham, MA, USA
GeneRuler™ 100 bp DNA ladder	Fermentas GmbH, St. Leon-Rot, DE
Giemsa stock solution (20x)	Carl Roth GmbH & Co. KG, Karlsruhe, DE
Glycerol	Merck, Darmstadt, DE
Glycine	Sigma-Aldrich, St. Louis, MO, USA

Hematoxylin solution Gill no. 3	Sigma-Aldrich, St. Louis, MO, USA
HEPES	Carl Roth GmbH & Co. KG, Karlsruhe, DE
Hydrochloric acid (HCl), 37%	Sigma-Aldrich, St. Louis, MO, USA
Hydrogen peroxide (H_2O_2) 30%	Merck, Darmstadt, DE
Luminol	Sigma-Aldrich, St. Louis, MO, USA
Magnesium chloride	Carl Roth GmbH & Co. KG, Karlsruhe, DE
Methanol	Carl Roth GmbH & Co. KG, Karlsruhe, DE
Mounting medium Cytoseal™ XYL	Thermo Fisher Scientific Inc., Waltham, MA, USA
N,N,N',N'-Tetramethylethylenediamine (TEMED)	Sigma-Aldrich, St. Louis, MO, USA
N,N-dimethylformamide	Sigma-Aldrich, St. Louis, MO, USA
Nonidet P40	Roche Deutschland Holding GmbG, Grenzach-Wyhlen, DE
PageRuler™ Plus prestained protein ladder	Thermo Fisher Scientific Inc., Waltham, MA, USA
Paraformaldehyde	Sigma-Aldrich, St. Louis, MO, USA
p-Coumaric acid	Sigma-Aldrich, St. Louis, MO, USA
Peanut oil	Sigma-Aldrich, St. Louis, MO, USA
Penicillin-Streptomycin	Sigma-Aldrich, St. Louis, MO, USA
Phosphatase inhibitor mix I	SERVA Electrophoresis GmbH, Heidelberg, DE
Powdered milk blotting grade	Carl Roth GmbH & Co. KG, Karlsruhe, DE
Proteinase K	AppliChem GmbH, Darmstadt, DE
Reaction buffer S (for PCR)	Peqlab Biotechnologie GmbH, Erlangen, DE
RNase-dree DNase set	Qiagen GmbH, Hilden, DE
ROTI®Histofix 4%	Carl Roth GmbH & Co. KG, Karlsruhe, DE
ROTI®Histol	Carl Roth GmbH & Co. KG, Karlsruhe, DE
Sodium chloride (NaCl)	Merck, Darmstadt, DE
Sodium hydroxide 1M solution (NaOH)	AppliChem GmbH, Darmstadt, DE
Sucrose	Sigma-Aldrich, St. Louis, MO, USA
Tamoxifen	Sigma-Aldrich, St. Louis, MO, USA
Taq DNA polymerase	Qiagen GmbH, Hilden, DE
Thiazolyl blue tetrazolium bromide (MTT) 98%	Sigma-Aldrich, St. Louis, MO, USA
Tris hydrochloride	J.T.Baker® Chemicals, Phillipsburg, NJ, USA
TRIS Pufferan® ≥ 99.8%	Carl Roth GmbH & Co. KG, Karlsruhe, DE
Tris-Acetate-EDTA (TAE) buffer 50x	Klinikum rechts der Isar der TUM-Krankenhausapotheke, Munich, DE
Triton™ X-100	Sigma-Aldrich, St. Louis, MO, USA
Trypan blue solution	Sigma-Aldrich, St. Louis, MO, USA
TrypZean® solution 1×	Sigma-Aldrich, St. Louis, MO, USA
Tween® 20	Sigma-Aldrich, St. Louis, MO, USA
Vectashield® mounting medium for fluorescence	Vector Laboratories Inc., Burlingame, CA, USA
Vectastain® elite ABC kit	Vector Laboratories Inc., Burlingame, CA, USA

4.4. Antibodies and Dyes

Table 5. Antibodies and dyes

Antibody or Dye	Source
Armenian hamster anti-mouse CD11c (N418), #14-0114-82, RRID:AB_467115	Thermo Fisher Scientific Inc., Waltham, MA, USA
Armenian hamster anti-mouse CD11c (N418), #14-0114-82, RRID:AB_467115; labeled with Alexa Fluor™ 488 Antibody Labeling Kit, #A20181	Thermo Fisher Scientific Inc., Waltham, MA, USA Thermo Fisher Scientific Inc., Waltham, MA, USA
Armenian hamster anti-mouse CD3e (145-2C11), #553058, RRID:AB_394591	Becton, Dickinson and Company (BD), Franklin Lakes, NJ, USA
Armenian hamster anti-mouse Podoplanin (eBio8.1.1 (8.1.1)), #14-5381-82, RRID:AB_1210505	Thermo Fisher Scientific Inc., Waltham, MA, USA
Biotinylated goat anti-mouse IgG (H+L), #BA-9200, RRID:AB_2336171	Vector Laboratories Inc., Burlingame, CA, USA
Biotinylated goat anti-rabbit IgG (H+L), #BA-1000, RRID:AB_2313606	Vector Laboratories Inc., Burlingame, CA, USA
DAPI, #40011	Biotium Inc., Hayward, CA, USA
Donkey anti-goat IgG (H+L) Alexa Fluor® 594, #A11058, RRID:AB_2534105	Thermo Fisher Scientific Inc., Waltham, MA, USA

Donkey anti-rabbit IgG (H+L) Alexa Fluor® Plus 680, #A32802, RRID:AB_2762836	Thermo Fisher Scientific Inc., Waltham, MA, USA
Donkey anti-rat IgG (H+L) Alexa Fluor® 488, #A21208, RRID:AB_141709	Thermo Fisher Scientific Inc., Waltham, MA, USA
Donkey anti-rat IgG (H+L) Alexa Fluor® 594, #A21209, RRID:AB_2535795	Thermo Fisher Scientific Inc., Waltham, MA, USA
Goat anti-Armenian hamster IgF (H+L) Alexa Fluor® 647, #A21451, RRID:AB_1500615	Thermo Fisher Scientific Inc., Waltham, MA, USA
Goat anti-Armenian hamster IgG (H+L) Cy3, #127-165-160, RRID:AB_2338989	DIANOVA GmbH, Hamburg, DE
Goat anti-mouse Siglec-F, #AF1706, RRID:AB_354943	Research and Diagnostic (R&D) Systems Inc., Minneapolis, MN, USA
Goat anti-rabbit IgG (H+L) Alexa Fluor® 488, #A11034, RRID:AB_2576217	Thermo Fisher Scientific Inc., Waltham, MA, USA
Goat anti-rabbit IgG (H+L) Alexa Fluor® 594, #A11037, RRID:AB_2534095	Thermo Fisher Scientific Inc., Waltham, MA, USA
Goat anti-rabbit IgG (H+L) DyLight800 4X PEG, #SA5-35571, RRID:AB_2556775	Thermo Fisher Scientific Inc., Waltham, MA, USA
Goat anti-rat IgG (H+L) Alexa Fluor® 555, #A21434, RRID:AB_141733	Thermo Fisher Scientific Inc., Waltham, MA, USA
Goat anti-rat IgG (H+L) Alexa Fluor® 680, #A21096, RRID:AB_141554	Thermo Fisher Scientific Inc., Waltham, MA, USA
Goat peroxidase antibody anti-mouse IgG (Fab specific), #A9917, RRID:AB_258476	Sigma-Aldrich, St. Louis, MO, USA
Mouse anti-mouse E-cadherin (36/E-Cadherin), #610181, RRID:AB_397580	Becton, Dickinson and Company (BD), Franklin Lakes, NJ, USA
Phalloidin conjugated CF®633, #00046-T	Biotium Inc., Hayward, CA, USA
Rabbit anti-mouse CD4 (EPR19514), #ab183685, RRID:AB_2686917	Abcam, Cambridge, GB
Rabbit anti-mouse FoxP3, #ab75763, RRID:AB_1310238	Abcam, Cambridge, GB
Rabbit anti-mouse GAPDH (14C10), #2118S, RRID:AB_561053	Cell Signaling Technology Inc., Danvers, MA, USA
Rabbit anti-mouse Keratin 18, #SAB4501665, RRID:AB_10746153	Sigma-Aldrich, St. Louis, MO, USA
Rabbit anti-mouse Keratin 18, #SAB4501665, RRID:AB_10746153; labeled with Alexa Fluor™ 680 Antibody Labeling Kit, #A20188	Sigma-Aldrich, St. Louis, MO, USA Thermo Fisher Scientific Inc., Waltham, MA, USA
Rabbit anti-mouse Ki-67 (SP6), #ab16667, RRID:AB_302459	Abcam, Cambridge, GB
Rabbit anti-mouse Ki-67 (SP6), #KI681C01, RRID:AB_2722785	DCS Innovative Diagnostik-Systeme GmbH & Co. KG, Hamburg, DE
Rabbit anti-mouse NCR1, #ab199128, RRID:AB_2890127	Abcam, Cambridge, GB
Rat anti-mouse CD11b (M1/70), #553308, RRID:AB_394772	Becton, Dickinson and Company (BD), Franklin Lakes, NJ, USA
Rat anti-mouse CD11b (M1/70), eFluor® 450, #48-0112-82, RRID:AB_1582236	Thermo Fisher Scientific Inc., Waltham, MA, USA
Rat anti-mouse CD3 (17A2), #100201, RRID:AB_312658	BioLegend, San Diego, CA, USA
Rat anti-mouse CD3 (17A2), eFluor® 660, #50-0032-82, RRID:AB_10598657	Thermo Fisher Scientific Inc., Waltham, MA, USA
Rat anti-mouse CD4 (RM4-5), Alexa Fluor® 532, #58-0042-82, RRID:AB_11218891	Thermo Fisher Scientific Inc., Waltham, MA, USA
Rat anti-mouse CD45 (YW62.3), #MCA1031G, RRID:AB_321730	Bio-Rad Laboratories Inc., Hercules, CA, USA
Rat anti-mouse CD45R/B220 (RA3-6B2), #103201, RRID:AB_312986	BioLegend, San Diego, CA, USA
Rat anti-mouse CD45R/B220 (RA3-6B2), #103201, RRID:AB_312986; labeled with Alexa Fluor™ 594 Antibody Labeling Kit, #A20185	BioLegend, San Diego, CA, USA Thermo Fisher Scientific Inc., Waltham, MA, USA
Rat anti-mouse CD68 (FA-11), #MCA1957, RRID:AB_322219	Bio-Rad Laboratories Inc., Hercules, CA, USA
Rat anti-mouse CD8a (53-6.7), #14-0081-82, RRID:AB_467087	Thermo Fisher Scientific Inc., Waltham, MA, USA
Rat anti-mouse CD8a (53-6.7), Alexa Fluor® 488, #53-0081-82, RRID:AB_469897	Thermo Fisher Scientific Inc., Waltham, MA, USA

Rat anti-mouse E-cadherin (DECMA-1), #sc-59778, RRID:AB_781738	Santa Cruz Biotechnology Inc., Dallas, TX, USA
Rat anti-mouse F4/80 (BM8), eFluor® 660, #50-4801-82, RRID:AB_11149361	Thermo Fisher Scientific Inc., Waltham, MA, USA
Rat anti-mouse F4/80 (CI:A3-1), #MCA497, RRID:AB_2098196	Bio-Rad Laboratories Inc., Hercules, CA, USA
Rat anti-mouse FoxP3 (FJK-16s), eFluor® 450, #48-5773-82, RRID:AB_1518812	Thermo Fisher Scientific Inc., Waltham, MA, USA
Rat anti-mouse Ly6G/Ly6C (RB6-8C5), #14-5931-82, RRID:AB_467730	Thermo Fisher Scientific Inc., Waltham, MA, USA
Rat anti-mouse Ly6G/Ly6C (RB6-8C5), Alexa Fluor® 532, #58-5931-82, RRID:AB_11220477	Thermo Fisher Scientific Inc., Waltham, MA, USA
ToPro™-3 Iodide (642/661), #T3605	Thermo Fisher Scientific Inc., Waltham, MA, USA

4.5. Buffers and Solutions

Table 6. Buffers and solutions

Buffer or Solution	Component
0.5-3% BSA/0.1-0.5% Triton™ X-100	0.5-3% BSA 0.1-0.5% Triton™ X-100 Diluted in 1×PBS
3% BSA	3% BSA Diluted in 1×PBS
5x Protein loading buffer (Laemmli), pH 6.8	10% SDS 50% Glycerol 228 mM Tris hydrochloride 0.75 mM Bromophenol blue 5% 2-Mercaptoethanol Diluted in ddH_2O
10x Gitschier's buffer	670 mM Tris, pH 8.8 166 mM Ammonium sulfate 67 mM Magnesium chloride Diluted in ddH_2O
Soriano lysis buffer	0.5% Triton™ X-100 10% 10x Gitschier's buffer 1% 2-Mercaptoethanol Diluted in ddH_2O 400 µg/mL Proteinase K (add prior to use) DTT (add prior to use)
SucRot solution (for PCR)	1.5 mg/mL Cresol red 100 mM Tris (pH 9.0) 30% D(+)-saccharose
IP buffer, pH 7.9	50 mM HEPES 150 mM NaCl 1 mM EDTA 0.5% Nonidet P40

	10% Glycerol Diluted in ddH_2O and adjusted to pH 7.9 with NaOH 4% Phosphatase inhibitor (add prior to use) 1% Protease inhibitor (add prior to use)
Stacking gel buffer, pH 6.8	0.5 M Tris Diluted in ddH_2O and adjusted to pH 6.8 with HCl
Separating gel buffer, pH 8.8	1.5 M Tris Diluted in ddH_2O and adjusted to pH 8.8 with HCl
Running buffer	25 mM Tris 192 mM Glycine 0.1% SDS Diluted in ddH_2O
Transfer buffer	25 mM Tris 192 mM Glycine 2% Methanol Diluted in ddH_2O
PBS-T	1×PBS 0.1% Tween® 20
5% Milk	5% Powdered milk blotting grade Diluted in PBS-T
Solution A (for Chemiluminescence)	1.4 mM Luminol Diluted in 100 mM Tris hydrochloride, pH 8.6
Solution B (for Chemiluminescence)	6.7 mM p-Coumaric acid Diluted in DMSO
Chemiluminescence solution	1 mL Solution A 3 µL 30% H_2O_2 100 µL Solution B
Cancer cell medium (cell culture)	DMEM 10% FBS 1% Penicillin-Streptomycin
Freezing medium (cell culture)	70% DMEM 20% FBS 10% DMSO

4.6. Kits for DNA and RNA isolation

Table 7. Kits for DNA and RNA isolation

Kit	Source
GenElute™ Mammalian Genomic DNA Miniprep	Sigma-Aldrich, St. Louis, MO, USA
QIAshredder	Qiagen GmbH, Hilden, DE
Qubit® dsDNA BR assay kit	Thermo Fisher Scientific Inc., Waltham, MA, USA
RNeasy® Mini kit	Qiagen GmbH, Hilden, DE

4.7. Polymerase chain reactions (PCRs) and Primers

All primers were synthesized by Eurofins MWG GmbH (Ebersberg, DE) and dissolved in aqua sterile water to a concentration of 10 mM. For polymerase chain reaction (PCR) performance, the primers were further diluted in aqua sterile water to a concentration of 10 µM.

Table 8. Polymerase chain reactions and primers

PCR name	Primer name	Sequence (5' → 3')
Pdx1-Cre	Pdx-Prom-UP	GCTCATTGGGAGCGGTTTTG
	PdxKON-LP1	CACGTGGTTTACCCTGGAGC
	V-Cre-LP2	ACATCTTCAGGTTCTGCGGG
Pdx1-CreER^{T2}	Cre-ERTM-UP	AACCTGGATAGTGAAACAGGGGC
	ERTM-LP-mod1	CATGGAGCGAACGACGAGA
Pdx1-Flp	pdx5utr-scUP	AGAGAGAAAATTGAAACAAGTGCAGGT
	Flpopt-scLP	CGTTGTAAGGGATGATGGTGAACT
	Gabra-UP	AACACACACTGGAGGACTGGCTAGG
	Gabra-LP	CAATGGTAGGCTCACTCTGGGAGATGATA
LSL-Kras^{G12D}	Kras-WT-UP1	CACCAGCTTCGGCTTCCTATT
	Kras-URP-LP1	AGCTAATGGCTCTCAAAGGAATGTA
	KrasG12Dmut-UP	CCATGGCTTGAGTAAGTCTGC
FSF-Kras^{G12D}	Kras-WT-UP1	CACCAGCTTCGGCTTCCTATT
	Kras-URP-LP1	AGCTAATGGCTCTCAAAGGAATGTA
	R26-Tva-SA-mut	GCGAAGAGTTTGTCCTCAACC
LSL-Pik3ca^{H1047R}	pGL3-pA-pause4645-UP	TGAATAGTTAATTGGAGCGGCCGCAATA
	PI3K-genotyp reverse	AAATAGCCGCAGGTCACAAAGTCTCCG
LSL-Braf^{V637E}	BR_UP	TTTATCATAGTAGGGCTTGCTGTCTTGCTT
	BR_WT-LP	CAAATATGTTTTGAGCAAGACCTTTGTTCT
	BR_SA-LP	CCACTGACCAGAAGGAAAGTGGT
Cdh1^{fl}	E-cad_GT_P3	TCAATCTCAGAGCCCCACCTA
	E-cad_GT_del-LP2	TGCCATGATTGTCATGGAC
***Cdh1^{fl}* recombination**	Ecad-Fo9	CCCTGAGTGTGCAGGAAGTTAAC
	Ecad-PTA	CCCACCTACCGCTGCATT
	Ecad-co1-Rev	GCTCCCTGCCATGATTGTCATG
LSL-Trp53^{R172H}	Trp53R172H-WT-UP2	AGCCTTAGACATAACACACGAACT
	Trp53R172H-URP-LP	CTTGGAGACATAGCCACACTG
	Trp53R172H-mut-UP4	GCCACCATGGCTTGAGTAA
Trp53^{lox}	p53 lox UP-E	CACAAAAAACAGGTTAAACCCAGC
	p53 lox LP-F	GCACCTTTGATCCCAGCACATA
Trp53^{frt}	p53-frt1	CAAGAGAACTGTGCCTAAGAG
	p53-frt2	CTTTCTAACAGCAAAGGCAAGC
***Trp53^{frt}* recombination**	p53-frt1	CAAGAGAACTGTGCCTAAGAG
	p53-frt3	ACTCGTGGAACAGAAACAGGCAGA
Rosa26^{Tva}	R26-Tva-GT-UP	AAAGTCGCTCTGAGTTGTTAT
	R26-Tva-GT-SA-mut-LP	GCGAAGAGTTTGTCCTCAACC
	R26-Tva-GT-WT-LP	GGAGCGGGAGAAATGGATATG
CreER^{T2}	Cre-ER-T2-sc-UP3	GAATGTGCCTGGCTAGAGATC
	Cre-ER-T2-sc-LP1	GCAGATTCATCATGCGGA
Rosa26^{CAG}	R26-td-E-mutLP	TCAATGGGCGGGGGTCGTT
	R26-Tva-GT-UP	AAAGTCGCTCTGAGTTGTTAT
	R26-Tva-GT-WT-LP	GGAGCGGGAGAAATGGATATG
FSF-Stop	pGL3-pA-pause-4645-UP	TGAATAGTTAATTGGAGCGGCCGCAATA
	Cre-neu-LP	CAGGGTGTTATAAGCAATCCC
***FSF* recombination**	caggs-sc-UP4	GTTCGGCTTCTGGCGTGT
	Cre-neu-LP	CAGGGTGTTATAAGCAATCCC
Rosa26^{mTmG}	CAG-sc-LP	GTACTTGGCATATGATACACTTGATGTAC
	R26-Tva-GT-UP	AAAGTCGCTCTGAGTTGTTAT
	R26-Tva-GT-WT-LP	GGAGCGGGAGAAATGGATATG
***Rosa26^{mTmG}* recombination**	caggs-sc-UP4	GTTCGGCTTCTGGCGTGT
	tdTomato-tdEG-LP	GCTTGGTGTCCACGTAGTAGTAGC
	eGFP-tdEG-LP	CCATGTGATCGCGCTTCTCGT
CAG$^{dsRed\text{-}eGFP}$	dsRed-eGFP forward	CCC ATG GTC TTC TTC TGC AT
	dsRed-eGFP reverse	AAG GTG TAC GTG AAG CAC CC
Rosa26^{Dual}	R26-Tva-GT-UP	AAAGTCGCTCTGAGTTGTTAT
	Reni-end-UP	TGGAGCGCGTGCTGAAGAA

	R26-Tva-GT-WT-LP	GGAGCGGGAGAAATGGATATG
Mycoplasma test	Forward 1	CGCCTGAGTAGTACGTTCGC
	Forward 2	CGCCTGAGTAGTACGTACGC
	Forward 3	TGCCTGGGTAGTACATTCGC
	Forward 4	TGCCTGAGTAGTACATTCGC
	Forward 5	CGCCTGAGTAGTATGCTCGC
	Forward 6	CACCTGAGTAGTATGCTCGC
	Forward 7	CGCCTGGGTAGTACATTCGC
	Reverse 1	GCGGTGTGTACAAGACCCGA
	Reverse 2	GCGGTGTGTACAAAACCCGA
	Reverse 3	GCGGTGTGTACAAACCCCGA

4.8. Software

Table 9. Software

Software	Source
Aperio ImageScope v12.4.3.7001, RRID:SCR_020993	Leica Microsystems CMS GmbH, Germany
Aperio VERSA v1.04.125, RRID:SCR_021016	Leica Microsystems CMS GmbH, Germany
AxioVision v4.8, RRID:SCR_002677	Carl Zeiss AG, Oberkochen, DE
Epson Scan v1.2	Seiko Epson Corp., Suwa, JP
Microsoft Excel, RRID:SCR_016137	Microsoft Corp., Redmont, WA, USA
Fiji v1.53c, RRID:SCR_002285	National Institutes of Health, Stapleton, NY, USA
FlowJo v10.6.1, RRID:SCR_008520	Becton, Dickinson and Company (BD), Franklin Lakes, NJ, USA
GraphPad Prism 5.0 and 8.0, RRID:SCR_002798	GraphPad Software, San Diego, CA, USA
ImageJ v1.49, RRID:SCR_001935	National Institutes of Health, Stapleton, NY, USA
Imaris 9.5 and 9.6, RRID:SCR_007370	Bitplane AG, Zurich, CH
R v3.6.2, RRID:SCR_001905	The R Foundation, Indianapolis, IN, USA
Leica Application Suite X v3.6.1, RRID:SCR_013673	Leica Microsystems CMS GmbH, Germany
MARS® Data Analysis Software Version 3.20R2, RRID:SCR_021015	BMG Labtech, Ortenberg, DE
Image Studio Software v5.2.5, RRID:SCR_015795	Li-Cor Biosciences, Lincoln, NE, USA
PyRAT animal facility software v4.2-552	Scionics Computer Innovation GmbH, Dresden, DE
SnapGene Viewer, RRID:SCR_015052	GSL Biotech LLC, Chicago, IL, USA
ZEISS ZEN v2.3, RRID:SCR_013672	Carl Zeiss AG, Oberkochen, DE

5. Methods

5.1. Mouse experiments

All procedures with animals were conducted in compliance with European directives on the care and usage of laboratory animals. The protocol was reviewed and approved by the Institutional Animal Care and Use Committees (IACUC) of the local authorities of Technical University of Munich and the Regierung von Oberbayern.

5.1.1. Mouse strains

For tissue specific expression of targeted mutations, both conditional *Cre/loxP* and *Flp/frt* mouse models were used in this study. Mice carrying genes flanked by *loxP/frt* sites or silenced by an *LSL/FSF* cassette were interbed with a mouse strain expressing Cre or Flp recombinase under the control of the tissue-specific promoter *Pdx1* to allow conditional inactivation of genes or deletion of the LSL or FSF cassette to activate expression of genes. While a combination with *Flp/frt* recombination system for tumor initiation and a *Cre/loxP* system for secondary genetic manipulation allows sequential inactivation of genes of interest in PanIN lesions or in PDAC cells *in vivo* and *in vitro*. In Chapter I, Part B, for the analysis of the TME, mice harboring one oncogenic mutation (*Kras*^{G12D}, *Pik3ca*^{H1047R}, or *Braf*^{V637E}) were crossed with animals with *Pdx1-Cre* or *Pdx1-CreER*^{T2} promoters; PK mice were then crossed with animals harboring *Trp53*^{lox}, being then designated by PKP. All the animals used for this part of the present study were *Mus musculus*, on a C57BL/6J genetic background, 5 females and 10 males at the age of 7-40 weeks. In Chapter II, to study the effects of *Cdh1* loss on PDAC and posterior metastases formation, it was employed *Cdh1* gene inactivation using the *Cre/loxP* site-specific recombination system, which was then crossed with mice harboring *Pdx1-Cre*, *LSL-Kras*^{G12D}, and *Trp53*^{R172H} alleles and with mice harboring *Pdx1-Flp; FSF-Kras*^{G12D} with and without *Trp53*^{R172H} or *Trp53*^{frt}. Some mice additionally had a reporter labeling of PCCs (*Rosa26*^{mTmG}, *Rosa26*$^{dual/+}$, or *CAG*$^{dsRed\text{-}eGFP}$). All *Cdh1* animals were *Mus musculus*, on a mixed C57BL/6J;129/S6 genetic background, 56 females and 45 males at the age of 4-120 weeks.

Pdx1-Cre (Hingorani et al., 2003), RRID:IMSR_JAX:034623 – This transgenic mouse strain was kindly provided by Prof. David Tuveson (Cold Spring Harbor Laboratory, Princeton, NJ, USA). It was generated by injection of the *Pdx1-Cre* transgene into fertilized oocytes, having the founder mice a mosaic pattern expression of Cre in the pancreas.

***Pdx1-CreER*^{T2}** (Gu et al., 2002), RRID:IMSR_JAX:024968 – This transgenic mouse strain was kindly provided by Douglas Melton, Ph.D. (Harvard University, Cambridge, MA, USA). It was generated by pronucleus injection and it consists in a tamoxifen-inducible form of a Cre recombinase/estrogen receptor fusion protein that adjoined to *Pdx1* promoter drives a mosaic expression of Cre recombination in pancreas.

Pdx1-Flp (Schönhuber et al., 2014), RRID:MGI:6154332 – This transgenic mouse strain was generated in the laboratory of Prof. Dr. med. Dieter Saur. It consists of the fusion of the *Pdx1* promoter and the codon optimized *Flp-o* coding sequence, being expressed in pancreatic progenitor cells and in adult pancreatic islets.

LSL-Kras$^{G12D/+}$ (Hingorani et al., 2003; Jackson et al., 2001), RRID:IMSR_JAX:008179 – This knockin mouse strain was kindly provided by Prof. Tyler Jacks (Massachusetts Institute of Technology, Cambridge, MA, USA). *LSL-Kras$^{G12D/+}$* mice carry a point mutation in codon 12 (exon 2) that leads to glycine (G) → aspartic acid (D) substitution and corresponds to one of the most common mutations found in human PDAC. Upon Cre-mediated deletion of the *LSL* cassette, oncogenic *Kras* is expressed resulting in constitutive activation of RAS downstream pathways.

FSF-Kras$^{G12D/+}$ (Schönhuber et al., 2014), RRID:IMSR_JAX:008179 – This knockin mouse strain was generated in the laboratory of Prof. Dr. med. Dieter Saur. Similarly to the *LSL-Kras$^{G12D/+}$*, an oncogenic point mutation was introduced in the exon 2 of *Kras* gene. The expression of the oncogene is blocked by a STOP cassette flanked by *frt* sites and can be activated by Flp recombinase.

LSL-Pik3ca$^{H1047R/+}$ (Eser et al., 2013), RRID:IMSR_JAX:016977 – This knockin mouse strain was generated in the laboratory of Prof. Dr. med. Dieter Saur. *LSL-Pik3ca$^{H1047R/+}$* mice carry a point mutation in codon 1047 that leads to histidine (H) → arginine (R) substitution, the most common mutation of the *PIK3CA* among solid tumors, and it consists of an *LSL* silenced *Pik3ca^{H1047R}* expression cassette target to the first intron of *Rosa26* locus. After deletion of the *LSL* cassette by a Cre recombinase, the expression of *p110α^{H1047R}* results in a constitutive activation of PI3K signaling pathway.

LSL-Braf$^{V637E/+}$ (Rad et al., 2013), RRID:IMSR_JAX:017837 – This knockin mouse strain was kindly provided by Prof. Dr. Roland Rad (Klinikum rechts der Isar, Technical University of Munich, Munich, DE). *LSL-Braf$^{V637E/+}$* mice carry a point mutation in codon 637 (exon 18) that leads to valine (V) → glutamic acid (E) substitution, the most common somatic alteration in *BRAF*. Upon Cre-mediated deletion of the *LSL* cassette, oncogenic *Braf* is expressed resulting in constitutive activation of RAF downstream pathways.

Cdh1$^{fl/+}$ (Derksen et al., 2006), RRID:IMSR_JAX:002473 – This mouse strain was kindly provided by Dr. Jos Jonkers (Netherlands Cancer Institute, Amsterdam, NL). It consists in a conditional *Cdh1* gene inactivation using the *Cre/loxP* site-specific recombination system. Introns 3 and 15 of the murine *Cdh1* gene are flanked by *loxP* sites, which are recognized by the Cre recombinase, and leads to functional inactivation of E-cadherin.

LSL-Trp53$^{R172H/+}$ (Hingorani et al., 2005; Olive et al., 2004), RRID:IMSR_JAX:002659 – This knockin mouse strain was kindly provided by Prof. Tyler Jacks (Massachusetts Institute of Technology, Cambridge, MA, USA). *LSL-Trp53$^{R172H/+}$* mice carry a missense mutation in codon 172 of endogenous *Trp53* gene that leads to arginine (R) → histidine (H) substitution, which

corresponds to the human R175H mutation often found in oncological patients. Upon excision of the *LSL* cassette, the mutant p53 is expressed.

Trp53$^{lox/+}$ (Jonkers et al., 2001), RRID:IMSR_JAX:008462 – This mouse strain was kindly provided by Dr. Anton Berns, (University of Amsterdam, Amsterdam, NE). Exons 2 to 10 of the murine *Trp53* gene are flanked by two *loxP* cassettes. This mouse strain can be interbred with mice with the expression of Cre recombinase leading the conditional inactivation of *Trp53*.

Trp53$^{frt/+}$ (Lee et al., 2012), RRID:IMSR_JAX:017767 – This mouse strain was kindly provided by Dr. David Kirsch (Duke University School of Medicine, Durham, NC, USA). Exons 2 to 6 of the murine *Trp53* gene are flanked by *frt* sites, which are recognized by the Flp recombinase. Upon Flp recombination, these flanked exons are excised and *Trp53* gene is inactivated.

FSF-Rosa26$^{CAG\text{-}CreERT2/+}$ (Schönhuber et al., 2014), RRID:MGI:2176738 – This knockin mouse strain was generated in the laboratory of Prof. Dr. med. Dieter Saur. After excision of the *FSF* cassette by the Flp recombinase, *CreER^{T2}* is expressed under the control of the CAG promoter as a knockin at the *Rosa26* locus. By administration of tamoxifen, the Cre recombinase can be activated.

Rosa26$^{mTmG/+}$ (Muzumdar et al., 2007), RRID:IMSR_JAX:007576 – This reporter mouse strain was purchased from The Jackson Laboratory (Bar Harbor, ME, USA). It is a *Rosa26* knockin strain, where *loxP*-flanked membrane-targeted tandem dimer Tomato (tdTomato) is expressed under the control of the ubiquitously CAG promoter. Upon Cre-mediated excision of the tdTomato cassette, membrane-targeted enhanced green fluorescent protein (eGFP) is expressed.

Rosa26$^{Dual/+}$ (Chen et al., 2018), RRID:IMSR_JAX:007909 – This mouse strain was generated in the laboratory of Prof. Dr. med. Dieter Saur. Firefly luciferase (fLuc) and eGFP expression are induced by Flp recombinase, which in turn leads to recombination of fLuc-eGFP cassette by Cre and thereby activates renilla luciferase and tdTomato expression.

CAG$^{dsRed\text{-}eGFP}$ (De Gasperi et al., 2008), RRID:IMSR_JAX:008605 – This dual reporter mouse strain was purchased from The Jackson Laboratory (Bar Harbor, ME, USA). Being under the control of CAG promoter, the *loxP*-flanked optimized red fluorescent protein dsRed-Express is expressed directly in embryonic and adult tissues prior to Cre-mediated recombination. Upon Cre recombinase expression, the eGFP cassette is expressed.

5.1.2. Genotyping

At an age of 2-3 weeks, a 1 mm long piece of tail tip biopsy was taken from previously anesthetized mice with a sterile scalpel or, alternatively, ear punches used as mouse identifiers were collected. Tail and ear samples were used for isolation of genomic DNA and genotyping PCR analysis as described in section 5.4.1..

5.1.3. Tamoxifen treatment of mice

To induce *Braf*$^{V637E/+}$ mutation and to study the effect of *Cdh1* deletion on tumor progression, mice were treated with tamoxifen. *Braf* mice at age of 9-10 weeks were directly administrated once with 4 mg of tamoxifen by intraperitoneal (i.p.) injection, while the *Cdh1* mice at age of 3 months were administrated in 3 distinct days. Tamoxifen was dissolved in peanut oil containing 10% ethanol (EtOH) absolute at a concentration of 60 mg/mL.

5.1.4. Orthotopic implantation

For orthotopic implantation, 24 F1 hybrid C57BL/6J;129/S6 females at the age of 8-9 weeks were used. Conditions and instruments for implantation were kept as sterile as possible. After anesthesia of mice with MMF (5 mg/kg midazolam, 500 µg/kg medetomidine, 50 µg/kg fentanyl) via i.p. injection, a small abdominal incision in the skin of the abdomen was made and the pancreas was exposed gently pulling the spleen out. 5000 cells suspended in 20 µL of serum-free Dulbecco's Modified Eagle's Medium (DMEM) medium were injected directly into the pancreas using a microliter syringe with a 27-gauge needle. The peritoneum was sewed with sterile EthilonII fiber with at least 3 to 5 knots and subsequently the skin of the abdomen was closed using wound clips. After the operation, MMF anesthesia was antagonized by applying AFN (750 µg/kg atipamezole, 500 µg/kg flumazenil, 1.2 mg/kg naloxone) via subcutaneous injection and analgesic (Metacam) was also given to the mice. All animals were monitored until sacrificed at the same endpoint (5 weeks after implantation).

5.1.5. Mouse dissection

Mice were sacrificed with MMF via i.p. injection and terminal bleeding, fixed and disinfected with 70% EtOH. The abdomen was cut open and samples were collected under sterile conditions as possible. Pancreatic tissue samples for following DNA, RNA, and protein isolation were collected and all samples were snap frozen and stored at -80 °C until use. Additionally, in case of PDAC formation, a piece of the pancreatic tumor and metastatic tissues (liver, lung and/or peritoneum) were cut out and transferred to Petri dishes with sterile 1×phosphate-buffered saline (PBS) in order to isolate cell lines from the respective tissues. Under a biological safety cabinet, the tissue samples were cut with a sterile scalpel into small pieces and incubated in 5 mL cancer cell medium containing 200 U/mL collagenase type II at 37 °C for 24-36 hours. Afterwards, the cell suspension was centrifuged at 1200 rpm for 5 min, supernatant was aspirated, and the pellet was resuspended in 5 mL cancer medium and cultured in a 25 cm^2 tissue culture flask. For isolation of CTCs, blood from ascites was collected in a reaction tube containing sterile EDTA to avoid coagulation; the samples were then centrifuged at 1000 rpm for 5 min. Subsequently, the supernatant was discarded, and the cell pellet was resuspended in cancer cell medium and cultured in a 25 cm^2 tissue culture flask. The weight and the size of the pancreas tissue were measured and macroscopic pictures of the organs of interest were taken using the Zeiss Stemi SV 11 stereomicroscope. In addition, the metastatic sites and the number of macrometastases in

each secondary organ were also noted. Pancreas, spleen, and metastatic tissues (for example, liver and/or lung) were divided in two pieces: one piece for cryopreserved sections and the second piece for formalin-fixed paraffin-embedded (FFPE) sections (as described in section 5.2.1.). Liver, lung, heart, stomach, duodenum, and kidneys were also collected and processed for FFPE samples.

5.2. Histological analysis

5.2.1. Preparation of cryopreserved and FFPE tissues

Depending on the application, tissues were processed either for frozen sections or FFPE sections. Mouse tissues harvested for cryopreserved sectioning were fixed in 4% paraformaldehyde (PFA) without methanol for 2 hours at 4 °C. After washing thrice with 1×PBS, the samples were dehydrated in successive higher concentrated sucrose (15% sucrose for 4 hours and 30% sucrose overnight) at 4 °C. Tissues were then embedded in a sample vial filled with frozen section medium Richard-Allan Scientific NEG-50 and positioned in the bottom of the vial. Finally, the tissues were frozen using a dry ice and EtOH bath and stored for long term at -80 °C. Tissues were serially cut into 5-10 µm-thick sections using the Leica CM3050 S cryostat and posteriorly stored at -20 °C (for short term) or -80 °C (for long term) until further use.

Mouse tissues collected for FFPE sectioning were fixed in 4% ROTI®Histofix for 16-24 hours at 4 °C. Dehydration, clearing and paraffin wax infiltration were performed by the tissue processor ASP300S. Samples were subsequently embedded in paraffin using the heated paraffin embedding module HistoCore Arcadia H and stored at room temperature (RT) until further use. Series of 1-3 µm-thick sections were cut using the microtome Microm HM355S and dried overnight at RT or for 2 hours at 37 °C prior to staining.

5.2.2. Hematoxylin and eosin staining

Hematoxylin and eosin (H&E) staining was performed on both cryopreserved and FFPE sections for histopathological analysis and grading of tumors and assessment of micrometastases in secondary organs (liver and lungs). For cryosections, the tissues were post-fixed in 4% ROTI®Histofix for 10 min and then rinsed in tap water to remove the excess of fixative solution. The nuclei were stained with hematoxylin for 3 sec and immediately rinsed under tap water. The cytoplasm was stained with eosin 2% w/v for 3 sec. The sections were washed again in tap water and checked under the Leica microscope ICC50 W to evaluate the color balance between H&E on the tissues. The tissues were then dehydrated in ascending EtOH solutions (2 x 80% EtOH, 2 x 96% EtOH, and 2 x 100% EtOH; for 15 sec each) and incubated in ROTI®Histol (2 x 5 min). Finally, sections were mounted with Cytoseal™ XYL mounting medium. For Chapter I, Part B, more than 80 cryopreserved tissues were cut, H&E stained and evaluated using the Leica microscope ICC50 W. The tissues selected to be included in the TME analysis were then scanned

using Aperio Versa 8 Digital Scanner. Stained tissues were analyzed, photographed and images saved as .tif file using Aperio ImageScope software.

For FFPE sections from primary pancreatic tumor (PPT), liver and lungs, the tissues were deparaffinized in ROTI®Histol (2 x 5 min), rehydrated in successive EtOH solutions (2 x 100% EtOH, 2 x 96% EtOH, and 2 x 80% EtOH; for 3 min each), and in tap water (3 min). The nuclei were stained with hematoxylin for 30 sec and immediately rinsed under tap water to remove the excess of hematoxylin dye. The cytoplasm was stained with eosin 2% w/v for 20 sec. The sections were washed again in tap water, dehydrated in ascending EtOH solutions (2 x 80% EtOH, 2 x 96% EtOH, and 100% EtOH; for 15 sec each), and incubated in ROTI®Histol (2 x 5 min). Finally, sections were mounted with Cytoseal™ XYL mounting medium. For Chapter II, all the *Cdh1* stained tissues were then scanned using Aperio Versa 8 Digital Scanner and analyzed, photographed and images saved as .tif file using Aperio ImageScope software. The pathological grading was performed in collaboration with Dr. med. vet. Katja Steiger and Nils Wirges from the Core Facility Comparative Experimental Pathology at the Institute of Pathology, Technical University of Munich. The assessment of liver and lung micrometastases was done by analysis of the tissues under the Leica microscope ICC50 W for posterior labeling with E-cadherin antibody.

5.2.3. Immunofluorescence stainings

For Chapter I, Part A of the Results (section 6.1.), immunofluorescence (IF) staining was performed to determine which type of tissues (cryopreserved and FFPE tissues) would be used to establish the mIHC panels as well as to validate antibodies for immune cells' detection using splenic and hepatic tissues and to validate the tumor cell marker using PPT tissue. In addition, in Chapter I, Part B of the Results (section 6.2.), IF labeling was performed to determine the cellular (tumor, immune, and stromal) content in PPT tissues.

5.2.3.1. Determination of type of sections to use in the establishment of the multiplexed immunohistochemistry panels

To determine which type of sections (FFPE or cryopreserved tissues) would be used in the development of the mIHC protocols, IF staining was performed in both FFPE and cryopreserved sections using the following antibodies: F4/80, #MCA497; CD3, #100201; and CD45R/B220, #103201. FFPE tissues were deparaffinized in ROTI®Histol (2 x 5 min), rehydrated in successive EtOH solutions (2 x 100% EtOH, 2 x 96% EtOH, and 2 x 80% EtOH; for 3 min each), and in tap water (3 min). Heat-mediated antigen retrieval was performed by boiling the sections in a microwave at 500 W for 3 min and then at 350 W for 10 min in a citric acid-based antigen unmasking solution pH 6.0 (prepared according to the manufacturer's instructions). After cooling down for 20-30 min at RT in the citrate buffer solution and washing thrice with 1×PBS, the tissue sections were blocked with 10% donkey serum/3% BSA solution for 1 hour at RT. Then, the sections were incubated with each individual primary antibody diluted in 3% BSA (F4/80 and

CD3 at 1:100 and CD45R/B220 at 1:200) and incubated for 3 hours at RT. After washing thrice with 1×PBS, the secondary antibody donkey anti-rat Alexa Fluor® (AF) 488 was diluted 1:200 in 3% BSA and applied for 1 hour at RT. Subsequently, the tissues were washed thrice with 1×PBS and then incubated with DAPI diluted 1:1000 in 3% BSA for 10 min at RT. Finally, the tissues were washed thrice with 1×PBS, mounted in Vectashield® mounting medium, and stored at 4 °C until the imaging was performed.

For IF labeling of frozen samples, tissue sections were thawed on a hot plate for 1 min at 37 °C, air dried for 20 min at RT, and post-fixed with acetone for 6 min at 4 °C. After air drying once again for 20 min at RT, the tissues were rehydrated in 1×PBS for 10 min and then blocked with 10% donkey serum/3% BSA for 1 hour at RT. Then, the sections were incubated with each individual primary antibody diluted in 3% BSA (F4/80 and CD3 at 1:100 and CD45R/B220 at 1:200) and incubated for 3 hours at RT. After washing thrice with 1×PBS, the secondary antibody donkey anti-rat AF 488 was diluted 1:200 in 3% BSA and applied for 1 hour at RT. Subsequently, the tissues were washed thrice with 1×PBS and then incubated with DAPI diluted 1:1000 in 3% BSA for 10 min at RT. Finally, the tissues were washed thrice with 1×PBS, mounted in Vectashield® mounting medium, and stored at 4 °C until the imaging was performed.

5.2.3.2. Validation of antibodies and respective quality controls

All selected antibodies to detect immune and tumor cells were assessed by uniplex IF staining to optimize the antibody staining protocol. For the immune cell markers, splenic tissue from a wild-type (WT) mouse was used as positive tissue control and for the secondary antibody, autofluorescence, and cross-reaction controls. In addition, hepatic tissue from a WT animal and splenic tissue from a *Rag2/Il2rg*-knockout (KO; lacking mature T and B cells) mouse were used as negative tissue controls for immune cell markers. Uniplex IF staining was also applied to WT splenic tissue to validate directly-conjugated and -labeled antibodies. Regarding the tumor cell marker, PPT tissue was used as positive tissue control and WT splenic tissue as negative tissue control. Frozen sections were single stained for each individual marker (depicted in Table 10), using the indirect method of staining (i.e., unlabeled primary antibody against a target antigen and a labeled secondary antibody), as following described. For IF labeling, tissue sections were thawed on a hot plate for 1 min at 37 °C, air dried for 20 min at RT, and post-fixed with acetone for 6 min at 4 °C. After air drying once again for 20 min at RT, the tissues were rehydrated in 1×PBS for 10 min and then blocked with 10% serum/3% BSA for 1 hour at RT. Then, the sections were incubated with each individual primary antibody diluted in 3% BSA, at concentration indicated in Table 10, for 3 hours at RT. After washing thrice with 1×PBS, the respective secondary antibody (depicted in Table 10) diluted 1:200 in 3% BSA was applied for 1 hour at RT. Subsequently, the tissues were washed thrice with 1×PBS and then incubated with DAPI diluted 1:1000 in 3% BSA for 10 min at RT. Finally, the tissues were washed thrice with 1×PBS, mounted in Vectashield® mounting medium, and stored at 4 °C until the imaging was performed.

Table 10. Single stainings with immune and tumor cell markers established for cryopreserved sections using the indirect method

Primary antibody	Blocking serum	Dilution	Secondary antibody
Rat **CD11b**, #553308	Donkey	1:100	Donkey anti-rat Alexa Fluor® 488, #A21208
Rat **CD68**, #MCA1957	Donkey	1:100	Donkey anti-rat Alexa Fluor® 488, #A21208
Rat **F4/80**, #MCA497	Donkey	1:100	Donkey anti-rat Alexa Fluor® 488, #A21208
Armenian hamster **CD11c**, #14-0114-82	Goat	1:100	Goat anti-Armenian hamster Cy3, #127-165-160
Rat **Ly6G/Ly6C**, #14-5931-82	Donkey	1:100	Donkey anti-rat Alexa Fluor® 488, #A21208
Goat **Siglec-F**, #AF1706	Donkey	1:100	Donkey anti-goat Alexa Fluor® 594, #A11058
Rat **CD3**, #100201	Donkey	1:100	Donkey anti-rat Alexa Fluor® 488, #A21208
Armenian hamster **CD3e**, #553058	Goat	1:100	Goat anti-Armenian hamster Cy3, #127-165-160
Rabbit **CD4**, #ab183685	Goat	1:200	Goat anti-rabbit Alexa Fluor® 488, #A11034
Rat **CD8a**, #14-0081-82	Donkey	1:100	Donkey anti-rat Alexa Fluor® 488, #A21208
Rat **CD45R/B220**, #103201	Donkey	1:200	Donkey anti-rat Alexa Fluor® 488, #A21208
Rat **CD45**, #MCA1031G	Donkey	1:100	Donkey anti-rat Alexa Fluor® 488, #A21208
Rabbit **Keratin 18**, #SAB4501665	Goat	1:500	Goat anti-rabbit Alexa Fluor® 488, #A11034

CD, cluster of differentiation.

To test the specificity of the primary antibodies against their target antigen (cross-reaction control), double stainings with certain immune markers (depicted in Table 11) were also performed using the indirect method. A similar protocol to the single stainings was followed including the thawing, air drying, post-fixing with acetone, dehydrating, and blocking with 10% serum/3% BSA. Each combination of two primary antibodies was diluted in 3% BSA at concentrations indicated in Table 11 and incubated for 3 hours at RT. Followed by three washes with 1×PBS, the respective combination of secondary antibodies (depicted in Table 11) was diluted in 3% BSA and incubated for 1 hour at RT. Afterwards, the tissues were washed thrice with 1×PBS and incubated with DAPI diluted 1:1000 in 3% BSA for 10 min at RT. The tissues were subsequently washed thrice with 1×PBS, mounted in Vectashield® mounting medium, and stored at 4 °C until the imaging was performed. Stained cryosections were imaged using Leica TCS SP8 confocal microscope equipment with a HC PL APO CS2 40x/1.30 OIL objective and images were taken at 1024 x 1024 voxel density.

Table 11. Double stainings with immune cell markers established for cryopreserved sections

Combination of primary antibodies	Blocking serum(s)	Dilutions	Secondary antibodies
Rat **CD11b**, #553308 & Goat **Siglec-F**, #AF1706	Donkey	1:100 & 1:100	Donkey anti-rat Alexa Fluor® 488, #A21208 & Donkey anti-goat Alexa Fluor® 594, #A11058
Rat **F4/80**, #MCA497 & Goat **Siglec-F**, #AF1706	Donkey	1:100 & 1:100	Donkey anti-rat Alexa Fluor® 488, #A21209 & Donkey anti-goat Alexa Fluor® 594, #A11058
Rat **F4/80**, #MCA497 & Armenian hamster **CD3e**, #553058	Goat & Donkey	1:100 & 1:100	Donkey anti-rat Alexa Fluor® 488, #A21208 & Goat anti-Armenian hamster Cy3, #127-165-160
Armenian hamster **CD3e**, #553058 & Rat **CD45R/B220**, #103201	Goat & Donkey	1:100 & 1:100	Goat anti-Armenian hamster Cy3, #127-165-160 & Donkey anti-rat Alexa Fluor® 488, #A21208
Armenian hamster **CD3e**, #553058 & Rabbit **CD4**, #ab183685	Goat	1:100 & 1:200	Goat anti-Armenian hamster Cy3, #127-165-160 & Goat anti-rabbit Alexa Fluor® 488, #A11034
Armenian hamster **CD3e**, #553058 & Rat **CD8a**, #14-0081-82	Goat & Donkey	1:100 & 1:100	Goat anti-Armenian hamster Cy3, #127-165-160 & Donkey anti-rat Alexa Fluor® 488, #A21208
Rabbit **CD4**, #ab183685 & Rat **CD8a**, #14-0081-82	Goat & Donkey	1:200 & 1:100	Goat anti-rabbit Alexa Fluor® 594, #A11037 & Donkey anti-rat Alexa Fluor® 488, #A21208

CD, cluster of differentiation.

5.2.3.3. Labeling primary antibody using Antibody Labeling Kit

Antibody Labeling Kits provided by Thermo Fisher Scientific allowed us to directly fluorophore-label primary antibodies, which were previously validated and quality controlled. The concentration of the antibodies to be labeled was checked, since ideal antibody concentration for the labeling performance is ≥ 1 mg/mL. The Labeling the Protein and Purifying the Labeled Protein steps were following according to the manufacturer's instructions, except step 2.6 where the spin column was centrifuged thrice (instead of once) for 5 min at 1100 xg. In the end, we obtained labeled protein in approximately 100 µL of PBS with 2 mM sodium azide. To determine the efficacy of the labeling, splenic tissue from a WT animal was labeled as described in section 5.2.3.2. and stainings were compared with the ones obtained using the indirect method of IF.

5.2.3.4. Determination of cellular proportions in primary pancreatic tumor tissues

To determine the proportions of PCCs and TME cells in PPT tissues, cryopreserved sections were labeled for keratin 18 (CK18), PDPN and CD45, a protocol optimized by Tatiana Martins. Frozen sections were thawed on a hot plate for 1 min at 37 °C, air dried for 30 min at RT, and post-fixed with 4% PFA without methanol for 1 min at RT. Afterwards, the tissues were washed thrice in 1×PBS and incubated in 10% goat serum/3% BSA/0.1% Triton™ X-100 for 1 hour at RT. The sections were then incubated with primary antibodies PDPN (1:100) and CD45 (1:200) diluted in the blocking solution overnight at 4 °C. After washing thrice with 0.1% Triton™ X-100/PBS, the secondary antibodies goat anti-rat AF 555 and goat anti-Armenian hamster AF 647 were diluted 1:200 in the blocking solution and applied for 1 hour at RT. Subsequently, three washes with 0.1% Triton™ X-100/PBS were performed and CK18 antibody labeled with AF 680 diluted 1:100 in 10% rabbit serum/3% BSA/0.1% Triton™ X-100 was incubated for 3 hours at RT. The sections were washed thrice with 0.1% Triton™ X-100/PBS and incubated with DAPI diluted 1:1000 in 0.1% Triton™ X-100/PBS for 10 min at RT. The tissues were subsequently washed thrice with 0.1% Triton™ X-100/PBS, mounted in Vectashield® mounting medium, and stored at 4 °C until the imaging was performed. Stained cryosections were imaged using Leica TCS SP8 confocal microscope equipment with a HC PL APO CS2 40x/1.30 OIL objective and Z-stacked images were taken in two distinct regions of interest, using a 3 x 3 tile scan, and at 1024 x 1024 voxel density. Posteriorly, all imaged cells were segmented in Imaris 9.6 software, and number of total segmented objects was noted, and ratios were calculated using Excel software. In addition, statistical information of the segmented cells, namely x,y position, was exported into FlowJo v10.6.1 software for spatial visualization of the tumor (CK18-positive), immune (CD45-positive), and stromal (PDPN-positive) populations using both dot and density plots.

5.2.4. Immunohistochemistry stainings

FFPE sections of PPT, liver, and lung tissues were labeled for E-cadherin and PPT tissues were additionally stained for Ki-67 by IHC staining. Tissues were deparaffinized in ROTI®Histol (2 x 5 min), rehydrated in successive EtOH solutions (2 x 100% EtOH, 2 x 96% EtOH, and 2 x 80% EtOH; for 3 min each), and in tap water (3 min). Heat-mediated antigen retrieval was performed by boiling the sections in a microwave at 500 W for 3 min and then at 350 W for 15 min in a citric acid-based antigen unmasking solution pH 6.0 (prepared according to the manufacturer's instructions). After cooling down for 20-30 min at RT in the citrate buffer solution and washing thrice with 1×PBS, the sections were incubated with 3% H_2O_2 solution for 20 min at RT to block endogenous peroxidase activity. The tissue sections were blocked with a 5% goat serum/avidin/PBS solution for 1 hour at RT. The primary antibodies E-cadherin and Ki-67 were individually diluted in 5% goat serum/biotin/PBS solution (mouse E-cadherin, #610181, 1:100; and rabbit Ki-67, #KI681C01, 1:50) and sections were incubated overnight at 4 ºC. Afterwards, the tissues were washed thrice with 1×PBS before incubation with the appropriate biotinylated secondary antibodies (goat anti-mouse, #BA-9200, for E-cadherin staining detection; and goat anti-rabbit, #BA-1000, for Ki-67 labeling detection), which were separately diluted 1:500 in 5%

goat serum/PBS solution, for 1 hour at RT. The sections were washed thrice with 1×PBS and the detection of positive staining was performed using the Vectastain® elite ABC kit prepared according to the manufacturer's instructions. This step was followed by development with 3,3'-Diaminobenzidine (DAB; prepared according to manufacturer's protocol) for 1min:30sec for both E-cadherin and Ki-67 stainings. Hematoxylin counterstaining was performed for 2-3 sec and, finally, sections were dehydrated in ascending EtOH solutions (2 x 80% EtOH, 2 x 96% EtOH, and 100% EtOH; for 15 sec each), incubated in ROTI®Histol (2 x 5 min) and mounted with Cytoseal™ XYL mounting medium. All the stained tissues were scanned using Aperio Versa 8 Digital Scanner and analyzed, photographed and images saved as .tif file using Aperio ImageScope software. For the quantification of E-cadherin-negative lesions, determination of the optical density of E-cadherin staining, and quantification of Ki-67-positive cells, five random snapshots of each tissue in a 20x zoom were taken and save as .tiff files. E-cadherin-negative lesions were counted in each field of view. Using Fiji v1.53 software, the number of Ki-67-positive cells was determined as well as the total number of nuclei. Regarding the optical density of E-cadherin staining, the deconvoluted channel of IHC/DAB staining was measure as "Mean gray value"; this mean value was noted, and the optical density was calculated using the following formula in Excel software:

$$OD = \log\left(\frac{max\ intensity}{mean\ intensity}\right), where\ max\ intensity = 255\ for\ 8\text{-}bit\ images$$

5.3. *In vitro* analysis

5.3.1. Culture conditions and handling of primary murine pancreatic tumor cell lines

Primary murine PCCs were established from tumor mice (as described in section 5.1.5.), handled under sterile conditions in a laminar flow bench and were maintained in fresh pre-warmed cancer cell medium (depicted in Table 6) at 37 ºC and 5% CO_2. Upon reaching a confluency of 80-95%, the cells were passaged as following described. The medium was aspirated, cells were washed with sterile 1×PBS and detached from the surface of the tissue culture flask by incubation with 1×trypsin solution at 37 ºC for an appropriate time period. Trypsinization was stopped by adding medium to the cell suspension, which subsequently was transferred into a new tissue culture flask or seeded in Petri dishes or cell culture microplates depending on the experimental design. When applicable, cell number was determined using a Neubauer hemacytometer prior to the seeding step.

For cryopreservation, trypsinized cells were transferred to a conical tube and centrifuged at 450 ×g for 5 min. After aspirating the supernatant, the pellet was resuspended in ice-cold freezing medium (depicted in Table 6), transferred to CryoPure tubes, frozen at -80 ºC, and stored in a liquid nitrogen cryogenic sample storage.

5.3.2. Authentication of cell lines

Cultured tumor cell lines were routinely tested for mycoplasma contamination by PCR and authenticated by regenotyping of cells and corresponding mice. Cell lines were cultured in DMEM only supplemented with 10% FBS (without 1% penicillin-streptomycin) until the medium turned yellow. Afterwards, 2 mL of medium was collected and centrifuged for 2 min at 250 ×g. The supernatant was collected and centrifuged for 10 min at maximum speed (about 18,000 ×g). The supernatant was discarded, the pellet was resuspended in 30 µL of distilled water (dH_2O) and heated for 3 min at 95 ºC. The resulting suspension was processed as described in section 5.4.2.3. or stored at -20 ºC until the PCR performance.

5.3.3. Documentation of cell morphology

Bright-field pictures of murine cell lines were documented with the microscope Leica DM IL LED equipped with 5x, 10x and 20x objectives and Leica Application Suite X software.

5.3.4. 4-hydroxytamoxifen treatment of primary murine pancreatic tumor cells

To induce the activity of $CreER^{T2}$ *in vitro*, primary murine PCCs were treated with vehicle (100% EtOH) or 600 nM 4-OHT for 7 days to delete the *loxP*-flanked sequences of the *Cdh1* allele. Subsequently, treated cells were seeded for several assays, including MTT assay, clonogenic assay, immunocytochemistry (ICC) staining, and generation of $Cdh1^{fl/fl}$ and $Cdh1^{\Delta/\Delta}$ clones (as described in sections 5.3.5. to 5.3.8.).

5.3.5. MTT assay

The MTT assay is a colorimetric assay used to measure cellular metabolic activity as an indicator of cell viability, proliferation, and cytotoxicity. The water soluble MTT reagent (3-(4,5-dimethylthiazol-2-yl)-2,5-diphenyltetrazolium bromide) with a yellow coloration is taken up by the cells and converted into an insoluble formazan product with a purple coloration. Cells were counted and seeded in a concentration of 2000, 1000, and 500 cells/well in five 96-well plates (one per each five consecutive days of the assay) as pentaplicates. 20 µL of MTT reagent were added to 100 µL of cancer cell medium (final concentration of MTT reagent: 1 mg/mL) of each well and incubated for 4 h at 37 ºC. Subsequently, the medium was discarded, and the water-insoluble formazan crystals were solubilized by adding 100 µL of 100% EtOH/DMSO solution (1:1, v/v). The 96-well plate was incubated on a shaker for 10 min at RT. After solubilization of the formazan, the concentration of the colorimetric product was determined by an optical density measurement at 570 nm by the multimode microplate reader CLARIOstar. Technical triplicates in three independent experiments were carried out.

5.3.6. Clonogenic assay

Colony formation assay is based on the ability of a single cell to divide and grow into a colony. Cells were counted and seeded in a concentration of 2000 cells/well in a 6-well plate as triplicates. After allowing cellular growth for 8 days and showing visible colonies, cancer cell medium was aspirated, and cells were fixed with 99% ice-cold methanol on a shaker for 30 min at 4 ºC. After methanol was removed, colonies were washed with cold 1×PBS and stained with Giemsa solution (diluted 1:20 in dH_2O) on a shaker overnight at RT. Afterwards, Giemsa solution was removed, cells were washed with dH_2O and plates were air dried. The 6-well plates were then scanned using an Epson scanner Perfection V370 Photo and the number of colonies was determined using the ImageJ software.

5.3.7. Immunocytochemistry staining

Cells were seeded on sterile coverslips placed in a 6-well plate for the performance of ICC staining to detect E-cadherin protein with or without Ki-67 marker. When the cell confluency reached 70-80%, the cells were fixed with 4% PFA without methanol for 20 min at 4 ºC. After washing the cells thrice with 1×PBS, a blocking step was performed using a 10% goat serum/3% BSA solution during 1 hour at RT. Afterwards, the cells were incubated overnight at 4 ºC with primary antibodies E-cadherin (1:100, rat, #sc-59778) and Ki-67 (1:50, rabbit, #ab16667) together with Phalloidin CF633 (1:1000) diluted in 0.5% BSA/0.5% Triton™ X-100. After washing thrice with 1×PBS, the secondary antibodies goat anti-rat AF 680 and goat anti-rabbit AF 488 were diluted 1:200 in 3% BSA and applied for 1 hour at RT. Three washes with 1×PBS were performed, and the nuclei were labeled with DAPI (1:5000) diluted in 3% BSA and incubated 10 min at RT. The cells were subsequently thrice washed with 1×PBS, mounted in Vectashield® mounting medium, and stored at 4 °C until the imaging was performed. Confocal images of ICC stainings were acquired using Leica TCS SP8 confocal microscope equipment with a HC PL APO CS2 40x/1.30 OIL objective and the fluorescent signals were detected, as depicted in Table 12. Images of five random fields of view were taken at 1024 x 1024 voxel density. Using Fiji v1.53 software, the number of E-cadherin-negative and Ki-67-positive cells were determined as well as the total number of nuclei per field of view.

Table 12. Confocal microscope settings for the image acquisition of immunocytochemistry staining

Sequence	Marker	Laser (nm; %)	Detector	Emission (nm)	Gain (% or V)
Seq. 1	Ki-67	490; 7.80	HyD2	508-533	100.0
	E-cadherin	670; 22.5	HyD4	689-719	100.0
Seq. 2	Phalloidin	630; 5.20	HyD4	638-662	100.0
	DAPI	405; 3.50	PMT1	441-476	862.0

%, percentage; HyD, hybrid detector; nm, nanometer; PMT, photomultiplier tube detector; Seq., sequence; V, volt.

5.3.8. Generation of *Cdh1$^{fl/fl}$* and *Cdh1$^{Δ/Δ}$* clones

To analyze the effect of *Cdh1* loss *in vitro*, six *Cdh1$^{fl/fl}$* cell lines were treated with 4-OHT for 7 days and seeded in the same manner as a clonogenic assay. For each cell line, each growing colony was picked with a sterile pipette tip and transferred to a single well of a 96-well plate with 100 µL of cancer cell medium. Once a colony was formed in the well of a 96-well plate, the medium was discarded, and the cells were gently washed with 1×PBS. Then, 1×trypsin solution was added to the well and the plate was incubated at 37 ºC until the cells detached. Trypsinization was stopped by adding medium to the cell suspension, which was then transferred into a well of a 24-well plate. When the well was confluent, the cells were transferred to a well of a 6-well plate, as previously described, and DNA was isolated to determine the recombination status of *Cdh1* of the clones. Clones harboring both *Cdh1^{fl}* and *Cdh1^{Δ}* alleles were discarded, whilst *Cdh1$^{fl/fl}$* (*Cdh1*-proficient) and *Cdh1$^{Δ/Δ}$* (*Cdh1*-deficient) generated clones were then cultured in 25 and 75 cm^2 tissue culture flasks until it would be possible to freeze the cells for further analysis.

5.3.9. Preparation of cells for implantation

For implantation, a *Cdh1$^{fl/fl}$* cell line treated with vehicle and 4-OHT and two *Cdh1$^{fl/fl}$* and two *Cdh1$^{Δ/Δ}$* generated clones from that 4-OHT-treated cell line were selected. All the cells were cultured in cancer cell medium. On the implantation day, the cells were trypsinized until they detached from the bottom of the flask. The cell suspension was then centrifuged for 5 min at 350 ×g, medium was discarded, and the cell pellet was resuspended in DMEM medium without FCS or penicillin/streptomycin. The cell number was determined with Neubauer hemocytometer and the cells were suspended in 2000 mL of DMEM medium without FCS or penicillin/streptomycin at a final concentration of 5000 cells per 20 µL of injection.

5.4. Molecular biology

5.4.1. Isolation of genomic DNA

Isolation of genomic DNA from mouse tail tips, tissues or cell pellets for PCR analysis was done by adding 50 µL of Soriano lysis buffer freshly supplemented with proteinase K and DTT. Lysis was performed in a thermocycler for 90 min at 55 ºC followed by proteinase K inactivation for 15 min at 95 ºC. After vigorously vortexing the sample, the DNA-containing supernatant was separated from the debris by centrifugation for 5 min at 1000 ×g, transferred into a new reaction tube and stored at 4 ºC for short term or at -20 ºC for longer time period until PCR analysis was performed.

5.4.2. Polymerase chain reaction (PCR)

Standard PCR was used for genotyping of mice tail DNA, analysis of recombination in murine tissues and cell lines. A pre-mix for PCR containing 10× buffer S, polymerase and dNTPs was used, as shown in Table 13. The standard PCR reaction mix and conditions are depicted in Tables 14 and 15. The primer amount was individually optimized depending on the PCR product. PCR products were stored at 4 ºC until further analysis by gel electrophoresis as described in section 5.4.2.4..

Table 13. Composition of polymerase chain reaction pre-mix

Component	Volume (µL) for one reaction
dH_2O	4.375
10x buffer S	2.5
30% sucrose	2.5
SucRot	2.5
PeqTaq	0.125
dNTPs (10 µM each)	0.5

%, percentage; µL, microliter; µM, micromolar; dH_2O, distilled water; dNTP, deoxyribonucleotide triphosphate.

Table 14. Polymerase chain reaction mix

Component	Volume (µL) for one reaction
PCR pre-mix	12.5
Forward primer (10 µM)	0.25 – 2
Reverse primer (10 µM)	0.25 – 2
DNA template	1 – 2
dH_2O	add up to 24 µL

µL, microliter; µM, micromolar; dH_2O, distilled water; PCR, polymerase chain reaction.

Table 15. Conditions for standard polymerase chain reaction

Step	Temperature (ºC)	Time (seconds)	Cycles
Initial denaturation	95	180	
Denaturation	95	30-45	40x
Annealing	55 - 65	30-60	
Elongation	72	60-90	
Final elongation	72	300	
Storage	25	hold	

ºC, degree Celsius.

5.4.2.1. Genotyping and recombination PCR

To determine the genotype of a mouse, regenotype a cell line and/or analyze the activity of a recombinase in a tissue or cell line, isolated genomic DNA (isolation described in section 5.4.1.) was used to perform genotyping or recombination PCR, respectively. For each allele, specific primers were designed (Table 8), annealing temperatures were adjusted, and PCR products were determined as listed in Table 16.

Table 16. Annealing temperatures and polymerase chain reaction products

PCR name	Annealing temperature (ºC)	PCR products (bp)
Pdx1-Cre	64	674 (mut) / 202 (internal control)
Pdx1-CreER^{T2}	58	410 (mut) / 300 (WT)
Pdx1-Flp	56	620 (mut) / 300 (WT)
LSL-Kras^{G12D}	55	300 (rec) / 270 (WT) / 170 (mut)
FSF-Kras^{G12D}	55	351 (mut) / 306 (rec) / 270 (WT)
LSL-Pik3ca^{H1047R}	64	630 (mut)
LSL-Braf^{V637E}	63	413 (mut) / 357 (WT)
Cdh1^{fl}	60	330 (mut) / 190 (WT)
Cdh1^{fl} recombination	63	450 (rec) / 308 (mut) / 185 (WT)
LSL-Trp53^{R172H}	60	570 (WT) / 270 (mut)
Tr53^{lox}	64	370 (mut) / 288 (WT)
Trp53^{frt}	57	292 (mut) / 258 (WT)
Trp53^{frt} recombination	55	352 (rec)
Rosa26^{Tva}	62	600 (WT) / 400 (*Pik3ca^{H1047R}*) / 310 (mut)
CreER^{T2}	55	190 (mut)
Rosa26^{CAG}	62	650 (WT) / 450 (mut) / 350 (*R26^{mTmG}*)
FSF-Stop	60	600 (mut)
FSF recombination	60	490 (rec)
Rosa26^{mTmG}	62	650 (WT) / 450 (mut)
Rosa26^{mTmG} recombination	62	1023 (eGFP) / 852 (tdTomato)
CAG$^{dsRed-eGFP}$	65	220 (mut)
Rosa26^{Dual}	60	916 (mut) / 650 (WT)

bp, base pair; eGFP, enhanced green fluorescent protein; mut, mutated allele; PCR, polymerase chain reaction; rec, mutated allele without stop element after recombination; tdTomato, tandem dimer tomato; WT, wild-type.

5.4.2.2. Mycoplasma contamination test PCR

Samples for mycoplasma contamination test were obtained as described in section 5.3.2.. The PCR for mycoplasma detection was carried out in a final volume of 30.0 µL in 15.0 µL of the PCR pre-mix (Table 13), 2 µL of forward-primer mix and 2 µL of reverse-primer mix (in a final concentration of 10 µM; Table 8), 9 µL of dH_2O, and 2 µL of the DNA suspension. To perform the PCR, the reaction solution was initially denatured at 95 °C for 15 min, then 40 cycles of 94 ºC for 1 min (denaturation), 60 ºC for 1 min (annealing), and 74 ºC for 1 min (elongation) were run and lastly a final elongation step was performed at 72 ºC for 10 min. Fifteen µL of the PCR product were loaded on a 2.0% agarose gel and analyzed by electrophoresis as described section 5.4.2.4.. Negative samples for mycoplasma contamination show no band, while positive samples present a band at 500 bp.

5.4.2.3. Agarose gel electrophoresis of PCR products

Agarose gels were prepared at a concentration of 1.5-2.0%, depending on the size of the expected bands. Agarose was dissolved in 1× TAE buffer by boiling in a microwave and was mixed with a magnetic stirrer until cooled down to around 60 ºC. Ethidium bromide, which intercalates into nucleic acids, was added (1 mg/mL) before the gel was poured into a chamber with combs. PCR products and GeneRuler™ 100 bp DNA ladder were loaded into the wells and separated in 1× TAE buffer by electrophoresis at 110-120 V for 1-2.5 hours or until the bands had

been separated sufficiently. DNA bands were visualized by ultraviolet (UV) light and documented with Gel documentation system UVP UVsolo touch.

5.4.3. RNA sequencing

5.4.3.1. Isolation of RNA from bulk tumors and cells

Bulk tumor samples for RNA extraction were homogenized in 600 µL of RLT buffer supplemented with 1% 2-mercaptoethanol using SilentCrusher M. Cell lines were cultured in 10 cm Petri dishes until they reached around 70-80% confluency, washed with ice cold 1× PBS, and harvested in 600 µL of RLT buffer supplemented with 1% 2-mercaptoethanol. Lysate was collected with a scraper and stored at -80 ºC until further isolation. RNA extraction was carried out with QIAshredder spin columns and the RNeasy mini kit according to the manufacturer's protocol. DNA was eliminated using the RNase-free DNase set. RNA concentration was determined with Qubit® 2.0 Fluorometer and the isolated RNA was stored at -80 °C.

5.4.3.2. RNA sequencing and Bioinformatic analysis

To analyze the interactions between TME and tumor cells and to compare gene signatures and underlying signaling pathways, RNA-seq of bulk tumors and murine pancreatic cell lines was performed in collaboration with the laboratory of Prof. Roland Rad (Klinikum rechts der Isar, Technical University of Munich, Munich, DE). 2 ug of each sample were further processed for Illumina sequencing with the TruSeq® Stranded mRNA Sample Preparation Kit with Agencourt AMPure XP Beads and SuperScript II as reverse transcriptase.

Bioinformatical analysis of RNA-seq data, library preparation and alignment were carried out using R version 3.6.2. (R Development Core Team, 2014) by Fabio Boniolo as described by Müller and colleagues (Mueller et al., 2018). For deconvolution of RNA-seq data, the immunedeconv R package was used after normalization (Sturm et al., 2019). In particular, the 'MCPcounter' method was modified to predict the abundances of cell types distinct from the ones detected in the original publication (Becht et al., 2016). New signatures were defined, as shown in Table 17, based on literature and avoiding genes common to different cellular types (Radens et al., 2019; Szabo et al., 2019; Yun et al., 2019; Zilionis et al., 2019). The correlation between the resulting abundance score was then visualized using the corrplot R package. Differential expression analysis between the PK and PPI3K groups was performed using DESeq2 package (Love et al., 2014), while for over-representation analysis of Kyoto Encyclopedia of Genes and Genomes (KEGG) pathways, the upregulated genes in the PPI3K cohort compared to PK cohort (LFC > 2 and adjusted $p < 0.05$) were represented using the clusterProfiler R package (Yu et al., 2012). For the ssGSEA, the fgsea package with the method 'ssgsea' was used (Korotkevich et al., 2016). The 50 cancer hallmark gene sets from the Molecular Signature Database (MSigDB) (Liberzon et al., 2015) were used as gene sets for enrichment.

Table 17. Defined signatures of cellular types present in pancreatic ductal adenocarcinoma

Cell type	Signature
B cells	Bank1, CD19, CD22, CD79a, CD79b, Ebf1, Fcrl1, Klhl14, Pax5, Ralgps2
Neutrophils	PI3, Tgm3, Cxcr2, Cxcr1, Kcnj2, Ceacam1, Megf9, Btnl3, Slc25a33, Lrrc40, Slc25a43, Slc25a22, Slc25a38, Lrrc47, Prok2, Phospho1, Pnpl2la2
Dendritic cells	Clec10a, Clec9a, CD1e, CD207, Crip3, CD1c, Lgals2, Acpp
Macrophages	Kynu, MerTK, Adap2, Rassf4, C1qa, Tfec, Htr2c, Mcsfr, Tlr2, Ccl19, CD301b
Eosinophils	Ccl23, Prss33, Thbs4, Epx, Fam170b, CD44r0, CD48, CD58, CD66, CD67
Basophils	CD41, CD49b, Fcer1a, CD203c, Cpa3, Ms4a3, Ms4a2, IL4, Gata2, CD200r1l, Trim64b, Trim51bp, Trim49d1, Rhoxf1p1, Ugt2b11, Rnu4-18p
CD8$^+$ T cells	CD8a, CD8b, Trgv10, Trbv28, Trgv9, Trgv2, Trgc2
CD4$^+$ T cells	CD4, Ccr4, IL1r1, IL6ra, IL21r, Ccr8, Ifngr2, Tnfrsf4, Ephx2, CD40lg, Trav8-4, Trav9-2, Trbv7-2, Trbv12-3, Icos
Tumor cells	Krt7, Krt8, Krt17, Krt18, Krt19, Epcam
MyCAFs	Mmp11, Col11a1, C1qtnf3, Cthrc1, Col12a1, Col10a1, Lrrc15, Itga11

CD, cluster of differentiation; MyCAF, myofibroblastic cancer-associated fibroblast; +, positive or high expression.

5.5. Protein biochemistry

5.5.1. Protein extraction

Cell lines were cultured in 10 cm Petri dishes until they reached around 70-80% confluency, washed with ice cold 1× PBS, and harvested in 180 µL of IP buffer supplemented with proteinase and phosphatase inhibitors (Table 6) to obtain whole cell lysate. Lysate was collected with a scraper, placed on ice for 30 min, and centrifuged for 15 min at 4 ºC at maximum speed (about 18,000 ×g). The supernatant was transferred into a new reaction tube, immediately snap frozen in liquid nitrogen, and stored at -80 ºC until further use.

5.5.2. Determination of protein concentration by Bradford assay

The whole cell protein extraction samples were thawed on ice and the protein concentration was determined by Bradford assay (Bradford, 1976). Bradford reagent was diluted 1:5 with dH_2O and 300 µL of this solution were distributed per each necessary well of a 96-well plate. For the standard curve, duplicates of 1 mg/mL BSA solution were used as reference in crescent amounts of protein (0 µL, 0.5 µL, 1 µL, 2 µL, 4 µL and 8 µL). For the measurement of the protein concentration of the samples of interest, triplicates were carried out by adding 1 µL of the sample per well. The absorbance was measured at 595 nm in the multimode microplate reader CLARIOstar. Protein concentration was calculated using the standard curve and all samples were then adjusted to a final protein concentration of 3.5 µg/µL by adding IP buffer and protein loading buffer (Laemmli, 1970). Finally, the protein samples were denatured for 5 min at 95 ºC and stored at -20 ºC until further analysis.

5.5.3. Sodium dodecyl sulfate polyacrylamide gel electrophoresis

Sodium dodecyl sulfate polyacrylamide gel electrophoresis (SDS-PAGE) (Laemmli, 1970) was performed to separate the proteins according to their molecular weight. Therefore, 10% separating gel and stacking gel were prepared according to Table 18. At first, the compounds for the separating gel were mixed, being APS and TEMED the last two reagents to be added. The separating gel was poured into a gel caster, covered with a layer of 2-propanol to remove air bubbles, and allowed to polymerize. The stacking gel mixture was prepared, poured onto the separating gel, and the comb with 10- or 15-wells was added. The gel was allowed to polymerize. 70 ug of the protein samples were loaded onto the SDS polyacrylamide gel together with PageRuler™ Plus prestained protein ladder to estimate approximate molecular weight. For concentration of the proteins in the stacking gel, electrophoresis was carried out at 60 V for about 45 min in running buffer (Table 6). Once the samples entered the separating gel, the voltage was increased to 100-120 V for 1 hour to allow the separation of the proteins.

Table 18. Protocol for preparation of sodium dodecyl sulfate polyacrylamide gels

Component	Volume (µL) for 10% separating gel	Volume (µL) for stacking gel
dH_2O	6150.0	4500.0
Separating gel buffer	3900.0	n/a
Stacking gel buffer	n/a	1950.0
Rotiphorese® gel 30	4950.0	1125.0
10% SDS	150.0	75.0
10% APS	75.0	37.5
TEMED	22.5	15.0

%, percentage; µL, microliter; APS, ammonium persulfate; dH_2O, distilled water; n/a, not applicable; SDS, sodium dodecyl sulfate; TEMED, N,N,N',N'-tetramethylethylenediamine.

5.5.4. Immunoblot

After separation with SDS-PAGE, the proteins were blotted onto a nitrocellulose blotting membrane Amersham™ Protran™ 0.2 µm NC in a tank blot system. Transfer from the gel into the membrane was performed for 2 hours at 300 mA and 4 ºC in transfer buffer (Table 6). To prevent unspecific antibody binding, the membrane was incubation with 5% milk (Table 6) on shaker for 60 min at RT. Subsequently, the membrane was incubated by gently agitation with the first antibody mouse anti-mouse E-cadherin (36/E-Cadherin, #610181) diluted 1:1000 in 5% milk over two nights at 4 ºC. After washing the membrane thrice with PBS-T (Table 6) for 5 min, the membrane was incubated with secondary antibody goat peroxidase antibody anti-mouse IgG (#A9917-1ML) diluted 1:5000 in 5% milk for 1 hour at RT in the dark with gentle shaking. The membrane was washed again thrice with PBS-T before it was incubated with chemiluminescence solution (Table 6) for 2 min at RT in the dark. Afterwards, the membrane was scanned at 700 nm, 800 nm, and Chemi modes using Odyssey® Fc imaging system. Glyceraldehyde 3-phosphate dehydrogenase (GAPDH) was used as loading control.

5.6. Statistical analysis

Graphical depiction, data correlation, and statistical analyses were performed with GraphPad Prism 5.0 and 8.0 software. Biological replicates were reported, and data obtained were presented as mean values ± standard error of mean (SEM), except for the pie charts and bar graphs, which represent the mean of the replicates or proportions within a single dataset, and violin plots, which indicate the median and the quartiles. To calculate statistical differences, distinct statistical tests were employed depending on the dataset. Two-tailed Student's unpaired t test selecting pair groups for comparison was applied to cellular ratios, cell-to-cell distances, percentage of E-cadherin-negative lesions, optical density of E-cadherin staining and tumor weight, while one-way analysis of variance (ANOVA) with post-hoc Tukey test was employed to determine statistical differences of E-cadherin-negative cells among the *Cdh1* cell lines with distinct recombination status and between vehicle- and 4-OHT-treated *Cdh1*$^{fl/fl}$ cell lines. Survival curves were done using Kaplan-Meier survival analysis and log rank (Mantel-Cox) test for statistical analysis. To determine statistical differences of tumor types, histopathological grading, and macrometastases formation, Chi-square test with 95% of confidence interval was performed selecting pairs of groups for comparison. In all statistical tests, $p < 0.05$ was considered to be statistically significant and the resulting p-values are indicated in the respective figures. No statistical method was used to predetermine sample size.

6. Results

6.1. Chapter I, Part A: *Establishment of multiplexed immunohistochemistry (mIHC) panels for immune- and tumor-profiling of cryopreserved murine tumor tissues using confocal microscopy*

Immune cells within the TME interact among themselves and with tumor cells to create a favorable environment to tumor progression. Characterization of the TME using mIHC has several crucial implications for clinical translation and has emerged as a potent tool for immune-profiling analysis (Gorris et al., 2018; Tsujikawa et al., 2017). Besides allowing simultaneous detection of multiple biomarkers within a single specimen, mIHC also preserves the morphology of the tissue, which is lost with other techniques such as flow cytometry or RNA-seq. These advantages of the mIHC technique enable the study of co-expression, spatial organization, and/or distribution of multiple targets, leading to a better understanding of the architecture of a disease at a cellular level. In the present study, our goal was to establish a mIHC panel using a range of immune marker antibodies, including those against IICs and AICs, and confocal microscopy to further apply in PDAC tissues and characterize their immune cell content. In this Chapter I, Part A, we reported on the development, optimization, and application of mIHC panels, consisting of: 1) IIC panel – CD11b, CD11c, Ly6G/Ly6C, and F4/80 markers; 2) AIC panel – CD3 and CD45R/B220 markers; and 3) T cell panel – CD3, CD8a, CD4, and FoxP3 markers; and all panels were completed with CK18 and ToPro-3 stainings. These established panels posteriorly allowed the quantification of nine different cellular types on three consecutive tissue sections.

The development of a mIHC panel to detect immune cells consisted in a multistep process, as depicted in Fig. 5 and it involved the following phases: 1) determination of the tissue sections to use (FFPE or cryopreserved); 2) selection of the cells of interest (immune and tumor cells); 3) validation of the antibodies to detect the cells of interest and performance of the respective quality controls using uniplex IF staining; 4) determination of the fluorophores to integrate a single mIHC panel; 5) development of the multiplex staining protocols, including optimization of blocking/permeabilization step, readjustment of the selected antibodies validated by uniplex IF staining, and test the sequential antibody incubations; and 6) application of the established panels in the tissue of interest (PPT tissue). Throughout this section, we highlighted the critical steps to consider while establishing a mIHC panel, encountered challenges and limitations of the technique, and timing implicated in the process (from preparation of the specimens to data analysis and visualization). The work described in this section counted with the collaboration of Dr. Chuan Shan, Dr. Markus Tschurtschenthaler, and Dr. Sabine Klein, who generated the animals used for the establishment of the mIHC panels.

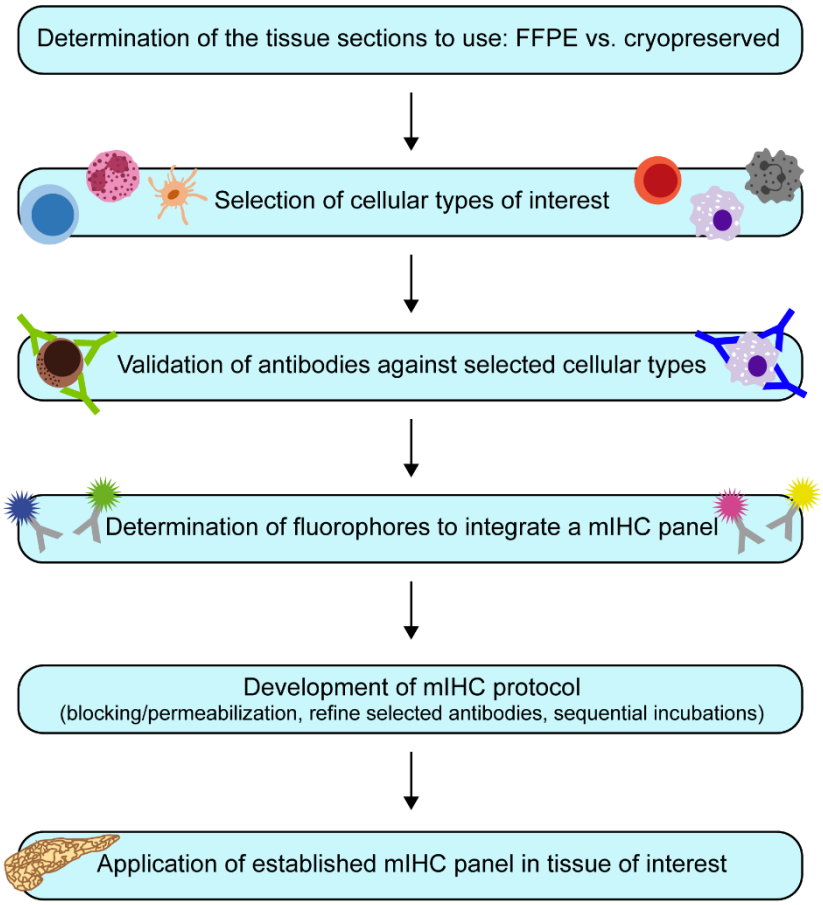

Fig. 5. Flowchart with the steps of the multiplexed immunohistochemistry protocol development.
The multistep process of establishing multiplexed immunohistochemistry (mIHC) panels ranged from the determination of the tissue sections to use (formalin-fixed paraffin-embedded (FFPE) or cryopreserved samples), selection of cells of interest (immune and tumor cells), validation of antibodies with the performance of quality controls and determination of fluorophores to use in a single mIHC panel to the development of the mIHC protocol, which included the optimization of blocking/permeabilization step, readjustment of selected antibodies and respective dilutions and performance of sequential incubations of antibodies, and finally the application of the established mIHC panel in the tissue of interest (primary pancreatic tumor tissue).
FFPE denotes formalin-fixed paraffin-embedded, mIHC the multiplex immunohistochemistry.

6.1.1. mIHC panels were optimized on cryopreserved sections

Most of mIHC protocols available in the literature are performed in FFPE samples due to their availability in the clinical practice (Gorris et al., 2018; Parra et al., 2017; Tsujikawa et al., 2017). We took advantage of the availability of distinct GEMMs and murine tissues collected throughout the years in our research group. Since both FFPE and frozen samples were available, the first step of the establishment of a mIHC panel was to determine the type of sections to use (Fig. 6). To answer this initial question, three different immune cell markers (F4/80, CD3, and CD45R/B220) were tested in both FFPE and cryopreserved splenic tissues from WT mice using IF staining, as shown in Fig. 6A. In the cryosections, all labelings with the markers F4/80, CD3, and CD45R/B220 worked, being located in the membrane of the respective immune cells as expected. In contrast, in the FFPE sections, only the CD45R/B220 antibody staining worked targeting the clusters of B cells present in the spleen. In addition, the FFPE tissue presented

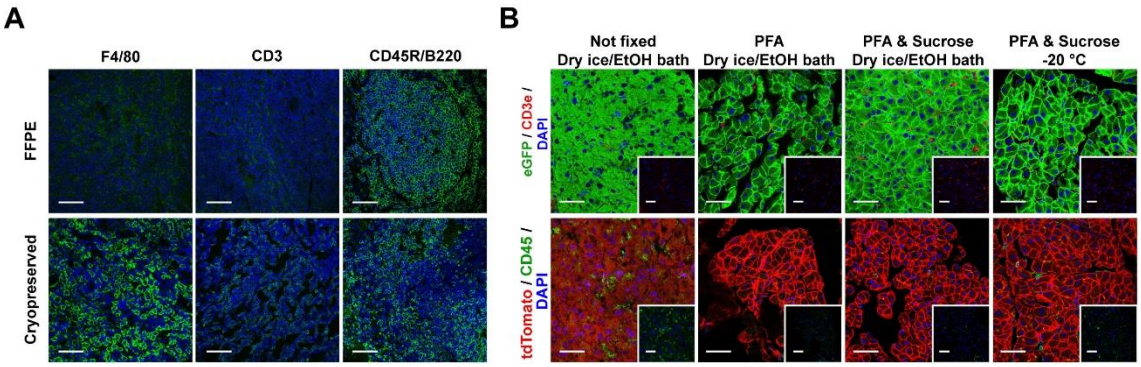

Fig. 6. Selection of formalin-fixed paraffin-embedded or cryopreserved tissues to optimize the multiplexed immunohistochemistry panels.
(A) Formalin-fixed paraffin-embedded (FFPE) and cryopreserved sections of splenic tissue from wild-type mice stained with F4/80, cluster of differentiation (CD)3, and CD45R/B220 antibodies.
(B) Pancreatic tissues harvested from *Ptf1a-p48^{Cre}; Rosa26$^{mTmG/+}$* and *Villin-Cre; Rosa26$^{mTmG/+}$* mice, expressing enhanced green fluorescent protein (eGFP) and tandem dimer Tomato (tdTomato) in the pancreatic cells respectively, were used to test fixation and freezing methods for cryopreserved samples. No fixation, only 4% paraformaldehyde (PFA) without methanol, and 4% PFA without methanol with two successive sucrose solutions were the fixation conditions tested, while dry ice/ethanol (EtOH) bath and -20 ºC were used to freeze the tissues. The different combinations tested are indicated above each column of representative images. In addition, on the tissue with eGFP-positive pancreatic cells, CD3e staining was performed, while on the tissue with tdTomato-positive pancreatic cells, CD45 staining was done. The inserts show CD3e and CD45 stainings in the respective tissues.
All scale bars indicate 50 µm. Animals used for these analyses were generated by Dr. Chuan Shan and Dr. Markus Tschurtschenthaler, both members of the laboratory of Prof. Dr. med. Dieter Saur. °C denotes the degree Celsius, CD the cluster of differentiation, eGFP the enhanced green fluorescent protein, EtOH the ethanol, FFPE the formalin-fixed paraffin-embedded, PFA the paraformaldehyde, tdTomato the tandem dimer Tomato.

endogenous autofluorescence, which was not evident in the frozen sample. Thus, the cryopreserved tissue proved to be more precise for immune cell detection.

The next step was to test different methods of fixation and freezing to process and prepare specimens for cryopreservation conserving the structure of the tissue and maintaining the epitopes intact. Pancreatic tissues harvested from *Ptf1a-p48^{Cre}; Rosa26$^{mTmG/+}$* and *Villin-Cre; Rosa26$^{mTmG/+}$* mice, expressing eGFP and tdTomato respectively, were used for this test (Fig. 6B). To fix the tissues, the three following conditions were applied: 1) no fixation; 2) fixation with only 4% PFA without methanol for 2 hours; and 3) fixation with 4% PFA without methanol for 2 hours followed by two successive sucrose solutions (15% sucrose for 4 hours and 30% sucrose overnight). Regarding the freezing methods, a dry ice/EtOH bath and -20 ºC were tested. Upon fixation and freezing, the *Ptf1a-p48^{Cre}; Rosa26$^{mTmG/+}$* tissues were stained with CD3e antibody, while the *Villin-Cre; Rosa26$^{mTmG/+}$* samples were labeled with the pan-leukocyte marker CD45. As observed in Fig. 6B, both not fixed tissues presented a diffused cytoplasmic localization of the respective endogenous reporter proteins. In contrast, in all fixed tissues, both eGFP and tdTomato fluorescent proteins were observed in the membrane of the respective pancreatic cells as expected. In addition, CD3e and CD45 stainings were performed to access the immunoreactivity of the epitopes and positive cells for each marker were detected in all fixed tissues. Comparing the different combinations of fixation and freezing methods, the best results were obtained with

the combination of 4% PFA and sucrose followed by dry ice/EtOH bath, since endogenous autofluorescence was not detected in these tissues and they presented less unspecific staining compared to the other conditions tested. Based on this test, we concluded that the best method to cryopreserve the tissue was the fixation with 4% PFA for 2 hours followed by successive higher concentrated sucrose (15% sucrose for 4 hours and 30% sucrose overnight) at 4 °C and freezing using a dry ice/EtOH bath.

► **CRITICAL STEP:** The right fixation and freezing methods require optimization based on the application and the target antigen to be stained.

6.1.2. Immune cells of interest needed to be selected

The second step of the establishment of the mIHC panel was the selection of cells of interest. The identification of immune cell types is typically based on an assessment of the presence or absence of expression of lineage-specific markers, cell surface markers or transcription factors. As depicted in Fig. 7, the immune system comprises a large number of cell types and subtypes that can be identified by general and specific markers. CD45 was selected as a general marker to identify immune cells due to its exclusively expression on leukocytes, allowing to distinguish between these cells and other cellular types present in our tissue of interest, such as tumor cells and fibroblasts (Trowbridge & Thomas, 1994). In addition, since our goal was to have an overview of the cellular populations present and may have a role in PDAC, the main selection criterion was based on the relevance and abundance of the immune cell type in this disease according to the literature. Thus, we decided to select the main populations of myeloid and lymphoid cells, namely granulocytes (neutrophils and eosinophils), cDCs, macrophages, NK cells, and T and B lymphocytes, covering both innate and adaptive immune systems. After selecting the cells of interest, it is imperative to know which markers are necessary to accurately identify the cells. Considering exclusively expressed and co-expressed markers, we selected the following ones: CD11b (myeloid cells), Ly6G (neutrophils), Siglec-F (eosinophils), CD11c and CD68 (cDCs), F4/80 and CD68 (macrophages), CD335 (NK cells), CD3 (T cells), CD4 (Th cells), CD8 (CTLs), CD4 and FoxP3 (Tregs), and CD45R/B220 (B lymphocytes). Upon selection of the cells of interest and respective markers, antibodies against the markers were purchased from commercial manufacturers and validated using WT splenic or hepatic murine specimens.

IMPORTANT TIP: Check the literature to investigate the cells/antigens/proteins that could integrate your mIHC panel and their respective abundances and levels of expression in the tissue of interest.

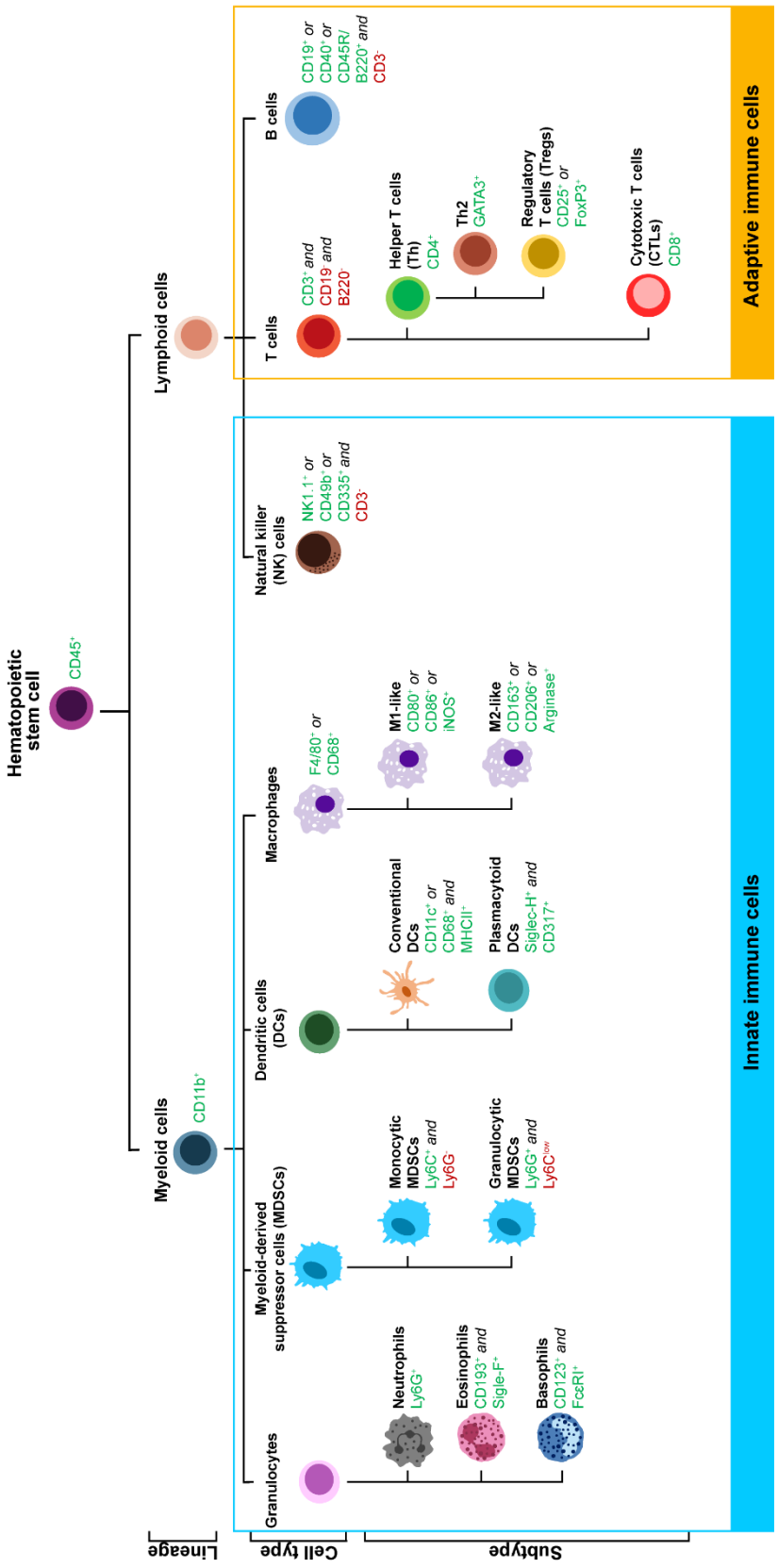

(legend on the next page)

6.1.3. Antibodies against selected immune cells were validated by indirect method of immunofluorescence staining

Extensive literature exists on immunostaining and antibody applications in both research and clinical settings, being a robust and ease of handling tool. Nevertheless, the specificity and reproducibility are well known to be influenced by a range of analytical factors including processing of the samples, and aspects intrinsic to the antibody, such as its generation, the extent of conjugation, dilution, and incubation conditions. Due to these facts, some commercially available antibodies work well, whereas others work poorly or not at all. Thus, the third step of the mIHC panel establishment was to perform proper validation of the reliability of the selected markers/antibodies using the adequate quality controls (Hewitt et al., 2014). The following quality controls were included:

i. Positive tissue control: staining was performed in a tissue that expresses the protein of interest (e.g., splenic tissue for immune cell detection and PPT tissue for labeling of tumor cells);

ii. Negative tissue control: staining was performed in a tissue in which the protein of interest is not expressed, preferably a tissue harvested from a KO animal (e.g., *Rag2/Il2rg*-KO tissue for validation of NK, T, and B cell markers and hepatic tissue for the remain immune cell antibodies);

iii. Secondary antibody only control: tissue was processed using the established IF staining protocol omitting the primary antibody incubation, allowing to control unspecific binding of the secondary antibody;

iv. Autofluorescence/endogenous tissue background staining control: unstained tissue was processed as the established IF staining protocol omitting both primary and secondary antibody incubations, allowing to control the endogenous background resultant from the fixation step;

Fig. 7. Schematic illustration of the hierarchical immune cells and respective markers.
Hematopoietic stem cells, which express cluster of differentiation (CD)45, differentiate into myeloid and lymphoid cell lineages. Myeloid cells are characterized by the expression of CD11b, and they can convert into several cell types, such as granulocytes, myeloid-derived suppressor cells (MDSCs), dendritic cells (DCs) and macrophages. The granulocytes are divided into neutrophils that express Ly6G, eosinophils identified by CD193 and Siglec-F, and basophils that express CD123 and high affinity IgE receptor (FcεRI). MDSCs acquire monocytic or granulocytic phenotypes, expressing Ly6C and Ly6G, respectively. Regarding the DCs, these myeloid cells can be divided into conventional DCs that are identified by CD11c or CD68 and class of major histocompatibility complex class II (MHCII) and plasmacytoid DCs that express the markers Siglec-H and CD317. Lastly, markers of macrophages include F4/80 and CD68 and these myeloid cells can be categorized in two extreme polarization states: M1-like expressing CD80, CD86 and inducible nitric oxide synthase (iNOS); and M2-like identified by CD163, CD206 and arginase. Regarding the lymphoid lineage, this lineage comprises the natural killer (NK) cells, T and B cells. NK cells, which belong to the innate immune system together with the myeloid cells, express NK1.1, CD49b, CD335 and do not express CD3. T cells together with B cells compose the adaptive immune system. T lymphocytes are characterized by the expression of CD3 and negative expression of B cell markers such as CD19 and CD45R/B220. In addition, T cells are divided into $CD4^+$ helper T cells (Th), such as Th2 that additionally express GATA binding protein 3 (GATA3) and regulatory T cells (Tregs) identified by CD25 or FoxP3, and $CD8^+$ cytotoxic T cells (CTLs).
CD denotes the cluster of differentiation, CTL the cytotoxic T cell, DC the dendritic cell, FcεRI the high affinity IgE receptor, iNOS the inducible nitric oxide synthase, GATA3 the GATA binding protein 3, MHCII the major histocompatibility complex class II, MDSC the myeloid-derived suppressor cell, NK the natural killer, Th the helper T cell, Treg the regulatory T cell, + the positive or high expression in green, - the negative or low expression in red.

v. Cross-reaction control: cross-reactivity between antigens occurs when an antibody directed against one specific antigen binds to another, different antigen. Each individual staining was performed as well as double stainings to assess the specificity of the antibodies.

After selection of the cells of interest, each marker indicated in Table 19 was validated by indirect method of uniplex IF staining, i.e., each antibody was individually applied in the tissue and detected with the appropriate fluorophore-conjugated secondary antibody (e.g., AF and cyanine - Cy), as depicted in Fig. 8. As a positive tissue control for immune cells, we used splenic tissue from a WT mouse. As shown in Fig. 8A, all the markers exhibited membranous expression in the respective targeted immune cells. For example, CD3 and CD45R/B220, the markers for T and B cells respectively, were expressed in small round cells, while Ly6G/Ly6C and Siglec-F, the markers to detect neutrophils and eosinophils respectively, presented stainings where multi-lobed nuclei were visible. The membrane localization was also observed in the FoxP3 staining, a transcription factor localized in the nuclei of Tregs (Colamatteo et al., 2019). This result indicated that this labeling was not specific, and polyclonal antibody against FoxP3 (#ab75763) was not binding to the correct epitope and consequently it was excluded from further analysis. Thus, when using any tissue or cell line for antibody testing, the staining should be evaluated according to the specific cell type to be detected (e.g., macrophage or lymphocyte by morphological features), subcellular localization (membrane, cytoplasm, and/or nucleus), strength of signal, and signal-to-noise ratio.

Table 19. Immune cell markers used during validation of antibodies by uniplex immunofluorescence staining

Primary antibody	Target cell(s)	Primary antibody	Target cell(s)
CD11b, #553308	Myeloid cells	**CD3**, #100201	T cells
CD68, #MCA1957	Macrophages and cDCs	**CD3e**, #553058	T cells
F4/80, #MCA497	Macrophages	**CD4**, #ab183685	Helper T cells
CD11c, #14-0114-82	cDCs	**CD8a**, #14-0081-82	Cytotoxic T cells
NCR1/CD335, #ab199128	NK cells	**FoxP3**, #ab75763	Regulatory T cells
Ly6G/Ly6C, #14-5931-82	Neutrophils	**CD45R/B220**, #103201	B cells
Siglec-F, #AF1706	Eosinophils	**CD45**, #MCA1031G	Leukocytes

CD, cluster of differentiation; cDC, conventional dendritic cell; NK, natural killer.

In addition to the positive tissue control, the remaining quality controls mentioned above were done to validate the selected antibodies. The negative tissue control was performed using both splenic tissue from a *Rag2/Il2rg*-KO mouse to test the markers against NK, T and B cells and hepatic tissue from a WT mouse was used for the remaining antibodies, as depicted in Fig. 8B. Regarding the stainings performed on WT hepatic tissue, none of the markers (CD11b, F4/80,

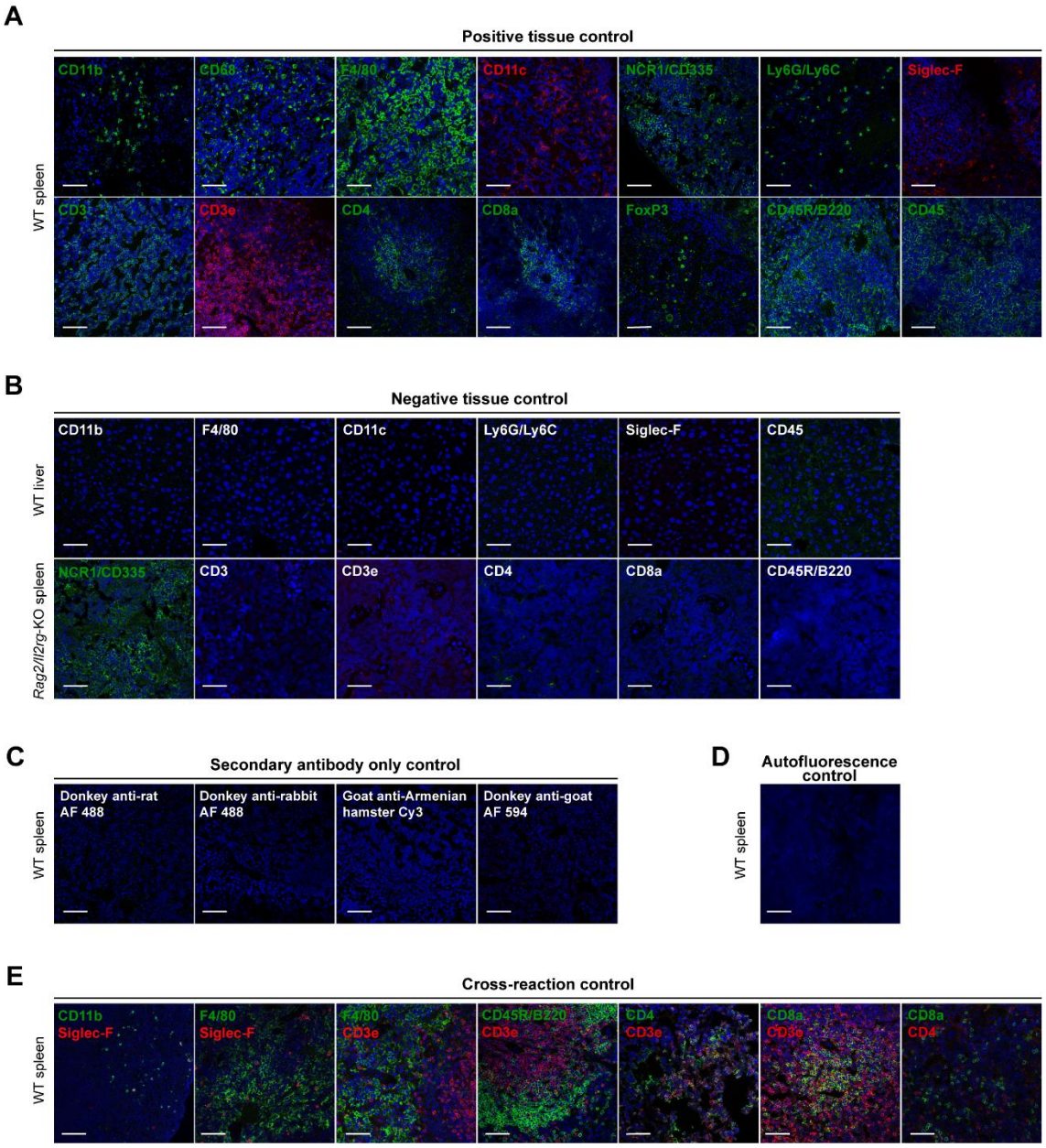

Fig. 8. Validation of antibodies and quality controls.
(A) Representative pictures of the positive tissue quality control performed for immune cell markers cluster of differentiation (CD)11b (myeloid cells), CD68 (conventional dendritic cells – cDCs – and macrophages), F4/80 (macrophages), CD11c (cDCs), NCR1/CD335 (natural killer cells), Ly6G/Ly6C (neutrophils), Siglec-F (eosinophils), CD3 and CD3e (T cells), CD4 (helper cells), CD8a (cytotoxic cells), FoxP3 (regulatory cells), CD45R/B220 (B cells), and CD45 (leukocytes) using the indirect method of uniplex immunofluorescence (IF) staining in wild-type (WT) splenic tissue.
(B) Representative pictures of the negative tissue quality control performed using hepatic tissue from a WT mouse to validate CD11b, F4/80, CD11c, Ly6G/Ly6C, Siglec-F, and CD45 antibodies, and splenic tissue from a *Rag2/Il2rg*-knockout (KO) animal to validate NCR1/CD335, CD3, CD3e, CD4, CD8a, and CD45R/B220 antibodies.
(C) Representative pictures of the secondary antibody only control using WT splenic tissue. In this control, the tissue was incubated with the secondary antibodies used to detect the antibodies in Fig. 8A (donkey anti-rat Alexa Fluor® (AF) 488, donkey anti-rabbit AF 488, goat anti-Armenian hamster cyanine 3 (Cy3) and donkey anti-goat AF 594).
(D) Autofluorescence control was performed in WT splenic specimen to assess the endogenous tissue background.
(E) Representative pictures of the cross-reaction control using double stainings for immune cell markers by indirect method of IF staining.
All the scale bars indicate 50 µm. Animals used for these analyses were generated by Dr. Chuan Shan and Dr. Markus Tschurtschenthaler, both members of the laboratory of Prof. Dr. med. Dieter Saur. AF denotes the Alexa Fluor®, CD the cluster of differentiation, cDC the conventional dendritic cell, Cy the cyanine, IF the immunofluorescence, KO the knockout, WT the wild-type.

CD11c, Ly6G/Ly6C, Siglec-F, and CD45) presented a positive signal. The same was observed for the labelings with CD3, CD3e, CD4, CD8a, and CD45R/B220 antibodies on the *Rag2/Il2rg*-KO splenic tissue. The only exception was the section stained with NCR1/CD335 antibody, where the staining was similar to the one observed in the positive tissue control (Fig. 8A). For this reason, similarly to FoxP3 antibody, the polyclonal antibody against NCR1/CD335 was also excluded from further analysis.

To control the unspecific binding of the secondary antibodies, the secondary antibody only control using WT splenic tissue was performed, as shown in Fig. 8C. To perform this quality control, the secondary antibodies donkey anti-rat AF 488, donkey anti-rabbit AF 488, goat anti-Armenian hamster Cy3, and donkey anti-goat AF 594 used to detect the primary antibodies showed in Fig. 8A and 8B, were incubated in the splenic tissue. No unspecific binding was observed, proving that the obtained stainings against the selected immune cells were specific.

Autofluorescence is a natural characteristic of all cells and its emission ranges from 450 to 540 nm (Jun et al., 2017). Endogenous tissue background staining control was performed to assess the autofluorescence present in the sample prior to labeling, as depicted in Fig. 8D. The WT splenic tissue fixed with PFA followed by two successive concentrations of sucrose and frozen in a dry ice/EtOH bath did not present any autofluorescence. Thus, the detection of dim markers on the 450 to 540 nm fluorescent range should not be impaired.

Finally, after the performance of the individual stainings, double or duplex IF stainings were done to check potential cross-reactivity of the antibodies and to assess their specificity (Fig. 8E and Table 20). As observed in Fig. 8E, all the markers detected the respective immune cell and, as expected, co-localization was observed on the double stainings using CD11b and Siglec-F (myeloid eosinophils), CD3e and CD4 (Th cells), and CD3e and CD8a (CTLs) markers. In

Table 20. Overview of the validation of immune cell antibodies by duplex immunofluorescence staining

Combination of Primary antibodies	Target cells	Expected staining	Obtained staining as expected?
CD11b, #553308 & **Siglec-F**, #AF1706	Myeloid cells & Eosinophils	Colonization of Siglec-F and CD11b in addition to $CD11b^+$ $Siglec\text{-}F^-$ cells	Yes
F4/80, #MCA497 & **Siglec-F**, #AF1706	Macrophages & Eosinophils	Two distinct populations: one $F4/80^+$ and another $Siglec\text{-}F^+$	Yes
F4/80, #MCA497 & **CD3e**, #553058	Macrophages & T cells	Two distinct populations: one $F4/80^+$ and another $CD3e^+$	Yes
CD3e, #553058 & **CD45R/B220**, #103201	T cells & B cells	Two distinct populations: one $CD3e^+$ and another $CD45R/B220^+$	Yes
CD3e, #553058 & **CD4**, #ab183685	Helper $CD4^+$ T cells	Colonization of CD4 and CD3e in addition to $CD3e^+$ $CD4^-$ cells	Yes
CD3e, #553058 & **CD8a**, #14-0081-82	Cytotoxic $CD8a^+$ T cells	Colonization of CD8a and CD3e in addition to $CD3e^+$ $CD8a^-$ cells	Yes
CD4, #ab183685 & **CD8a**, #14-0081-82	Helper $CD4^+$ T cells & Cytotoxic $CD8a^+$ T cells	Two distinct populations: one $CD4^+$ and another $CD8a^+$	Yes

CD, cluster of differentiation; + the positive or high expression; - the negative or low expression.

addition, two distinct populations were detected in the combinations with F4/80 and Siglec-F (macrophages and eosinophils, respectively), and CD4 and CD8a (Th and CLTs, respectively) antibodies. These results allowed to confirm that all selected antibodies were specific against the respective epitopes.

After validating and performing the quality controls for the antibodies against the immune cells of interest, only NCR1/CD335 (#ab199128) and FoxP3 (#ab75763) were excluded from the next step of the establishment of the mIHC panel, as summarized in Table 21.

Table 21. Overview of the immune cell markers validated and quality controlled

Primary antibody	IF staining worked?	Passed the quality controls?	Comments
CD11b, #553308	Yes	Yes	
CD68, #MCA1957	Yes	Yes	
F4/80, #MCA497	Yes	Yes	
CD11c, #14-0114-82	Yes	Yes	
NCR1/CD335, #ab199128	Yes	No	Positive staining in a *Rag2/Il2rg*-KO (negative) tissue
Ly6G/Ly6C, #14-5931-82	Yes	Yes	
Siglec-F, #AF1706	Yes	Yes	
CD3, #100201	Yes	Yes	
CD3e, #553058	Yes	Yes	
CD4, #ab183685	Yes	Yes	
CD8a, #14-0081-82	Yes	Yes	
FoxP3, #ab75763	No	n/a	Incorrect localization of staining (membrane instead of nuclear)
CD45R/B220, #103201	Yes	Yes	
CD45, #MCA1031G	Yes	Yes	

CD, cluster of differentiation; IF, immunofluorescence; KO, knockout; n/a, not applicable.

► **CRITICAL STEP:** Know the biology of the target of interest, investigate about the expected localization of the selected marker, and use the appropriate controls to validate it.

6.1.4. Multiplexed immunohistochemistry panels for immune-profiling and tumor cell detection required further validation

After testing all of the markers by uniplex IF staining, we started to optimize the protocol of the mIHC panel for immune-profiling. Ideally, we aimed to include as many markers as possible in a single mIHC panel. However, there were a few challenges and limitations that needed to be considered regarding the chosen antibodies (e.g., host species, commercial availability), the fluorophores (their broad excitation and emission spectrums, bleed-through of neighboring fluorophores), and the instrument used for the image acquisition (limited excitation spectrum – between 405 and 670 nm – of the Leica TCS SP8 confocal microscope). For these reasons,

markers that would allow us to visualize all the immune cells of interest were selected, fluorophores to use were defined, and then assigned to each marker, and, when applicable, directly fluorophore-conjugated primary antibodies were purchased or labeled in our laboratory using an antibody labeling kit.

6.1.4.1. Specific markers to detect immune cells of interest were selected

To decide which markers would integrate the mIHC panels, the main criterion was to select specific markers that would detect the immune cells of interest. Hence, from the validated markers (Table 21), CD45 was excluded from the mIHC panel design, due to its expression in all leukocytes, as well as CD68, because it can be detected in both macrophages and cDCs (Chistiakov et al., 2017). Since we were still interested in identifying Tregs, FoxP3 was included as a marker to incorporate the mIHC panels, however a new antibody against this transcription factor needed to be purchased. Thus, after considering the immune cell markers to integrate the mIHC panels, as summarized in Table 22, we could assign a fluorophore to each mark of interest.

Table 22. Immune cell markers to integrate the multiplexed immunohistochemistry panels

Immune cell	Marker(s)	Immune cell	Marker(s)
Myeloid cell	CD11b	T cell	CD3
Neutrophil	Ly6G/Ly6C	T helper cell	CD3, CD4
Eosinophil	Siglec-F	T regulatory cell	CD3, CD4, FoxP3
Conventional dendritic cell	CD11c	Cytotoxic T cell	CD3, CD8a
Macrophage	F4/80	B cell	CD45R/B220

CD, cluster of differentiation.

6.1.4.2. Fluorophores were assessed and assigned to each marker of interest

To avoid ambiguous results especially in biological imaging, the fluorophores to match with each marker of interest needed to be carefully selected. Fluorophore availability, spectral signatures and brightness, levels of marker expression and co-expression as well as spectral spillover were few factors considered for the rigorous selection of the fluorescent dyes. In Table 23, we listed several commercially available fluorophores that were taken into consideration for our mIHC panel. For this selection, the online fluorescence spectra viewer Fluorescence SpectraViewer tool from Thermo Fisher Scientific was particularly useful, providing a visual perception of the fluorophore emission spectrums. All listed fluorophores have unique spectral signatures, i.e., regardless of the degree of spectral overlap with other probes, each fluorophore possesses a characteristic emission fingerprint. Since our Leica TCS SP8 confocal microscope is equipped with a UV laser that excites at 405 nm and a white light laser whose excitation ranges from 470 to 670 nm, it was clear that only one fluorophore in the UV range (AF 350, eFluor 450, or Pacific Blue) could be selected. Due to excitation of the UV laser at 405 nm, the AF 350 would

Table 23. Commercially available fluorophores taking into consideration and respective maximum excitation and emission wavelength and brightness according to Thermo Fisher Scientific website

Fluorophore	Excitation (nm)	Emission (nm)	Brightness
Alexa Fluor 350	346	442	1
eFluor 450	405	450	2
Pacific Blue	410	455	2
Alexa Fluor 488	490	525	4
Alexa Fluor 532	532	554	3
Alexa Fluor 546	556	573	4
Alexa Fluor 555	555	580	3
Qdot 585	405	585	5
Alexa Fluor 594	590	617	5
eFluor 660	633	669	4
Alexa Fluor 680	679	702	3

nm, nanometer; Qdot, quantum dot.

not be excited, so this fluorescent dye was excluded, leaving the eFluor 450 and Pacific Blue as two options for the UV range of the spectrum. In addition, we noticed a significant spectral overlap between AF 546, AF 555, and quantum dot (Qdot) 585 and, due to its brightness, this last fluorophore would be the best probe among the 570 to 590 nm range. The selection of fluorochromes with little or no spectral overlap can be conflicting when trying to select the brightest fluorophores, however it ensures the minimum overlap and spillover. This is particularly important when matching fluorophores to co-expressed markers, such as CD11c and Siglec-F or CD3 and CD4. In this step, we realized that it would not the possible to assign all ten immune markers to ten distinct fluorophores. For this reason, two distinct mIHC panels were delineated: one to detect IICs and a second one to identify AICs –, reducing to five the immune markers to detect in a single tissue specimen and thus facilitating the assignment of fluorophores to each mark.

Furthermore, it is generally good practice to pair antibodies detecting the lowest expressing targets with the brightest fluorophores. For example, since CD4 and CD45R/B200 are widely expressed antigens, they could be assigned to dimmer fluorophores, whilst the markers CD11c and FoxP3 have a low abundance so they should be matched with the brightest probes (Hensel et al., 2019). Moreover, since the majority of the validated primary antibodies was generated in rat (see Tables 5 and 10), limiting the combinations between these antibodies, we decided to purchase directly-conjugated antibodies. The commercially availability of directly-conjugated primary antibodies also presented as a limitation for antibody-fluorophore pairing. In this process, it also helped to record the availability of the fluorophore-conjugated antibodies for each marker of interest using online tools, such as biocompare.com. While searching for these conjugated antibodies, it was also important to decide on the same clones as the ones of the validated, unconjugated primary antibodies (Table 24). Primary antibodies, such as CD11c

Table 24. Validated, unconjugated primary antibodies, directly-conjugated primary antibodies and assigned fluorophores

Validated, unconjugated primary antibody	Directly-conjugated primary antibody	Assigned fluorophore
Rat anti-mouse CD11b (M1/70), #553308	Rat anti-mouse CD11b (M1/70), eFluor® 450, #48-0112-82	eFluor 450
Armenian hamster anti-mouse CD11c (N418), #14-0114-82	Armenian hamster anti-mouse CD11c (N418), #14-0114-82; labeled with Alexa Fluor™ 488 Antibody Labeling Kit, #A20181	Alexa Fluor 488
Rat anti-mouse Ly6G/Ly6C (RB6-8C5), #14-5931-82	Rat anti-mouse Ly6G/Ly6C (RB6-8C5), Alexa Fluor® 532, #58-5931-82	Alexa Fluor 532
Goat anti-mouse Siglec-F, #AF1706	n/a	Alexa Fluor 594
Rat anti-mouse F4/80 (Cl:A3-1), #MCA497	Rat anti-mouse F4/80 (BM8), eFluor® 660, #50-4801-82	eFluor 660
n/a	Rat anti-mouse FoxP3 (FJK-16s), eFluor® 450, #48-5773-82	eFluor 450
Rat anti-mouse CD8a (53-6.7), #14-0081-82	Rat anti-mouse CD8a (53-6.7), Alexa Fluor® 488, #53-0081-82	Alexa Fluor 488
Rabbit anti-mouse CD4 (EPR19514), #ab183685	Rat anti-mouse CD4 (RM4-5), Alexa Fluor® 532, #58-0042-82	Alexa Fluor 532
Rat anti-mouse CD45R/B220 (RA3-6B2), #103201	Rat anti-mouse CD45R/B220 (RA3-6B2), #103201; labeled with Alexa Fluor™ 594 Antibody Labeling Kit, #A20185	Alexa Fluor 594
Rat anti-mouse CD3 (17A2), #100201	Rat anti-mouse CD3 (17A2), eFluor® 660, #50-0032-82	eFluor 660

CD, cluster of differentiation.

(N418) and CD45R/B220 (RA3-6B2), that were not commercially available with fluorophores of interest were then labeled with the fluorescent probes (AF 488 and AF 594 respectively) using Antibody Labeling Kits. After the antibody-fluorophore pairing, all the antibodies were validated using splenic tissue from a WT animal as positive tissue control.

► **CRITICAL STEP:** Rank available fluorophores according to their intrinsic brightness, assign the brightest fluorophore to the weakly expressed antigen, and minimize spillover.

6.1.4.3. Directly fluorophore-conjugated and -labeled primary antibodies were integrated into the mIHC panels

Multiple primary antibodies derived from the same species can easily be used in the same staining if they are directly-labeled with a fluorescent probe. Although the signal obtained using the direct method of IF staining is weaker, a directly-conjugated primary antibody often produces less unspecific binding, provides a lower background fluorescence, and minimizes species cross-reactivity. To validate the directly fluorophore-conjugated primary antibodies, these antibodies were tested in splenic tissue from a WT animal and compared to the result obtained in the indirect method of uniplex IF staining (Fig. 9). As observed in Fig. 9A, with the exceptions of F4/80 conjugated with eFluor 660 and FoxP3 conjugated with eFluor 450, all stainings with the direct method with conjugated antibodies worked similarly to the staining obtained with the

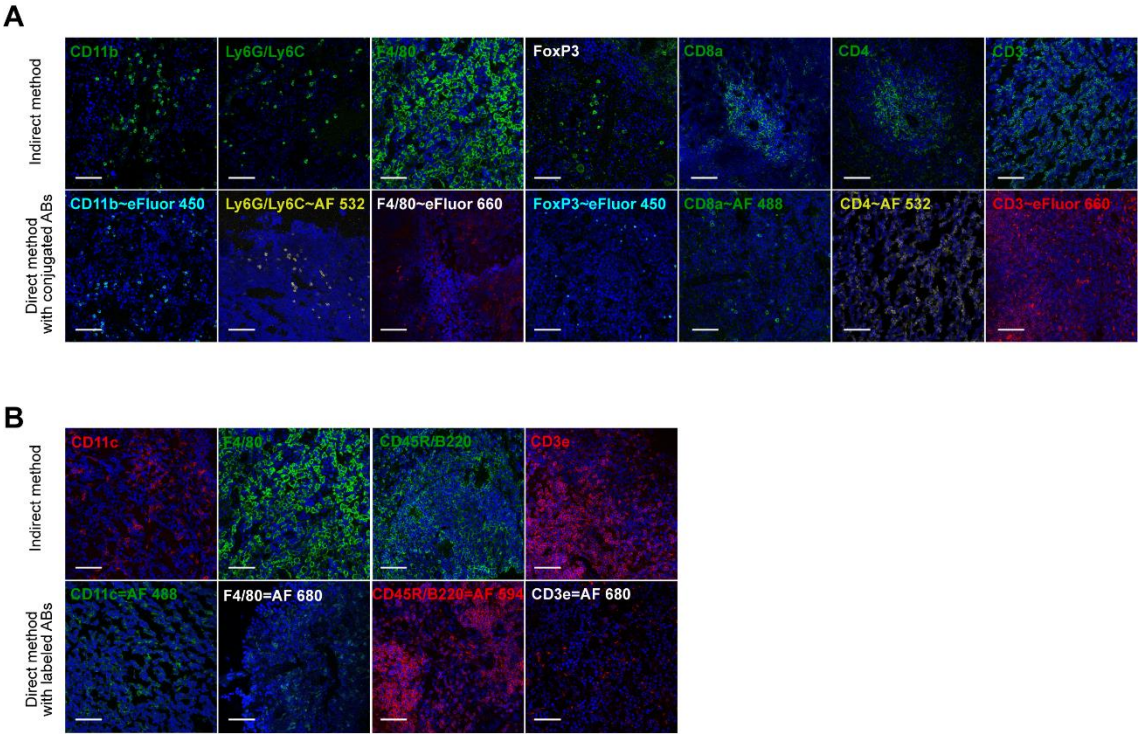

Fig. 9. Comparison between stainings obtained with validated, unconjugated primary antibodies and with directly-conjugated and -labeled antibodies.
(A) Top, representative images of stainings performed using the indirect method of immunofluorescence (IF) staining, as shown in Fig. 8A; and bottom, representative images of stainings obtained with the directly-conjugated primary antibodies (ABs). As indicated on the left upper corner of the images, cluster of differentiation (CD)11b, Ly6G/Ly6C, F4/80, FoxP3, CD8a, CD4, and CD3 markers were tested.
(B) Top, representative images of stainings performed using the indirect method of IF staining, as shown in Fig. 8A; and bottom, representative images of the stainings obtained with ABs labeled with the Antibody Labeling Kits. As indicated on the left upper corner of the images, CD11c, F4/80, CD45R/B220, and CD3e markers were tested.
All stainings were performed using splenic tissue from a wild-type mouse. Animals used for these analyses were generated by Dr. Chuan Shan and Dr. Markus Tschurtschenthaler, both members of the laboratory of Prof. Dr. med. Dieter Saur. All the scale bars indicate 50 µm. AB denotes the antibody, AF the Alexa Fluor®, CD the cluster of differentiation, IF the immunofluorescence, ~ the directly-conjugation of the primary antibody, = the directly-labeling of the primary antibody using Antibody Labeling Kit.

unconjugated primary antibodies. In fact, the labeling with directly-conjugated FoxP3 antibody (#48-5773-82) was observed in the nuclei of the cells as expected, in contrast with the staining obtained using the polyclonal antibody (#ab75763). Moreover, the staining using CD3 conjugated with eFluor 660 antibody presented a lot of unspecific binding compared not only to the indirect method staining, but also to the remaining stainings performed with directly-conjugated markers. Thus, from the purchased directly-conjugated primary antibodies, only the F4/80 and CD3 markers did not work properly. To overcome this issue, two options were presented: 1) label the antibodies with an Antibody Labeling Kit; or 2) use secondary antibodies to detect these markers once the mIHC protocol was performed.

To overcome the limitations of the commercially availability of directly fluorophore-conjugated primary antibodies and complete the mIHC panels, we purchased Antibody Labeling Kits provided by Thermo Fisher Scientific. We attempted to label the unconjugated primary antibodies CD11c (#14-0114-82) with AF 488, F4/80 (#MCA497) with AF 680, CD45R/B220

(#103201) with AF 594, and CD3e (#553058) with AF 680. As shown in Fig. 9B, CD11c labeled with AF 488 and CD45R/B220 labeled with AF 594 antibodies reproduced the stainings obtained with the indirect method, whilst the F4/80 and CD3e both labeled with AF 680 dye only presented unspecific binding. Thus, upon validation of directly fluorophore-conjugated and -labeled primary antibodies, we defined the antibody-fluorophore pairs and divided the markers into IIC Panel and AIC Panel, as summarized in Table 25. The IIC panel would be composed by the markers CD11b, CD11c, Ly6G/Ly6C, Siglec-F and F4/80, while the AIC panel would comprise the antibodies against FoxP3, CD8a, CD4, CD45R/B220 and CD3. With the immune cell markers and fluorophores defined and assigned, the next step of the mIHC panel construction was the selection of the marker to identify tumor cells as well as the correspondent fluorochrome-conjugated secondary antibody.

Table 25. Overview of the immune cell markers and respective fluorophores that were validated or taken into consideration for the construction of the multiplexed immunohistochemistry panels

mIHC Panel	Primary antibody	Conjugated fluorophore	Possible assign fluorophore	Comments
Innate immune cell Panel	**CD11b**, #48-0112-82	eFluor 450	n/a	
	CD11c, #14-0114-82	AF 488	n/a	
	Ly6G/Ly6C, #58-5931-82	AF 532	n/a	
	Siglec-F, #AF1706	n/a	AF 594	Comparing to F4/80, the expression of Siglec-F is lower; therefore, the best option was to assign the brightest fluorophore to this marker
	F4/80, #MCA497	n/a	AF 680	Abundance of F4/80 antigen is high enough to be detected with secondary antibody AF 680
Adaptive immune cell Panel	**FoxP3**, #48-5773-82	eFluor 450	n/a	
	CD8a, #53-0081-82	AF 488	n/a	
	CD4, #58-0042-82	AF 532	n/a	
	CD45R/B220, #103201	AF 594	n/a	
	CD3, #100201	n/a	AF 680	Abundance of CD3 antigen is high enough to be detected with secondary antibody AF 680

AF, Alexa Fluor®; CD, cluster of differentiation; mIHC, multiplex immunohistochemistry; n/a, not applicable.

6.1.4.4. Keratin 18 and Alexa Fluor 680 were selected as marker and fluorescent dye to detect tumor cells

One of our goals for the establishment of the mIHC panels was to include a marker to detect tumor cells that would allow the study of the interactions between malignant and immune cells. Among the epithelial cell markers expressed by pancreatic cancer, we encountered CK7, CK18, CK19, and Epcam (Karantza, 2011). CK18 was the marker selected to identify PCCs, as

shown in Fig. 10. Since the fluorophores eFluor 450, AF 488, AF 532, AF 594, and AF 680 were already assigned to immune cell markers, we tried to integrate the Qdot 585 probe by pairing it with the CK18 antibody. To validate this primary antibody, we performed IF staining in two consecutive PPT sections using two distinct secondary antibodies conjugated with AF 488 or Qdot 585 fluorophores. As depicted in Fig. 10A, the staining produced by the combination CK18-AF 488 was clear and localized in the membrane of cells forming pancreatic lesions, whilst the labeling with the Qdot 585 was weak and the extremely high and dispersed unspecific binding did not allow to discriminate between PCCs and TME cells. To verify the origin of the unspecific binding, we performed a secondary antibody only quality control with the goat anti-rabbit Qdot 585 secondary antibody omitting the CK18 incubation step (Fig. 10B). In this control, the tissue still presented some unspecific staining especially in the stroma surrounding the lesions. Thus, we concluded that the goat anti-rabbit Qdot 585 alone was producing the unspecific binding detected in the IF staining. Finally, the CK18 antibody was validated using a WT spleen as the negative tissue control (Fig. 10C), where no staining was detected, as expected. Altogether, we concluded that CK18 was a good marker to identify tumor cells, however the fluorophore Qdot 585 could not be used due to its unspecific binding, which required a few adjustments to the final mIHC panels.

IMPORTANT TIP: As the primary antibodies, always validate the secondary antibodies that will integrate a mIHC panel.

6.1.4.5. Final adjustments to the multiplexed immunohistochemistry panels

The optimization of the mIHC panels was a multistep process involving the selection of

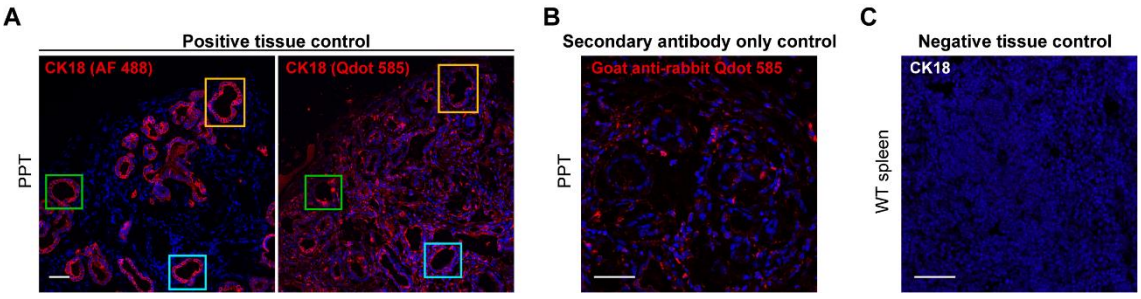

Fig. 10. Validation of keratin 18 antibody and selection of the paired fluorophore.
(A) Representative pictures of keratin 18 (CK18) antibody stainings performed with goat anti-rabbit Alexa Fluor® (AF) 488 (on the left) and goat anti-rabbit Qdot 585 (on the right) secondary antibodies in two consecutive sections of primary pancreatic tumor (PPT) used as positive tissue control. Orange, blue, and green rectangles allow the comparison of these two stainings in three different lesions.
(B) Representative picture of the secondary antibody only control performed with the goat anti-rabbit Qdot 585 antibody using a PPT section.
(C) Representative picture of negative tissue quality control performed using wild-type (WT) splenic tissue to validate the CK18 antibody.
This validation was performed in three independent experiments with similar results. All the scale bars indicate 50 µm. AF denotes the Alexa Fluor®, CK18 the keratin 18, PPT the primary pancreatic tumor, Qdot the quantum dot, WT the wild-type.

cells of interest and definition of the markers to identify them, validation of the primary antibodies against the selected targets and assignment of these antibodies to the most suitable fluorophores, and culminated into three distinct panels, as depicted in Fig. 11. Our initial idea was to integrate as many as possible markers into a single mIHC panel and, until the validation of the CK18 and goat anti-rabbit Qdot 585 antibodies, we aimed to generate two 7-color mIHC protocols (5 immune cell markers, 1 tumor cell marker, and 1 nuclei staining) to identify IICs or AICs and additionally cancer cells and nuclei. However, the secondary antibody conjugated with the Qdot 585 fluorophore did not produce a satisfactory staining to label PCCs and thus requiring few final adjustments to the panels. In addition, being the UV range channel occupied by the primary antibodies conjugated with eFluor 450 fluorophore (CD11b and FoxP3), it was not possible to include DAPI (max excitation: 350 nm; max emission: 470 nm) as a nuclear fluorescent dye. Instead, the far-red ToPro-3 dye (max excitation: 642 nm; max emission: 661 nm; similar to the AF 647) was selected to label the nuclei in the tissues. To maintain the minimum spectral overlap and avoid spillover between distinct markers, we needed to compromise and only integrate 6 fluorophores – eFluor 450, AF 488, AF 532, AF594, ToPro-3/AF 647 and AF 680 – into the panels.

Regarding the ICC panel, the two adjustable pairing fluorophores were the AF 594 and AF 680 and since the CK18 was highly expressed in pancreatic tissue, this marker was paired with the AF 680 probe, leaving the AF 594 to be combined with a primary antibody. F4/80 and

A *mIHC panel for innate immune cells*

Antibody	Target cell(s)	Fluorophore
CD11b	Myeloid cells	eFluor 450#
CD11c	Dendritic cells	AF 488*
Ly6G/Ly6C	Neutrophils	AF 532#
F4/80	Macrophages	AF 594

B *Panel for adaptive immune cells*

Antibody	Target cell(s)	Fluorophore
CD3	T cells	AF 488
CD45R/B220	B cells	AF 594*

C *mIHC panel for T cells*

Antibody	Target cell(s)	Fluorophore
FoxP3	Regulatory cells	eFluor 450#
CD8a	Cytotoxic cells	AF 488#
CD4	Helper cells	AF 532#
CD3	T cells	AF 594

D *Additionally to each panel:*

Antibody	Target	Fluorophore	Antibody	Target cell(s)	Fluorophore
ToPro-3	Nuclei	AF 647	CK18	Tumor cells	AF 680

Fig. 11. Established fluorescent panels to identify immune and tumor cells in cryopreserved tissues.
(A) Multiplexed immunohistochemistry (mIHC) panel to identify innate immune cells includes the markers for myeloid lineage cells (rat cluster of differentiation (CD)11b eFluor 450, clone M1/70, #48-0112-82), dendritic cells (Armenian-hamster CD11c, clone N418, #14-0114-82, labeled with Alexa Fluor™ (AF) 488 Antibody Labeling Kit, #A20181), neutrophils (rat Ly6G/Ly6C AF 532, clone RB6-8C5, #58-5931-82), and macrophages (rat F4/80, clone Cl:A3-1, #MCA497, detected with donkey anti-rat AF 594 secondary antibody, #A21209).
(B) Panel to identify adaptive immune cells comprises the markers for T cells (rat CD3, clone 17A2, #100201, detected with donkey anti-rat AF 488 secondary antibody, #A21208) and B cells (rat CD45R/B220, clone RA3-6B2, #103201, labeled with AF 594 Antibody Labeling Kit, #A20185).
(C) mIHC panel to identify T cell subtypes includes the markers for regulatory cells (rat FoxP3 eFluor 450, clone FJK-16s, #48-5773-82), cytotoxic cells (rat CD8a AF 488, clone 53-6.7, #53-0081-82), helper cells (rat CD4 AF 532, clone RM4-5, #58-0042-82), and T cells (rat CD3, clone 17A2, #100201, detected with donkey anti-rat AF 594 secondary antibody, #A21209).
(D) Additionally to each panel, the nuclei were stained with ToPro™-3 Iodide (#T3605), which possesses a far-red fluorescent signal similar to the AF 647 fluorophore, and the tumor cells were stained with rabbit keratin 18, #SAB4501665, detected with donkey anti-rabbit AF Plus 680 secondary antibody, #A32802).
AF denotes the Alexa Fluor, CD the cluster of differentiation, CK18 the keratin 18, mIHC the multiplex immunohistochemistry, # the directly-conjugated primary antibody, * the directly-labeled primary antibody using Antibody Labeling Kit.

Siglec-F were the two validated IIC markers available to be adjusted and integrated in this mIHC panel. Applying the criterion of the abundance and relevance in PDAC, we decided to integrate the F4/80 antibody paired with AF 594 fluorophore within the IIC panel, because macrophages are described to be more abundant in the TME than eosinophils, having a relevant role in pancreatic cancer (Gitto et al., 2020; Nielsen et al., 2016). Thus, the IIC panel depicted $CD11b^+$ myeloid cells, $CD11c^+$ cDCs, $Ly6G/Ly6C^+$ neutrophils, $F4/80^+$ macrophages, $CK18^+$ tumor cells, and $ToPro\text{-}3^+$ nuclei (Fig. 11A and 11D).

Similarly to the ICC panel and to generate a consistent protocol, CK18 paired with AF 680 and ToPro-3 were also integrated into the AIC panel. Since the CD3 antibody was originally thought to be detected with the AF 680 fluorophore (Table 25), we needed to divide the initial AIC panel into two panels to identify both T cell subtypes and B lymphocytes. Hence, the new AIC panel detected $CD3^+$ T and $CD45R/B220^+$ B lymphocytes, $CK18^+$ tumor cells, and $ToPro\text{-}3^+$ nuclei (Fig. 11B and 11D), while the T cell panel comprised $CD3^+$ $CD4^+$ Th cells, $CD3^+$ $CD4^+$ $FoxP3^+$ Tregs, $CD3^+$ $CD8a^+$ CTLs, $CK18^+$ tumor cells, and $ToPro\text{-}3^+$ nuclei (Fig. 11C and 11D). Concluding these final adjustments in the panels, we processed to the establishment of the mIHC staining protocols.

6.1.5. Full procedure of the established multiplexed immunohistochemistry panels

Cryopreserved tissue sections were labeled simultaneously for cancer cells with CK18, nuclei with ToPro-3 and distinct immune cells using three different mIHC panels, as depicted in Fig. 12: 1) IIC panel includes the markers CD11b, CD11c, Ly6G/Ly6C, and F4/80 (Fig. 12A); 2) AIC panel with the markers CD3 and CD45R/B220 (Fig. 12B); and 3) T cell panel comprises the markers CD4, CD8a, FoxP3, and CD3 (Fig. 12C). Ultimately, each panel would be applied in a single tissue section belonging to a series of 3 consecutive cuts.

6.1.5.1. Staining protocols

IIC Panel

Frozen section was thawed on a hot plate for 1 min at 37 °C, air dried for 20 min at RT and post-fixed with acetone for 6 min at 4 °C. After air drying once again for 20 min at RT, the tissue was rehydrated in 1×PBS for 10 min and then blocked with 10% donkey serum/3% BSA for 1 hour at RT. Afterwards, the section was incubated for 3 hours at RT with the primary antibodies F4/80 (1:100) and CK18 (1:500) diluted in 3% BSA. Upon washing thrice with 1×PBS, the donkey anti-rat AF 594 and donkey anti-rabbit AF Plus 680 secondary antibodies were diluted 1:200 in 3% BSA and applied for 1 hour at RT. The tissue was washed thrice with 1×PBS and then blocked with 10% rat serum/3% BSA for 1 hour at RT. The primary antibody Ly6G/Ly6C conjugated with AF 532 was diluted 1:50 in 3% BSA and incubated for 3 hours at RT. The section was washed thrice with 1×PBS and incubated for 3 hours at RT with a third round of primary antibodies composed by CD11b conjugated with eFluor 450 (1:200) and CD11c labeled with AF 488 (antibody labeled with Antibody Labeling Kit according to the manufacturer's instructions;

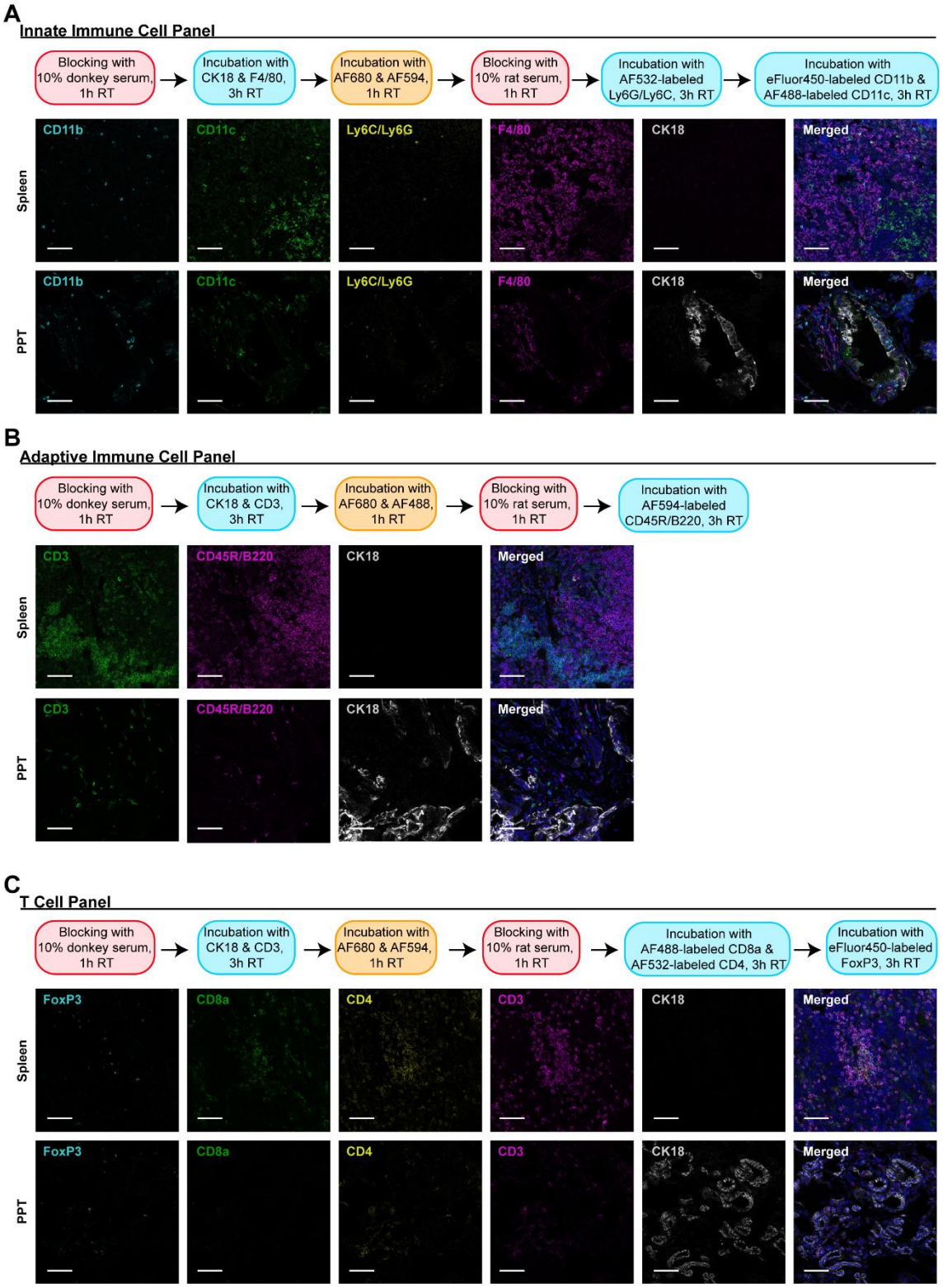

Fig. 12. Main steps of the protocols of the fluorescent panels to identify immune and tumor cells using splenic and pancreatic cryopreserved tissues.
(A) Top, experimental design of protocol for innate immune cell panel; Bottom, representative pictures of each marker (cluster of differentiation (CD)11c, CD11b, Ly6G/Ly6C, F4/80, and keratin 18 – CK18) included in the panel as well as the merged image using splenic and primary pancreatic tumor (PPT) tissues.
(B) Top, experimental design of protocol for adaptive immune cell panel; Bottom, representative pictures of each marker (CD3, CD45R/B220, and CK18) included in the panel as well as the merged image using splenic and PPT tissues.
(C) Top, experimental design of protocol for T cell panel; Bottom, representative pictures of each marker
(legend continues on the next page)

1:50) diluted in 0.5% BSA/0.5% Triton™ X-100 solution. After washing thrice with 1×PBS, the tissue was incubated for 10 min at RT with ToPro-3 diluted 1:75000 in 3% BSA. Finally, the section was washed thrice with 1×PBS, mounted in Vectashield® mounting medium, and stored at 4 °C until the image acquisition was performed.

AIC panel

Frozen section was thawed on a hot plate for 1 min at 37 °C, air dried for 20 min at RT and post-fixed with acetone for 6 min at 4 °C. After air drying once again for 20 min at RT, the tissue was rehydrated in 1×PBS for 10 min and then blocked with 10% donkey serum/3% BSA for 1 hour at RT. Afterwards, the section was incubated for 3 hours at RT with primary antibodies CD3 (1:100) and CK18 (1:500) diluted in 3% BSA. Upon washing thrice with 1×PBS, the donkey anti-rat AF 488 and donkey anti-rabbit AF Plus 680 secondary antibodies were diluted 1:200 in 3% BSA and applied for 1 hour at RT. The tissue was washed thrice with 1×PBS and then blocked with 10% rat serum/3% BSA for 1 hour at RT. The primary antibody CD45R/B220 labeled with AF 594 (antibody labeled with Antibody Labeling Kit according to the manufacturer's instructions) was diluted 1:100 in 3% BSA and incubated for 3 hours at RT. After washing thrice with 1×PBS, the tissue was incubated for 10 min at RT with ToPro-3 diluted 1:75000 in 3% BSA. Finally, the section was washed thrice with 1×PBS, mounted in Vectashield® mounting medium, and stored at 4 °C until the image acquisition was performed.

T cell panel

Frozen section was thawed on a hot plate for 1 min at 37 °C, air dried for 20 min at RT and post-fixed with acetone for 6 min at 4 °C. After air drying once again for 20 min at RT, the tissue was rehydrated in 1×PBS for 10 min and then blocked with 10% donkey serum/3% BSA for 1 hour at RT. Afterwards, the section was incubated for 3 hours at RT with primary antibodies CD3 (1:100) and CK18 (1:500) diluted in 3% BSA. Upon washing thrice with 1×PBS, the donkey anti-rat AF 594 and donkey anti-rabbit AF Plus 680 secondary antibodies were diluted 1:200 in 3% BSA and applied for 1 hour at RT. The tissue was washed thrice with 1×PBS and then blocked with 10% rat serum/3% BSA for 1 hour at RT. The primary antibodies CD8a conjugated with AF 488 and CD4 conjugated with AF 532 were both diluted 1:50 in 3% BSA and incubated for 3 hours at RT. The section was washed thrice with 1×PBS and incubated for 3 hours at RT with FoxP3 conjugated with eFluor 450 diluted 1:50 in 0.5% BSA/0.5% Triton™ X-100 solution. After washing

(FoxP3, CD8a, CD4, CD3, and CK18) included in the panel as well as the merged image using splenic and PPT tissues.
This validation was performed in three independent experiments using different pairs of splenic and PPT tissues with similar results. All the scale bars indicate 50 µm. Pink rectangles in the experimental design schemes represent blocking steps, blue rectangles indicate incubations with primary antibodies and orange rectangles represent incubations with secondary antibodies. AF denotes the Alexa Fluor®, CD the cluster of differentiation, CK18 the keratin 18, h the hour, PPT the primary pancreatic tumor, RT the room temperature.

thrice with 1×PBS, the tissue was incubated for 10 min at RT with ToPro-3 diluted 1:75000 in 3% BSA. Finally, the section was thrice washed with 1×PBS, mounted in Vectashield® mounting medium, and stored at 4 °C until the image acquisition was performed.

► **CRITICAL STEP:** Determine the optimal dilution of each primary antibody and fluorescent dye used in the mIHC panels, which may differ from the dilution used during the antibody validation. The optimal dilution is achieved when there is a high signal-to-noise ratio and the spillover into other fluorophore channels is minimal.

► **CRITICAL STEP:** It is essential to optimize the order in which the antibodies are applied in the tissue section during a mIHC protocol, since the detected fluorescent signal of a primary antibody may be affect by the relative position within the panel.

IMPORTANT TIP: When using two primary antibodies produced in the same host species (e.g., rat CD3 and rat CD45R/B220), it is essential to add a second blocking step with the serum of the species (in this example, rat serum) to block all the unbinding sites of the first primary antibody incubation and guarantee that the second primary antibody will only bind to its specific target.

6.1.5.2. Image acquisition using confocal microscopy

A Leica TCS SP8 confocal microscope with a motorized stage for tiled imaging and LAS X Navigator module were used for image acquisition. Throughout the development of the mIHC panels, it was noticed that the high numerical aperture (NA) objective with 40x magnification (HC PL APO CS2 40x/1.30 OIL) provided sufficiently resolved and smoothly tiled images and allowed the imaging of the totality of the tissue area in a reasonable amount of time (depending on the area to image, the acquisition could go up to 3 hours per slide). The design of the mIHC panels largely relied on fluorophores with spectral separation of the emission spectrums by photon collection using separate detectors (photomultiplier tube detector – PMT – and hybrid detector – HyD). For each panel, each fluorophore was excited with the respective laser line and a specific laser power (%), which was adjusted when necessary, and the fluorescent signal was detected with emission wavelength ranges by specific detectors, as depicted in Tables 26-28. To minimize fluorophore spectral spillover, sequential laser excitation and detection were used as well as line average of 2 in certain sequences to reduce the noise/background signal. Images were taken at 1024 x 1024 voxel density.

IMPORTANT TIP: The image acquisition using a confocal microscope equipped with laser light allows the detection of adjustable, narrow emission wavelengths enabling a better spectral separation of the detected fluorophores, contrarily to a microscope that possesses filter cubes.

Table 26. Confocal microscope settings for the image acquisition of the innate immune cell panel

Sequence	Marker	Laser (nm; %)	Detector	Emission (nm)	Gain (% or V)	Comment
Seq. 1	CD11b	405; 1.20	HyD2	433-467	72.0	With Line Average 2
	Ly6G/Ly6C	532; 25.0	HyD4	543-565	105.0	
	CK18	670; 4.30	HyD5	694-716	100.0	
Seq. 2	CD11c	490; 37.5	HyD2	504-531	118.5	With Line Average 2
	F4/80	590; 3.40	HyD4	607-630	100.0	
Seq. 3	ToPro-3	642; 17.0	PMT3	648-667	775.5	

%, percentage; CD, cluster of differentiation; CK18, keratin 18; HyD, hybrid detector; nm, nanometer; PMT, photomultiplier tube detector; Seq., sequence; V, volt.

Table 27. Confocal microscope settings for the image acquisition of the adaptive immune cell panel

Sequence	Marker	Laser (nm; %)	Detector	Emission (nm)	Gain (% or V)
Seq. 1	CK18	670; 3.80	HyD5	694-716	100.0
Seq. 2	CD3	490; 5.50	HyD2	504-531	100.0
	CD45R/B220	590; 6.0	HyD4	607-630	120.0
Seq. 3	ToPro-3	642; 17.0	PMT3	648-667	775.5

%, percentage; CD, cluster of differentiation; CK18, keratin 18; HyD, hybrid detector; nm, nanometer; PMT, photomultiplier tube detector; Seq., sequence; V, volt.

Table 28. Confocal microscope settings for the image acquisition of the T cell panel

Sequence	Marker	Laser (nm; %)	Detector	Emission (nm)	Gain (% or V)	Comment
Seq. 1	FoxP3	405; 14.2	HyD2	433-467	100.0	With Line Average 2
	CD4	532; 29.3	HyD4	543-565	120.0	
	CK18	670; 3.80	HyD5	694-716	100.0	
Seq. 2	CD8a	490; 21.0	HyD2	504-531	100.0	With Line Average 2
	CD3	590; 3.20	HyD4	607-630	100.0	
Seq. 3	ToPro-3	642; 17.0	PMT3	648-667	775.5	

%, percentage; CD, cluster of differentiation; CK18, keratin 18; HyD, hybrid detector; nm, nanometer; PMT, photomultiplier tube detector; Seq., sequence; V, volt.

6.1.5.3. Image processing and data analysis

For visualization and image analysis of mIHC stainings, Imaris 9.5 and 9.6 software was used. This software allowed the determination of marker-positive cells, their position, and the shortest distance to a cell belonging to another population. The .lif files from the Leica confocal microscope were converted to an .ims format, a compatible format to Imaris software. Using the "Display Adjustment" tool of Imaris, the intensity of each individual channel was adjusted in the displayed Imaris image, controlling the channel visibility and color by setting the appropriate minimum and maximum intensity range. With this tool, it was also possible to select the channels to be displayed in the image (e.g., activating CD3, CD4, and ToPro-3 channels and disabling FoxP3, CD8a, and CK18 channels), facilitating the visualization of the cells of interest (e.g., Th cells) without the disturbance of the remaining stainings. Furthermore, quantitative and phenotypic analyses could be achieved by segmenting imaged cells into individual objects. To this end, membrane-based Imaris module "Surfaces" was used to create artificial cell surface renderings, based on the fluorescent signal expressed by the cells of interest, and separated into

discrete cellular objects via watershed segmentation algorithms. Imaris modules are step-wise algorithms and the following settings were used:

Step i: Select a pre-saved parameters creation (if applicable) and enable the algorithm settings “Segment only a Region of Interest”, “Process entire Image finally” and “Shortest Distance Calculations”. When working with big imaging datasets such as a whole-slide image, it was recommended to segment a region of interest, adjusting all the parameters in this region, and finally applying the settings to the entire image;

Step ii: Demark a region of interest, which must contain positive cells for the marker to be segmented;

Step iii: Select the source channel, i.e., the marker to be segmented;

Step iv: Adjust the threshold in order to capture all the positive staining, excluding as much as possible areas where no staining is observed. In this step, it was easier if only the marker (or markers in case of co-localization) of interest and the nuclei were displayed in the image. For a better separation, “Split Touching Objects” option was enabled with a seed point diameter of 8.00 for the segmentations of the nuclei and $CK18^{+}$ cells and 5.00 for all immune cell markers;

Step v: With the “Quality” filter selected, the value was adjusted until each individual positive cell would be marked by a single gray dot;

Step vi: Filters such as “Intensity Mean Ch=x Img=1”, “Intensity Max Ch=x”, and/or “Area” were used to obtain the segmentation of individual objects positive for a certain marker. The marker was designated by “Ch=x”, being x the number of the channel of the marker of interest. The segmentation using the Surfaces module presented few challenges, especially when multiple cells were physically touching one another (e.g., CK18-positive cells) or were clustered (e.g., T lymphocytes). To overcome this issue that would lead to inaccurate cell segmentation, a nuclear-based filter (Intensity Center Ch=y Img=1, where y represents the number of the channel of the nuclear staining) was added to the membrane marker filters;

Step vii: Once the parameters were set up in the region of interest, they were applied to the entire image.

Afterwards, the set parameters were saved and used in posterior images that would possess the same marker. From batch to batch, the intensity threshold values were normally adjusted to allow a better and more accurate segmentation. Once the cell surface objects were generated, relevant statistics, such as the total number of segmented objects and the shortest distance of surfaces, were extracted, further analyzed in Excel and plotted using GraphPad Prism software. For the determination of the percentage of cells in contact, we calculated, among the total number of cells analyzed, which ones presented a distance of 0.0 µm to another cell type. It is important to note that many of the processing steps described above demanded substantial hands-on expertise and processing time. Cell segmentation often required empirical testing of different algorithm settings during the surface creation. Furthermore, Imaris software occasionally became instable with large image datasets, not allowing the processing of these datasets in a short period of time. Thus, we concluded that, regardless of the challenges and limitations, image

analysis using mIHC, confocal microscopy and post-processing with Imaris were useful and powerful tools to study TME cells, namely distinct immune cell populations.

IMPORTANT TIP: Good quality of the stained tissue prior to image analysis, meaning minimal background signal and/or unspecific binding, allows a more accurate image and data processing.

6.1.6. Challenges and Limitations

In the last decade, mIHC and related techniques have been developed to stain and visualize multiple targets in a single sample, especially in complex tissues such as cancer identities (Taube et al., 2020). Regardless the noticeable advantage of this technique and the fact that we were able to establish three distinct manual panels to identify tumor and immune cells, mIHC also presented inherent challenges and limitations. The most significant limitation of this technique was the optimization time: the AIC and T cell panels took one year to be designed, while almost two years were required for the establishment of the IIC panel. Regarding the primary antibodies, the main limitations were the commercially availability against the targets of interest (even though there was a vast selection of antibodies against immune-related targets) and the production of the antibodies in the same host species (the majority being produced in rat). This last limitation was partially overcome with sequential staining incubations, which in turn resulted in a labor-intensive protocol, and the inclusion of directly-conjugated or -labeled primary antibodies, even though their fluorescent signal was not as intense as the one provided by the incubation with a secondary antibody. Other limitation was the number of fluorophores that could be integrated in a single mIHC panel to avoid spectral emission overlap, leading to the limited selection of 6 distinct fluorescent probes. Furthermore, even though the confocal microscope used for the image acquisition was equipped with a laser light allowing the manual adjustment of the emission wavelengths of each fluorophore, there was a limitation of excitation spectrum (from 405 nm up to 670 nm), reducing the number of fluorescent dyes that could be used in the mIHC panels (e.g., Leica TCS SP8 confocal microscope was not able to detect the AF 350 and AF 700 probes). Regarding the image acquisition, especially the whole-slide image acquisition of the three panels, it was not a fast process. On one hand, the imaging speed was influenced by the separate detection of the fluorophores in 3 distinct sequences (Tables 26-28), increasing the acquisition time compared with the imaging using a single sequence. On the other hand, the scan of the entire section required the delimitation of the area of interest, the addition of focus points and the adjustment of these points in each field of view, which also added some additional time to the image acquisition process. Finally, the following factors created some challenges during the image analysis of the tissues: 1) the image was only a 2D projection lacking the 3D structure present *in vivo* (however, the inclusion of Z-stack would dramatically increase the acquisition time not allowing the imaging of entire tissues); 2) tumor sections possessed a very heterogenous cellular content, which usually were not structured and/or organized; 3) the tumor and immune cells were generally close to each other overlapping and/or forming clusters; and 4) the large image datasets extended the processing time, however application of automated image analysis

method led to a more accurate segmentation. Regardless of the limitations and challenges, we were able to establish mIHC panels, acquire the stainings, and perform the image and data analyses.

6.1.7. Timing

To give an estimation of the timing implicated in the process from the preparation of the cryopreserved tissue samples to the data analysis and visualization, we summarized the timings, as depicted in Table 29. Note that all times in this work were rough estimates influenced by the number of markers collected, the available imaging equipment as well as the mode of acquisition, the computational capacity of the image analysis station and the research questions being addressed.

Table 29. Timings of the multiplexed immunohistochemistry process

Step of mIHC process	Timing
Preparation of the cryopreserved tissue (fixation and freezing)	18-24 hours
Preparation of consecutive cuts of cryopreserved tissue	0.5 hours per tissue sample
Performance of mIHC panels	15 hours for IIC and T cell panels; divided into 2 days; 12 hours for AIC panel that could be divided into 2 days.
Image acquisition (whole-slide imaging)	1-4 hours per panel
Image processing	8-72 hours computing time per panel
Data analysis and visualization	Several days to weeks, depending on the research question and investigator's computational expertise

AIC, adaptive immune cell; IIC, innate immune cell; mIHC, multiplex immunohistochemistry.

Once the process of mIHC protocol establishment was concluded, the panels were applied to study how distinct driver mutations and differentiation status of the tumor may alter the TME content in PDAC as described in the following section 6.2. Chapter I, Part B of this work. However, the applicability was not limited to the present work. The established mIHC panels were also used to understand how the T cell content changes upon *in vivo* drug treatment in PDAC (work performed by Jeannine Heetmeyer) and to investigate the TME in other cancer entities such as colorectal adenocarcinoma (work done by Antonio Zaurito and Zeynep Ünal). Furthermore, the development of the immune cell mIHC panels in our research group also provided the tools and facilitated the establishment of multiplexed protocols to detect subtypes of CAFs (work developed by Tatiana Martins). Thus, the mIHC technique may be applied to distinct research projects, assisting to answer different scientific questions related to the tumor-TME cell interactions, and ultimately help to improve clinical outcomes.

6.2. Chapter I, Part B: *Driver mutations and tumor differentiation shape the immune landscape of pancreatic ductal adenocarcinoma*

A mIHC approach with specific multiple markers can provide valuable distinguishment of the tumor and TME compartments and thus allow for a more detailed characterization of the cancer topography. Additionally, it has the potential to enhance the clinical significance, improving the diagnosis and guiding the prognosis and treatment strategies. Knowing the numbers or ratios, cell populations, and spatial location of TME cells, especially of immune cells, within the tumor is thought to be essential to understand their mechanisms of action. We analyzed the tumor-associated cellular composition of murine primary PDAC specimens harboring different oncogenes, such as *Kras*, *Pik3ca*, or *Braf*, and, in the case of Kras tissues, two distinct differentiation status. These analyses allowed us to assess which populations of immune cells are present in the TME, how inflammatory cells interact with the malignant cells, and investigate the impact of the driver mutation and differentiation status modulating and altering the cell content within the PDAC tissues. As depicted in Fig. 13, the study the TME in PDAC involved a series of steps as following described: 1) selection of cryopreserved samples according to the genotype; 2) performance of histopathological analysis based on H&E staining to assess the differentiation status, and acinar, necrotic, and potential imaging areas of each tumor; 3) addition of the tissue samples that met the necessary requirements to the respective cohort (Kras-, Pik3ca- or Braf-driven) and subsequential sectioning of the samples in serial consecutive cuts; 4) performance of IF labeling for CK18, CD45, and PDPN and histocytometry analysis to determine the tumor, immune, and stromal contents in each cohort; and lastly 5) performance of the mIHC staining and analysis to assess the specific immune cell populations and their interactions with tumor cells. Furthermore, we compared the imaging data analyses with RNA-seq bulk tumor data to access rather this last method reflected the histological observations. The work described in this section was done together with Tatiana Martins and Fabio Boniolo. The animals used in the described work were generated, breed and sacrificed by all members of the laboratory of Prof. Dr. med. Dieter Saur.

6.2.1. Hematoxylin and eosin (H&E) staining helped to define the cohorts to be analyzed

The usage of GEMMs harboring solely an oncogenic aberration to better understand the impact of PDAC driver mutations on the TME can unveil new personalized targets according to the genetic background of the tumor. To provide insights into how the composition of the TME can be modulated by genetic aberrations such as *Kras*, *Pik3ca*, and *Braf*, we selected cryopreserved pancreatic tissues harvested from mice harboring one of these oncogenes. Histopathological analysis was performed based on H&E staining, and cohorts were defined according to the driver mutation and, in case of Kras tumors, these tissues were additionally divided regarding their differentiation status, as shown in Fig. 14. Taking advantage of *Cre/loxP*-

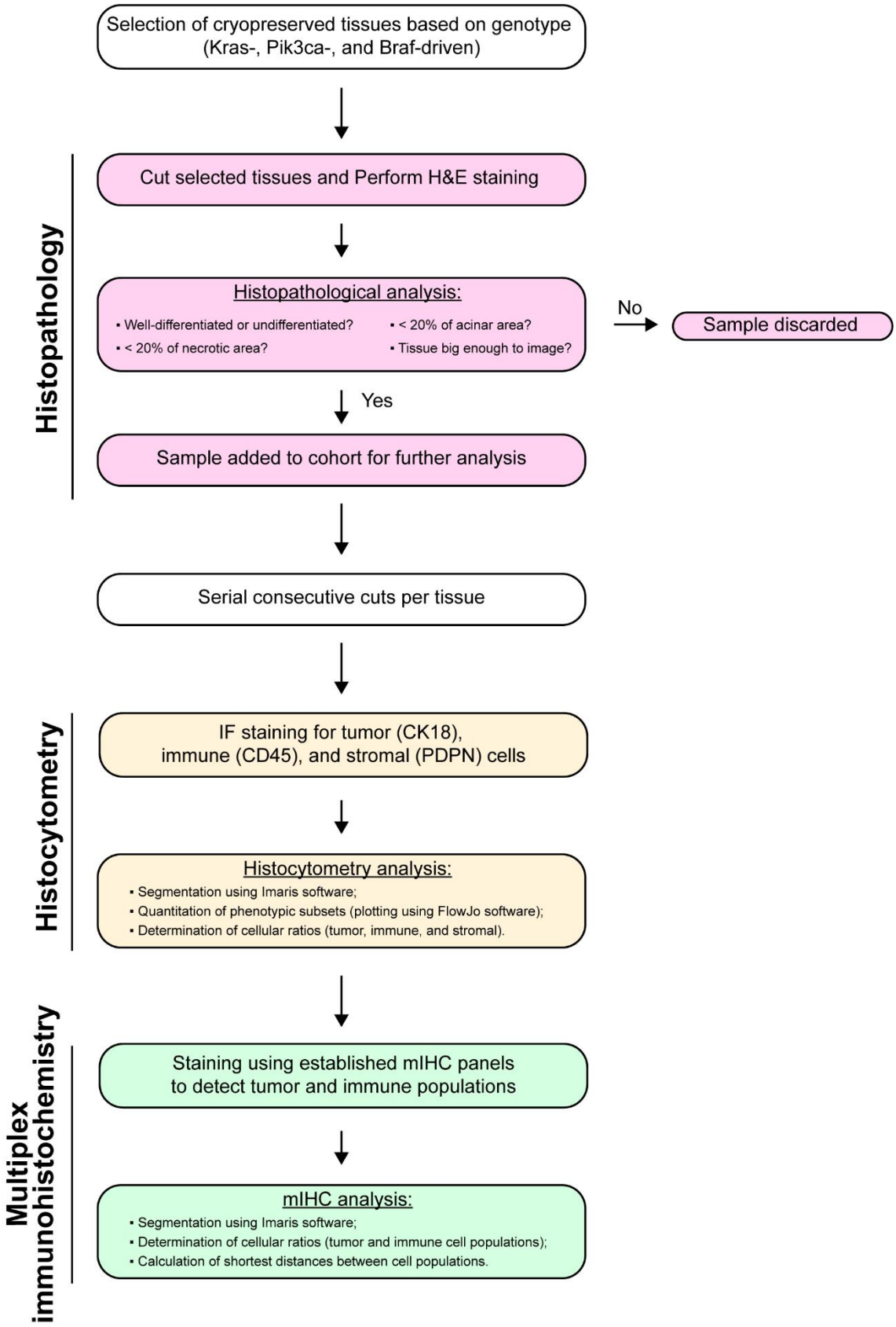

Fig. 13. Flowchart with the steps involving the study of the tumor microenvironment in pancreatic ductal adenocarcinoma.
This study ranged from the selection of tissues and establishment of cohorts based on histopathological analysis to histocytometry analysis and application of the multiplex immunohistochemistry (mIHC) panels to detect immune and tumor cells. After the selection of cryopreserved tissues based on their driver mutation

(legend continues on the next page)

based system, we collected tissues from animals that expressed one of the three *Kras*^{G12D}, *Pik3ca*^{H1047R}, or *Braf*^{V637E} mutations in the pancreas (Fig. 14A). Additionally, the mice from the Kras model carried one conditional floxed allele for *Trp53* that, upon activation of Cre recombinase, resulted in ablation of this tumor suppressor gene. After a pre-selection of cryopreserved tissues from the *Pdx1-Cre; LSL-Kras*$^{G12D/+}$*; Trp53*$^{lox/+}$ (PKP), *Pdx1-Cre; LSL-Pik3ca*$^{H1047R/+}$ (PPI3K), and *Pdx1-CreER*^{T2}*; LSL-Braf*$^{V637E/+}$ (PBR) mouse models (42, 31, and 14 specimens, respectively), they were cut, and H&E stained. As illustrated in Fig. 14B, the Kras-driven tissues were divided into differentiated and undifferentiated tumors, being the first ones characterized by duct-like structures embedded in a desmoplastic stroma, while the higher graded tumors presented single cell infiltrations (Haeberle & Esposito, 2019). In contrast, the selected tissues harboring *Pik3ca* mutation presented differentiated structures surrounded by a more prominent desmoplastic stromal reaction than the differentiated PKP tumors and we often observed a lymph node attached to the tumor. Regarding the Braf animals, the pancreatic tissue of these animals only presented PanINs as previously described by Collisson and colleagues (Collisson et al., 2012), being these precursor lesions generally surrounded by stromal cells and normal acinar tissue. After the histopathological evaluation, we defined the Kras, Pik3ca, and Braf cohorts composed by a total of 8 Kras animals (4 animals with G1/G2 tumors and 4 animals with G4 tumors), 4 Pik3ca differentiated tumors, and 3 Braf tissues with PanIN lesions, as summarized in Fig. 14C. The TME of the selected tissues was further characterized by histocytometry and mIHC.

6.2.2. Histocytometry analysis showed that driver mutation has a strong impact on the abundance of tumor microenvironment cells

To identify and quantify major cellular subsets – tumor, immune, and stromal – present in PDAC tissues, histocytometry analysis was performed (Gerner et al., 2012), as depicted in Fig. 15. We stained the selected tissues from the Kras, Pik3ca, and Braf cohorts with the set of antibodies CK18, CD45, and PDPN to discriminate between the cancer, immune, and stromal cells, respectively. Regions of interest of each section were imaged and semiautomatic volumetric rendering and segmentation of positive cells from each marker were performed using the Imaris

(*Kras*, *Pik3ca*, or *Braf*), the tissues were cut, and hematoxylin and eosin (H&E) staining was performed to assess the differentiation status of the tumor (well-differentiated or undifferentiated), the percentage of necrotic and acinar areas was not higher than 20% and if the tissue was big enough to be imaged. When the sample complied with the necessary requirements, the tissue was added to the respective cohort for further analysis, whilst other cryopreserved samples were discarded. The selected tissues were cut in consecutive sections and posteriorly histocytometry and multiplex immunohistochemistry (mIHC) were performed. For histocytometry, the selected tissues were labeled with keratin 18 (CK18; tumor cells), cluster of differentiation (CD)45 (CD45; immune cells), and podoplanin (PDPN; stromal cells) to quantify the phenotypic subsets and determine the cellular ratios based on the segmentation done using Imaris software. Furthermore, the cryopreserved tissues were stained using the established mIHC panels to detect tumor and immune populations and the imaging analyses, such as determination of cellular ratios and calculation of shortest distances between cell populations, were done based on the segmentation on Imaris software. CD denotes the cluster of differentiation, CK18 the keratin 18, H&E the hematoxylin and eosin staining, mIHC the multiplex immunohistochemistry, PDPN the podoplanin.

A

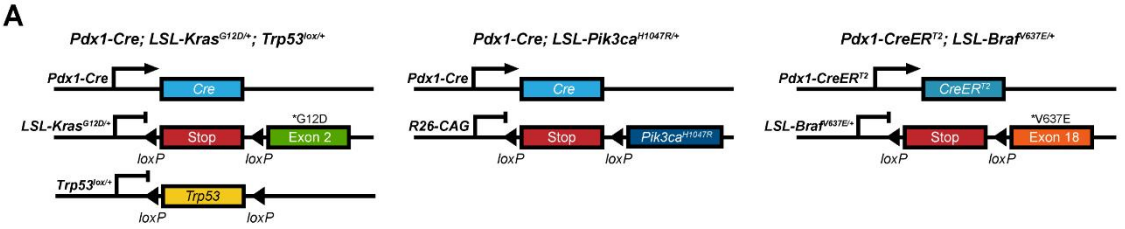

B

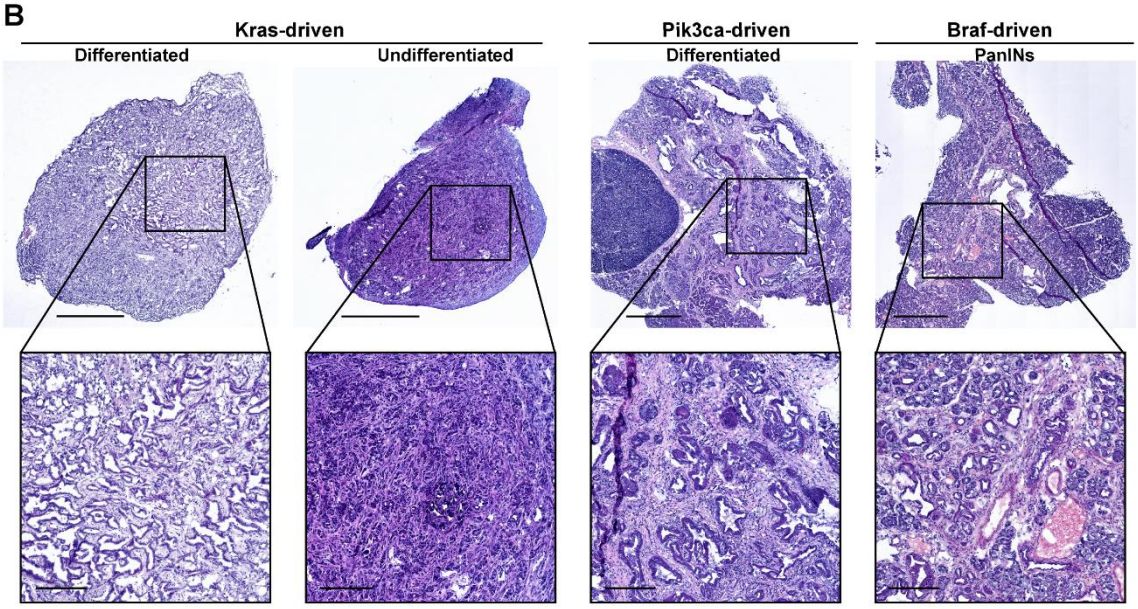

C

Cohort	Kras-driven		Pik3ca-driven	Braf-driven
Grading/Diff status	G1-G2/Diff	G4/Undiff	G1-G2/Diff	PanINs
Mice ID	13663 AA785 AA966 B97	6719 13871 14193 P283	AK1234 LPT175 LPT1223 Pi3kTg11637	TRM-391 TRM-512 TRM-602

Fig. 14. Kras-, Pik3ca-, and Braf-driven cohorts are defined based on histopathological evaluation for posterior characterization of the tumor microenvironment in pancreatic ductal adenocarcinoma.
(A) Genetic schemes of *Pdx1-Cre; LSL-Kras$^{G12D/+}$; Trp53$^{lox/+}$* (PKP), *Pdx1-Cre; LSL-Pik3ca$^{H1047R/+}$* (PPI3K), and *Pdx1-CreER^{T2}; LSL-Braf$^{V637E/+}$* (PBR) mouse models.
(B) Top, representative scans of murine primary pancreatic tissues stained for hematoxylin and eosin (H&E) from mice harboring *Kras* (both differentiated and undifferentiated tumors), *Pik3ca* (differentiated tumor), or *Braf* (pancreatic intraepithelial neoplasias - PanINs) oncogene. H&E staining was also carried out using the remaining mice of each cohort with similar results.
Scale bars of the fit images indicate 900 µm. Bottom, the inserts show an amplified area of each tissue. Scale bars of the inserts indicate 200 µm.
(C) Murine tissues used for the characterization of the tumor microenvironment according to the respective cohort (Kras-, Pik3ca-, or Braf-driven) and to their grading/differentiation status. The Kras cohort comprised a total of 8 animals (4 animals with G1/G2 tumors and 4 animals with G4 tumors), Pik3ca cohort was composed by 4 animals with differentiated tumors, while the Braf cohort comprised of 3 animals with PanIN lesions.
The histopathological analysis and definition of the tissue cohorts were performed together with Tatiana Martins and the animals were generated and sacrificed by all the members in the laboratory of Prof. Dr. med. Dieter Saur. Diff denotes the differentiation/differentiated status, ID the identification number, PanIN the pancreatic intraepithelial neoplasia, PBR the *Pdx1-CreER^{T2}; LSL-Braf$^{V637E/+}$* mice, PKP the *Pdx1-Cre; LSL-Kras$^{G12D/+}$; Trp53$^{lox/+}$* mice, PPI3K the *Pdx1-Cre; LSL-Pik3ca$^{H1047R/+}$* mice, Undiff the undifferentiated status, + the wild-type allele.

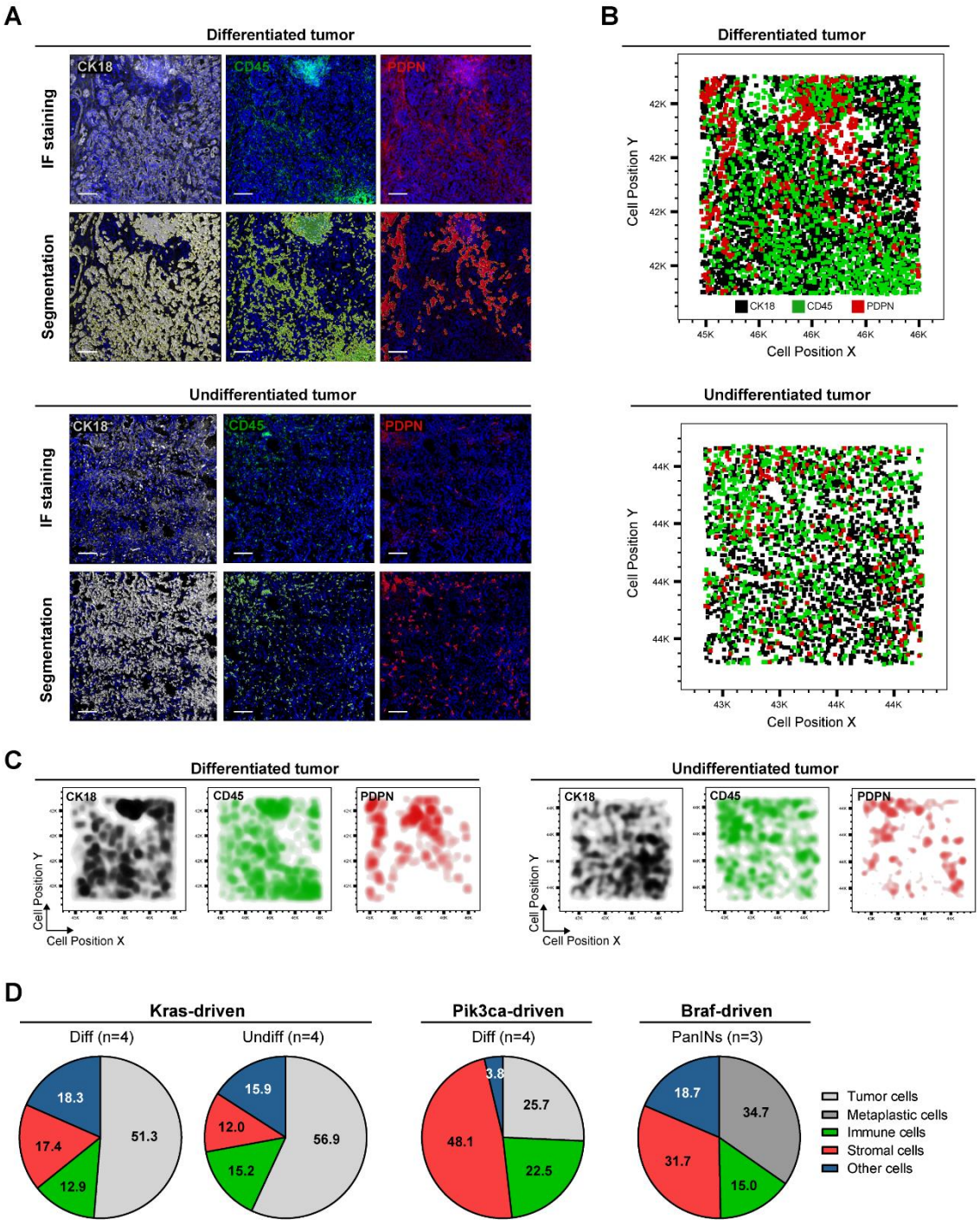

Fig. 15. Driven mutation of pancreatic ductal adenocarcinoma has a stronger impact on the abundance of tumor microenvironment cells than the differentiation status of the tumor.
(A) Immunofluorescence (IF) staining for keratin 18 (CK18), cluster of differentiation (CD)45, and podoplanin (PDPN) (upper panels) and respective segmentation (bottom panels) using Imaris 9.5 software of both differentiated and undifferentiated tumors. IF staining was also carried out using the remaining mice of each cohort with similar results. Scale bars indicate 100 µm.
(B) All imaged cells were segmented, and their statistical information was imported into FlowJo v10.6.1 software for spatial visualization of the different tumor ($CK18^+$), immune ($CD45^+$), and stromal ($PDPN^+$) populations of both differentiated and undifferentiated tumors using dot plots.
(C) Segmented cellular populations were also displayed as density XY positional plots to highlight regionalized cell distribution.
(D) Pie charts of tumor/metaplastic, immune, and stromal ratios in Kras, Pik3ca, and Braf cohorts. n=4 biologically independent animals were examined in the each Kras and Pik3ca groups, while n=3 biologically independent animals were analyzed in the Braf cohort, as indicated above the respective pie chart.
The histocytometry analysis was performed together with Tatiana Martins and the animals used for this

(legend continues on the next page)

9.5 software (Fig. 15A). The CK18, CD45, and PDPN triple IF labeling allowed to observe that the majority of the imaged area was occupied by cancer cells, regardless of the differentiation status of the tumor. It is also noteworthy to examine the higher number of $CD45^+$ and $PDPN^+$ cells in the differentiated tumor compared to the undifferentiated one. Plotting the 3D surface object data created after the cell segmentation revealed the discrimination of each cellular subset and their spatial distribution with patterns similar to the data derived from the IF staining (Fig. 15B). As expected, the x,y positional dot plots showed that the three cellular types were not spatially organized in defined areas within the tumor. Moreover, the $CD45^+$ cells were in close proximity to $CK18^+$ cells, while the $PDPN^+$ cells had the tendency to occupy surrounding areas of tumor cells. We also observed the localization of computed tumor, immune, and stromal cell surfaces as density plots (Fig. 15C). CK18 and CD45 markers presented the highest densities in both differentiated and undifferentiated tumors. In addition, similarly to the dot plots, the density plots showed that the highly dense areas of $CD45^+$ cells corresponded to areas highly occupied by $CK18^+$ cells, while $PDPN^+$ cells were present in areas with lower density of cancer cells. As illustrated in Fig. 15D, the Kras differentiated tumors presented slightly higher percentage of stromal cells compared to the undifferentiated tissues (17.4% and 12.0%, respectively). In contrast, the immune cell content appeared to not be drastically affected by the differentiation status of tumor (12.9% and 15.2% vs. PKP, Undiff). However, it was striking that the Pik3ca-driven tumors presented an ~2-fold increase of immune cells (22.5% and 12.9% vs. PKP, Diff; $p < 0.05$) and ~3-fold higher stromal content (48.1% and 17.4% vs. PKP, Diff; $p < 0.0001$) in comparison to the Kras differentiated cohort. Regarding the PBR cohort, it was curious to observe the balance among the three cell types analyzed, having a similar amount of both CAFs and metaplastic cells (~35.0% of each cell population), while the immune cells represented 15.0% of the cellular content in these tissues. Altogether, the histocytometry-based cell positioning analyses allowed to conclude that immune cells are in closer proximity to cancer cells than CAFs and that the driver mutation may have a stronger impact on TME abundance than the differentiation status of the tumor.

6.2.3. Macrophages were the most abundant immune population and Pik3ca-driven differentiated tumors had high infiltration of adaptive immune cells

To characterize the subtypes of immune cells within the TME of PDAC tissues and understand how they may be altered by the driver mutation, we applied the mIHC panels described in the previous section of this work (section 6.1. Chapter I, Part A). Three consecutive tissue sections of each animal from the Kras, Pik3ca, and Braf cohorts were stained for IIC, AIC, and T cell panels and whole-slide imaging was performed and analyzed, as depicted in Fig. 16.

analysis were generated and sacrificed by all the members in the laboratory of Prof. Dr. med. Dieter Saur. CD denotes the cluster of differentiation, CK18 the keratin 18, Diff the differentiated tumor, IF the immunofluorescence, PanIN the pancreatic intraepithelial neoplasia, PDPN the podoplanin, Undiff the undifferentiated tumor.

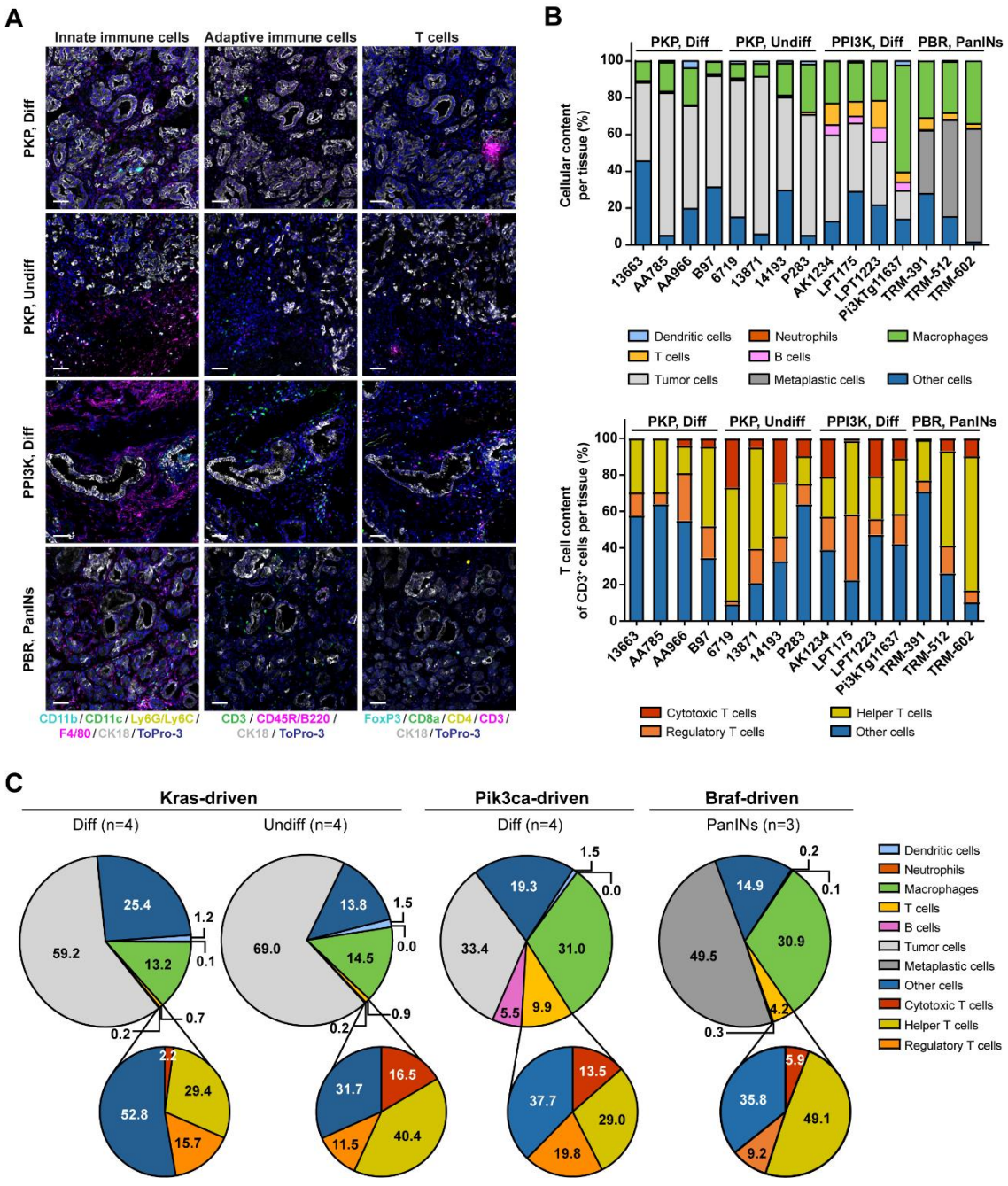

Fig. 16. Pik3ca cohort presents a high abundance of adaptive immune cells.
(A) Representative images of the three immune cell panels – innate immune cell panel, adaptive immune cell panel, and T cell panel – applied in three consecutive tissue sections of primary pancreatic tumors from mice harboring *Kras*, *Pik3ca*, or *Braf* mutation. The markers of each panel are identified below the respective column of images. Multiplex immunohistochemistry staining was also carried out using the remaining mice of each cohort with similar results. Scale bars indicate 50 µm.
(B) Top, immune and tumoral cellular content in percentage of each individual animal from the Kras, Pik3ca, and Braf cohorts included in the analysis of the tumor microenvironment. Bottom, content in percentage of cytotoxic, helper, and regulatory cells among the cluster of differentiation (CD)3-positive cells of each individual animal from the Kras, Pik3ca, and Braf cohorts.
(C) Pie charts with the immune and tumoral cellular content of all animals distributed according to their oncogene (*Kras*, *Pik3ca*, and *Braf*) and grading/differentiation status of the tumors. The smaller pie charts depict the percentage of cytotoxic, helper, and regulatory T cells among the CD3-positive cells. n=4 biologically independent animals were examined in the each Kras and Pik3ca groups, while n=3 biologically independent animals were analyzed in the Braf cohort, as indicated after the grading/differentiation status. Animals used for this analysis were generated and sacrificed by all the members in the laboratory of Prof. Dr. med. Dieter Saur. % denotes the percentage, CD the cluster of differentiation, CK18 the keratin 18, Diff

(legend continues on the next page)

As observed in the histocytometry analysis, the mIHC images consistently showed that the PKP and PBR tissues presented higher number of CK18$^+$ cells and consequently lower desmoplastic reaction compared to PPI3K samples (Fig. 16A). In the three cohorts analyzed, F4/80$^+$ macrophages were the most predominant immune cell subtype, especially on tissues from animals harboring *Pik3ca* or *Braf* mutation. These myeloid cells presented distinct spatial distributions, being in close proximity or in contact with CK18$^+$ cells or far away from the cancer or metaplastic cells. Curiously, Pik3ca tissues comprised a higher number of AICs, especially CD3$^+$ T cells, compared with Kras and Braf cohorts. Similarly to the macrophages, the lymphocytes were also found near and distant to CK18$^+$ lesions. Analysis of mIHC panels showed that there was a consistent cellular composition within each analyzed cohort, with special emphasis on the PKP cohort where all differentiated and undifferentiated tumors presented similar cellular contents (Fig. 16B). The tumor and metaplastic cells expressing CK18 were the most abundant cellular type within the tissues followed by F4/80$^+$ macrophages. In addition, compared with Kras and Braf tissues, the Pik3ca ones had a remarkably higher percentage of both AICs, varying between 5.0-15.0% of T cells and 4.0-8.0% of B lymphocytes in these tissues. For an in-depth analysis of the T cell subpopulations within the TME, we analyzed these lymphocytes among the total CD3$^+$ cells using the data obtained with the mIHC T cell panel. Regardless of the heterogenous composition of T cell subtypes among the cohorts and within each group, CD4$^+$ Th cells were the most abundant T lymphocyte subpopulation in all the analyzed animals, whilst the CD8a$^+$ CTLs and CD4$^+$ FoxP3$^+$ Tregs composition presented a more extensive variability. Interestingly, no CTLs were detected in half of the PKP differentiated tissues, and in one PPI3K and one PBR mice, the amount of these T cells was less than 1.5% of all CD3$^+$ cells. Furthermore, to have a general overview of the cellular content within the tumor, we grouped the 15 analyzed animals according to their driver mutations and grading (Fig. 16C). The Kras cohort presented the higher number of malignant cells regardless of the differentiation status of the tumor (59.2% in the differentiated tumors vs. 69.0% in the undifferentiated tumors), followed by the Braf-driven tissues composed by 49.5% of CK18$^+$ cells, and finally the Pik3ca cohort had ~2-fold less tumor content compared to the differentiated Kras tumors. In contrast, the PPI3K tumors had the higher percentage of immune cells (47.3% in PPI3K, Diff > 35.7% in PBR, PanINs > 17.1% in PKP, Undiff > 15.5% in PKP, Diff), especially of macrophages (31.0%) and AICs (9.9% and 5.5% of T and B cells, respectively). It is worth noting that the cellular composition of the Braf tissues seemed to be an intermediate between the Kras and Pik3ca tissues, with a high percentage of CK18$^+$ cells as the Kras tumors and a high amount of both macrophages and T cells as the Pik3ca tissues. Regarding the general composition of T cell subtypes, the PPI3K cohort showed the most balanced distribution of these cells with 29.0% of Th cells, 19.8% of

the differentiated tumor, PanIN the pancreatic intraepithelial neoplasia, PBR the *Pdx1-CreER^{T2}; LSL-Braf$^{V637E/+}$* mice, PKP the *Pdx1-Cre; LSL-Kras$^{G12D/+}$; Trp53$^{lox/+}$* mice, PPI3K the *Pdx1-Cre; LSL-Pik3ca$^{H1047R/+}$* mice, Undiff the undifferentiated tumor, + the positive or high expression.

Tregs, and 13.5% of CTLs, while in Braf tissues half of the infiltrated $CD3^+$ cells were Th cells. Although the numbers of $CD3^+$ cells were negligible in the PKP cohort (0.7% and 0.9% in the differentiated and undifferentiated tumors, respectively), it was interesting to note that, from the lower to the higher graded tumors, there was an increase of both Th cells (from 29.4% to 40.4%, respectively) and CTLs (from 2.2% to 16.5%, respectively; $p < 0.05$). Thus, these results showed that among the immune cells macrophages were the most abundant cells within the TME of PDAC tissues and the PPI3K cohort was characterized by a high infiltration of AICs, supporting the evidence that the immune cell content may be influenced rather by the driver mutation than by the differentiation status of the tumors.

6.2.4. Interactions between immune and tumor cells and between distinct immune cell populations may favor a tumor-friendly environment

Intercellular communication of cancer cells with different types of cells within their surrounding TME has an impact in regulating tumor growth and progression as well as in the therapy efficacy (D'Errico et al., 2019; Holokai et al., 2020). Therefore, using the processed mIHC data, we explored the interactions between the tumor and immune cells and the cross-talk among the cells composing the immune system (Fig. 17-19). The IIC panel allowed the study of the communication between tumor cells and IICs, such as macrophages and cDCs, as well as between these two last immune cell populations (Fig. 17). Regarding the Kras cohort, the differentiation status seemed to not have an impact on the number of infiltrated $F4/80^+$ cells interacting with $CK18^+$ cells (42.9% in PKP, Diff vs. 41.7% in PKP, Undiff), as depicted in Fig. 17A. However, macrophages were in closer proximity to undifferentiated tumor cells compared to differentiated $CK18^+$ cells (median of 2.4 µm and 3.5 µm vs. PKP, Diff; $p < 0.0001$). Moreover, despite of being the most abundant immune cell population present in Pik3ca tumors, macrophages showed to be significantly distant to cancer cells harboring this mutation compared to Kras-driven ones (median of 24.1 µm and 3.5 µm vs. PKP, Diff; $p < 0.0001$). Interestingly, Pik3ca tumors also had 2 times less $F4/80^+$ cells in direct contact with $CK18^+$ cells when compared to Kras differentiated tissues (19.6% and 42.9% vs. PKP, Diff). Among the three cohorts, Braf had the shortest distance mean between macrophages and cancer cells (median of 0.4 µm) and the highest percentage of $F4/80^+$ cells in direct contact with $CK18^+$ cells (49.1%). Furthermore, the interactions between cDCs and malignant cells followed a similar tendency as the one presented by the macrophages in both Kras and Pik3ca cohorts, as illustrated in Fig. 17B. cDCs were found in closer contact with Kras-driven $CK18^+$ cells compared to Pik3ca-driven ones (median of 3.6 µm and 26.4 µm vs. PPI3K, Diff; $p < 0.0001$). However, in contrast to macrophages, $CD11c^+$ cells presented a heterogenous spatial distribution towards Braf-driven $CK18^+$ cells, having a distance ranging between 0.00 µm and 326.56 µm, and only 22.3% of the cDCs were detected in direct contact with the metaplastic cells. Since macrophages and cDCs were reported to synergistically infiltrate the tumor and to share similar tissue distributions and locations (Bonnardel et al., 2017; Guiducci et al., 2005), we also verified the intercellular communication between these two IIC

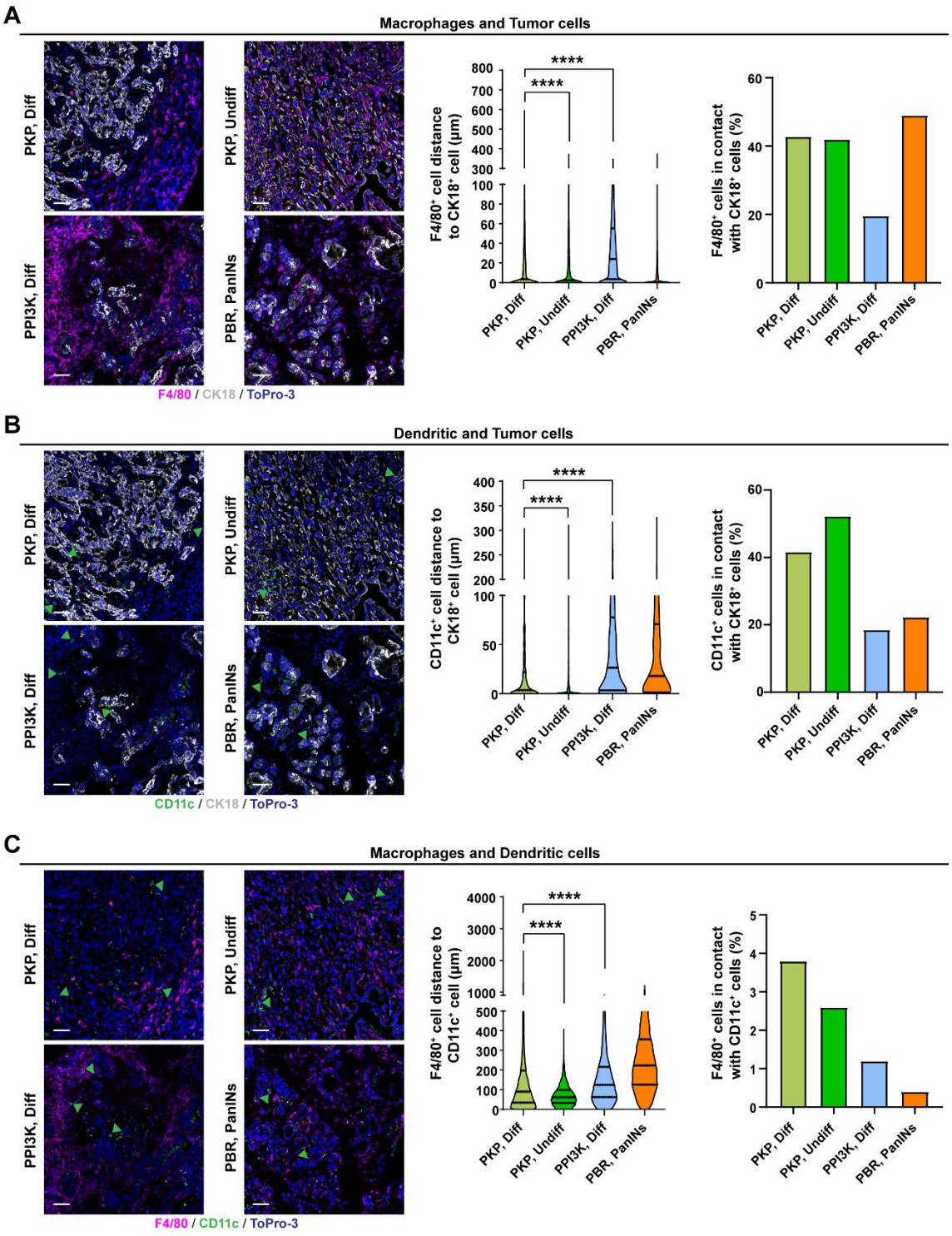

Fig. 17. Innate immune cells are in closer proximity to Kras-driven tumor cells.
(A) Left, representative images of F4/80 and keratin 18 (CK18) staining in Kras, Pik3ca, and Braf tissues. Middle, shortest distance between F4/80$^+$ and CK18$^+$ cells. PKP, Diff: minimum 0.0 µm, median 3.5 µm, maximum 598.5 µm, mean 23.8 µm, standard deviation (SD) 47.2 µm, standard error of mean (SEM) 0.5 µm. PKP, Undiff: minimum 0.0 µm, median 2.4 µm, maximum 376.0 µm, mean 21.4 µm, SD 37.0 µm, SEM 0.3 µm. PPI3K, Diff: minimum 0.0 µm, median 24.1 µm, maximum 350.6 µm, mean 37.3 µm, SD 42.7 µm, SEM 0.2 µm. PBR, PanINs: minimum 0.0 µm, median 0.4 µm, maximum 376.9 µm, mean 18.0 µm, SD 47.6 µm, SEM 0.3 µm. Right, the percentage of F4/80$^+$ cells in contact with CK18$^+$ cells according to the driver mutation and differentiation status.
(B) Left, representative images of cluster of differentiation (CD)11c and CK18 staining in Kras, Pik3ca, and Braf tissues; the green arrowheads indicate CD11c$^+$ cells. Middle, shortest distance between CD11c$^+$ and CK18$^+$ cells. PKP, Diff: minimum 0.0 µm, median 3.6 µm, maximum 304.7 µm, mean 21.9 µm, SD 43.2 µm,

(legend continues on the next page)

populations. As showed in Fig. 17C, even though macrophages and cDCs were observed in the same field of view, only up to ~4.0% of F4/80$^+$ cells interacted with CD11c$^+$ cells in PKP differentiated tumors. Thus, the IICs appeared to have a higher degree of cell-to-cell contact with Kras-driven tumor cells, which may correlate with the balance between pro-tumorigenic and anti-tumorigenic properties of these immune cells.

We further characterized the intercellular communications between AICs and cancer cells (Fig. 18). In addition to having the highest amount of infiltrated T lymphocytes, the PPI3K cohort also presented a significant shortest distance between these AICs and the malignant cells compared with Kras differentiated tumors (median of 18.1 µm and 33.6 µm vs. PKP, Diff; $p < 0.0001$), as depicted in Fig. 18A. Surprisingly, the Pik3ca-driven tumors did not present a higher percentage of T cells in direct contact with malignant cells. In fact, all three analyzed cohorts showed a similar percentage (~18.0%) of CD3$^+$-CK18$^+$ cell interactions. In addition, T cells in the PKP undifferentiated tumors were 1.7-fold closer to malignant cells compared to differentiated tumors from the same cohort, presenting a similar distance distribution as the PPI3K tissues. Regarding the B lymphocytes, these cells presented a higher number of intercellular interactions with tumor cells than the T lymphocytes, especially in the differentiated tissues (Fig. 18B). In contrast, the Kras undifferentiated tumors showed a similar interaction pattern of B and tumor cells as the T cells (~18.0% of CD3$^+$ and CD45R/B220$^+$ cells were in direct contact with CK18$^+$ cells). Since in hepatocellular carcinoma, the cross-talk between T and B lymphocytes showed to have a role in promoting the progression of the tumors (Garnelo et al., 2017), we assessed the interactions of these two AIC populations in PDAC. Our results showed that both differentiated and undifferentiated Kras tumors presented a low percentage of cell-to-cell

SEM 2.1 µm. PKP, Undiff: minimum 0.0 µm, median 0.0 µm, maximum 311.9 µm, mean 11.6 µm, SD 29.4 µm, SEM 0.8 µm. PPI3K, Diff: minimum 0.0 µm, median 26.4 µm, maximum 318.3 µm, mean 49.3 µm, SD 57.5 µm, SEM 1.6 µm. PBR, PanINs: minimum 0.0 µm, median 17.9 µm, maximum 326.6 µm, mean 41.5 µm, SD 51.3 µm, SEM 3.6 µm. Right, the percentage of CD11c$^+$ cells in contact with CK18$^+$ cells according to the driver mutation and differentiation status.

(C) Left, representative images of F4/80 and CD11c staining in Kras, Pik3ca, and Braf tissues; the green arrowheads indicate CD11c$^+$ cells. Middle, shortest distance between F4/80$^+$ and CD11c$^+$ cells. PKP, Diff: minimum 0.0 µm, median 90.2 µm, maximum 2315.3 µm, mean 178.6 µm, SD 245.8 µm, SEM 2.0 µm. PKP, Undiff: minimum 0.0 µm, median 61.9 µm, maximum 411.5 µm, mean 71.2 µm, SD 52.4 µm, SEM 0.5 µm. PPI3K, Diff: minimum 0.0 µm, median 125.2 µm, maximum 934.2 µm, mean 161.2 µm, SD 136.4 µm, SEM 0.6 µm. PBR, PanINs: minimum 0.0 µm, median 223.5 µm, maximum 1223.2 µm, mean 265.6 µm, SD 190.1 µm, SEM 1.2 µm. Right, the percentage of F4/80$^+$ cells in contact with CD11c$^+$ cells according to the driver mutation and differentiation status.

Multiplex immunohistochemistry staining was also carried out using the remaining mice of each cohort with similar results. All scale bars indicate 50 µm. Animals used for this analysis were generated and sacrificed by all the members in the laboratory of Prof. Dr. med. Dieter Saur. n=4 biologically independent animals were examined in the each Kras and Pik3ca groups, while n=3 biologically independent animals were analyzed in the Braf cohort. Data represent shortest distance in µm between two indicated cell populations and the dashed lines of the violin plots indicate the median and the doted lines the quartiles; for the calculation of the cell pairs in direct contact, only the pairs with a 0.00 µm of distance were considered. ****$p < 0.0001$, two-tailed Student's unpaired t test between selected pair groups. % denotes the percentage, µm the micrometer, CD the cluster of differentiation, CK18 the keratin 18, Diff the differentiated tumor, PanIN the pancreatic intraepithelial neoplasia, PBR the *Pdx1-CreER^{T2}; LSL-Braf$^{V637E/+}$* mice, PKP the *Pdx1-Cre; LSL-Kras$^{G12D/+}$; Trp53$^{lox/+}$* mice, PPI3K the *Pdx1-Cre; LSL-Pik3ca$^{H1047R/+}$* mice, SD the standard deviation, SEM the standard error of mean, Undiff the undifferentiated tumor, + the positive or high expression.

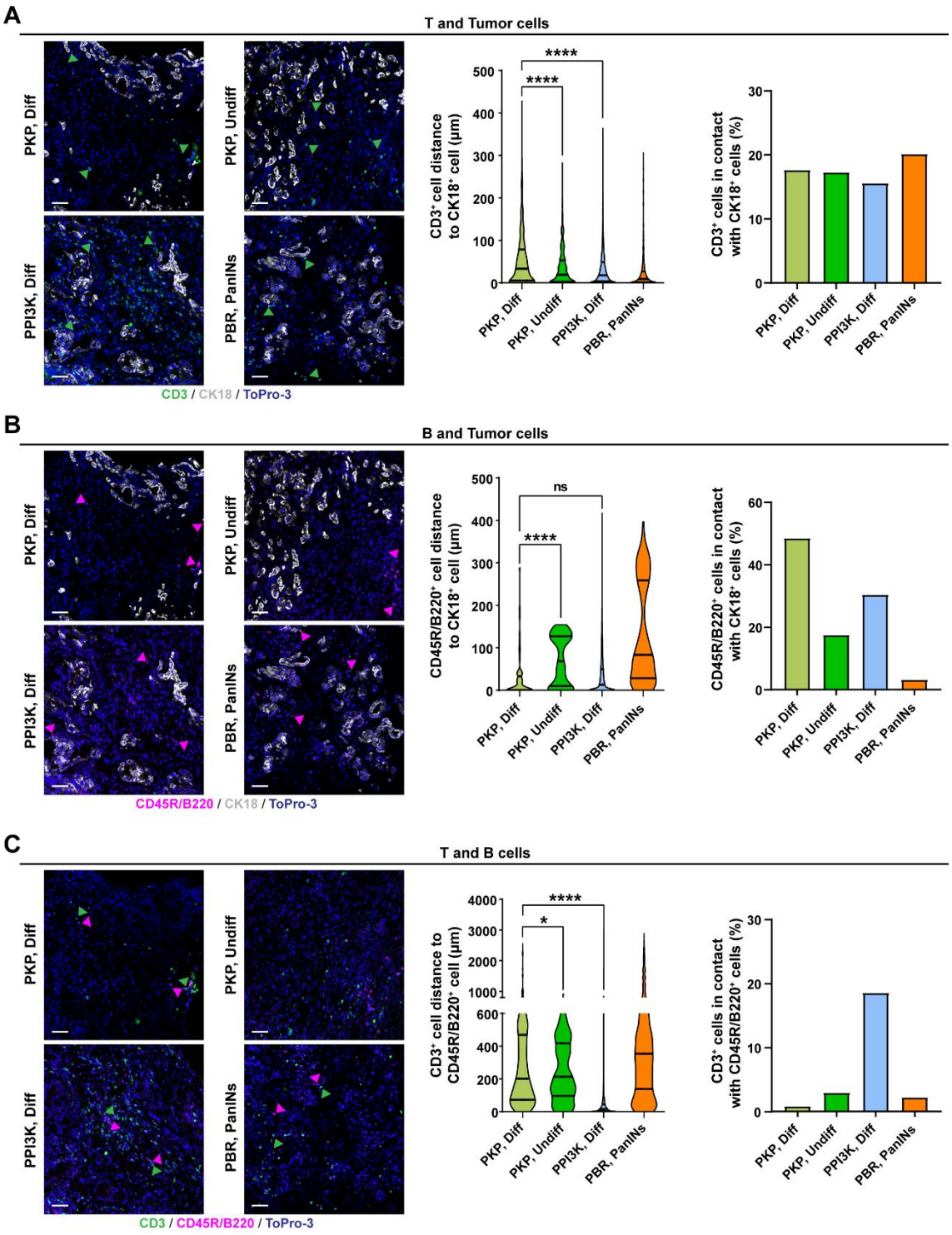

Fig. 18. Adaptive immune cells present more interactions with differentiated tumor cells.
(A) Left, representative images of cluster of differentiation (CD)3 and keratin 18 (CK18) staining in Kras, Pik3ca, and Braf tissues; the green arrowheads indicate $CD3^+$ cells. Middle, shortest distance between $CD3^+$ and $CK18^+$ cells. PKP, Diff: minimum 0.0 µm, median 33.6 µm, maximum 430.3 µm, mean 53.3 µm, standard deviation (SD) 60.5 µm, standard error of mean (SEM) 2.5 µm. PKP, Undiff: minimum 0.0 µm, median 19.4 µm, maximum 283.9 µm, mean 35.0 µm, SD 40.6 µm, SEM 1.4 µm. PPI3K, Diff: minimum 0.0 µm, median 18.1 µm, maximum 365.4 µm, mean 34.3 µm, SD 43.6 µm, SEM 0.3 µm. PBR, PanINs: minimum 0.0 µm, median 9.4 µm, maximum 308.2 µm, mean 27.2 µm, SD 49.9 µm, SEM 0.8 µm. Right, the percentage of $CD3^+$ cells in contact with $CK18^+$ cells according to the driver mutation and differentiation status.
(B) Left, representative images of CD45R/B220 and CK18 staining in Kras, Pik3ca, and Braf tissues; the magenta arrowheads indicate $CD45R/B220^+$ cells. Middle, shortest distance between $CD45R/B220^+$ and

(legend continues on the next page)

interactions (up to 3.0%) and a median shortest distance between T and B cells of ~200 µm (Fig. 18C). In contrast, the PPI3K cohort presented a closer communication between these lymphocytes (median of 16.0 µm and 201.6 µm vs. PKP, Diff; $p < 0.0001$) as well as 21 times more T cells in direct contact with B lymphocytes in comparison to PKP differentiated tumors. Thus, the cross-talk between T and B lymphocytes may be influenced by the driver mutation harbored by the tumor cells.

Although the T cell abundance in the TME of PDAC may vary, previous studies described that PDAC immunity predominantly comprises of heterogenous infiltrated T lymphocyte populations and their spatial proximity towards the cancer cells is reported to be correlated with overall patient survival (Carstens et al., 2017; Knudsen et al., 2017). In this regard, differential immune cell infiltration as well as their spatial distribution could be reflective of distinct immunosuppressive or immunostimulatory roles within the tumor. We examined the intercellular communications between CTLs, Th cells, and Tregs and the tumor cells and the interactions between the T cell subpopulations (Fig. 19). All the T cell subtypes showed to be in significantly closer proximity to Kras tumor cells than to Pik3ca-driven ones, as depicted in Fig. 19A-C. In addition, PKP differentiated tumors also presented the highest number of interactions between tumor cells and T cell subpopulations, especially with $CD8a^+$ cells (87.0% and 6.6% vs. PPI3K, Diff). Moreover, the increased percentages of CTLs, Th cells, and Tregs interacting with metaplastic cells in the Braf tissues (48.8%, 37.7%, and 43.2%, respectively) may indicate a crucial role of these three lymphocytic populations in mediating tumor growth control in Braf

$CK18^+$ cells. PKP, Diff: minimum 0.0 µm, median 0.6 µm, maximum 289.1 µm, mean 26.4 µm, SD 51.0 µm, SEM 6.0 µm. PKP, Undiff: minimum 0.0 µm, median 68.5 µm, maximum 154.8 µm, mean 71.7 µm, SD 57.4 µm, SEM 3.9 µm. PPI3K, Diff: minimum 0.0 µm, median 13.3 µm, maximum 418.4 µm, mean 33.6 µm, SD 46.3 µm, SEM 0.4 µm. PBR, PanINs: minimum 0.0 µm, median 83.7 µm, maximum 397.4 µm, mean 134.3 µm, SD 117.3 µm, SEM 8.0 µm. Right, the percentage of $CD45R/B220^+$ cells in contact with $CK18^+$ cells according to the driver mutation and differentiation status.

(C) Left, representative images of CD3 and CD45R/B220 staining in Kras, Pik3ca, and Braf tissues; the green arrowheads indicate $CD3^+$ cells, while the magenta ones shortest distance between $CD3^+$ and $CD45R/B220^+$ cells. PKP, Diff: minimum 0.0 µm, median 201.6 µm, maximum 2573.5 µm, mean 307.4 µm, SD 334.1 µm, SEM 14.1 µm. PKP, Undiff: minimum 0.0 µm, median 213.9 µm, maximum 916.3 µm, mean 249.1 µm, SD 184.4 µm, SEM 12.9 µm. PPI3K, Diff: minimum 0.0 µm, median 16.0 µm, maximum 857.4 µm, mean 34.1 µm, SD 48.4 µm, SEM 0.3 µm. PBR, PanINs: minimum 0.0 µm, median 354.0 µm, maximum 2901.8 µm, mean 515.3 µm, SD 542.7 µm, SEM 8.6 µm. Right, the percentage of $CD3^+$ cells in contact with $CD45R/B220^+$ cells according to the driver mutation and differentiation status.

Multiplex immunohistochemistry staining was also carried out using the remaining mice of each cohort with similar results. All scale bars indicate 50 µm. Animals used for this analysis were generated and sacrificed by all the members in the laboratory of Prof. Dr. med. Dieter Saur. n=4 biologically independent animals were examined in the each Kras and Pik3ca groups, while n=3 biologically independent animals were analyzed in the Braf cohort. Data represent shortest distance in µm between two indicated cell populations and the dashed lines of the violin plots indicate the median and the doted lines the quartiles; for the calculation of the cell pairs in direct contact, only the pairs with a 0.00 µm of distance were considered. ns denotes not significant, $*p < 0.05$, $****p < 0.0001$, two-tailed Student's unpaired t test between selected pair groups. % denotes the percentage, µm the micrometer, CD the cluster of differentiation, CK18 the keratin 18, Diff the differentiated tumor, PanIN the pancreatic intraepithelial neoplasia, PBR the *Pdx1-CreER^{T2}; LSL-Braf$^{V637E/+}$* mice, PKP the *Pdx1-Cre; LSL-Kras$^{G12D/+}$; Trp53$^{lox/+}$* mice, PPI3K the *Pdx1-Cre; LSL-Pik3ca$^{H1047R/+}$* mice, SD the standard deviation, SEM the standard error of mean, Undiff the undifferentiated tumor, + the positive or high expression.

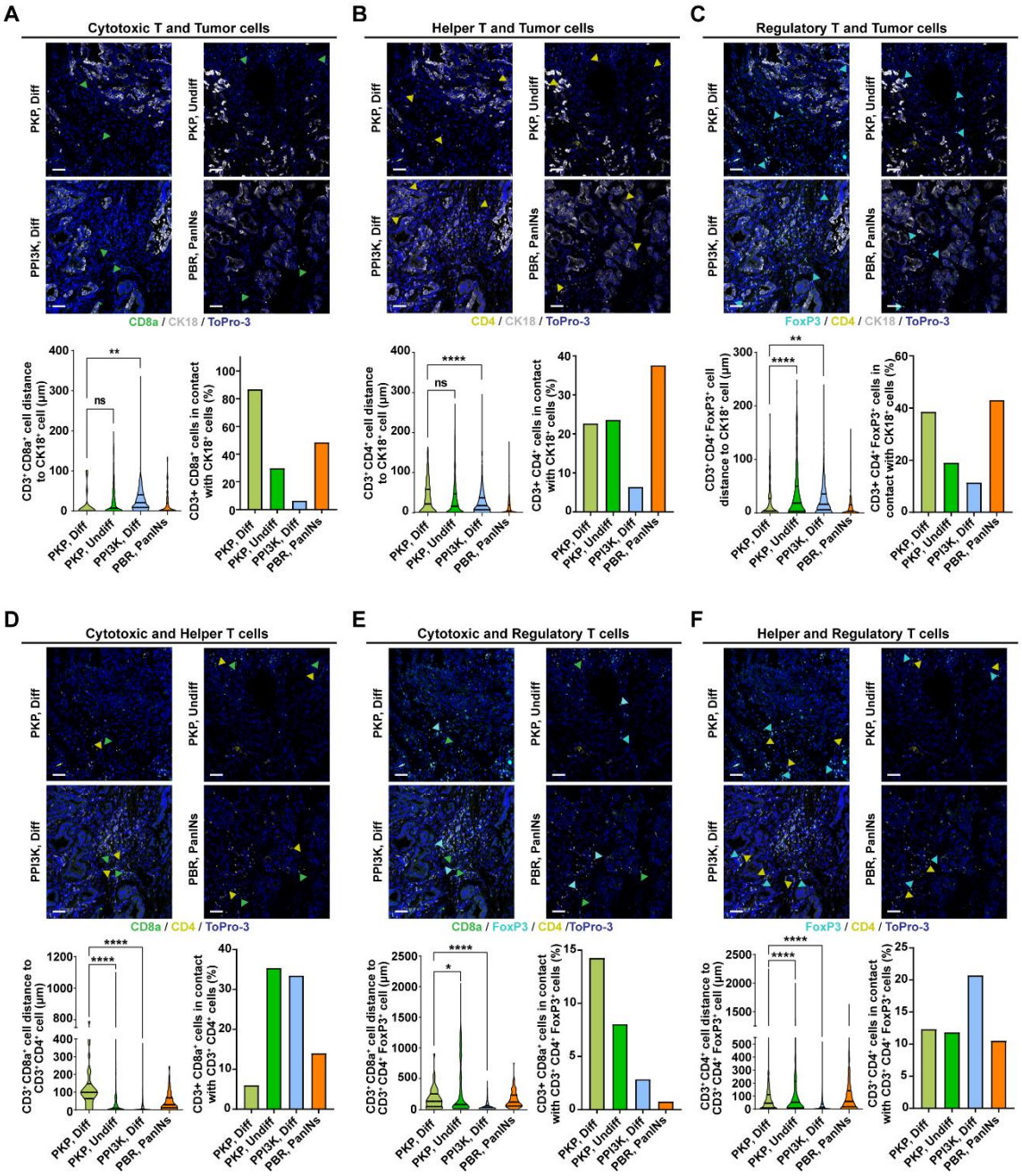

Fig. 19. T cell populations are in closer proximity to Kras tumor cells and Braf metaplastic cells.
(A) Top, representative images of cluster of differentiation (CD)8a and keratin 18 (CK18) staining in Kras, Pik3ca, and Braf tissues; the green arrowheads indicate $CD8a^+$ cells. Bottom left, shortest distance between $CD8a^+$ and $CK18^+$ cells. PKP, Diff: minimum 0.0 µm, median 0.0 µm, maximum 101.3 µm, mean 10.8 µm, standard deviation (SD) 29.6 µm, standard error of mean (SEM) 6.2 µm. PKP, Undiff: minimum 0.0 µm, median 6.8 µm, maximum 197.6 µm, mean 23.8 µm, SD 35.3 µm, SEM 1.4 µm. PPI3K, Diff: minimum 0.0 µm, median 20.5 µm, maximum 336.3 µm, mean 27.1 µm, SD 24.8 µm, SEM 0.3 µm. PBR, PanINs: minimum 0.0 µm, median 0.7 µm, maximum 134.8 µm, mean 16.0 µm, SD 28.3 µm, SEM 2.5 µm. Bottom right, the percentage of $CD8a^+$ cells in contact with $CK18^+$ cells according to the driver mutation and differentiation status.
(B) Top, representative images of CD4 and CK18 staining in Kras, Pik3ca, and Braf tissues; the yellow arrowheads indicate $CD4^+$ cells. Bottom left, shortest distance between $CD4^+$ and $CK18^+$ cells. PKP, Diff: minimum 0.0 µm, median 22.1 µm, maximum 164.6 µm, mean 35.4 µm, SD 38.9 µm, SEM 2.0 µm. PKP, Undiff: minimum 0.0 µm, median 16.6 µm, maximum 272.6 µm, mean 34.1 µm, SD 45.7 µm, SEM 1.2 µm. PPI3K, Diff: minimum 0.0 µm, median 18.1 µm, maximum 296.9 µm, mean 26.2 µm, SD 27.6 µm, SEM 0.3 µm. PBR, PanINs: minimum 0.0 µm, median 4.1 µm, maximum 178.5 µm, mean 13.8 µm, SD 22.6 µm, SEM 0.6 µm. Bottom right, the percentage of $CD4^+$ cells in contact with $CK18^+$ cells according to the driver

(legend continues on the next page)

animals. Furthermore, among the T cell subpopulations, the highest number of direct communications was observed between CD8a$^+$ and CD4$^+$, particularly in undifferentiated PKP and differentiated PPI3K tumors (35.5% and 33.6%, respectively), as shown in Fig. 19D-F. In contrast, the CD8a$^+$ and CD4$^+$ FoxP3$^+$ cells presented the lowest percentage of interactions, especially in Pik3ca and Braf tissues (2.9% and 0.8%, respectively). It is also noteworthy to mention the ~2-fold increased number of interactions between Th cells and Tregs in Pik3ca-driven tumors compared to the rest of the groups analyzed. Altogether, these results described that the cross-talk between malignant cell and certain immune cell populations, such as macrophages, cDCs, and Tregs, appeared to be modulated by the driver mutation, while other

mutation and differentiation status.
(C) Top, representative images of CD4, FoxP3, and CK18 staining in Kras, Pik3ca, and Braf tissues; the cyan arrowheads indicate CD4$^+$ FoxP3$^+$ cells. Bottom left, shortest distance between CD4$^+$ FoxP3$^+$ and CK18$^+$ cells. PKP, Diff: minimum 0.0 µm, median 22.1 µm, maximum 164.6 µm, mean 35.4 µm, SD 38.9 µm, SEM 2.0 µm. PKP, Undiff: minimum 0.0 µm, median 16.6 µm, maximum 272.6 µm, mean 34.1 µm, SD 45.7 µm, SEM 1.2 µm. PPI3K, Diff: minimum 0.0 µm, median 18.1 µm, maximum 296.9 µm, mean 26.2 µm, SD 27.6 µm, SEM 0.3 µm. PBR, PanINs: minimum 0.0 µm, median 4.1 µm, maximum 178.5 µm, mean 13.8 µm, SD 22.6 µm, SEM 0.6 µm. Bottom right, the percentage of CD4$^+$ FoxP3$^+$ in contact with CK18$^+$ cells according to the driver mutation and differentiation status.
(D) Top, representative images of CD8a and CD4 staining in Kras, Pik3ca, and Braf tissues; the green arrowheads indicate CD8a$^+$ cells, while the yellow ones indicate CD4$^+$ cells. Bottom left, shortest distance between CD8a$^+$ and CD4$^+$ cells. PKP, Diff: minimum 0.0 µm, median 99.2 µm, maximum 790.5 µm, mean 155.6 µm, SD 182.5 µm, SEM 26.1 µm. PKP, Undiff: minimum 0.0 µm, median 8.1 µm, maximum 1103.0 µm, mean 48.3 µm, SD 117.5 µm, SEM 4.8 µm. PPI3K, Diff: minimum 0.0 µm, median 3.9 µm, maximum 377.8 µm, mean 18.1 µm, SD 31.0 µm, SEM 0.4 µm. PBR, PanINs: minimum 0.0 µm, median 29.4 µm, maximum 246.2 µm, mean 46.7 µm, SD 50.4 µm, SEM 4.4 µm. Bottom right, the percentage of CD8a$^+$ cells in contact with CD4$^+$ cells according to the driver mutation and differentiation status.
(E) Top, representative images of CD8a, CD4, and FoxP3 staining in Kras, Pik3ca, and Braf tissues; the green arrowheads indicate CD8a$^+$ cells, while the cyan ones indicate CD4$^+$ FoxP3$^+$ cells. Bottom left, shortest distance between CD8a$^+$ and CD4$^+$ FoxP3$^+$ cells. PKP, Diff: minimum 0.0 µm, median 127.1 µm, maximum 905.2 µm, mean 170.9 µm, SD 173.7 µm, SEM 24.8 µm. PKP, Undiff: minimum 0.0 µm, median 75.8 µm, maximum 2060.0 µm, mean 287.3 µm, SD 395.8 µm, SEM 16.3 µm. PPI3K, Diff: minimum 0.0 µm, median 27.7 µm, maximum 463.2 µm, mean 49.8 µm, SD 63.6 µm, SEM 0.9 µm. PBR, PanINs: minimum 0.0 µm, median 115.6 µm, maximum 758.0 µm, mean 155.1 µm, SD 134.1 µm, SEM 11.8 µm. Bottom right, the percentage of CD8a$^+$ cells in contact with CD4$^+$ FoxP3$^+$ cells according to the driver mutation and differentiation status.
(F) Top, representative images of CD4 and FoxP3 staining in Kras, Pik3ca, and Braf tissues; the yellow arrowheads indicate CD4$^+$ cells, while the cyan ones indicate CD4$^+$ FoxP3$^+$ cells. Bottom left, shortest distance between CD4$^+$ and CD4$^+$ FoxP3$^+$ cells. PKP, Diff: minimum 0.0 µm, median 45.4 µm, maximum 2255.9 µm, mean 87.6 µm, SD 154.5 µm, SEM 3.8 µm. PKP, Undiff: minimum 0.0 µm, median 52.0 µm, maximum 2007.6 µm, mean 188.8 µm, SD 316.9 µm, SEM 9.7 µm. PPI3K, Diff: minimum 0.0 µm, median 37.5 µm, maximum 520.4 µm, mean 30.8 µm, SD 50.1 µm, SEM 0.5 µm. PBR, PanINs: minimum 0.0 µm, median 59.4 µm, maximum 1637.0 µm, mean 107.3 µm, SD 146.9 µm, SEM 3.7 µm. Bottom right, the percentage of CD4$^+$ cells in contact with CD4$^+$ FoxP3$^+$ cells according to the driver mutation and differentiation status.
Multiplex immunohistochemistry staining was also carried out using the remaining mice of each cohort with similar results. All scale bars indicate 50 µm. Animals used for this analysis were generated and sacrificed by all the members in the laboratory of Prof. Dr. med. Dieter Saur. n=4 biologically independent animals were examined in the each Kras and Pik3ca groups, while n=3 biologically independent animals were analyzed in the Braf cohort. Data represent shortest distance in µm between two indicated cell populations and the dashed lines of the violin plots indicate the median and the doted lines the quartiles; for the calculation of the cell pairs in direct contact, only the pairs with a 0.00 µm of distance were considered. ns denotes not significant, *p < 0.05, ****p < 0.0001, two-tailed Student's unpaired t test between selected pair groups. % denotes the percentage, µm the micrometer, CD the cluster of differentiation, CK18 the keratin 18, Diff the differentiated tumor, PanIN the pancreatic intraepithelial neoplasia, PBR the *Pdx1-CreER^{T2}; LSL-Braf$^{V637E/+}$* mice, PKP the *Pdx1-Cre; LSL-Kras$^{G12D/+}$; Trp53$^{lox/+}$* mice, PPI3K the *Pdx1-Cre; LSL-Pik3ca$^{H1047R/+}$* mice, SD the standard deviation, SEM the standard error of mean, Undiff the undifferentiated tumor, + the positive or high expression.

inflammatory cell types, such as B cells, CTLs and Tregs, seemed to be also influenced by the differentiated status of the tissue.

6.2.5. Profile of tumor microenvironment cell distribution patterns in pancreatic ductal adenocarcinoma can be assessed using RNA sequencing bulk tumor samples

mIHC offered a good opportunity to study and characterize the cellular content within the TME in PDAC tissues and the cross-talk between the different cellular populations. Regardless of its advantages, it was clear that this imaging technique would not allow high-throughput assessment of tumor and immune profiles. For this reason, we attempted to introduce a cost-effective RNA-seq method to study immune and stromal populations in PDAC bulk tumor samples (25 PK and 6 PPI3K tumors), as depicted in Fig. 20, and compare the data generated by this sequencing technique and mIHC. Firstly, correlation matrixes based on RNA-seq bulk tumor data were performed and used to infer communication between TME and tumor cell pairs. As shown in Fig. 20A, tumor cells correlated negatively with macrophages and B cells in both PK and PPI3K samples, correlation that was also observed in the imaging data (Fig. 16). In addition, $CD8^+$ T cells correlated positively with B cells and macrophages, especially in the PPI3K cohort, however these correlations were not clear in the mIHC immune profiling data. Unexpectedly, the malignant cells presented a contrary correlation with CTLs and Th cells in Pik3ca bulk tumor samples, while the numbers of both T cell subtypes increased when a reduction of tumor cells was detected in the cryopreserved tissues analyzed. Finally, the correlations with myCAFs, such as the positive correlation between myCAFs and macrophages showed in the PK cohort, need to be further validated using a staining technique.

To systemically understand the central pathways involved in PDAC and how they may be affected by the driver mutations, we conducted KEGG pathway analysis of the differentially expressed genes. As depicted in Fig. 20B, several signaling pathways, such as gene downregulation by Kras activation, p53 pathway, and mTORC1 signaling, were showed to be altered, and they were previously reported to be related to $p110^{H1047R}$ expression in pancreas (Eser et al., 2013; Payne et al., 2015). Surprisingly, we did not detect a significant increase of inflammation-related pathways in the PPI3K samples as observed in the imaging data, indicating that some signalings can be diluted in the RNA-seq data, due to the cellular abundance and variety present in bulk tumors (Shen-Orr & Gaujoux, 2013). Regardless of this limitation of the sequencing technique, we next sought to determine the expression pattern of the genes that were differentially expressed between the PK and PPI3K cohorts (Fig. 20C). Our analysis identified 57 differently expressed genes and some of them were already described to be TME-related genes. *Hmga2*, *Fbln2*, and *Ankrd1* were amongst the genes that were expressed at higher levels in the PK compared to PPI3K bulk tumors (Table 30). Conversely, *Lcn2*, *Cxcl5*, *Ccl20*, *Serpina9*, *Fcgbp*, and *Iyd* were found to be highly expressed in the PPI3K cohort compared to PK bulk tumors. The expression of a higher number of inflammation-related genes in the Pik3ca cohort may suggest that the tissues harboring this mutation have a more inflammatory environment compared to the ones from the Kras cohort.

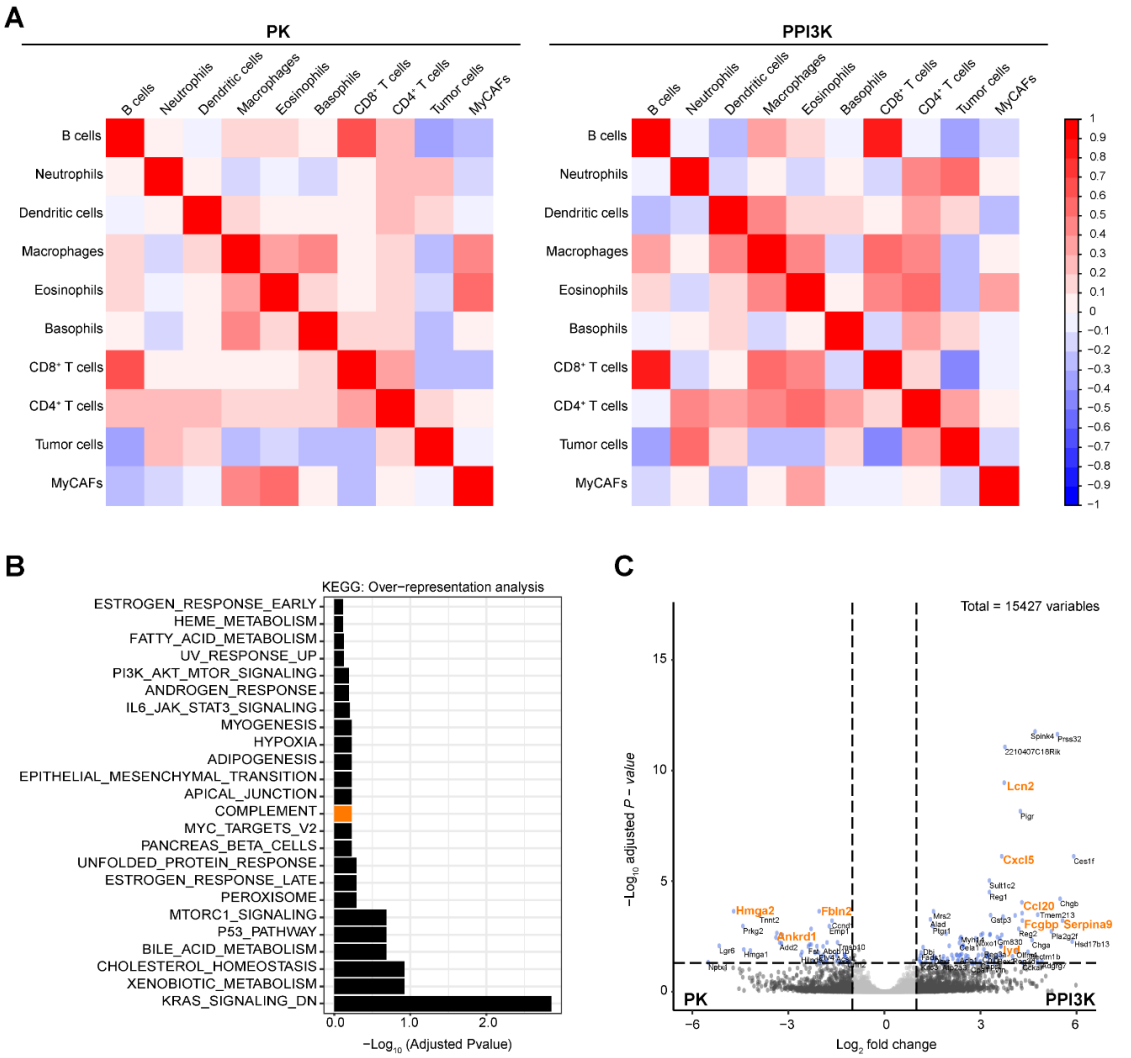

Fig. 20. PPI3K tumors present stronger immune cell interactions based on RNA sequencing bulk tumor samples.

(A) Left, correlation matrix of *Pdx1-Cre; LSL-Kras*$^{G12D/+}$ (PK) cohort and right, correlation matrix of *Pdx1-Cre; LSL-Pik3ca*$^{H1047R/+}$ (PPI3K) samples based on gene signatures defined in Table 17. Red represents positive correlation, blue represents negative ones and darker the color, stronger the correlation.

(B) Kyoto Encyclopedia of Genes and Genomes (KEGG) over-representation analysis of signaling pathways based on differentially expressed genes in PPI3K compared to PK bulk tumors, highlighted in orange the immune-related Complement pathway.

(C) Volcano plot, where the tumor microenvironment-related genes were highlighted in orange.

These bioinformatic analyses were performed by Fabio Boniolo and animals used for these analyses were generated and sacrificed by all the members in the laboratory of Prof. Dr. med. Dieter Saur. n=25 biologically independent PK animals and n=6 biologically independent PPI3K animals were used in these bioinformatic analyses. KEGG denotes Kyoto Encyclopedia of Genes and Genomes, myCAF the myofibroblastic cancer-associated fibroblast, PK the *Pdx1-Cre; LSL-Kras*$^{G12D/+}$ mice, PPI3K the *Pdx1-Cre; LSL-Pik3ca*$^{H1047R/+}$ mice, + the positive or high expression.

Table 30. Tumor microenvironment-related genes upregulated in Kras and Pik3ca cohorts and their potential role within the tumor

Cohort	Upregulated gene	TME-related role	Ref
PK	*Hmga2*	Hmga2 status in tumor cells significantly correlates with abundance of PDGFRβ-defined stromal cells	(Strell et al., 2017)
	Fbln2	Fibulin 2 molecules might induce the metastatic potential through interaction with other molecules present in the TME on lung cancer	(Avsar et al., 2019)
	Ankrd1	Ankrd1 modulates inflammatory responses in myoblasts through feedback inhibition of NF-κB signaling activity	(Liu et al., 2015)
PPI3K	*Lcn2*	Macrophage-derived lipocalin-2 transports iron in the TME and enhances tumor cell proliferation	(Mertens et al., 2018)
	Cxcl5	CXCL5 binds to its receptors (e.g., CXCR2) to recruit immune cells and promote angiogenesis, tumor growth, and metastasis	(W. Zhang et al., 2020)
	Ccl20	Ccl20 signaling from tumor cells or macrophages mediates Tregs infiltration into TME	(W. Chen et al., 2020)
	Serpina9	$CD20^+$ B cells produce high levels of Serpina9, which directly inhibits the growth of NSCLC cells	(J. Chen et al., 2020)
	Fcgbp	Enriched gene in $CD8^+$ T cells, associated with disease progression in tissues of endodermal origin and metastasis formation in CRC	(Lyons et al., 2017; Qi et al., 2016; Stamp et al., 2012)
	Iyd	Candidate protein regulator of immune trafficking	(Qi et al., 2016)

CCL, chemokine ligand; CD, cluster of differentiation; CRC, colorectal cancer; CXCL, chemokine (C-X-C motif) ligand; CXCR, chemokine (C-X-C motif) receptor; NF-κB, nuclear factor kappa-light-chain-enhancer of activated B cells; NSCLC, non-small-cell lung carcinoma; PDGFRβ, platelet-derived growth factor receptor beta; PK, *Pdx1-Cre; LSL-Kras$^{G12D/+}$* mice; PPI3K, *Pdx1-Cre; LSL-Pik3ca$^{H1047R/+}$* mice; TME, tumor microenvironment; Treg, T regulatory cell; +, positive or high expression.

6.3. Chapter II: *Cdh1 deletion does not induce overt epithelial-to-mesenchymal transition*

E-cadherin, encoded by *Cdh1*, is an adhesion protein of the AJs that interacts with cytoplasmic catenin proteins (e.g., β-catenin) to support regulation of functional characteristics and integrity of epithelia (Apte & Wilson, 2005; Huber et al., 2001). Under physiological conditions, the regulation of the cadherin-mediated cell-cell adhesion ensures homeostasis and maintenance of the epithelial tissue, while its deregulation is associated with carcinogenesis in the presence of an oncogene and posterior metastases formation (Kaneta et al., 2020; Serrill et al., 2018). In pathological conditions, E-cadherin is one of the most studied proteins as a marker of morphological changes, such as EMT, a process whereby epithelial cells downregulate the expression of epithelial markers (e.g., E-cadherin and cytokeratin) and upregulate the expression of mesenchymal proteins (e.g., N-cadherin and vimentin) (Zhou et al., 2017). EMT is triggered by the activation of transcription factors, such as Snail, Slug and ZEB1/2, which in turn repress E-cadherin expression. Furthermore, dynamic regulation of E-cadherin is essential for collective cell migration during tumor dissemination and invasion (Cai et al., 2014; Shamir et al., 2014), conferring an advantage in survival compared to an individual cell and contributing hence to the metastatic spread. With regard to pancreatic cancer, reduction or loss of E-cadherin expression has been observed in up to 60% of human PDAC samples, especially in undifferentiated tumors (von Burstin et al., 2009). This suggests that the reduction of cell-cell adhesion mediated by E-cadherin loss promotes tumor progression and invasiveness. However, there is little evidence that cancers undergo morphological changes due to *Cdh1* loss and the precise functional impact of this loss in EMT induction and PDAC progression remains to be determined. In this study, we investigated the contributions of E-cadherin in pancreas tumorigenesis using pancreas-specific *Cdh1*-KO GEMMs and *in vitro* models and explored the metastatic potential mediated by the loss of this epithelial protein. Breedings, mice dissection, and establishment of primary murine PCCs from *Cdh1* mice were done in part by Dr. Kathleen Schuck and the generated data was adapted to the work described in this section. The control animals and cell lines used for comparison were generated, breed and sacrificed by all members of the laboratory of Prof. Dr. med. Dieter Saur.

6.3.1. Conditional inactivation of *Cdh1* reduced the survival time of *Cdh1* animals and increased the incidence of cystic tumors compared to control mice

To elucidate the effects of *Cdh1* loss on pancreatic tumorigenesis, we generated and characterized a conditional *Cdh1* deletion mouse model as well as the primary murine PCCs established from the tumor mice, as depicted in Fig. 21. We employed conditional *Cdh1* gene inactivation regulated through *Cre/loxP*-based recombination system expression (Derksen et al., 2006) and crossed the resulting $Cdh1^{fl}$ animals with *Pdx1-Cre* transgenic mice, which expressed Cre recombinase (Fig. 21A). In addition, the resulting *Pdx1-Cre;* $Cdh1^{fl}$ animals were then crossed with *LSL-*$Kras^{G12D/+}$*; LSL-*$Trp53^{R172H/+}$ mice, resulting in a GEMM with conditional deletion of *Cdh1* in pancreatic tissue upon Cre activation at early embryonic stages of development. As illustrated

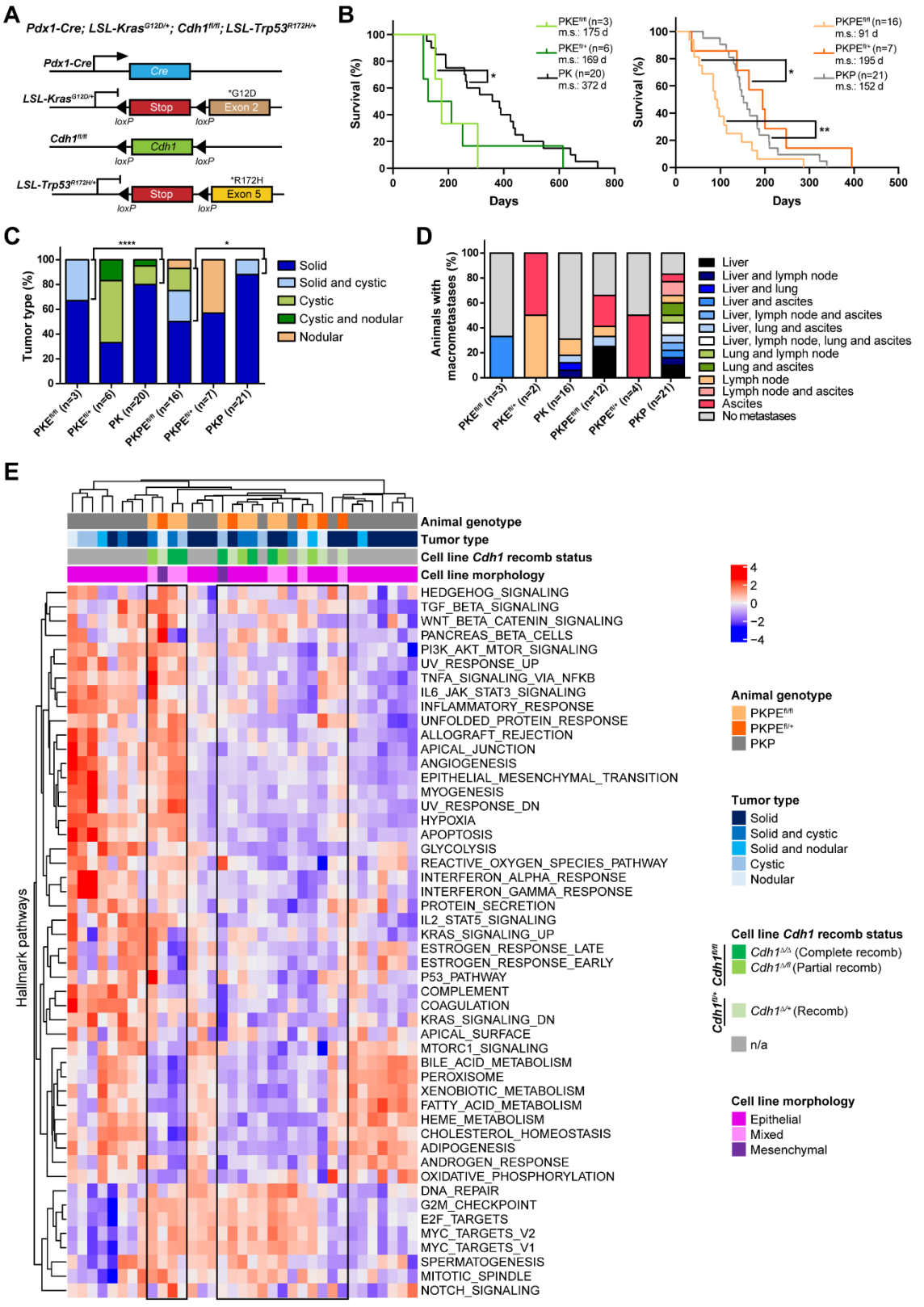

Fig. 21. Conditional *Cdh1* deletion shortens the mice lifespan, increases the incidence of cystic tumors, and upregulates proliferation-related signaling pathways.
(A) Genetic scheme of *Pdx1-Cre; LSL-Kras$^{G12D/+}$; Cdh1$^{fl/fl}$; LSL-Trp53$^{R172H/+}$* genetically engineered mouse model to study the role of *Cdh1* loss.
(B) Left, Kaplan-Meier survival analysis of the following genotypes: PKE$^{fl/fl}$ – *Pdx1-Cre; LSL-Kras$^{G12D/+}$; Cdh1$^{fl/fl}$*, PKE$^{fl/+}$ – *Pdx1-Cre; LSL-Kras$^{G12D/+}$; Cdh1$^{fl/+}$*, PK – *Pdx1-Cre; LSL-Kras$^{G12D/+}$*. Right, Kaplan-Meier
(legend continues on the next page)

in Fig. 21B, the homozygous deletion of *Cdh1*, with and without mutant *Trp53*, significantly reduced the survival of these animals compared to the respective control mice. *Pdx1-Cre; LSL-Kras$^{G12D/+}$; Cdh1$^{fl/fl}$* (PKE$^{fl/fl}$) animals showed a median survival of 175 days in comparison to *Pdx1-Cre; LSL-Kras$^{G12D/+}$* (PK) mice that lived 372 days ($p < 0.05$). The additional *LSL-Trp53$^{R172H/+}$* allele in mice with homozygous *Cdh1* (PKPE$^{fl/fl}$) shortened the survival to 91 days, ~2-fold less the median survival time of the *Pdx1-Cre; LSL-Kras$^{G12D/+}$; LSL-Trp53$^{R172H/+}$* (PKP) mice (152 days; $p < 0.01$). Interestingly, the PKPE$^{fl/+}$ mice presented a similar median survival to the PKP animals (195 days vs. 152 days, respectively), a survival restorage that was not observed in the heterozygous animals without the *Trp53* allele. Furthermore, we macroscopically analyzed the tumors formed by PKE and PKPE mice as well as by the respective control animals (PK and PKP cohorts) (Fig. 21C). Even though solid tumors were the most prominent tumor type among the analyzed animals, it was curious to observe a higher frequency of cystic tumors in animals with homozygous deletion of *Cdh1* comparing to the control mice. This incidence of cystic tumors was particularly notable between PKPE$^{fl/fl}$ and PKP murines, with an ~4-fold increase of this tumor type in the animals with *Cdh1* loss (43.8% and 9.5%, respectively; $p < 0.05$). Regarding the macrometastases observed in the animals, no clear metastatic pattern seemed to be favored by the KO of *Cdh1 in vivo* (Fig. 21D). However, an overall analysis of the metastatic potential of the animals that loss *Cdh1* showed a preference to metastasize the liver and lymph nodes. In addition, it was interesting to notice a high incidence of ascites formation among this GEMM with an average of 41.7% of PKE and PKPE animals presenting accumulation of peritoneal fluid

survival analysis of the following genotypes: PKPE$^{fl/fl}$ – *Pdx1-Cre; LSL-Kras$^{G12D/+}$; LSL-Trp53$^{R172H/+}$*; *Cdh1$^{fl/fl}$*, PKPE$^{fl/+}$ – *Pdx1-Cre; LSL-Kras$^{G12D/+}$; LSL-Trp53$^{R172H/+}$*; *Cdh1$^{fl/+}$*, PKP – *Pdx1-Cre; LSL-Kras$^{G12D/+}$; LSL-Trp53$^{R172H/+}$*. Number of animals analyzed is indicated after each genotype and only tumor mice were plotted. *$p < 0.05$; **$p < 0.01$, log-rank (Mantel-Cox) test.

(C) Tumor type developed by PKE$^{fl/fl}$, PKE$^{fl/+}$, PKPE$^{fl/fl}$ and PKPE$^{fl/+}$ animals as well as by PK and PKP control mice. Data represents percentage of tumor type and respective n mice analyzed per genotype is indicated in the graph. *$p < 0.05$, ****$p < 0.0001$, Chi-square test with 95% of confidence interval.

(D) Metastatic potential of PKE-, PKPE-, PK- and PKP-mice bearing solid pancreatic tumors based on macroscopic observation. Data represents percentage of secondary tumor location and respective n mice analyzed per genotype is indicated in the graph.

(E) Unsupervised clustering heatmap illustrating the single-sample gene set enrichment analysis (ssGSEA) hallmark pathway score of PKPE- and epithelial PKP-driven cell lines. *Cdh1* cell lines are emphasized based on the animal genotype (PKPE$^{fl/fl}$ or PKPE$^{fl/+}$) and *Cdh1* recombination status (Complete or Partial recombined for *Cdh1$^{fl/fl}$* cell lines and Recombined for *Cdh1$^{fl/+}$* ones). Tumor type (solid, solid and cystic, solid and nodular, cystic and nodular) and morphology of the cell lines (Epithelial, Mixed or Mesenchymal) are also annotated. The color code of the annotated characteristics is explained in the legend on the right side of the heatmap. The ssGSEA analysis was performed by Fabio Boniolo. n=9 biologically independent PKPE$^{fl/fl}$ animals, n=5 biologically independent PKPE$^{fl/+}$ mice and n=21 biologically independent PKP animals were used in this bioinformatic analysis.

Animals used for these analyses were generated and sacrificed and cell lines were established by all members of the laboratory of Prof. Dr. med. Dieter Saur. % denotes the percentage, d the day, fl the conditional allele with the *loxP* sites, m.s. the median survival in days, n/a the not applicable, PKE$^{fl/fl}$ the *Pdx1-Cre; LSL-Kras$^{G12D/+}$; Cdh1$^{fl/fl}$* mice, PKE$^{fl/+}$ the *Pdx1-Cre; LSL-Kras$^{G12D/+}$; Cdh1$^{fl/+}$* mice, PK the *Pdx1-Cre; LSL-Kras$^{G12D/+}$* mice, PKPE$^{fl/fl}$ the *Pdx1-Cre; LSL-Kras$^{G12D/+}$; LSL-Trp53$^{R172H/+}$; Cdh1$^{fl/fl}$* mice, PKPE$^{fl/+}$ the *Pdx1-Cre; LSL-Kras$^{G12D/+}$; LSL-Trp53$^{R172H/+}$; Cdh1$^{fl/+}$* mice, PKP the *Pdx1-Cre; LSL-Kras$^{G12D/+}$; LSL-Trp53$^{R172H/+}$* mice, recomb the recombination, ssGSEA the single-sample gene set enrichment analysis, Δ the recombined allele, + the wild-type allele.

(29.3% vs. PK and PKP animals), which is a source of CTCs (Peterson et al., 2013; Y. Zhang, J. Zhao, et al., 2020). Moreover, to study *Cdh1* loss *in vitro* and assess the signaling pathways that may be affected by the deletion of this epithelial gene, we successfully established PCCs from PKPE mice. As annotated in Fig. 21E, 55.6% of the PCCs generated from PKPE$^{fl/fl}$ animals presented complete recombination of *Cdh1* alleles (*Cdh1*$^{\Delta/\Delta}$), assessed by PCR, whilst the remaining cell lines retained a floxed allele being designated by partially recombined (*Cdh1*$^{\Delta/fl}$). Furthermore, the *Cdh1*$^{\Delta/\Delta}$ PCCs did not exhibit a more mesenchymal morphology compared with both *Cdh1*$^{\Delta/fl}$ and *Cdh1*$^{\Delta/+}$ malignant cells, suggesting that the inactivation of this gene alone may not drive EMT. We performed the ssGSEA on the PKPE cell lines using the hallmark gene sets from the Molecular MSigDB Collections (Liberzon et al., 2015) and compared these samples with epithelial cells established from PKP mice, as illustrated in Fig. 21E. Regardless of their recombination status, the *Cdh1* PCCs were mainly distributed in two clusters in the heatmap separated by three distinct subgroups of PKP samples: cluster 1 composed by PKP cells (on the left side of the heatmap), cluster 2 comprised by 4 PKPE cell lines (3 with a mixed morphology and 1 with mesenchymal features), cluster 3 containing 3 PKP samples, cluster 4 comprising the remaining 10 *Cdh1* cell lines and including all the *Cdh1* cells with an epithelial morphology, and finally cluster 5 composed by PKP cells (on the right side of the heatmap). The *Cdh1* clusters were especially distinct because, the majority of the *Cdh1* PCCs from cluster 4 as well as the PKP cells from the clusters 3 and 5 presented downregulation of pathways related to inflammation (e.g. inflammatory response, interferon alpha and gamma responses, and complement), EMT and apical junction, and apoptosis, while these signaling pathways were upregulated in the *Cdh1* cells from cluster 2 and the PKP cells composing the cluster 1. Nevertheless, the two clusters of PKPE cell lines also shared similar pathway expressions, such as the downregulation of metabolism-related signalings (e.g. heme and fatty acid metabolism) and upregulation of proliferation-related ones (e.g. G2M checkpoint, E2F targets, and Myc targets). In addition, the cell lines completely recombined for *Cdh1* showed different levels of regulation of Wnt/β-catenin signaling, suggesting an unclear impact of loss of E-cadherin expression in this pathway. Altogether, these results suggest that the deletion of *Cdh1* at an early stage of the development and posteriorly in a context of the *Kras* mutation shortens the survival of animals with loss of the epithelial gene and increases the frequency of cystic tumors. *In vitro*, *Cdh1* loss does not seem to induce EMT, but it upregulates proliferation-related pathways in the *Cdh1*-KO malignant cells.

6.3.2. Tamoxifen-treatment induced a mosaic knockout of *Cdh1* in *Pdx1-Flp* animals and decreased the incidence of high grade tumors compared to control mice

E-cadherin plays a crucial role in the growth and maintenance of the pancreas and regulation of homeostatic signaling in the postnatal stage (Kaneta et al., 2020; Serrill et al., 2018). The deletion of *Cdh1* leads to progressive deterioration of exocrine architecture, significant reductions of body weight and blood glucose levels, as well as postnatal lethality, which can likely be attributed to pancreatic insufficiency. In addition, as shown by our endogenous *Cdh1*-KO mouse model, deletion of this gene at the postnatal stage posteriorly plays a role in *Kras*^{G12D}-

induced PDAC initiation, contributing to a shortened lifespan of the mice compared to control animals (Fig. 21B). However, it remains unclear whether the loss of *Cdh1* is also necessary for tumor progression. Thus, for long-term analysis of the effects of *Cdh1* deletion, a tamoxifen-inducible, conditional dual-recombined mouse model independent from the PDAC-initiating $Kras^{G12D}$ mutation needed to be employed, as shown in Fig. 22. *Pdx1-Flp; FSF-*$Kras^{G12D/+}$*; FSF-*$Rosa26^{CAG\text{-}CreERT2}$*;* $Cdh1^{fl/fl}$ mice were generated (Fig. 22A) and, at 3 months of age, the animals were intraperitoneally administrated with tamoxifen (Fig. 22B). This enabled a time- and stage-controlled tamoxifen-mediated deletion of *Cdh1* in $Kras^{G12D}$-induced PanIN lesions, as previously described by Schönhuber and colleagues (Schönhuber et al., 2014). Afterwards, *Cdh1* recombination in the tissues was assessed by PCR. Due to the mosaic Cre recombination using the *Pdx1* promoter (Gannon et al., 2000) and to the presence of cellular types that do not express this gene in the pancreas, such as immune cells and fibroblasts, it was not observed a complete recombination of *Cdh1* in the pancreatic tissue. Moreover, similarly to the endogenous *Cdh1*-KO mouse model, we also observed a significant reduction of the median survival time of the tamoxifen-treated $Cdh1^{fl/fl}$ animals, living 110 days less than the non-induced $Cdh1^{fl/fl}$ mice (192 days and 302 days, respectively; $p < 0.05$; Fig. 22C). Similarly, the mean survival of the tamoxifen-treated $Cdh1^{fl/fl}$ animals was also significantly shortened in ~170 days compared to the control *Pdx1-Flp; FSF-*$Kras^{G12D/+}$ (PK) mice (192 days and 364 days, respectively; $p < 0.001$). Regarding the survival times of non-treated $Cdh1^{fl/fl}$ and the heterozygous animals, no significant differences were observed between them and the PK mice. Additionally, we macroscopically analyzed the primary tumors formed by *Cdh1* animals (Fig. 22D and 22E) and no significant differences in pancreas weight were observed within the *Cdh1* groups and comparing to the control mice (Fig. 22D). However, as illustrated in Fig. 22E, there was a remarkable higher incidence of cystic tumors in both tamoxifen-treated $Cdh1^{fl/fl}$ animals (41.9% and 15.4% vs. PK; $p < 0.05$) and $Cdh1^{fl/+}$ mice (30.0% and 15.4% vs. PK; $p < 0.0001$). To evaluate tumor differentiation dependent on *Cdh1* deletion, we conducted H&E staining for the pancreatic tissues of all animals and two pathologists independently evaluated the histologic tumor grade (Fig. 22F and 22G). Curiously, we observed a significant reduction of undifferentiated (G4) tumors in tamoxifen-induced $Cdh1^{fl/fl}$ animals in comparison to the non-treated homozygous mice (6.5% and 19.1%, respectively; $p < 0.001$; Fig. 22F) and to the PK murines (6.5% and 30.8%, respectively; $p < 0.0001$). In addition, by collapsing well (G1) and moderately (G2) differentiated tumors into a low grade category and poor (G3) and undifferentiated (G4) tumors into a high grade category, we found that the homozygous *Cdh1* animals treated with tamoxifen had the highest percentage of low grade tumors and the lowest percentage of high grade tissues (25.8% each) among the five groups analyzed. Moreover, as expected, the non-treated $Cdh1^{fl/fl}$ animals presented a similar pattern distribution of histopathological grading to PK mice, even though the control murines had a higher percentage of high grade tumors (42.9% and 57.7%, respectively). Thus, the mosaic KO of *Cdh1* does not increase the invasiveness of the pancreatic tumors. Next, we performed IHC labeling for E-cadherin and it was clear by direct observation of the pancreatic tissues that there was a decrease

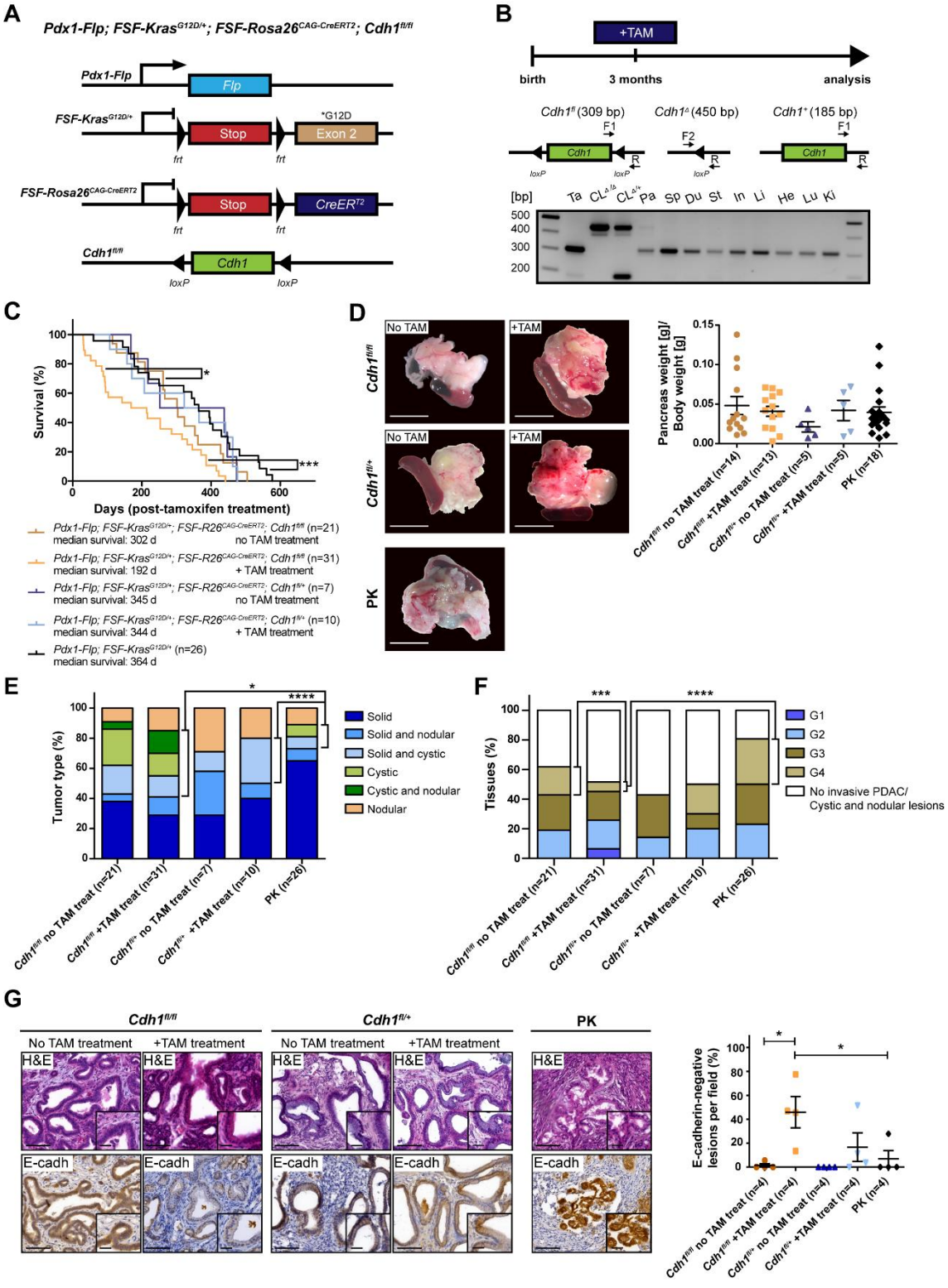

Fig. 22. Tamoxifen-inducible *Cdh1*-knockout increases the incidence of cystic lesions and reduces the frequency of high grade tumors.

(A) Genetic scheme of *Pdx1-Flp; FSF-Kras*$^{G12D/+}$*; FSF-Rosa26*$^{CAG\text{-}CreERT2}$*; Cdh1*$^{fl/fl}$ mouse model to delete *Cdh1* in established pancreatic intraepithelial neoplasia (PanIN) lesions by time- and stage-controlled tamoxifen (TAM)-mediated CreER^{T2} activation. Expression of *Kras*^{G12D} mutation induces PanIN lesions and *Cdh1* is deleted upon CreER^{T2} activation by TAM administration.

(B) Top, scheme of TAM treatment, where selected *Cdh1* animals were treated at 3 months of age and analyzed at the endpoint. Middle, genotyping strategy to detect *Cdh1* alleles by polymerase chain reaction (PCR) analysis, where F1 and F2 represent the forward primers and R the reverse one. Bottom, PCR

(legend continues on the next page)

of this epithelial protein on the tamoxifen-treated *Cdh1*$^{fl/fl}$ animals (Fig. 22G). This observation was then confirmed by quantification of E-cadherin-negative lesions. The tamoxifen-induced *Cdh1*$^{fl/fl}$ animals presented a significantly higher percentage of E-cadherin-negative lesions in the pancreatic tumor tissue in comparison to both non-treated homozygous mice (45.8% and 1.4%, respectively; $p < 0.05$) and PK murines (45.8% and 7.0%, respectively; $p < 0.05$). The recombination efficacy of the *in vivo* tamoxifen-treatment and consequent mosaic deletion of *Cdh1* were reflected in the heterogenous distribution of negative lesions among the treated mice as well as by the presence of both E-cadherin-deficient and -proficient lesions in tamoxifen-induced *Cdh1* animals. Altogether, these results showed that *in vivo* treatment with tamoxifen can induce mosaic deletion of *Cdh1* in the *Pdx1-Flp* mouse model, which leads to an increased incidence of cystic tumors and E-cadherin-negative lesions within the pancreatic tissues, but it does not have an impact on the invasiveness of the tumors.

analysis of *Cdh1* recombination status, where the band at 185 bp represents the wild- type allele, at 309 bp the floxed allele, and at 450 bp the recombined allele, in a tail (Ta), *Cdh1*$^{\Delta/\Delta}$ cell line (CL$^{\Delta/\Delta}$), *Cdh1*$^{\Delta/+}$ cell line (CL$^{\Delta/+}$), and tissues from pancreas (Pa), spleen (Sp), duodenum (Du), stomach (St), intestine (In), liver (Li), heart (He), lungs (Lu), and kidneys (Ki) from a TAM-treated *Cdh1*$^{fl/fl}$ animal.
(C) Kaplan-Meier survival analysis of indicated genotypes. The median survival time is in days after the TAM treatment and the number of animals per genotype are indicated in the legend of the graph, being only plotted tumor mice. *p < 0.05, ***p < 0.001, log-rank (Mantel-Cox) test.
(D) Left, representative macroscopic view of tumors and spleens from non-TAM-treated and TAM-treated *Cdh1*$^{fl/fl}$ and *Cdh1*$^{fl/+}$ animals as well as from a *Pdx1-Flp; FSF-Kras*$^{G12D/+}$ (PK) mouse. Scale bars indicate 1 cm. Right, weight of pancreata from non-TAM-treated and TAM-treated *Cdh1*$^{fl/fl}$ and *Cdh1*$^{fl/+}$ animals as well as from PK mice. Data represents mean ± SEM. *Cdh1*$^{fl/fl}$ no TAM treat: mean 0.05 g; n=14 biologically independent animals. *Cdh1*$^{fl/fl}$ + TAM treat: mean 0.04 g; n=13 biologically independent mice. *Cdh1*$^{fl/+}$ no TAM treat: mean 0.02 g; n=5 biologically independent animals. *Cdh1*$^{fl/+}$ + TAM treat: mean 0.04 g; n=5 biologically independent mice. PK: mean 0.04 g; n=18 biologically independent animals.
(E) Tumor type developed by non-TAM-treated and TAM-treated *Cdh1*$^{fl/fl}$ and *Cdh1*$^{fl/+}$ animals as well as from PK mice. Data represents percentage of tumor type and n=4 biologically independent mice were analyzed per genotype, as indicated in the graph. *p < 0.05, ****p < 0.0001, Chi-square test with 95% of confidence interval.
(F) Histopathological grading of non-TAM-treated and TAM-treated *Cdh1*$^{fl/fl}$ and *Cdh1*$^{fl/+}$ as well as from PK animals correspondent to the mice represented in the survival curve in Fig. 22C. The pathological evaluation was performed by Dr. med. vet. Katja Steiger and Nils Wirges. Data represents percentage of graded tissues and respective n mice analyzed per genotype is indicated in the graph. ***p < 0.001, ****p < 0.0001, Chi-square test with 95% of confidence interval.
(G) Left, representative hematoxylin and eosin (H&E) and E-cadherin (E-cadh) stainings of pancreatic sections from non-TAM-treated and TAM-treated *Cdh1*$^{fl/fl}$ and *Cdh1*$^{fl/+}$ animals as well as from a PK mouse. Scale bars of the images indicate 100 µm and of the inserts indicate 30 µm. Right, quantification of E-cadh-negative lesions on tissues of non-TAM-treated and TAM-treated *Cdh1*$^{fl/fl}$ and *Cdh1*$^{fl/+}$ as well as from PK animals. Data represents mean ± SEM. *Cdh1*$^{fl/fl}$ no TAM treat: mean 1.4%; n=4 biologically independent animals. *Cdh1*$^{fl/fl}$ + TAM treat: mean 45.8%; n=4 biologically independent mice. *Cdh1*$^{fl/+}$ no TAM treat: mean 0.0%; n=4 biologically independent animals. *Cdh1*$^{fl/+}$ + TAM treat: mean 16.7%; n=4 biologically independent mice. PK: mean 7.0%; n=4 biologically independent animals. H&E and immunohistochemistry stainings were also carried out using the remaining mice of each cohort with similar results. *p < 0.05, two-tailed Student's unpaired t test between selected pair groups.
Animals used for these analyses were generated and sacrificed by all members of the laboratory of Prof. Dr. med. Dieter Saur. % denotes the percentage, bp the base pair, CL the cell line, d the day, Du the duodenum, E-cadh the E-cadherin, fl the conditional allele with the *loxP* sites, F1 the forward primer 1, F2 the forward primer 2, g the gram, He the heart, H&E the hematoxylin and eosin staining, In the intestine, Ki the kidney, Lu the lung, Pa the pancreas, PDAC the pancreatic ductal adenocarcinoma, PK the *Pdx1-Flp; FSF-Kras*$^{G12D/+}$ mice, R the reverse primer, SEM the standard error of mean, Sp the spleen, St the stomach, Ta the tail, TAM the tamoxifen, treat the treatment/treated mice, Δ the recombined allele, + the wild-type allele.

6.3.3. Mosaic *Cdh1*-knockout in primary pancreatic tumors may lead to formation of distant metastases via seeding of multiple clones

Since the *Cdh1* PCCs analyzed by ssGSEA (Fig. 21E) presented an upregulation of several proliferation-related signaling pathways, we were prompted to determine the *in vivo* proliferative and metastatic potentials of *Cdh1*-KO (Fig. 23). We performed IHC labeling for Ki-67, a widely used cell proliferation marker (Khan et al., 2013; Varga et al., 2019), on the pancreatic tumor tissues of non-induced and treated $Cdh1^{fl/fl}$ animals as well as from control mice (Fig. 23A). No differences of Ki-67-positive cell numbers were observed among the groups analyzed, all presenting ~18.0% of proliferative cells. However, we noticed that the animals with higher number of proliferative cells corresponded to the ones with lower expression of E-cadherin in the pancreatic lesions. Furthermore, the potential for metastatic dissemination of *Cdh1* deletion was assessed by analysis of the distribution of macrometastases in distant organs (Fig. 23B). Evaluation of secondary tumors showed that PCCs typically metastasized to the liver, lungs, and lymph nodes, as already described by Hingorani and colleagues (Hingorani et al., 2003). The *Cdh1* inactivation did not result in a higher metastatic potential, however a significant decrease of liver metastases was notable in tamoxifen-treated $Cdh1^{fl/fl}$ animals compared to the non-treated homozygous mice (31.3% and 38.5%, respectively; $p < 0.001$; Fig. 23B) and to the PK mice (31.3% and 42.9%, respectively; $p < 0.0001$). Curiously, 6.3% of the tamoxifen-treated $Cdh1^{fl/fl}$ animals exclusively presented pulmonary metastases, being the only mice with this metastatic pattern among the analyzed animals. Next, we performed H&E and E-cadherin stainings in both hepatic and pulmonary tissues from $Cdh1^{fl/fl}$ and PK mice (Fig. 23C, 23D, 23E and 23F). Compared to the PK animals, the tamoxifen-treated $Cdh1^{fl/fl}$ mice showed a higher percentage of E-cadherin-negative metastases in the liver (47.8% and 0.0% vs. PK; $p < 0.05$; Fig. 23C) and in the lungs (58.1% and 0.0% vs. PK; $p < 0.05$; Fig. 23D). Similarly to the PPT tissues (Fig. 22G), it is worth noting that we observed the presence of both E-cadherin-negative and -positive lesions in the secondary tissues, especially in tissues of individual animals induced with tamoxifen (Fig. 23E and 23F). This result could not only reflect the inter- and intra-tumor heterogeneity of the primary malignant mass, but also indicate that this heterogeneity has an impact in the consequent formation of distant metastases. Furthermore, the quantification of the E-cadherin labeling intensity by optical density followed a reverse tendency as the number of negative lesions for this epithelial protein, with the treated animals showing the lowest expression of E-cadherin in both hepatic (0.08 and 0.17 vs. PK; $p < 0.01$; Fig. 23C) and pulmonary (0.11 and 0.17 vs. PK; Fig. 23D) metastases. Thus, mosaic deletion of *Cdh1* in the primary tumor appears to lead to the formation of both E-cadherin-deficient and -proficient lesions in secondary organs, suggesting not only that the metastatic dissemination may occur via seeding of multiple clones, but also that this epithelial protein may not be essential for metastases formation in secondary organs.

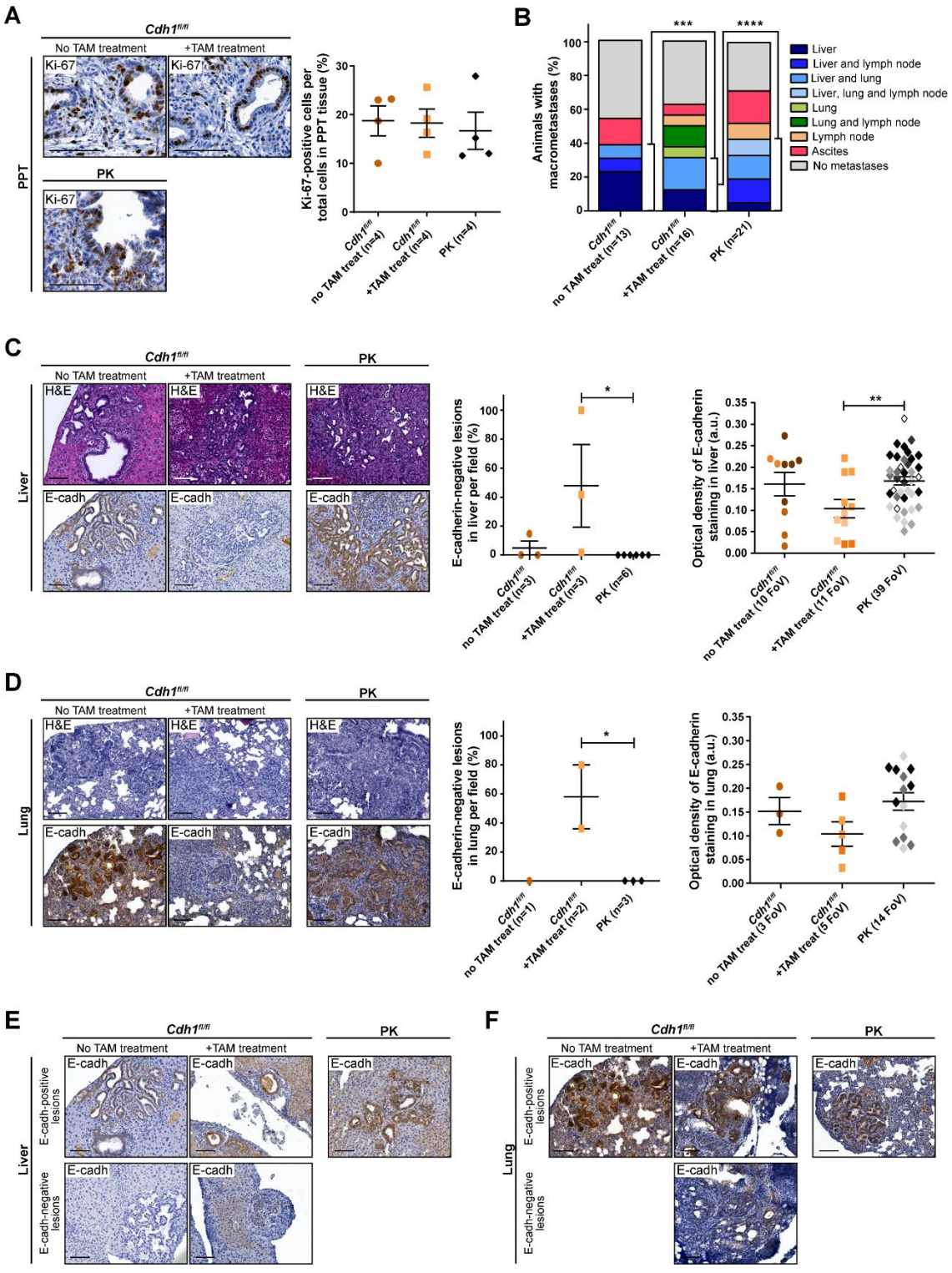

Fig. 23. Mosaic deletion of *Cdh1* in primary pancreatic tumors gives rise to both E-cadherin-negative and -positive metastatic lesions in secondary organs.

(A) Left, representative immunohistological labeling for Ki-67 of pancreatic sections from non-tamoxifen (TAM)-treated and TAM-treated *Cdh1*$^{fl/fl}$ mice as well as from a *Pdx1-Flp; FSF-Kras*$^{G12D/+}$ (PK) animal. Right, quantification of Ki-67-positive cells in representative primary pancreatic tumor (PPT) tissues. Data represents mean ± SEM. *Cdh1*$^{fl/fl}$ no TAM treat: mean 18.7%; n=4 biologically independent animals. *Cdh1*$^{fl/fl}$ + TAM treat: mean 18.2%; n=4 biologically independent mice. PK: mean 16.7%; n=4 biologically independent animals.

(B) Metastatic potential of *Cdh1*- and PK-mice bearing solid pancreatic tumors based on macroscopic

(legend continues on the next page)

6.3.4. *Cdh1* cell lines presented a range of recombination status and complete *Cdh1*-knockout cells showed an epithelial morphology

To further elucidate the molecular mechanisms underlying the functions of *Cdh1* deletion, we generated primary murine PCCs from pancreatic and metastatic tissues of *Cdh1* mice (Fig. 24). We successfully established cell lines from homozygous and heterozygous *Cdh1* tumor animals, including mice with mutant (*Trp53*^{R172H}) or inactivated (*Trp53*^{frt}) *Trp53*, and from several origins, such as PPT, liver, lung, lymph node, peritoneum, and ascites (Fig. 24A). Firstly, to assess loss of *Cdh1* or E-cadherin expression, we characterized the established cell lines through PCR, Western Blot, and ICC staining (Fig. 24B, 24C and 24D, respectively). The PCCs were divided into five distinct groups based on the *Cdh1* recombination status: from the *Cdh1*$^{fl/fl}$ mice, we had partial recombined (*Cdh1*$^{\Delta/fl}$; cell lines #1 and #2), complete recombined (*Cdh1*$^{\Delta/\Delta}$; cell lines #3 and #4), and not recombined (*Cdh1*$^{fl/fl}$; cell lines #5 and #6) cell lines, while from *Cdh1*$^{fl/+}$ mice there were recombined (*Cdh1*$^{\Delta/+}$; cell lines #7 and #8) and not recombined (*Cdh1*$^{fl/+}$; cell lines #9 and #10) cell lines (Fig. 24B). It is noteworthy that the cell line #6 did not present any recombined band although it was isolated from a tamoxifen-treated animal. At a genomic level,

observation. Data represents percentage of secondary tumor location and respective n mice analyzed per genotype is indicated in the graph. ***p < 0.001, ****p < 0.0001, Chi-square test with 95% of confidence interval.

(C) Left, representative hepatic sections presenting metastases from non-TAM-treated and TAM-treated *Cdh1*$^{fl/fl}$ mice as well as from a PK animal were stained for hematoxylin and eosin (H&E) and E-cadherin (E-cadh). Middle, quantification of E-cadh-negative lesions. Data represent mean ± SEM. *Cdh1*$^{fl/fl}$ no TAM treat: mean 4.9%; n=3 biologically independent animals. *Cdh1*$^{fl/fl}$ + TAM treat: mean 47.8%; n=3 biologically independent mice. PK: mean 0.0%; n=6 biologically independent animals. Right, quantification of optical density for E-cadh staining in individual hepatic metastases from non-TAM-treated and TAM-treated *Cdh1*$^{fl/fl}$ mice as well as from PK animals. Data represent mean ± SEM. *Cdh1*$^{fl/fl}$ no TAM treat: mean 0.16 a.u.; n=10 biologically independent fields of view (FoV) with metastases in total. *Cdh1*$^{fl/fl}$ + TAM treat: mean 0.08 a.u.; n=11 biologically independent FoV with metastases in total. PK: mean 0.17 a.u.; n=39 biologically independent FoV with metastases in total. *p < 0.05, **p < 0.01, two-tailed Student's unpaired t test between selected pair groups.

(D) Left, representative pulmonary sections presenting metastases from non-TAM-treated and TAM-treated *Cdh1*$^{fl/fl}$ mice as well as from a PK animal were stained for H&E and E-cadh. Middle, quantification of E-cadh-negative lesions. Data represent mean ± SEM. *Cdh1*$^{fl/fl}$ no TAM treat: mean 0.0%; n=1 biologically independent animals. *Cdh1*$^{fl/fl}$ + TAM treat: mean 58.1%; n=2 biologically independent mice. PK: mean 0.0%; n=3 biologically independent animals. Right, quantification of optical density for E-cadh staining in individual pulmonary metastases from non-TAM-treated and TAM-treated *Cdh1*$^{fl/fl}$ mice as well as from PK animals. Data represent mean ± SEM. *Cdh1*$^{fl/fl}$ no TAM treat: mean 0.15 a.u.; n=3 biologically independent FoV with metastases in total. *Cdh1*$^{fl/fl}$ + TAM treat: mean 0.11 a.u.; n=5 biologically independent FoV with metastases. PK: mean 0.17 a.u.; n=14 biologically independent FoV with metastases. *p < 0.05, two-tailed Student's unpaired t test between selected pair groups.

(E) Representative hepatic sections presenting E-cadh-positive and -negative metastases from non-TAM-treated and TAM-treated *Cdh1*$^{fl/fl}$ mice as well as from a PK animal.

(F) Representative pulmonary sections presenting E-cadh-positive and -negative metastases from non-TAM-treated and TAM-treated *Cdh1*$^{fl/fl}$ mice as well as from a PK animal.

H&E and immunohistochemistry stainings were also carried out using the remaining mice of each cohort with similar results. Scale bars of the images indicate 100 µm. Animals used for these analyses were generated and sacrificed by all members of the laboratory of Prof. Dr. med. Dieter Saur. % denotes the percentage, a.u. the arbitrary unit, E-cadh the E-cadherin, FoV the field of view, fl the conditional allele with the *loxP* sites, H&E the hematoxylin and eosin staining, met the micrometastases, PK the *Pdx1-Flp; FSF-Kras*$^{G12D/+}$ mice, PPT the primary pancreatic tumor, SEM the standard error of mean, TAM the tamoxifen, treat the treatment/treated mice.

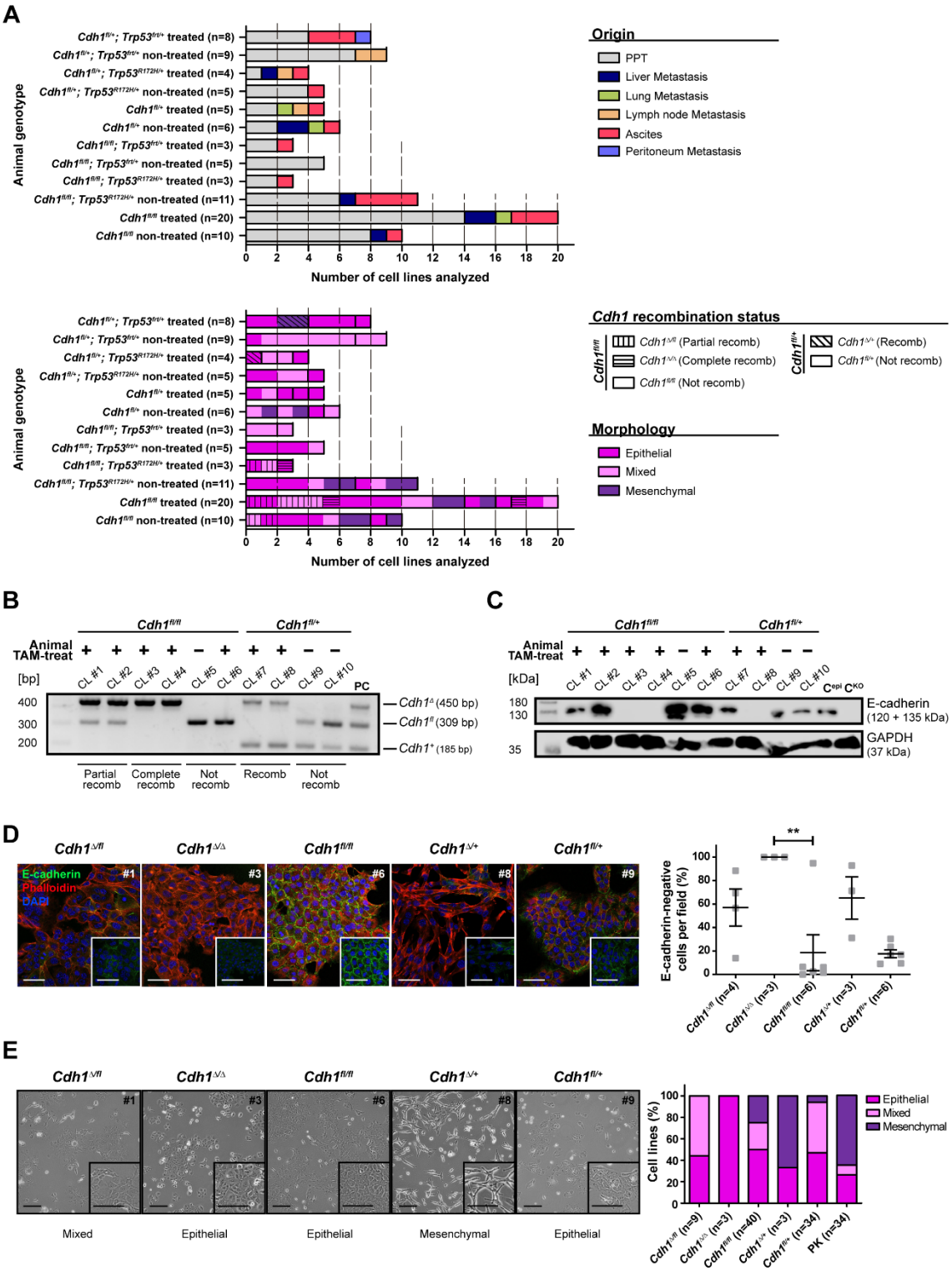

Fig. 24. *Cdh1*-knockout does not induce epithelial-to-mesenchymal transition *in vitro*.
(A) Top, graph with number of *Cdh1* cell lines (CLs) analyzed, according to the genotype of the animal from where the cells were generated and their respective origin. Bottom, graph of the *Cdh1* recombination status assessed by polymerase chain reaction (PCR) and morphology of the CLs represented in the graph above. The color and mark codes are explained in the legend on the right side of the illustration.
(B) *Cdh1* recombination PCR from CLs of each recombination group, indicating the *in vivo* tamoxifen treatment (above the image) and the recombination status (below the image). DNA from a CL with endogenous knockout of *Cdh1* mixed with DNA from a tail of a heterogenous animal were used as positive control (PC).

(legend continues on the next page)

Cdh1$^{\Delta/fl}$ and *Cdh1*$^{\Delta/+}$ PCCs still presented the floxed or WT alleles respectively, leading to the expression of E-cadherin in a protein level in most of the cells, while the *Cdh1*$^{\Delta/\Delta}$ cell lines lost *Cdh1* and did not show any expression of this epithelial protein (Fig. 24B and 24C). In addition, ICC labeling confirmed the expression of the E-cadherin in the membrane of cells possessing floxed and/or WT alleles (Fig. 24D). These cell lines were characterized by having a mixed composition of E-cadherin-negative and -positive cells, especially the *Cdh1*$^{\Delta/fl}$ and *Cdh1*$^{\Delta/+}$ PCCs that presented ~60% of negative cells for this cell-cell adhesion protein. Moreover, *Cdh1*$^{\Delta/\Delta}$ cell lines presented a significant increased number of E-cadherin-deficient cells compared with *Cdh1*$^{fl/fl}$ ones (100.0% and 18.6%, respectively; $p < 0.01$). It is worth mentioning that the only *Cdh1*$^{fl/fl}$ cell line composed by 94.8% of E-cadherin-negative cells (Fig. 24D) possessed a mesenchymal morphology (Fig. 24E), being used as an internal control in further analyses. Moreover, all the complete *Cdh1*-KO cell lines did not show any membranous E-cadherin, although they presented an epithelial morphology (Fig. 24D and 24E). Hence, similarly to the phenotypes shown by the cell lines generated from the conditional *Cdh1*-KO GEMM (Fig. 21E), the *Cdh1*$^{\Delta/\Delta}$ PCCs from the tamoxifen-inducible mouse model did not exhibit a more mesenchymal morphology compared to *Cdh1*$^{fl/fl}$ (0.0% and 25.0%, respectively) and PK (0.0% and 64.7%, respectively) cells, reinforcing that the inactivation of *Cdh1* alone may not induce EMT. In addition, we observed an even distribution of cells with epithelial or mixed properties among the *Cdh1*$^{\Delta/fl}$ and *Cdh1*$^{\Delta/+}$ cell lines (41.7% of each morphology), while only 16.6% of the cell lines presented a mesenchymal phenotype. Once this characterization was concluded, we illustrated the cell lines generated from PPT and metastatic tissues according not only to the respective animal genotype and if the *in vivo* tamoxifen treatment was performed or not, but also to their *Cdh1* recombination

(C) Immunoblot analysis of E-cadherin expression using protein extracted from the same CLs represented in Fig. 24B. The *in vivo* tamoxifen treatment is indicated above the image. Protein extracts prepared from an epithelial CL (C^{epi}) and a CL harboring endogenous *Cdh1*-KO (C^{KO}) were used as controls. Glyceraldehyde 3-phosphate dehydrogenase (GAPDH) served as loading control.
(D) Left, representative pictures of immunocytochemistry (ICC) staining for E-cadherin (green), Phalloidin CF633 (red) and DAPI (blue) of CLs grouped based on *Cdh1* recombination PCR. The inserts show the E-cadherin staining in the respective CL. On the right upper corner of each image is indicated the number corresponding to the CL analyzed in Fig. 24B and 24C. ICC staining was also carried out using the remaining CLs of each group with similar results. Scale bars of the images indicate 50 µm and of the inserts indicate 25 µm. Right, quantification of E-cadherin-negative cells according to *Cdh1* recombination status. Data represents mean ± SEM. *Cdh1*$^{\Delta/fl}$: mean 57.1%; n=4 biologically independent CLs. *Cdh1*$^{\Delta/\Delta}$: mean 100.0%; n=3 biologically independent CLs. *Cdh1*$^{fl/fl}$: mean 18.6%; n=6 biologically independent CLs. *Cdh1*$^{\Delta/+}$: mean 65.1%; n=3 biologically independent CLs. *Cdh1*$^{fl/+}$: mean 17.6%; n=6 biologically independent CLs. **$p < 0.01$, one-way ANOVA with post-hoc Tukey test.
(E) Left, representative brightfield pictures of cells according to *Cdh1* recombination status with the annotation of the morphology of the respective CL (below the images). On the right upper corner of each image is indicated the number corresponding to the CL analyzed in Fig. 24B, 24C, and 24D. Scale bars of the images indicate 100 µm and of the inserts indicate 50 µm. Right, graph of morphology distribution of CLs according to *Cdh1* recombination status. Data represents percentage of CLs with the indicated morphology and respective n CLs analyzed per group is indicated in the graph.
CLs used for these analyses were established by all members of the laboratory of Prof. Dr. med. Dieter Saur. % denotes the percentage, bp the base pair, CL the cell line, C^{epi} the epithelial control cell line, C^{KO} the *Cdh1*-knockout control cell line, fl the conditional allele with the *loxP* sites, GAPDH the glyceraldehyde 3-phosphate dehydrogenase, ICC the immunocytochemistry, kDa the kilodalton, PC the positive control, PCR the polymerase chain reaction, PPT the primary pancreatic tumor, recomb the recombined/recombination, SEM the standard error of mean, TAM the tamoxifen, treat the treatment/treated mice, Δ the recombined allele, + the wild-type allele.

status and morphology (Fig. 24A). It was interesting to verify that only 30.2% of the cell lines established from tamoxifen-treated animals presented recombination of this gene, either complete (*Cdh1*$^{\Delta/\Delta}$) or partial (*Cdh1*$^{\Delta/fl}$) when generated from *Cdh1*$^{fl/fl}$ animals or recombined (*Cdh1*$^{\Delta/+}$) when established from heterozygous mice. This suggests that *Cdh1*-KO may confer a disadvantage for cell growth *in vitro* and/or simply reflects the heterogeneous composition of the primary and secondary tumors upon mosaic deletion of *Cdh1 in vivo* (Fig. 22G and 23C-F), leading then to the establishment either of *Cdh1*-deficient or -proficient cell lines depending on the sampling harvested for the establishment of cell lines. Altogether, the results of the *in vitro* characterization of PCCs derived from tamoxifen-induced *Cdh1* animals allow us to infer that, due to its mosaic deletion *in vivo* and/or due to the polyclonality presented by pancreatic and metastatic tumors (Maddipati & Stanger, 2015), not all the cultured tumor cells were recombined for *Cdh1* and/or there is a growth advantage presented by the malignant cells that retain the expression of E-cadherin.

6.3.5. Genetic, histological, and morphological profiles of the primary pancreatic tumor can differ from the metastatic profiles

Upon performing a comprehensive characterization of the tamoxifen-inducible *Cdh1*-KO mouse model, we detected that the features exhibited by the primary tumor had an impact on the characteristics of the distant metastases. However, these analyses were done considering a cohort composed by several animals and cell lines sharing the same genotype, *in vivo* treatment, and *Cdh1* recombination status, and not the individual mice and respective cell lines. Thus, we combined the data derived from the *ex vivo* and *in vitro* analyses of PPT and metastatic tissues and cell lines, respectively, to assess how the genetic, histological, and morphological profiles of the primary tumor of *Cdh1* mice are revealed on the metastatic sites (Fig. 25). As illustrated in Fig. 25A, we had the paired data from the primary tumor and metastases of three *Pdx1-Flp; FSF-Kras*^{G12D}*; Rosa26*$^{FSF\text{-}CAG\text{-}CreERT2}$*; Cdh1*$^{fl/fl}$ mice: two non-induced animals (A and B) and one tamoxifen-treated (animal C). From animal A, 94.5% (52 in 55 lesions) of the analyzed lesions in PPT tissue were E-cadherin-positive and the cell line derived from this tissue was not genetically recombined for *Cdh1*, had an epithelial morphology and 93.5% of the cells expressed E-cadherin in their membranes. In addition, all the hepatic and pulmonary metastases (19 and 16 metastatic lesions, respectively) observed in animal A metastatic tissues were E-cadherin-positive, indicating that in this animal *Cdh1*-proficient malignant cells from the primary tumor colonized both distal organs. Regarding the cell lines of metastases from animal A, only the one derived from liver metastases was successfully established and presented comparable genetic and morphological profiles as the pair PPT cell line (not recombined for *Cdh1* and epithelial phenotype). Similarly to animal A, the mouse B was also not treated with tamoxifen, therefore it was not surprising that 100.0% of the PPT lesions were positive for E-cadherin. However, unexpectedly, this cell-to-cell protein was not observed in 14.7% (5 in 34 metastases) of the metastases in the liver of the animal B. Furthermore, in contrast to the mentioned mice, the tamoxifen-treatment of animal C

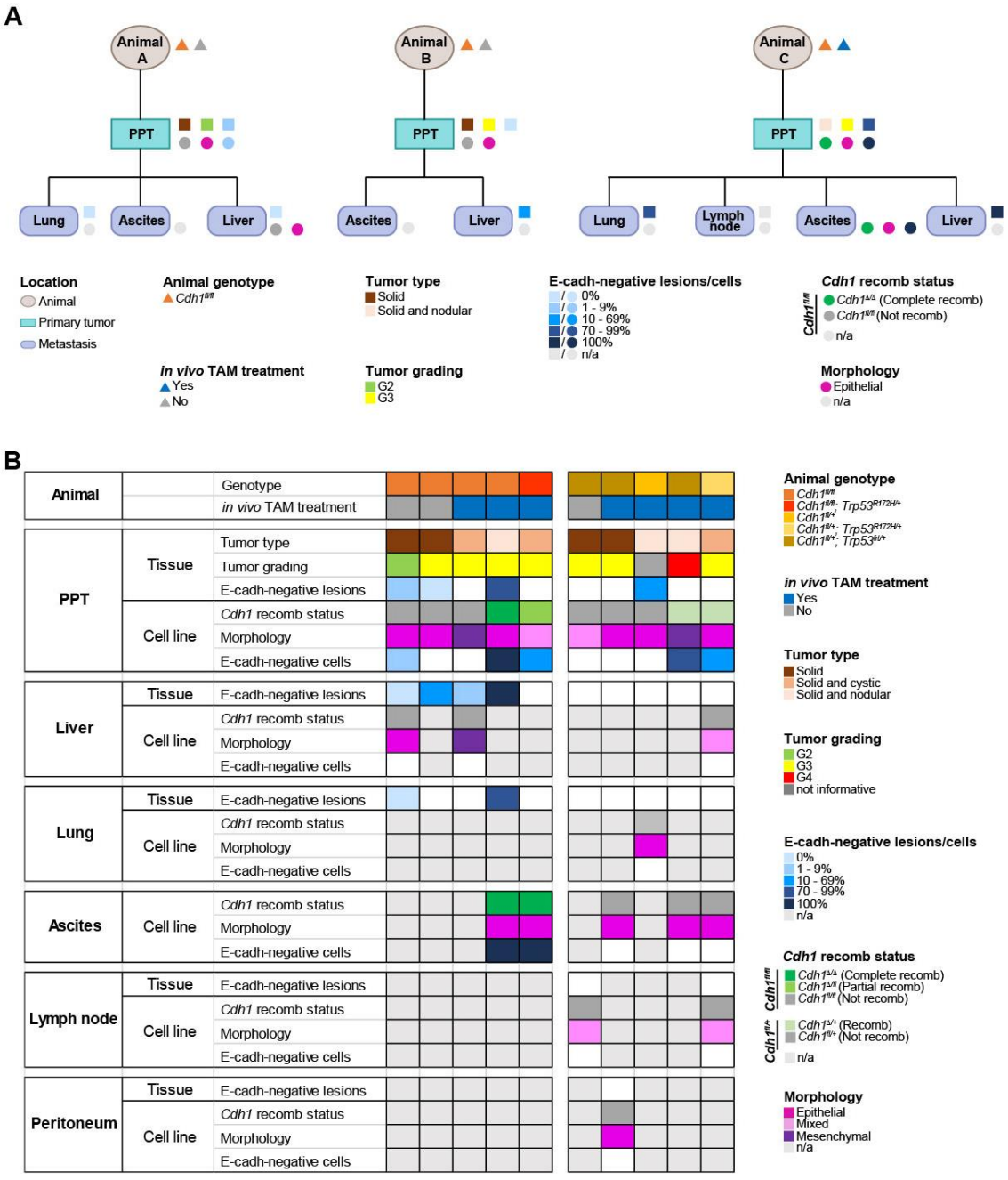

Fig. 25. Genetic, histological, and morphological profiles of the tissues and cell lines of primary pancreatic tumors are not always observed in the metastatic sites.
(A) Phylogenetic reconstructions illustrating the relationship of the primary pancreatic tumor (PPT) and the respective metastases of three *Pdx1-Flp; FSF-Kras*$^{G12D/+}$*; Rosa26*$^{FSF\text{-}CAG\text{-}CreERT2}$*; Cdh1*$^{fl/fl}$ mice. The illustrations are based on data collected from the *in vivo*, *ex vivo*, and *in vitro* characterizations of the tamoxifen-inducible *Cdh1* mouse model. The color code of the features is explained in the legend below the illustrations, being the characteristics of the animal represented by triangles, the histological features by squares and the cell line characteristics by circles.
(B) Illustration of 5 *Cdh1*$^{fl/fl}$ and 5 *Cdh1*$^{fl/+}$ mice with respect to their genetic, histologic, immunolabeling, and morphological profiles of the tissues and cell lines from PPT and metastatic sites. The color code of the features is explained in the legend on the right side of the illustration; the white squares represent the missing information.
Animals used for these analyses were generated and sacrificed and cell lines were established by all members of the laboratory of Prof. Dr. med. Dieter Saur. % denotes the percentage, E-cadh the E-cadherin, fl the conditional allele with the *loxP* sites, n/a the not applicable, PPT the primary pancreatic tumor, recomb the recombination/recombined, TAM the tamoxifen, treat the treatment, Δ the recombined allele, + the wild-type allele.

led to a mosaic deletion of *Cdh1* in the pancreatic tumor and consequently 77.5% (55 in 71 lesions) of the lesions examined in the primary malignant mass were E-cadherin-negative. Although the remaining 22.5% of the PPT lesions were *Cdh1*-proficient, the cell line established from this tissue was completely recombined for *Cdh1*, presented an epithelial morphology, and none of the cells expressed E-cadherin. Regarding the metastatic tissues, the majority of the hepatic and pulmonary secondary lesions did not express E-cadherin (11 in 11 liver metastases and 4 in 5 lung metastases). From animal C, we generated a stable cell line from ascites, which presented the same genetic, immunolabeling, and morphological profiles as the PPT one. However, as proven by the *ex vivo* data, not always the primary and secondary tumors share the same features. For this reason, we gathered the information of 7 additional animals (5 $Cdh1^{fl/fl}$ and 5 $Cdh1^{fl/+}$ mice, in total) with respect to their genetic, histologic, immunolabeling, and morphological profiles of the tissues and cell lines from PPT and metastatic sites (Fig. 25B). The $Cdh1^{fl/fl}$; $Trp53^{R172H/+}$ animal (fifth mouse represented in the illustration) is worth mentioning because the genetic and morphological profiles of the PPT and ascites cell lines were different, with the cells from the primary tumor being partially recombined for *Cdh1*, presenting a mixed morphology, and 43.5% of cells being E-cadherin-positive, while cells harvested from ascites were fully recombined, epithelial, and all were negative for this epithelial protein. Similarly, the profiles of PPT and the metastases cell lines from the $Cdh1^{fl/+}$; $Trp53^{R172H/+}$ animal (tenth mouse represented in the illustration) were also distinct; while the PPT cells were recombined for *Cdh1* and presented an epithelial phenotype, the cells from liver and lymph node metastases were not recombined and exhibited a mixed morphology. In addition, together with the E-cadherin staining performed on the PPT cell line showing that 68.8% of the cells expressed this protein, we predict that the primary tumor of the $Cdh1^{fl/+}$; $Trp53^{R172H/+}$ animal was composed by *Cdh1*-proficient and -deficient malignant cells, which posteriorly led to the generation of cell lines with distinct characteristics. Thus, these results show that the biological profile of a primary tumor may not always be mirrored in the distal metastases.

6.3.6. Cell lines with higher recombination efficacy had lower levels of *Cdh1* protein after 7 days of 4-OHT treatment, but did not present a growth advantage compared to lower recombination efficacy cells

To analyze rather *Cdh1* deletion influences cell growth *in vitro*, PCCs from non-induced $Cdh1^{fl/fl}$ mice were firstly cultured and treated with vehicle (EtOH) or 600 nM 4-OHT for 7 days and DNA and protein were harvested at days 1, 3, 5, and 7. The recombination efficacy of 4-OHT treatment was assessed by both PCR and Western Blot (Fig. 26A and 26B, respectively). As illustrated in Fig. 26A, an incubation with 4-OHT for 24 hours was enough to induce partial recombination of *Cdh1*, however it was not possible to achieve a fully recombined cell line, even when the treatment was extended up to 21 days and higher concentrations of 4-OHT were used (data not shown). At a protein level, we could divide the 4-OHT-treated PCCs into three groups based on their E-cadherin expression: 1) mesenchymal cell line that served as an internal control

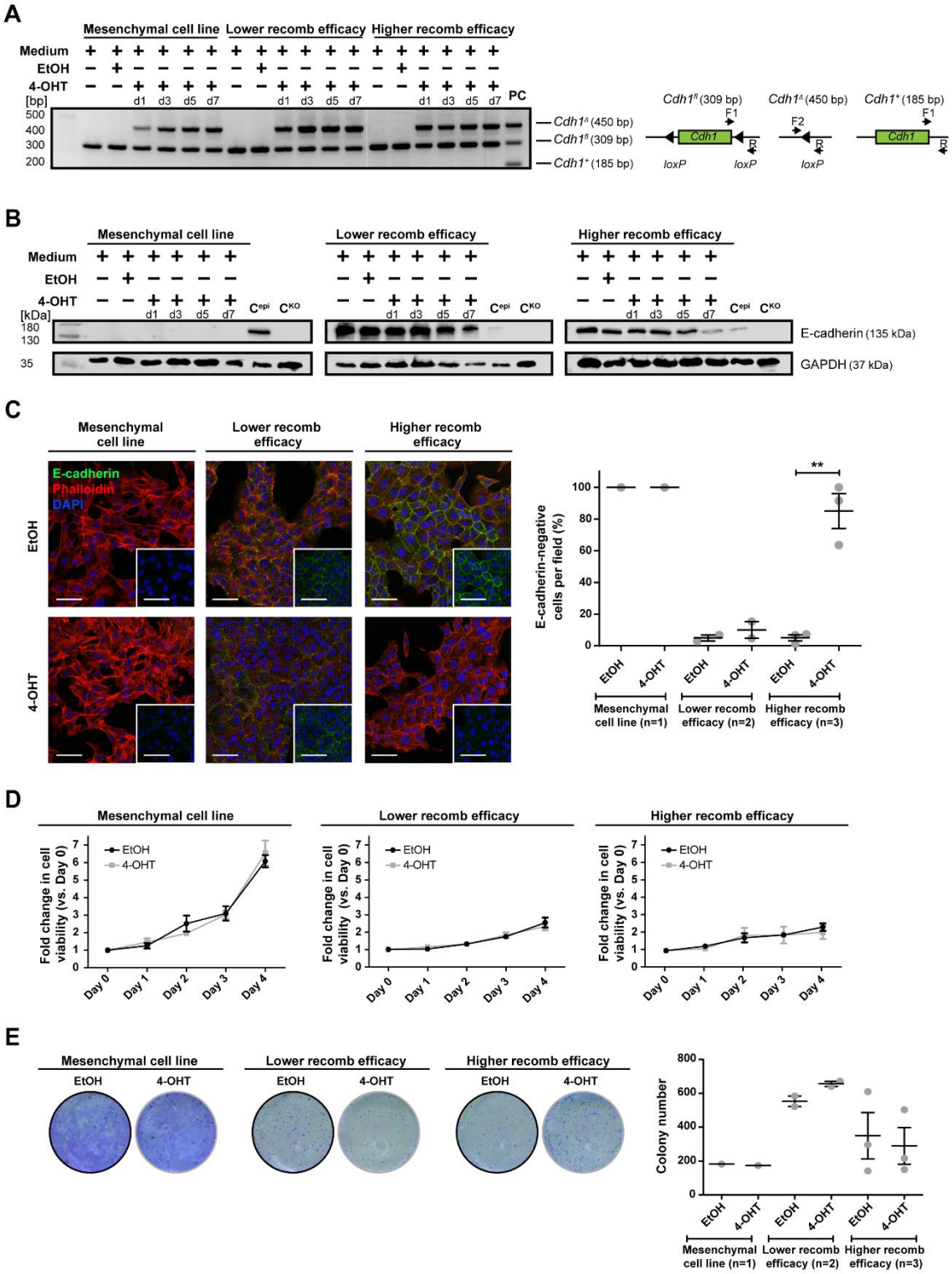

Fig. 26. *Cdh1*-knockout induction does not affect the growth and proliferation *in vitro*.
(A) Left, primary murine pancreatic cancer cells isolated from non-induced *Pdx1-Flp; FSF-Kras*$^{G12D/+}$*; Rosa26*$^{FSF\text{-}CAG\text{-}CreERT2}$*; Cdh1*$^{fl/fl}$ mice were incubated with Dulbecco's Modified Eagle's Medium (DMEM) supplemented with fetal calf serum, ethanol (EtOH) as control or with 600 nM of 4-hydroxytamoxifen (4-OHT) throughout 7 days of treatment. *Cdh1* recombination polymerase chain reaction (PCR) was performed after day 1, 3, 5, and 7 of treatment and the agarose gel electrophoresis result from a mesenchymal, a lower recombination efficacy, and a higher recombination efficacy cell lines (CLs) is shown in the figure. DNA from a CL with endogenous knockout of *Cdh1* mixed with DNA from a tail of a heterogenous animal were used as positive control (PC). Right, genotyping strategy to detect *Cdh1* alleles by PCR analysis, where the floxed allele has 309 bp, the recombined allele has 450 bp and the wild-type allele has 185 bp.

(legend continues on the next page)

for subsequent functional experiments; 2) lower recombination efficacy cell lines presented an expression of E-cadherin during the 7 days of treatment comparable to the expression observed in the medium and EtOH controls; and 3) higher recombination efficacy when a reduction of E-cadherin expression was detected throughout the 4-OHT treatment having the lowest levels of this epithelial protein on day 7 (Fig. 26B). Furthermore, as expected, PCCs with lower recombination efficacy presented E-cadherin on the cell membrane in both vehicle- and 4-OHT-treated cells, as showed in Fig. 26C. In contrast, the highly recombined cells expressed this protein on cell-to-cell junctions when treated with EtOH, expression that was not detected on the 4-OHT-induced cells. These observations based on the ICC labeling for E-cadherin were confirmed by quantification of negative cells present in these groups. The lower recombination efficacy PCCs only had up to 15.3% of *Cdh1*-deficient cells upon 4-OHT treatment. With regard of the highly recombined cell lines, a significant increase of ~17-fold of E-cadherin-negative cells was detected between the vehicle- and 4-OHT-treated cells (5.1% and 85.0%, respectively; $p < 0.01$; Fig. 26C). Regardless of the reduction of E-cadherin expression, we did not observe remarkable morphological changes in these cell lines throughout the 4-OHT treatment. Furthermore, cell viability based on metabolic activity, proliferation, and determination of survival of cancer cells upon 4-OHT treatment were assessed by both MTT and clonogenic assays (Fig. 26D and 26E, respectively). The mesenchymal cell line presented the biggest growth advantage

(B) Representative immunoblot analysis of E-cadherin expression throughout 7 days of EtOH or 4-OHT treatment from a mesenchymal, a lower recombination efficacy CL, and a higher recombination efficacy CL. Protein extracts prepared from an epithelial CL (C^{epi}) and a CL harboring endogenous *Cdh1*-knockout (C^{KO}) were used as controls. Glyceraldehyde 3-phosphate dehydrogenase (GAPDH) served as loading control.
(C) Left, representative pictures of immunocytochemistry staining for E-cadherin (green), Phalloidin CF633 (red) and DAPI (blue) of CLs grouped based on the *Cdh1* recombination efficacy. The inserts show the E-cadherin staining in the respective CL. Immunocytochemistry staining was also carried out using the remaining CLs of each *Cdh1* recombination efficacy group with similar results. Scale bars of the images indicate 50 µm and of the inserts indicate 25 µm. Right, quantification of E-cadherin-negative cells grouped according to the *Cdh1* recombination efficacy. Data represents mean ± SEM. Mesenchymal CL: EtOH mean 100.0% and 4-OHT mean 100.0%; n=1 CL. Lower recombination efficacy CLs: EtOH mean 5.0% and 4-OHT mean 10.1%; n=2 biologically independent CLs. Higher recombination efficacy CLs: EtOH mean 5.1% and 4-OHT mean 85.0%; n=3 biologically independent CLs. **$p < 0.01$, one-way ANOVA with post-hoc Tukey test.
(D) MTT assay of a mesenchymal, a lower recombination efficacy CL, and a higher recombination efficacy CL treated with 4-OHT compared to the correspondent EtOH treatment. Data represent mean ± SEM and this assay was performed over 3 independent experiments. MTT assay was also carried out using the remaining CLs of each *Cdh1* recombination efficacy group with similar results.
(E) Left, clonogenic assay of a mesenchymal, a lower recombination efficacy CL, and a higher recombination efficacy CL treated with EtOH or 4-OHT. Right, quantification of the number of colonies formed based on the *Cdh1* recombination efficacy. Data represents mean ± SEM. Mesenchymal CL: EtOH mean 182 colonies and 4-OHT mean 174 colonies; n=1 CL. Lower recombination efficacy CLs: EtOH mean 553 colonies and 4-OHT mean 656 colonies; n=2 biologically independent CLs. Higher recombination efficacy CLs: EtOH mean 350 colonies and 4-OHT mean 290 colonies; n=3 biologically independent CLs. This assay was performed in triplicates. Clonogenic assay was also carried out using the remaining CLs of each *Cdh1* recombination efficacy group with similar results.
CLs used for these analyses were established by Dr. Kathleen Schuck, a previous member of the laboratory of Prof. Dr. med. Dieter Saur. % denotes the percentage, bp the base pair, CL the cell line, C^{epi} the epithelial control cell line, C^{KO} the *Cdh1*-knockout control cell line, d the day, DMEM the Dulbecco's Modified Eagle's Medium, EtOH the ethanol, fl the conditional allele with the *loxP* sites, F1 the primer forward 1, F2 the primer forward 2, GAPDH the glyceraldehyde 3-phosphate dehydrogenase, kDa the kilodalton, PC the positive control, PCR the polymerase chain reaction, R the primer reverse, recomb the recombination, SEM the standard error of mean, 4-OHT the 4-hydroxytamoxifen, Δ the recombined allele, + the wild-type allele.

of all tested PCCs, and no differences were observed on the vehicle- or 4-OHT-treated cell lines, regardless of their recombination efficacy (Fig. 26D). Moreover, the clonogenic assay corroborated that the number of colonies formed by vehicle- or 4-OHT-treated malignant cells were comparable despite the different *Cdh1* recombination efficacies (Fig. 26E). To conclude, although the *Cdh1*$^{fl/fl}$ PCCs may present the same genotype and morphological characteristics, the recombination efficacy of the 4-OHT treatment may vary among these cell lines and the higher efficacy of recombination does not confer a growth advantage for the *Cdh1*-KO cells. Nevertheless, the partial recombination of the *Cdh1*$^{fl/fl}$ cell lines makes this inducible system not suitable to study the effect of the complete deletion of this gene *in vitro*.

6.3.7. *Cdh1*-knockout clones did not have any growth advantage compared to vehicle- or 4-OHT-treated cell line and to *Cdh1*-proficient clones

To overcome the limitations of the inducible *in vitro* system, *Cdh1*-KO clones were generated from 4-OHT-induced *Cdh1*$^{fl/fl}$ PCCs and further characterized (Fig. 27). *Cdh1*$^{fl/fl}$ cell lines that previously showed high recombination efficacy for *Cdh1* were treated with 4-OHT for 7 days and seeded in the same setting as a clonogenic assay. Growing colonies were picked and recultured until DNA could be collected. The *Cdh1* recombination status was assessed by PCR, as shown in Fig. 27A. We were able to generate 2-20 *Cdh1*$^{\Delta/\Delta}$ and 3-57 *Cdh1*$^{fl/fl}$ clones per each cell line, with an ~3-fold lower frequency of complete recombined clones compared with *Cdh1*$^{fl/fl}$ ones (10.2% and 28.0%, respectively; Table 31). *Cdh1*$^{\Delta/\Delta}$ and *Cdh1*$^{fl/fl}$ clones were recultured until they could be frozen and used for further analyses. Three *Cdh1*$^{\Delta/\Delta}$ and three *Cdh1*$^{fl/fl}$ clones from one cell line (cell line #12) were further characterized by Western Blot, ICC staining, and MTT and clonogenic assays (Fig. 27B, 27C, 27D, and 27E, respectively). The three *Cdh1*$^{fl/fl}$ clones showed similar E-cadherin expression to the vehicle-treated cell line, while, as expected, the three *Cdh1*$^{\Delta/\Delta}$ clones did not present any epithelial protein although they exhibited an epithelial morphology (Fig. 27B and 27C). The same was observed in the ICC labeling for E-cadherin, where E-cadherin expression was detected on the cell membrane of the *Cdh1*$^{fl/fl}$ clones, in contrast to the *Cdh1*$^{\Delta/\Delta}$ clones that were negative for this epithelial protein (Fig. 27C). In addition to E-cadherin, we also labeled the clones and the correspondent vehicle- or 4-OHT-treated cell lines for the proliferation marker Ki-67. Although no significant difference of number of Ki-67-positive cells was detected among the groups analyzed, there was a slight decrease of

Table 31. Frequency of *Cdh1* recombined clones derived from *Cdh1*$^{fl/fl}$ cell lines with high recombination efficacy upon treated with 4-hydroxytamoxifen (4-OHT) for 7 days

Cell line ID	*Cdh1*$^{\Delta/\Delta}$ clones	*Cdh1*$^{\Delta/fl}$ clones	*Cdh1*$^{fl/fl}$ clones	Total picked clones
CL #6	20 (21.1%)	72 (75.8%)	3 (3.2%)	95
CL #11	2 (6.5%)	17 (54.8%)	12 (38.7%)	31
CL #12	4 (3.0%)	74 (54.8%)	57 (42.2%)	135

%, percentage; CL, cell line; fl, conditional allele with the *loxP* sites; ID, identification number; Δ, recombined allele.

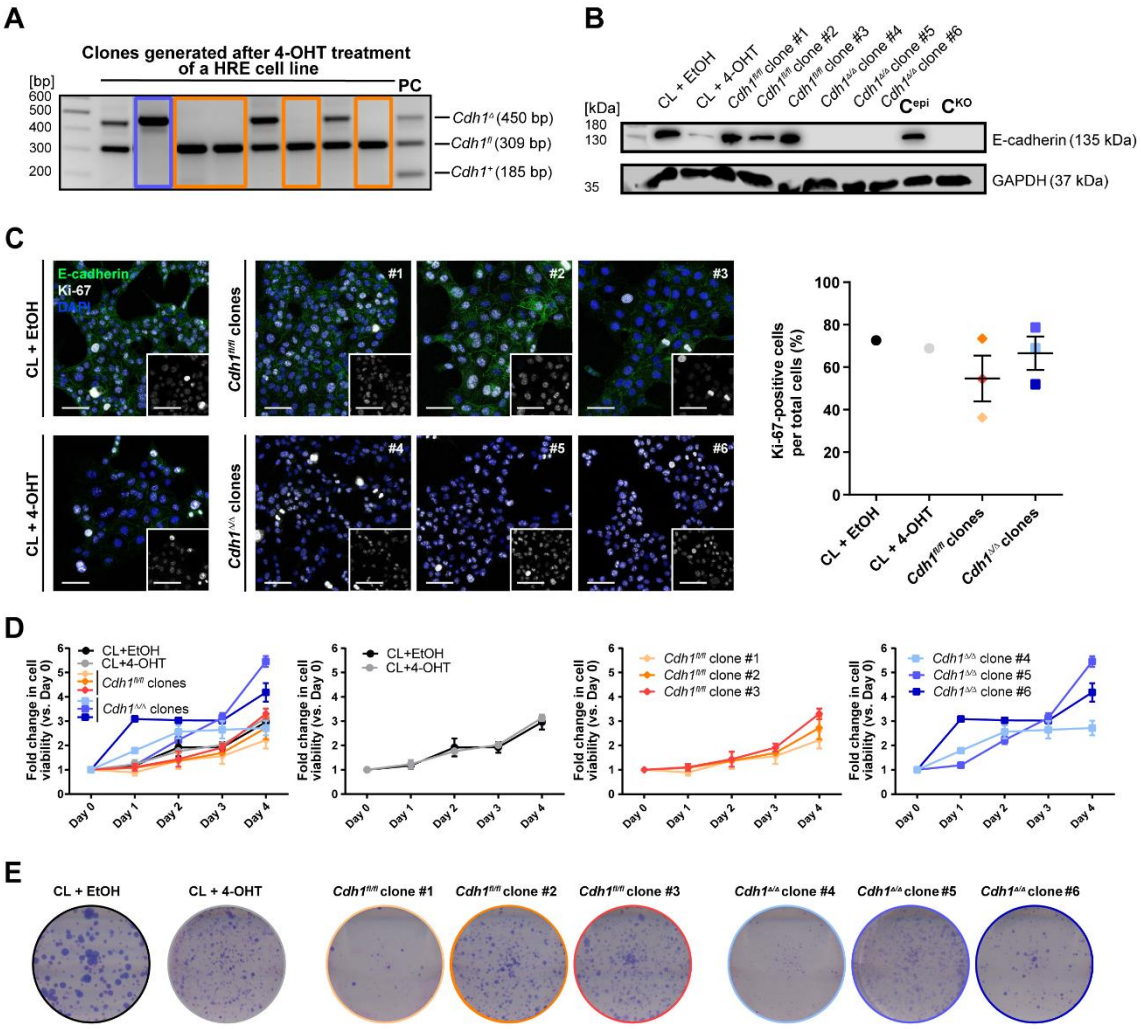

Fig. 27. Fully recombined *Cdh1* clones do not present a growth and proliferative advantage compared to *Cdh1*-proficient clones.

(A) Recombination of *Cdh1* locus in clones generated from a 4-hydroxytamofien (4-OHT)-treated cell line (CL) with high recombination efficacy (HRE) assessed by polymerase chain reaction (PCR). Representative $Cdh1^{\Delta/\Delta}$ clone is highlighted by a blue rectangle, while the $Cdh1^{fl/fl}$ clones are highlighted by orange rectangles. DNA from a CL with endogenous knockout of *Cdh1* mixed with DNA from a tail of a heterogenous animal were used as positive control (PC).

(B) Representative immunoblot analysis of E-cadherin expression of a CL with HRE including the EtOH- or 4-OHT-treated cells, 3 $Cdh1^{fl/fl}$ clones and 3 $Cdh1^{\Delta/\Delta}$ clones. Protein extracts prepared from an epithelial CL (C^{epi}) and a CL harboring endogenous *Cdh1*-KO (C^{KO}) were used as controls. Glyceraldehyde 3-phosphate dehydrogenase (GAPDH) served as loading control.

(C) Left, representative pictures of immunocytochemistry staining for E-cadherin (green), Ki-67 (white) and DAPI (blue) in EtOH- or 4-OHT-treated cells, and $Cdh1^{fl/fl}$ and $Cdh1^{\Delta/\Delta}$ clones. The inserts show the Ki-67 staining in the respective cells. Scale bars of the images indicate 50 µm and of the inserts indicate 25 µm. Right, quantification of Ki-67-positive cells in these CLs and clones (light orange, $Cdh1^{fl/fl}$ clone #1; orange, $Cdh1^{fl/fl}$ clone #2; red, $Cdh1^{fl/fl}$ clone #3; light blue, $Cdh1^{\Delta/\Delta}$ clone #4; blue, $Cdh1^{\Delta/\Delta}$ clone #5; dark blue, $Cdh1^{\Delta/\Delta}$ clone #6). Data represents mean ± SEM. CL + EtOH: mean 72.6%; n=1 CL. CL + 4-OHT: mean 68.9%; n=1 CL. $Cdh1^{fl/fl}$ clones: mean 54.7%; n=3 biologically independent clones. $Cdh1^{\Delta/\Delta}$ clones: mean 66.5%; n=3 biologically independent clones.

(D) First graph, MTT assay of all samples including EtOH- or 4-OHT-treated CLs, 3 $Cdh1^{fl/fl}$ clones and 3 $Cdh1^{\Delta/\Delta}$ clones; Second graph, MTT assay of CLs treated with EtOH or 4-OHT; Third graph, of $Cdh1^{fl/fl}$ clones; Fourth graph, of $Cdh1^{\Delta/\Delta}$ clones. Data represent mean ± SEM and n=1 CL treated either with EtOH or 4-OHT were examined as well as n=3 biologically independent $Cdh1^{fl/fl}$ and $Cdh1^{\Delta/\Delta}$ clones were analyzed. This assay was performed over 3 independent experiments.

(E) Clonogenic assay of EtOH- or 4-OHT-treated *Cdh1* CLs and $Cdh1^{fl/fl}$ and $Cdh1^{\Delta/\Delta}$ clones. This assay was performed in triplicates.

CLs used for these analyses were established by Dr. Kathleen Schuck, a previous member of the laboratory of Prof. Dr. med. Dieter Saur. % denotes the percentage, bp the base pair, CL the cell line, C^{epi} the epithelial

(legend continues on the next page)

proliferative cells in the *Cdh1*$^{fl/fl}$ clones compared to the *Cdh1*$^{\Delta/\Delta}$ ones (54.7% and 66.5%, respectively). Furthermore, cell viability, proliferation, and survival of the clones were assessed by both MTT and clonogenic assays (Fig. 27D and 27E). As depicted in Fig. 27D, no significant growth advantage was detected between vehicle- or 4-OHT-treated cell lines and the generated clones. However, we interestingly observed that the cell viability was very consistent among the *Cdh1*$^{fl/fl}$ clones, in contrast to the *Cdh1*$^{\Delta/\Delta}$ clones that followed three different viability patterns. *Cdh1*$^{fl/fl}$ clone #1 and *Cdh1*$^{\Delta/\Delta}$ clone #4, which showed the lowest cell viability, also had a reduced colony formation in the clonogenic assay in comparison to the remaining clones in the respective group (Fig. 27E). Thus, the generation of *Cdh1*-deficient clones might present a good strategy to overcome the incomplete efficacy of *in vitro* 4-OHT treatment, however further and more detailed characterization of these clones must be performed to unveil potential advantages or effects of *Cdh1* deletion in tumor cells.

6.3.8. Animals implanted with *Cdh1*-deficient clones had a lower incidence of liver metastases than the ones implanted with *Cdh1*-proficient clones

To reevaluate the impact of *Cdh1* deletion on tumor growth, proliferation, and subsequent metastases formation, *Cdh1*$^{\Delta/\Delta}$ and *Cdh1*$^{fl/fl}$ clones as well as the respective cell line treated with vehicle- or 4-OHT were orthotopically implanted into the pancreata of C57BL/6J;129/S6 females (Fig. 28). As illustrated in Fig. 28A, the *Cdh1*$^{fl/fl}$ #2, *Cdh1*$^{fl/fl}$ #3, *Cdh1*$^{\Delta/\Delta}$ #4, and *Cdh1*$^{\Delta/\Delta}$ #6 clones were selected to be implanted into mice due to their similar number of proliferative cells and cell viability (Fig. 27C and 27D, respectively). All animals were then monitored and sacrificed 35 days post-implantation. By macroscopic analysis of the pancreatic tumors, we observed that the cell line treated with vehicle developed less heterogeneous tumors compared to the remaining groups analyzed (Fig. 28B). In contrast, the higher heterogeneity of tumor sizes was detected on the animals implanted with the clones *Cdh1*$^{\Delta/\Delta}$, which may be explained by the distinct viability patterns presented by these clones *in vitro* (Fig. 27D). Besides the significant difference observed between the tumor weight from animals inoculated with the cell line treated with EtOH and the mice implanted with *Cdh1*$^{fl/fl}$ clones (0.003 g and 0.015 g, respectively; $p < 0.01$; Fig. 28C), no other differences were assessed either in tumor weight or volume (Fig. 28C). The *Cdh1*$^{\Delta/\Delta}$ clones developed larger malignant masses in weight (0.019 g and 0.015 g vs. *Cdh1*$^{fl/fl}$ clones) and in volume (782.5 mm^3 and 466.9 mm^3 vs. *Cdh1*$^{fl/fl}$ clones) compared to the *Cdh1*$^{fl/fl}$ clones. Due to the contact of the pancreas with the peritoneum, 96.0% (23 in 24 implanted mice) of the implanted animals showed peritoneal tumors (data not shown). Furthermore, to determine the metastatic potential of the cell lines treated with vehicle or 4-OHT and of the *Cdh1* clones, we macroscopically assessed the metastasized sites and the number of hepatic metastases formed

control cell line, C^{KO} the *Cdh1*-knockout control cell line, EtOH the ethanol, fl the conditional allele with the *loxP* sites, GAPDH the glyceraldehyde 3-phosphate dehydrogenase, HRE the high recombination efficacy, kDa the kilodalton, PC the positive control, PCR the polymerase chain reaction, SEM the standard error of mean, 4-OHT the 4-hydroxytamoxifen, Δ the recombined allele.

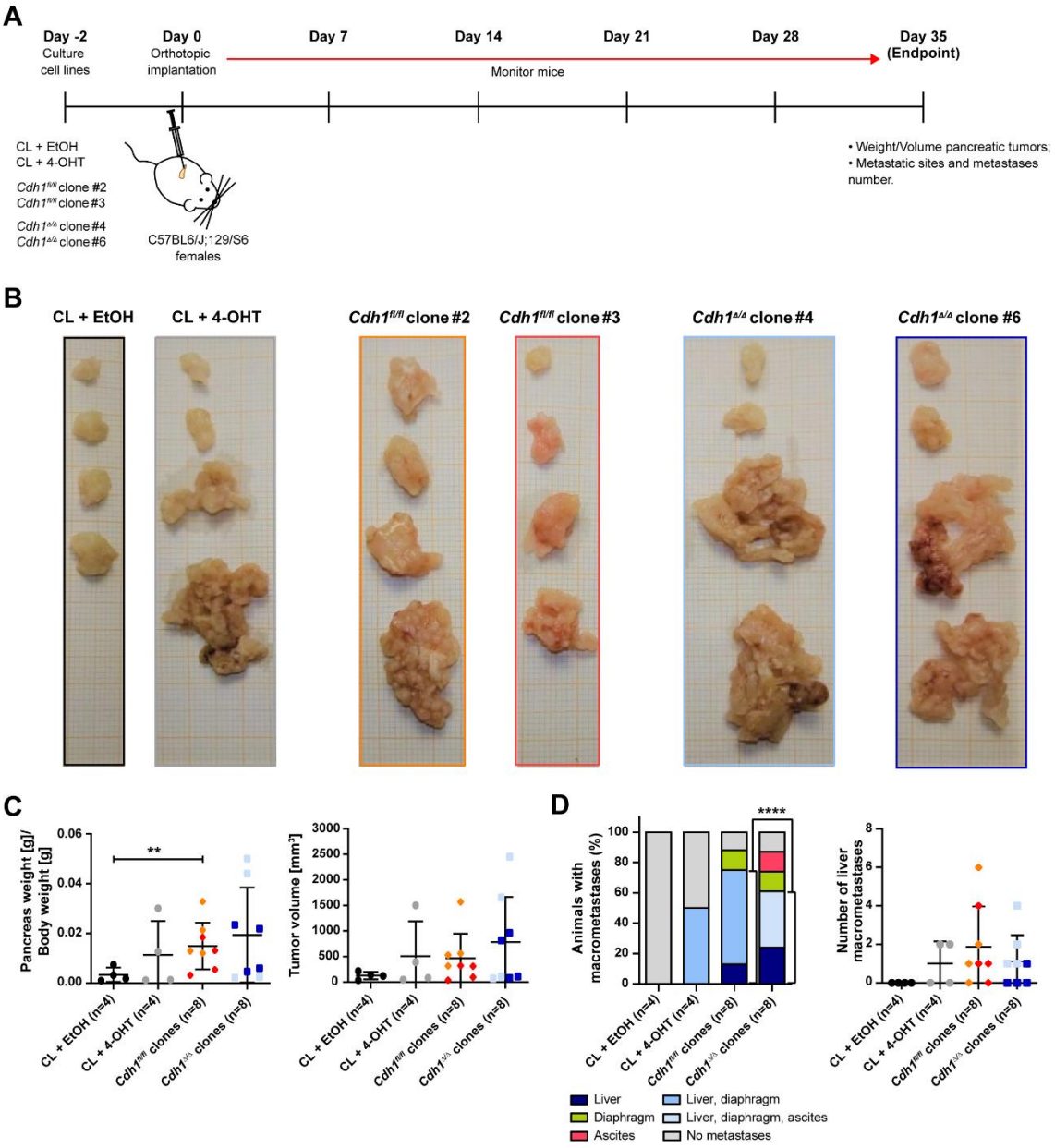

Fig. 28. Liver metastases formation is less frequent in animals implanted with *Cdh1*-deficient clones.
(A) Schematic representation of the orthotopic implantation setting of vehicle- or 4-hydroxytamoxifen (4-OHT)-treated *Cdh1*$^{fl/fl}$ cell lines (CLs) and two *Cdh1*$^{fl/fl}$ and two *Cdh1*$^{Δ/Δ}$ clones into C57BL6/J;129/S6 females (n=4 animals per cell line and per clone). The orthotopic implantations were performed together with Chiara Falcomatà, Stefanie Bärthel, and Saskia Ettl. The animals were monitored, and were all sacrificed 35 days after the orthotopic implantation to assess tumor growth, proliferation, and subsequent metastases formation.
(B) Pictures of tumor morphology of tumor-bearing mice implanted with EtOH- or 4-OHT-treated *Cdh1*$^{fl/fl}$ CLs as well as *Cdh1*$^{fl/fl}$ or *Cdh1*$^{Δ/Δ}$ clones. Each small square represents 1 mm.
(C) Left, tumor weight and Right, volume of tumor-bearing animals implanted with EtOH- or 4-OHT-treated *Cdh1*$^{fl/fl}$ CLs as well as *Cdh1*$^{fl/fl}$ or *Cdh1*$^{Δ/Δ}$ clones. Data represent mean ± SEM. CL + EtOH: mean 0.003 g and 128.0 mm^3; n=4 biologically independent animals. CL + 4-OHT: mean 0.011 g and 506.0 mm^3; n=4 biologically independent animals. *Cdh1*$^{fl/fl}$ clones: mean 0.015 g and 466.9 mm^3; n=8 biologically independent animals. *Cdh1*$^{Δ/Δ}$ clones: mean 0.019 g and 782.5 mm^3; n=8 biologically independent animals. Orange diamonds represent the animals implanted with the *Cdh1*$^{fl/fl}$ clone #2, the red ones the mice implanted with the *Cdh1*$^{fl/fl}$ clone #3, the light blue squares represent the animals implanted with the *Cdh1*$^{Δ/Δ}$ clone #4 and the dark blue ones the mice implanted with the *Cdh1*$^{Δ/Δ}$ clone #6. **p < 0.01, two-tailed Student's unpaired t test between selected pair groups.
(D) Left, metastatic potential of tumor-bearing mice implanted with vehicle- or 4-OHT-treated *Cdh1*$^{fl/fl}$ CLs as well as *Cdh1*$^{fl/fl}$ or *Cdh1*$^{Δ/Δ}$ clones based on macroscopic observation. Data represents percentage of

(legend continues on the next page)

in each group of animals (Fig. 28D). Curiously, none of the animals implanted with the vehicle-treated cell line formed metastases and only 50.0% of the mice injected with 4-OHT-treated cells had liver and diaphragm metastases. Regarding the clones, 87.5% (7 in 8 animals of each group) of mice implanted with *Cdh1*$^{fl/fl}$ or *Cdh1*$^{\Delta/\Delta}$ clones presented metastases, especially in the liver. Hepatic secondary tumors were observed in 75.0% of the mice injected with *Cdh1*$^{fl/fl}$ clones with a mean of three metastases per animal, and in 62.5% of the animals implanted with *Cdh1*$^{\Delta/\Delta}$ clones with a mean of two metastases per murine. Thus, the *Cdh1*-deficient clones had a significant decreased capacity to form liver metastasis compared to the *Cdh1*-proficient clones (62.5% and 75.0%, respectively; $p < 0.0001$; Fig. 28D). In addition, similarly to the conditional *Cdh1*-KO GEMM, it was interesting to observe a high incidence of ascites formation on the *Cdh1*$^{\Delta/\Delta}$ clone-implanted animals, one of the mice presenting up to 4.2 mL of peritoneal fluid. In conclusion, *Cdh1* deletion does not have an impact in tumor size, however it leads to a decrease of hepatic metastases formation in an orthotopic implantation model.

animals with secondary tumors and respective n mice analyzed per group is indicated in the graph. Right, number of liver macrometastases of tumor-bearing mice implanted with vehicle- or 4-OHT-treated *Cdh1*$^{fl/fl}$ CLs as well as *Cdh1*$^{fl/fl}$ or *Cdh1*$^{\Delta/\Delta}$ clones based on macroscopic observation. Data represents mean ± SEM. CL + EtOH: mean 0 metastasis; n=4 biologically independent animals. CL + 4-OHT: mean 1 metastasis; n=4 biologically independent animals. *Cdh1*$^{fl/fl}$ clones: mean 2 metastases; n=8 biologically independent animals. *Cdh1*$^{\Delta/\Delta}$ clones: mean 1 metastasis; n=8 biologically independent animals. Orange diamonds represent the animals implanted with the *Cdh1*$^{fl/fl}$ clone #2, the red ones the mice implanted with the *Cdh1*$^{fl/fl}$ clone #3, the light blue squares represent the animals implanted with the *Cdh1*$^{\Delta/\Delta}$ clone #4 and the dark blue ones the mice implanted with the *Cdh1*$^{\Delta/\Delta}$ clone #6. ****$p < 0.0001$, Chi-square test with 95% of confidence interval.
C57BL6/J; 129/S6 females used for these analyses were generated by Magdalena Zukowska and CLs were established by Dr. Kathleen Schuck, both members of the laboratory of Prof. Dr. med. Dieter Saur. % denotes the percentage, CL the cell line, EtOH the ethanol, fl the conditional allele with the *loxP* sites, g the gram, mm^3 the cubic millimeter, SEM standard error of mean, 4-OHT the 4-hydroxytamoxifen, Δ the recombined allele.

7. Discussion and Outlook

Chapter I, Part A: Development of 6-color multiplexed immunohistochemistry protocols for immune-profiling of cryopreserved murine tissues

In this part of the present study, we described the validation of manual mIHC panels with a range of immune and tumor cell antibodies and the application of these panels for whole-slide analysis of frozen PDAC tissues using confocal microscopy and imaging analysis Imaris software. While the general concept of mIHC in FFPE tissues is well-established (Gorris et al., 2018; Parra et al., 2017; Tsujikawa et al., 2017), the validation of this imaging technique remains a difficult task due to the lack of detailed studies deconstructing the complex multistep process, guiding step-wise, and pointing its limitations. In addition, there is also the requirement of a high level of both technical and interpretation expertise of the tests performed (Howat et al., 2014). Thereby, we presented a comprehensive mIHC strategy, highlighting critical steps, challenges, and limitations implicated in the process.

To facilitate the panel development, we selected antibodies that are used for clinical assessment and would allow the identification of the main innate and adaptive immune populations, including F4/80 (macrophages), CD11c (cDCs), CD3 (T cells), and CD45R/B220 (B cells), and the tumor cells with CK18 marker. The uniplex IF stainings and quality controls were performed to ensure the specificity of the selected antibodies and the best labeling conditions. The performance of proper controls, extensive revision of all staining controls, and comparison with stainings obtained by other research groups allowed us to conclude that antibodies against NCR1/CD335 (#ab199128) and FoxP3 (#ab75763) would not be suitable to integrate the mIHC panels due to positive labeling in the negative tissue control and wrong cellular localization, respectively. Only by identification and accurate characterization of expected staining patterns in well-defined tissue controls is possible to evaluate the quality of the technique and to monitor the impact of potential analytical changes. In addition, proper titrations of each antibody should have been done by serial dilution tests on contiguous sections to guarantee that a proper concentration would be applied in the tissue, avoiding unspecific staining and spillover of signal (Sun et al., 2021). Nevertheless, the final concentration of the selected antibodies was adjusted, when necessary, based on the intensity of the fluorescent signal presented on the positive tissue control and later on the tissue of interest.

One advantage of using cryopreserved tissues is the reduced autofluorescence presented by these samples in contrast to the strong endogenous fluorescence normally observed in FFPE tissues, especially in the blue-green range of the emission spectrum (Davis et al., 2014). Although later we observed a slight autofluorescence on the UV range of the spectrum while imaging the eFluor 450 directly-conjugated primary antibodies against CD11b and FoxP3, there was still a high fluorescent signal-to-background ratio. The reduced autofluorescence of our cryopreserved tissues could be attributed to the fixation method with PFA without methanol for 2 hours instead of PFA/formalin fixation overnight generally used to process the FFPE tissues (Davis et al., 2014).

Fluorescence channel spillover, also known as bleed-through or cross-talk, should be addressed when multiple fluorochromes are applied in a sample. A common solution for reducing cross-talk is unmixing of the individual fluorophore signals from the merged image post-imaging acquisition (Lopes et al., 2020). This solution normally requires an accurate spectral library of fluorescent spectral signatures (or fingerprints) matching the fluorophores used in the multiplexed sample and is particularly cumbersome for large-scale datasets (Lopes et al., 2020; Sadashivaiah et al., 2021). In order to obviate the need for spectral unmixing in our whole-slide images, we integrated up to six distinct fluorophores – eFluor 450, AF 488, AF 532, AF 594, ToPro-3/AF 647, and AF 680 – into the mIHC panels. The spectral separation of the fluorophores was also facilitated by the image acquisition using confocal microscopy. Particularly, a confocal microscope equipped with a laser light allows the manual adjustment of the emission wavelengths of each fluorophore without cross-talk from another probe (Lichtman & Conchello, 2005). Thus, laser confocal microscopy provides the laboratories with a tool to overcome few limitations related to intrinsic properties of available fluorophores.

Conventional mIHC involves incubation of antibody cocktails on a single sample, which requires those antibodies to be produced in different host species. However, since the majority of the immune cell antibodies is produced in rat, directly-conjugated and -labeled antibodies were included into the final mIHC protocols. As previously reported by Hunka and colleagues (Hunka et al., 2020), we also faced some challenges during the selection of conjugated primary antibodies due to their reduced commercially availability and/or limited fluorophore options. To overcome this hurdle, upon selection and validation of directly-conjugated antibodies, we purchased Antibody Labeling Kits to directly label validated, unconjugated primary antibodies with the desired fluorophore. Labeling of antibodies also revealed to be challenging with the following possible limitations needed to be considered: 1) the random binding of the dye molecules to the antibody may have an impact on the epitope binding site; and 2) the under or overlabeling can result in little or no fluorescence displayed by the directly-labeled antibody. These limitations probably explain the low efficacy of the antibody labeling, leading to only two primary antibodies being successfully directly-labeled (CD11c labeled with AF 488 and CD45R/B220 labeled with AF 594). Moreover, the direct method of staining lacks the signal amplification provided by secondary antibodies used in the indirect method of IF (Becheva et al., 2018), reflecting in a lower fluorescent signal presented by the directly-conjugated and -labeled primary antibodies.

Quantum dots, or Qdots, have been reported as having substantial advantages over traditional organic fluorophores, such as AF or Cy, for a variety of biological imaging (Matea et al., 2017; Zrazhevskiy & Gao, 2013). These fluorescent nanocrystals exhibit unique optical properties, including narrow emission spectra, improved brightness, and large Stokes shift (i.e., difference between the maximum absorption and emission of a fluorescent molecule), and photo-stability, which make them ideally suitable for multiplexed profiling. These reasons convinced us to purchase a secondary antibody conjugated with Qdot 585 to detect the CK18 marker. Contrarily to previous reports, the purchased Qdot 585 dye did not provide a specific labeling or stronger fluorescent signal when compared to AF 488 fluorophore. These issues could be attributed to the

following reasons: 1) the steric hindrance shown by the Qdots, which might be responsible for the reduced binding between these nanocrystals and the epitope of interest; and 2) to the usage of PBS solution as washing buffer and/or Vectashield® mounting medium (Abraham et al., 2017; Prost et al., 2016). We ended up not integrating the Qdot 585 into the final mIHC panels, replacing this probe by the secondary antibody conjugated with AF 680 for the detection of tumor cells.

During the assemble of the mIHC protocols, especially the one for the detection of IICs, we noticed that the position of the antibody incubation within the multiplexed staining panel was an important factor that may affect the signal of the added antibody as well as the remaining markers within a panel. This issue was previously described by Gorris and colleagues, who attributed the reduction of signal to the disruption of epitopes and removal of fluorophores due to repetitive epitope retrieval/microwave treatment (Gorris et al., 2018). Since the staining with cryopreserved sections does not require antigen retrieval step and we did not attempt to inactivate fluorophores using this heating method, we hypothesize that the problem might be related to reduced photostability of certain directly-conjugated and -labeled antibodies, namely Ly6G/Ly6C conjugated with AF 532 and CD11c labeled with AF 488, which may be affected by the combinatory incubation with other primary antibodies and/or by the repetitive washing steps. Therefore, we compared our multiplex staining results throughout the whole optimization process, starting from optimized uniplex to duplex stainings until eventually the 6-color mIHC protocols were established.

Whole-slide imaging acquisition is typically conducted with a confocal microscope equipped with low NA objectives that increase the speed of acquisition, but produce images of modest resolution unsuited to detect weak fluorophores and/or densely packed cells present within a tissue sample (Blom et al., 2017; Gerner et al., 2012). Throughout the development of the mIHC panels, we noticed that the 20x objective was suboptimal for accurate signal-cell allocation, not providing sufficient resolution to obtain morphological details. These issues were resolved with the 40x/1.30 NA objective, and whole-slide images were acquired. Thus, besides providing accurate signal allocation of multiple fluorophores, confocal microscopy also allows the scan of entire tissues in a reasonable time. Importantly, the quality of the obtained image was a major benefit that posteriorly permitted volumetric tissue reconstruction and imaging analysis. We performed whole-slide image analysis using Imaris, a software widely used for single cell segmentation (Gerner et al., 2012; Li et al., 2019). As discussed by Blom and colleagues (Blom et al., 2017), cellular segmentation can be challenging due to the diversity of cell morphologies in a single tissue section, to the lack of the intrinsic 3D structure of the tissue, and cell clusters and/or overlapping usually observed in solid tumors. Since manual tissue image analysis was not an option, due to its subjective natural and the impracticality to analyze whole tissue sections comprising thousands of cells, we tested the cell segmentation accuracy provided by Imaris (data not shown). The results of manual counting of cells of interest were comparable with the ones obtained by the segmentation algorithms in Imaris, being this software then used for our image analysis. However, we should point out that Imaris is not an open-source software, requires specific computational and dedicated workstations to process large datasets, and the

segmentation can be affected by software instability, as also reported by other researchers (Li et al., 2019). Such limitations are likely to be temporary, as substantial interest in whole-slide imaging has promoted the development of novel open-source solutions, such as the CellProfiler platform (Blom et al., 2017; Kamentsky et al., 2011), for data handling and analysis.

It is clear that mIHC is more sensitive than brightfield imaging and provide more information than uniplex IF staining, since it allows *in situ* identification of multiple markers on one single section. If additional markers need to be detected, cyclic mIHC (Banik et al., 2020; Gerdes et al., 2013; Lin et al., 2018) or alternative techniques are likely more appropriate, such as imaging mass cytometry, time-of-flight mass cytometry (CyTOF), or CO detection by indEXing (CODEX) (Tan et al., 2020). However, like any technique, these methods also present disadvantages, including specialized equipment, high cost to stain a single slide, impossibility of whole-slide imaging, and requirement for specialized bioinformatic support for data analysis. Regardless of the imaging techniques available, it is imperative for the users to understand the hypothesis and goals of their own work/research before they decide on which method would be more suitable to achieve their aims.

In conclusion, our study validated and optimized 6-plex mIHC protocols for frozen mouse PDAC tissues to identify myeloid and lymphocytic populations. In a relative short staining schedule time, every antigen was unequivocally identified by a single fluorophore without any extensive management of the slides nor necessity of additional equipment besides a confocal microscope. In summary, we have provided an easy to follow and repeatable procedure on how to develop a mIHC protocol having consistent staining for each marker and to obtain high-quality images and reliable imaging analysis data. We believe these data would provide a framework that enables a more robust and consistent development of multiplexed imaging techniques in a research lab setting, and fully customizable antibody panels would make this system a viable platform for oncological research.

Chapter I, Part B: Characterization of the tumor microenvironment according to driver mutation and differentiation status of pancreatic ductal adenocarcinoma

In this study, we investigated the TME in PDAC specimens using histopathology, histocytometry, and mIHC analyses. The imaging approach and analysis enabled quantitative assessment of stromal and immune infiltrates and provided comprehensive cellular spatial information. Our findings could lead to the identification of correlations between clinical and biological features that may bring great insights into the pathogenesis of PDAC and help in the development of novel immunotherapeutic strategies. Tissues were harvested from mice harboring different driver mutations, namely *Kras*^{G12D}, *Pik3ca*^{H1047R}, or *Braf*^{V637E}, and, in the case of PKP cohort, the distinction between differentiated and undifferentiated tumors was also made according to the histopathology analysis. We studied the cellular composition of tumor, stromal, and immune cells within these tissues based on histocytometry analysis. Furthermore,

comparison and quantification of specific immune cell populations as well as assessment of cell cross-talk by calculation of shortest distance amongst distinct cell types were performed using mIHC technique complemented by imaging acquisition with Leica TCS SP8 confocal microscope and post-processing imaging analysis with Imaris software.

Tumor driver mutations have proved to have an impact on the malignant cells as well as to play a role on the surrounding TME (Wellenstein & de Visser, 2018). However, no one to the best of our knowledge has systematically studied the impact of specific oncogenes on the TME of PDAC. Due to the high frequency of mutant *Kras* in PDAC, many studies have been conducted to investigate the effect of this genetic alteration on the microenvironment (Liou et al., 2015; Tape et al., 2016). In contrast to *Kras*, much less is known about the impact of tumor-related *Pik3ca* and *Braf* mutations. To better understand and study the TME on tumors generated by distinct genetic aberrations, we used GEMMs harboring solely an oncogenic mutation and characterized their respective microenvironments. In addition, the infiltration of immune cells has been shown to be correlated with the differentiation status of the tumor (Goebel et al., 2015; Helm, Mennrich, et al., 2014). Thus, besides the characterization of three distinct driver mutations, we also attempted to include both differentiated (G1/G2) and undifferentiated (G4) tumors in our cohorts. The inclusion of these two differentiation status was only possible in the Kras cohort. As observed in human PDAC (Lemstrova et al., 2017; Schonleben et al., 2006), our Kras mice developed both differentiated and undifferentiated tumors, while most Pik3ca-driven carcinomas presented poor or moderate invasiveness. Regarding the Braf animals, as previously described by Collisson and colleagues (Collisson et al., 2012), these mice did not develop PDAC tumors, however the PanIN lesions observed in the Braf tissues were generally surrounded by an abundance of stromal cells. Hence, we analyzed four groups of tissues: Kras, differentiated; Kras, undifferentiated; Pik3ca, differentiated; and Braf, PanINs.

Histocytometry analysis has the capacity to determine both individual cellular identities and the precise spatial distribution of multiple populations within highly heterogeneous and densely packed biological tissues, such as tumor tissues (Gerner et al., 2012). We applied the histocytometry analysis to directly visualize tumoral, stromal, and immune populations within the selected tissues and found that Kras differentiated tumors had a slightly higher desmoplastic reaction compared to undifferentiated tissues. In addition, Pik3ca-driven presented higher abundance of stromal and immune cells compared to the Kras differentiated tissues. These results may be explained not only by the distinct genetic aberrations that lead to different TME content, but also by the high abundance of malignant cells in Kras tumors. Our results corroborate an early study that showed an inverse correlation between tumor cellularity and stroma content in human PDAC tissues (Heid et al., 2017). In addition, poorly differentiated tumors have worse prognosis and reduced therapeutic response, which can also be correlated with the lower desmoplastic reaction in these carcinomas. Since our Kras mice carried one conditional floxed allele for *Trp53*, which usually reduces the survival time of the animals, it was not possible to draw any conclusion regarding the correlation between the TME content and the prognosis in our study.

The three fluorescent panels established herein enabled simultaneous evaluation of myeloid and lymphoid cell presence, respective ratios, and cellular cross-talk in cryopreserved tumor tissues. Our quantification analysis results revealed how the TME composition varies, namely the immune cell compartment, dependently on the PDAC driver mutation. Since macrophages were already described as being one of the most abundant immune cells present in the TME (Panni et al., 2019; Steele et al., 2020; Thorsson et al., 2018), it was not surprising to find that these myeloid cells were highly present in all of our cohorts. In contrast, it was striking that the mutant *Pik3ca* promoted an infiltration of AICs, especially T lymphocytes, to the microenvironment. The Pik3ca tumors were previously reported to have a T cell-rich TME in breast cancer, being the infiltration of these lymphoid cells probably promoted by PI3K/AKT signaling-mediated activation of the NF-κB pathway (Payne et al., 2015; Yang et al., 2008). Predicting that the composition of the T cell populations within the TME and their cross-talk may be detrimental to restrain tumor progression, we also analyzed these cells as well as their spatial distribution within the microenvironment. We found a higher abundance of Th cells and Tregs among all tumors and these T cell subpopulations also showed substantially high contact with $CK18^+$ cells. These results could reflect an immunosuppressive microenvironment that led to tumor restraining (Y. Zhang, J. Lazarus, et al., 2020), especially the ones harvest from animals harboring *Braf* mutation. Regarding the CTLs, the Kras differentiated tumors presented a lower amount of the $CD8^+$ T cells compared to the undifferentiated tissues. This observation contradicts early studies that described a reduction of CTLs in undifferentiated/advanced stage tumors compared to well-differentiated ones (Goebel et al., 2015; Helm, Mennrich, et al., 2014). Moreover, a higher number of interactions between CTLs and Th cells were detected in Pik3ca-driven tumors. These two T cell subpopulations are known to be cooperators in restraining tumor cell growth (Sivaram et al., 2019). $CD4^+$ Th cells secrete cytokines and chemokines, such as IL2 and IFNγ, that lead to the recruitment and enhance proliferation of $CD8^+$ CTLs, which ultimately have a cytolytic function in the tumors (Bos & Sherman, 2010). Altogether, our findings could yield valuable clues that not only provide an insight into the microenvironment of distinct PDAC oncogenes, but also benefit the development of novel and more targeted immunotherapies for this cancer entity.

Our work involving the mIHC technique clearly has some limitations, namely the inclusion of IIC and AIC markers in separate panels, which makes it impossible to study the interactions between the cells from these two immune systems. Nevertheless, we believe our work could be a starting point to answer other scientific questions regarding the interactions between myeloid and lymphoid cells, the T cell status within the TME, and even the composition of PDAC microenvironment in other genetic backgrounds. Since macrophages were reported to mediate anti-tumor immune responses orchestrated by $CD4^+$ T cells and to impede $CD8^+$ T cells from reaching tumor cells (Fauskanger et al., 2018; Peranzoni et al., 2018), it would be interesting to study the interactions between macrophages and the different T cell subpopulations in our tissues. These results could be achieved by modifying the T cell mIHC panel, replacing the general T cell marker CD3 for the macrophage marker F4/80, for example. Furthermore, since

the lymphocytic infiltrates have a high impact in the prognosis and response to therapy, it would be interesting to investigate the phenotype, differentiation, or activation status of T cells observed in the Pik3ca tumors. For this, a new mIHC or fluorescence-activated cell sorting (FACS) panel needed to be developed using makers, such as CD57, CD39, Tim3, and Lag3 (Sivakumar et al., 2021). Finally, taking advantage of the variety of GEMMs available in our research group, it would be valuable to apply our established mIHC protocols to other mouse models, such as animals harboring *Cdkn2a* or *Smad4* mutations, expanding the analysis and elucidating our knowledge regarding the TME on distinct clinically relevant genotypes.

Methods, such as IHC staining and FACS, have been used as gold standards to characterize the TME composition within a sample (Petitprez et al., 2018). However, each of the methods has its technical limitations, such as detection of limited number of cell type-specific markers and might not be generally applicable as a high-throughput technique. In theory, it is possible to infer the cancer, stromal, and immune cell content of a solid tumor from its bulk gene expression profile if reference gene expression profiles for each tumor-associated cell type can be established (Schelker et al., 2017). Based on scRNA-seq data, we defined signatures of cellular types present in PDAC, including the immune populations detected by mIHC. This strategy allowed us to assign genes that characterize each cell type, increasing the cell-specific identification and significantly reducing the spillover effect by removing genes commonly expressed by distinct populations (Sturm et al., 2019). However, as previously observed by Racle and colleagues (Racle et al., 2017), Th cells and Tregs cells were hard to distinguish, due to their highly similar gene expression profiles. For this reason and to guarantee a more accurate analysis, we grouped the Th cells and Tregs into a single "$CD4^+$ T cell" category. Regardless of this hurdle, RNA-seq bulk tumor data and deconvolution approaches presented here enable the estimation of correlations among cancer and TME cells, and of the differently expressed genes between Kras and Pik3ca cohorts. One possible explanation for the differences observed between the tissue imaging and sequencing data could be the inclusion of different animals in each method. So, we believe that it would be valuable to link the mIHC and RNA-seq analyses from the same animal. Nevertheless, we do not exclude the hypothesis that sampling of different areas of the tumor may also explain the variances between the two methods. Further validation of the cellular correlations identified by RNA-seq bulk tumor data needs to be performed using a staining technique. In addition, future analyses are planned, including the identification of the differently genes involved in cancer cell-intrinsic or -extrinsic mechanisms, taking special advantage of the available bulk tumor-cell line pairs and performing the same analysis in the RNA-seq data generated from PCCs. This would allow us to predict the contribution of the tumoral component as well as the impact of its surrounding microenvironment on gene expression and on signaling pathways (Li et al., 2018; Miller-Ocuin et al., 2019). Thus, with the development of novel and more advanced imaging and sequencing methods, we envision that our understanding of TME cells and their role can be greatly improved.

To summarize, imaging techniques have proven their value in a wide range of *in vitro*, *in vivo*, and *ex vivo* tissue characterization applications. Histocytometry and mIHC are not

exceptions and are particularly valuable in characterizing the cellular composition of the TME and the spatial distribution of different cell entities. Our observations indicate that tumor genetic characteristics affect the TME abundance and the spatial distribution and cellular interactions within the microenvironment may provide insights of the role of the inflammatory cells in PDAC. Thus, imaging techniques can also be effectively used as a metric for predicting clinical outcomes and therapeutic responses. In addition, together with mIHC, RNA-seq data analysis could provide important insights into potential interactions within the tumor and guide future development of biomarkers and therapeutic targets in PDAC.

Chapter II: Role of *Cdh1* deletion *in vivo* and *in vitro*

The ability of epithelial cells to acquire a mesenchymal phenotype is critical to fundamental biological processes, such as embryonic development, differentiation, regeneration, and tumorigenesis (Thiery et al., 2009). In cancer, downregulation or loss of E-cadherin expression has been widely implicated in the progression, invasiveness, and dissemination of malignant cells to distant organs (Corso et al., 2013; Liu et al., 2020; Otake et al., 2021). With regard to PDAC, the reduction or loss of this epithelial protein expression has been observed in up to 60% of human PDAC samples, especially in undifferentiated tumors (von Burstin et al., 2009). In pathological conditions, the abrogation of E-cadherin expression is frequently linked to EMT induction and consequently correlated to poor prognosis and development of resistance to chemotherapy. However, proof of a role of E-cadherin downregulation as a major driver or a consequence of EMT is still lacking. Here, we presented *in vivo* evidence that genetic deletion of *Cdh1* does not increase tumor invasiveness of PDAC, although there is an acceleration of the tumor formation, shortening of lifespan of mice from both conditional and inducible *Cdh1*-KO mouse models, and increasing of the incidence of cystic tumors. Moreover, the mosaic deletion of *Cdh1* in the tamoxifen-inducible GEMM also leads to a heterogenous malignant cell composition of the primary and secondary tumors, both presenting E-cadherin-negative and -positive lesions, and to a decreased frequency of hepatic metastases formation. Furthermore, our results showed that *Cdh1* deletion in cell lines does not promote a switch to a mesenchymal morphology and does not confer a growth advantage to these cells *in vitro*. In addition, ssGSEA revealed that the majority of the *Cdh1*-KO cells presents downregulation of EMT-, inflammation-, and apoptosis-related signaling pathways. Finally, in the orthotopic model, the mice implanted with *Cdh1*-deficient clones present a lower frequency of liver metastases and a higher incidence of ascites formation compared to the animals inoculated with $Cdh1^{fl/fl}$ clones.

E-cadherin is considered to act as a tumor suppressor, with mutations in its encoding gene contributing to tumorigenesis, invasion, and metastasis (Bruner & Derksen, 2018). In contrast to breast and gastric cancers, pancreatic tumors present a lower prevalence of somatic mutations of *Cdh1* with only up to 2.0% of human samples (3 in 143 samples analyzed) possessing a nucleotide substitution (Busch et al., 2017). The data reported by Busch and colleagues is corroborated by publicly available datasets, such as the cBioPortal for Cancer

Genomics, where from 848 PDAC patient samples only 0.6% showed an alteration in this epithelial gene (3 samples presented amplification of *Cdh1*, 1 missense mutation, and 1 inframe mutation). Thus, although the percentage of pancreatic patients possessing genetic alterations in *Cdh1* gene is low compared to other cancer entities, it is important to continue investigating the role of E-cadherin in cancer, namely in pancreatic cancer, and unravel the potential consequences of loss of function or expression of this epithelial protein in tumor cells. Mouse models employed in this study combined the conditional or inducible deletion of *Cdh1* and mutational *Kras* activation in pancreas. Both GEMMs showed loss of E-cadherin expression shortens the survival time of the respective animals. This result might not be particularly surprising given the fact that previous studies have already reported that downregulation of E-cadherin expression is associated with worst prognosis of patients with pancreatic, prostate, or gastric cancer (Chen et al., 2017; Corso et al., 2013; Ferreira et al., 2018). However, contrarily to the previous reports, the present work does not show evidence that *Cdh1* deletion induces EMT or increases the invasion, migration, and metastatic capacity of the malignant cells. On one hand, cell lines completely recombined for *Cdh1* did not present a more mesenchymal morphology, and, on the other hand, upon *in vivo* ablation of this gene, $Cdh1^{fl/fl}$ animals showed a lower percentage of high grade tumors when compared to control mice, indicating that decreased expression of E-cadherin in malignant cells does not increase their invasiveness. The histopathological analysis can be explained in part by the high incidence of cystic tumors in the tamoxifen-treated $Cdh1^{fl/fl}$ animals. Cystic lesions are considered to be precursors to invasive pancreatic cancer and somatic mutations, such as in *Rnf43*, PI3K (*Pik3ca*, *Tsc2*) and Wnt (*Apc*, *Ctnna2*, *Ctnnb1*) signaling pathway-related genes, were identified in these lesions (Matthaei et al., 2011; Noe et al., 2020). In the ssGSEA data, we observed different regulation levels of the Wnt/β-catenin signaling as well as of the PI3K/Akt/mTOR pathway among the *Cdh1*-depleted cell lines, but these levels do not seem to be correlated to the cystic tumor type presented by the animals. Thus, these findings argue that *Cdh1* is relevant to PDAC progression, growth, and local invasiveness of tumor cells. Further in-depth mechanistic characterization will answer whether *Cdh1* is a promising target for therapeutic development. Therefore, in the future, whole-exome and transcriptome analyses will be performed for *Cdh1*-deficient tumors to identify key genetic aberrations and pathways that may be future biomarkers or targets for cancer therapy and to unveil potential correlations with the formation of cystic lesions.

Metastases contribute to most cancer-related deaths. Developing successful therapeutic approaches to prevent and treat metastatic diseases requires understanding how malignant cells detach from the primary tumor, survive in the bloodstream, and colonize distant organs. If loss of *Cdh1* would be one of the mechanisms that induces cancer cells to dissociate from the primary tumor mass, then one would expect that animals with a reduction of E-cadherin expression in the primary carcinomas would be more likely to present metastases in secondary organs. In the present study, no clear correlation between *Cdh1* deficiency in pancreatic tumors and increased metastatic rate was detected. Yet, interestingly, our tamoxifen-induced $Cdh1^{fl/fl}$ mice developed fewer liver metastases and showed an increased incidence of lung metastases compared to the

control animals. The higher percentage of lesions in the lungs may be associated with *Cdh1*-related intrinsic mechanisms and/or with the fibrotic microenvironment of the lungs, which might be suitable for the metastatic colonization and growth of the tumor cells from tamoxifen-treated animals. In a breast cancer model, malignant cells were shown to secrete ILs, such as IL1α and IL1β, which in turn induce the production of chemokine ligands Cxcl9 and Cxcl10 in lung fibroblasts, fueling the growth of lung metastases (Pein et al., 2020). Regardless of potential tropism of *Cdh1*-KO PCCs to certain secondary organs, we observed a higher incidence of E-cadherin-negative of lesions in both liver and lung tissues of tamoxifen-induced *Cdh1*$^{fl/fl}$ animals. This result contradicts a previous study by Reichert and colleagues, who reported that sequential and mosaic *Cdh1* deletion in the primary tumor exerts a selective pressure to form E-cadherin-positive liver metastases and E-cadherin-deficient lung metastases (Reichert et al., 2018). This difference is likely explained by the small sample size in our study compared to the cohort analyzed by Reichert and colleagues. Furthermore, we also detected metastases expressing E-cadherin in metastatic tissues from animals treated with tamoxifen. One explanation for our findings might be connected to the mosaic deletion of *Cdh1* in the primary PDAC tumors of tamoxifen-induced mice that creates a malignant mass composed by *Cdh1*-deficient and -proficient cells, which posteriorly may give rise to metastases with distinct E-cadherin expression profiles. Regarding the dissemination and seeding of tumor cells in secondary organs, metastases have been reported to originate from a single clone (monoclonal seeding) or multiple clones (polyclonal seeding) (Hu et al., 2020; Maddipati & Stanger, 2015). Using multi-color lineage tracing technology in PDAC GEMMs, Maddipati and Stanger demonstrated that metastases are polyclonally seeded by distinct tumor sub-clones and that clonality during metastatic growth may lead to either monoclonal or polyclonal expansion (Maddipati & Stanger, 2015). Since we did not account for individual lesions composed by both E-cadherin-expressing and -deficient malignant cells, we reasoned that the metastases observed in our inducible mouse model may be the result of distinct single clones detaching from the primary mass, spreading into the secondary organs, and expanding independently. In addition, the presence of E-cadherin-negative metastatic lesions also argues with the requirement of MET to drive the formation of metastases. MET, the phenotypic reverse process to EMT, is considered to be one of the steps required to complete the metastatic cascade with the tumor cells reacquiring their epithelial properties, namely the re-expression of E-cadherin, to colonize the secondary organ (Aiello et al., 2018; Padmanaban et al., 2019; Williams et al., 2019). Padmanaban and colleagues reported that E-cadherin is crucial for metastasis formation, acting as a survival factor during the detachment from the primary tumor, systemic dissemination, and seeding in secondary organs by limiting reactive oxygen-mediated apoptosis (Padmanaban et al., 2019). This leads us to hypothesize that the lack of E-cadherin expression in our *Cdh1* models may activate compensatory mechanisms, such as the upregulation of other cell-to-cell adhesion genes, in the tumor cells, explaining not only the retention of cell-cell contact in metastatic cells, but also the epithelial phenotype presented by *Cdh1*-KO cell lines. These compensatory mechanisms were already reported in non-tumorigenic breast cells, where loss of *Cdh1* from the AJs was associated with an upregulation of cell-cell

adhesion genes encoding proteins involved in other intercellular junctions including TJs and GJs, while genes related to cell-substrate adhesion, namely ITGA1, COL4A2, and COL8A1, were significantly downregulated (Chen et al., 2014). In the future, further work will be performed to histologically analyze a bigger cohort of metastatic tissues from tamoxifen-induced *Cdh1*$^{fl/fl}$ animals to clarify whether there is a preference of *Cdh1*-deficient tumor cells to establish metastases in the lungs. Regarding the TME of tissues metastasized by *Cdh1*-KO cells, it would be interesting to look into chemoattractant proteins that represent candidates for a potential cross-talk between metastatic *Cdh1*-deficient PCCs and microenvironment cells. Moreover, multiregion sampling from PPT and metastatic tissues, histological, and RNA-seq analyses to integrate the morphologic and transcriptomic features of the primary and secondary tumors would allow us to extensively assess the intratumor heterogeneity of the primary tumor of the tamoxifen-induced *Cdh1*$^{fl/fl}$ mice and understand how it affects the metastatic dissemination. Finally, to further analyze compensatory mechanisms for loss of *Cdh1*, it would be interesting to investigate rather the downregulation of E-cadherin also leads to upregulation of TJ and GJ proteins in *Cdh1*-deleted PDAC tissues and cell lines.

Using primary murine pancreatic tumor cell lines, we provided experimental evidence supporting that the genetic deletion of *Cdh1* does not induce EMT nor significantly affects cell viability and growth *in vitro*. In addition to the majority of the *Cdh1*-KO malignant cells presenting an epithelial morphology, we also observed that these cells were characterized by a downregulation of EMT and apical junction signaling pathways while predicting the potential molecular mechanisms underlying the loss of *Cdh1* by bioinformatics analysis. This result was consistent with our hypothesis that *Cdh1* loss is not enough to drive EMT. However, in the ssGSEA, we also identified a small cluster composed by four *Cdh1*-KO cell lines, which presented an upregulation of the EMT signaling. Regarding their morphology, three of the cell lines had mixed characteristics and the fourth one presented a mesenchymal phenotype. Thus, even though these samples may have suffered a partial or complete EMT, it is more likely to be associated to other mechanisms rather than being a consequence of *Cdh1* deletion, since the upregulation of this signaling pathway was not observed in all the *Cdh1*-KO cells. Moreover, the ssGSEA also showed a differential expression of inflammation, and apoptosis signalings among the two clusters of *Cdh1*-depleted cells, being downregulated in most of these PCCs. Loss of *Cdh1* was already reported to influence the TME, namely the activity and recruitment of immune cells, in endometrial cancer and melanoma (Shields et al., 2019; Stodden et al., 2015). In endometrial cancer, inflammatory mediators, such as IL1β and S100a8, secreted by *Cdh1*-depleted tumor cells contributed to the stimulation and recruitment of macrophages into the TME (Stodden et al., 2015). In melanoma, low expression of E-cadherin in tumors showed to be related to reduced infiltration of $CD8^+$ $CD103^+$ lymphocytes, which in turn play a major role in effective tumor cell lysis (Le Floc'h et al., 2007; Shields et al., 2019). Since immune-mediated destruction of malignant cells is a major goal of immunotherapy and cells from the inflammatory system can play dual roles in tumorigenesis, further immune-profiling of E-cadherin-negative expressing tumors may reveal novel clinical strategies. Apoptosis or programmed cell death is crucial in the

regulation of tumor formation and blunting of therapeutic responses and can be initiated by intrinsic (also called mitochondrial) or extrinsic (also designated death receptor) cellular pathways (Ichim & Tait, 2016). Loss of E-cadherin has been reported to attenuate the extrinsic pathway of apoptosis, since the absence of this epithelial protein interrupts its bind to the cell-surface death receptors (DR)4 and DR5, thus leading to a reduction of caspase-8 activation (Lu et al., 2014). This previous study corroborates the downregulation of apoptosis signaling observed in our ssGSEA of *Cdh1*-KO cell lines, pointing a possible reason why these cells survived despite the depletion of this epithelial gene. Besides the different regulation levels of the mentioned signaling pathways, all the *Cdh1*-KO cells shared similar pathway expressions, such as downregulation of metabolism-related signalings and upregulation of proliferation-related ones. The cancer cells require core metabolic functions to support cell survival and proliferation, being fundamental a coordinated temporal regulation between metabolism and cell cycle (Kaplon et al., 2015). Together with Cdc20, E-cadherin is one of the essential coactivators of E3 ubiquitin ligase anaphase-promoting/cyclosome (APC/C), which targets crucial cell cycle proteins for proteasomal degradation (Li & Zhang, 2009). The decrease in the activity of APC/C-E-cadherin complex influences the proliferative responses in tumor cells. E-cadherin has also been associated with other metabolic player of cancer cells, the pyruvate kinase M2 (PKM2), which controls cell progression and survival through regulation of the glycolytic signaling pathway. Silencing of PKM2 induces the upregulation of E-cadherin, caspase 7, and Bad expressions and a decrease of MMP2 and MMP9, hypoxia-inducible factor 1-alpha, and VEGF, impairing cell proliferation and inducing apoptosis and cell cycle arrest (Miao et al., 2016). Although, these previous reports and our ssGSEA indicated a correlation between proliferation and E-cadherin, our *ex vivo* and *in vitro* analyses of the tamoxifen-inducible *Cdh1* model did not show an increase of proliferative cells upon *Cdh1* deletion. This difference may be in part explained by the fact that the ssGSEA was performed with cell lines established from the endogenous *Cdh1*-KO mouse model, while the other conclusions were taken throughout the characterization of the tamoxifen-inducible *Cdh1* GEMM. Thus, the deletion of this epithelial gene at early embryonic stages may favor the posterior growth of *Cdh1*-KO PCCs throughout the development of pancreatic tumor upon $Kras^{G12D}$ activation. In the future, it would be interesting to validate the data from the ssGSEA in PPT tissues from PKPE animals by performing stainings for immune cell markers (inflammation), Bcl-2 and cleaved caspase-3 (apoptosis), and Ki-67 (proliferation). In addition, transcriptome analysis will be performed for 4-OHT-treated $Cdh1^{fl/fl}$ cell lines and *Cdh1*-depleted clones and the comparison with the respective controls may identify another effector molecules and key mechanisms that are altered by the deletion of *Cdh1*.

Despite considerable and valuable findings made using cultured cells, this simplified *in vitro* system cannot faithfully recapitulate several physiological and pathological processes, lacking the complexity of the surrounding TME that may impact the cancer cell. Orthotopic implantations of $Cdh1^{\Delta/\Delta}$ and $Cdh1^{fl/fl}$ clones revealed a low incidence of liver metastases formation in animals engrafted with *Cdh1*-deficient clones, similarly to the metastatic potential observed in the tamoxifen-induced mice. Although, no lung metastases were observed in the

implanted animals, ascites formation was detected in 50% of the animals implanted with *Cdh1*$^{\Delta/\Delta}$ clones, as well as in 38.1% of the animals from the endogenous *Cdh1*-KO mouse model. The differences regarding the formation of pulmonary metastases observed between the tamoxifen-inducible and the orthotopic models may be partially explained by the fast process of tumor growth in the implanted animals that does not allow the malignant cells to reach and colonize the lungs. Additionally, in pancreatic cancer patients, the presence of ascites indicates advancement of disease, a grave prognostic sign, and a source of CTCs (Hicks et al., 2016). However, very little is known about the underlying mechanisms of ascites formation, and it remains unexplained why certain cancer cells preferentially accumulate in the peritoneal cavity and cause ascites rather than migrate to a secondary organ. Further histopathological analysis needs to be done to confirm the absence or presence of micrometastases in both liver and lung tissues of all implanted mice. Moreover, it would be interesting to explore if there is a correlation between *Cdh1* deletion and ascites formation by analyzing and comparing the transcriptome of CTCs collected from ascites of *Cdh1*-KO mice and the paired PPT cell line.

In summary, loss of *Cdh1* in pancreatic tumor cells does not enable independent growth, resulting in neither enhanced invasiveness *in vivo* and *in vitro*, nor leading to an EMT. However, the present study provides clear evidence for *Cdh1* deletion promoting worse prognosis and leading to hepatic and pulmonary metastases formation via sub-clonal seeding. Thus, our results support the hypothesis that KO of *Cdh1* is not a major contributor to EMT and cell detachment from the primary tumor mass and may only play a limited role in tumor metastasization. Future studies regarding the metastatic properties of *Cdh1*-deficient tumor cells and their interactions with the microenvironment of secondary organs should be performed to provide precise understanding of the molecular mechanisms underlying this process and ultimately highlighting novel therapeutic targets in PDAC.

Disclosures

The work described in this doctoral thesis is composed by mouse lines, experiments, and data analysis shared with other members from Prof. Dr. med. Dieter Saur's research group.

In Chapter I, together with Tatiana Martins, *Pdx1-Cre; LSL-Kras$^{G12D/+}$; Trp53$^{lox/+}$* (PKP), *Pdx1-Cre; LSL-Pik3ca$^{H1047R/+}$* (PPI3K), and *Pdx1-CreER^{T2}; LSL-Braf$^{V637E/+}$* (PBR) mouse lines were bred, weekly monitored, and sacrificed. Selection of the PKP, PPI3K, and PBR cohorts by H&E staining and histocytometry analysis were performed in collaboration with Tatiana Martins. Bulk tumor RNA-seq data analyses, namely correlation matrixes, KEGG analysis, and volcano plot representation between PK and PPI3K samples, were performed by Fabio Boniolo.

Regarding the work described in Chapter II, breedings, mice dissection, and establishment of primary murine PCCs from *Cdh1* mice were done in part by Dr. Kathleen Schuck. The data analysis was performed by Tânia Santos, except for ssGSEA done by Fabio Boniolo.

Acknowledgements

Hereby, I would like to thank everyone who contributed to the success of this PhD thesis.

Above all, I thank Prof. Dr. med. Dieter Saur for giving me the opportunity to work on the interesting projects that compose this thesis, for his advice, valuable comments, and support on the projects and revision of the thesis.

I owe my gratitude to Prof. Dr. Marc Schmidt-Supprian and Dr. Jan Böttcher for their kindness being members of my thesis committee and for promoting fruitful discussions and providing suggestions for the advancement of the projects.

I would like to thank Tatiana Martins for the synergistic work, constant discussion and sharing ideas, and Fabio Boniolo for his bioinformatic analyses, who contributed for the development of the project regarding the characterization of the TME in PDAC. In addition, I thank Dr. Kathleen Schuck for her previous fundamental work on the *Cdh1* project, breeding and dissecting mice and generating primary murine pancreatic tumor cell lines.

I would also like to thank Bettina Kratzer, Raphaela Blum, and Desislava Zlatanova from the TUM Graduate Center for the organization of the PhD Program Medical Life Science and Technology and their help with any questions concerning my graduation.

Furthermore, I owe my gratitude to…

… Dr. Chuan Shan, Dr. Markus Tschurtschenthaler, and Dr. Sabine Klein for the discussions and suggestions during the establishment of the mIHC panels.

… Yuexin Chen for the advice, discussion, and help concerning bioinformatical analysis of RNA sequencing data.

… Dr. med. vet. Katja Steiger and Nils Wirges for the histopathological evaluation of the *Cdh1* pancreatic tumor tissues.

… Dr. Chuan Shan (discussions and changing ideas), Barbara Seidler and Mingsong Wang (establishment of the *Cdh1* recombination PCR), Chen Zhao and Joanna Madej (generation of *Cdh1* clones), Chiara Falcomatà, Stefanie Bärthel, and Saskia Ettl (orthotopic implantations) for supporting and helping during the development of the *Cdh1* project.

… Joanna Madej for being my mouse partner and for helping with all mice-related work.

… Antonio Zaurito and Jack Barton for all the help with the FACS machine and respective data analysis.

… Magdalena Zukowska, Markus Raspe, Junika Pohl, and Kim Laus for the excellent technical support.

… all animal caretakers from the Zentrum für Präklinische Forschung, especially Dr. med. vet. Abebe Ashagire, Ilijana Malbasa, Ümit Karsli, Marina Geisler, and Susanne Frank, for caring for the mice.

… Dr. Christian Veltkamp and Dr. Markus Tschurtschenthaler for kindly revising the Abstract and Zusammenfassung.

… all other colleagues for the scientific discussions in and out the lab meetings.

Finally, I especially thank to my family and my friends who always supported and believed in me. Without them, my dissertation would not have been possible.

Especial thanks/Agradecimentos especiais

To Chen, for your brutal honesty that so many times made me so angry and for being the "dramaless" person that I needed so many times. I am still not sure if the purpose of my life was to come here and meet you, but it was a great honor to share this experience with you, man!

To Asia, for all the weird and amazing memories throughout these years, for all the thousands of memes that compose our Messenger conversation, and for always remind me what is the best of me. Never forget these two phrases: "*you is kind, you is smart, you is important*" and "*flowers bloom when they're ready*".

À Tatiana, por toda a galhofa depois das seis da tarde (quer dizer, nos últimos tempos nem precisavam de ser seis!) que fazia animar o espírito e lembrar que uma pessoa tem de apalhaçar e não levar tudo muito a sério. Não haverá melhor par de portuguesas na história do AG Saur!

To Krauß, thank you for your kindness and caring and cookie dough Ben & Jerry's and bear hugs that would always come in a good timing!

To Doctor Meng Lei, for always smiling from across the hall after hearing me scream "MENG LEI!" and for your strong and straightforward opinions and statements that would make anyone speechless. I will always be grateful to have meet you!

To Leila, for all the breaks in the rooftop and all the times that you called simply to ask "How are you, guuuuuurrl?".

To Bianca, for obliging me to leave my house, for sharing her amazing music taste with me and for showing me the best "bolos de arroz" in Munich!

To Jeannine, for being the second most chaotic bench partner ever, for allowing me to mock your disorganization, but also for your young, energetic, kind spirit that would always light the room.

To Daniel, for taking care of me in my last weeks in the lab and for our late evening karaoke/DJ sessions!

Ao Tides, por me trazeres de volta a chão firme quando tudo me parecia o fim do mundo e por me mostrares que isto tudo não passa de “algo para nos satisfazer o ego”!

À Mel, por todos os “motivational penguins” e pela amizade e telepatia que não deixam de funcionar apesar dos quilómetros que nos separam.

À Reis, por teres sempre os braços abertos para me receber quando estava a dar em doida aqui e pelas memórias passadas e que as futuras sejam ainda melhores!

À Sara, por todas as nerdices e pela excelente competição pelo título de pessoa que mais doces recebeu durante o doutoramento (vou autoproclamar-me vencedora desse título, como é óbvio!).

À Vinte, por me lembrares que, apesar da distância, nada muda e que estás sempre lá para mim! Gosto milhões de ti!

À Jámon, por todos os desabafos e amarguras partilhadas que acho que foram terapêuticas para ambas.

À Dade que me chama “Senhora Doutora” desde que sai da maternidade (quase)! Agora sim o título será real, mas é mais: Tânia Custódio Santos, Ph.D..

À minha titia Rute, a quem eu agradeço todo o amor, todas as fotografias de comida partilhadas e as palavras de conforto que só tu sabes expressar.

À minha mãe, obrigada pelos risos, por fazeres a secretária carregar encomendas de cinco quilos, por ouvires as minhas reclamações, por seres a mulher forte que és.

E, por fim, mas certamente não menos importante, ao meu mano, porque, sem ti, certamente não seria a pessoa que sou hoje. Obrigada!

References

Abel, A. M., Yang, C., Thakar, M. S., & Malarkannan, S. (2018). Natural Killer Cells: Development, Maturation, and Clinical Utilization. *Front Immunol*, *9*, 1869. https://doi.org/10.3389/fimmu.2018.01869

Abraham, L., Lu, H. Y., Falcao, R. C., Scurll, J., Jou, T., Irwin, B., Tafteh, R., Gold, M. R., & Coombs, D. (2017). Limitations of Qdot labelling compared to directly-conjugated probes for single particle tracking of B cell receptor mobility. *Sci Rep*, *7*(1), 11379. https://doi.org/10.1038/s41598-017-11563-9

Ahlgren, U., Jonsson, J., & Edlund, H. (1996). The morphogenesis of the pancreatic mesenchyme is uncoupled from that of the pancreatic epithelium in IPF1/PDX1-deficient mice. *Development*, *122*(5), 1409-1416. https://www.ncbi.nlm.nih.gov/pubmed/8625829

Aiello, N. M., Maddipati, R., Norgard, R. J., Balli, D., Li, J., Yuan, S., Yamazoe, T., Black, T., Sahmoud, A., Furth, E. E., Bar-Sagi, D., & Stanger, B. Z. (2018). EMT Subtype Influences Epithelial Plasticity and Mode of Cell Migration. *Dev Cell*, *45*(6), 681-695 e684. https://doi.org/10.1016/j.devcel.2018.05.027

Alagesan, B., Contino, G., Guimaraes, A. R., Corcoran, R. B., Deshpande, V., Wojtkiewicz, G. R., Hezel, A. F., Wong, K. K., Loda, M., Weissleder, R., Benes, C. H., Engelman, J., & Bardeesy, N. (2015). Combined MEK and PI3K inhibition in a mouse model of pancreatic cancer. *Clin Cancer Res*, *21*(2), 396-404. https://doi.org/10.1158/1078-0432.CCR-14-1591

Alexandrov, L. B., Nik-Zainal, S., Wedge, D. C., Aparicio, S. A., Behjati, S., Biankin, A. V., Bignell, G. R., Bolli, N., Borg, A., Borresen-Dale, A. L., Boyault, S., Burkhardt, B., Butler, A. P., Caldas, C., Davies, H. R., Desmedt, C., Eils, R., Eyfjord, J. E., Foekens, J. A., Greaves, M., Hosoda, F., Hutter, B., Ilicic, T., Imbeaud, S., Imielinski, M., Jager, N., Jones, D. T., Jones, D., Knappskog, S., Kool, M., Lakhani, S. R., Lopez-Otin, C., Martin, S., Munshi, N. C., Nakamura, H., Northcott, P. A., Pajic, M., Papaemmanuil, E., Paradiso, A., Pearson, J. V., Puente, X. S., Raine, K., Ramakrishna, M., Richardson, A. L., Richter, J., Rosenstiel, P., Schlesner, M., Schumacher, T. N., Span, P. N., Teague, J. W., Totoki, Y., Tutt, A. N., Valdes-Mas, R., van Buuren, M. M., van 't Veer, L., Vincent-Salomon, A., Waddell, N., Yates, L. R., Australian Pancreatic Cancer Genome, I., Consortium, I. B. C., Consortium, I. M.-S., PedBrain, I., Zucman-Rossi, J., Futreal, P. A., McDermott, U., Lichter, P., Meyerson, M., Grimmond, S. M., Siebert, R., Campo, E., Shibata, T., Pfister, S. M., Campbell, P. J., & Stratton, M. R. (2013). Signatures of mutational processes in human cancer. *Nature*, *500*(7463), 415-421. https://doi.org/10.1038/nature12477

Amantini, C., Morelli, M. B., Nabissi, M., Piva, F., Marinelli, O., Maggi, F., Bianchi, F., Bittoni, A., Berardi, R., Giampieri, R., & Santoni, G. (2019). Expression Profiling of Circulating Tumor Cells in Pancreatic Ductal Adenocarcinoma Patients: Biomarkers Predicting Overall Survival. *Front Oncol*, *9*, 874. https://doi.org/10.3389/fonc.2019.00874

Amit, M., & Gil, Z. (2013). Macrophages increase the resistance of pancreatic adenocarcinoma cells to gemcitabine by upregulating cytidine deaminase. *Oncoimmunology*, *2*(12), e27231. https://doi.org/10.4161/onci.27231

Apte, M. V., Haber, P. S., Applegate, T. L., Norton, I. D., McCaughan, G. W., Korsten, M. A., Pirola, R. C., & Wilson, J. S. (1998). Periacinar stellate shaped cells in rat pancreas: identification, isolation, and culture. *Gut*, *43*(1), 128-133. https://doi.org/10.1136/gut.43.1.128

Apte, M. V., Haber, P. S., Darby, S. J., Rodgers, S. C., McCaughan, G. W., Korsten, M. A., Pirola, R. C., & Wilson, J. S. (1999). Pancreatic stellate cells are activated by proinflammatory cytokines: implications for pancreatic fibrogenesis. *Gut*, *44*(4), 534-541. https://doi.org/10.1136/gut.44.4.534

Apte, M. V., & Wilson, J. S. (2005). The importance of keeping in touch: regulation of cell-cell contact in the exocrine pancreas. *Gut*, *54*(10), 1358-1359. https://doi.org/10.1136/gut.2005.070953

Aung, K. L., Fischer, S. E., Denroche, R. E., Jang, G. H., Dodd, A., Creighton, S., Southwood, B., Liang, S. B., Chadwick, D., Zhang, A., O'Kane, G. M., Albaba, H., Moura, S., Grant, R. C., Miller, J. K., Mbabaali, F., Pasternack, D., Lungu, I. M., Bartlett, J. M. S., Ghai, S., Lemire, M., Holter, S., Connor, A. A., Moffitt, R. A., Yeh, J. J., Timms, L., Krzyzanowski, P. M., Dhani, N., Hedley, D., Notta, F., Wilson, J. M., Moore, M. J., Gallinger, S., & Knox, J. J. (2018). Genomics-Driven Precision Medicine for Advanced Pancreatic Cancer: Early Results from the COMPASS Trial. *Clin Cancer Res*, *24*(6), 1344-1354. https://doi.org/10.1158/1078-0432.CCR-17-2994

Avsar, M., Tambas, M., Yalniz, Z., Akdeniz, D., Tuncer, S. B., Kilic, S., Sukruoglu Erdogan, O., Ciftci, R., Dagoglu, N., Vatansever, S., & Yazici, H. (2019). The expression level of fibulin-2 in the circulating RNA (ctRNA) of epithelial tumor cells of peripheral blood and tumor tissue of patients with metastatic lung cancer. *Mol Biol Rep*, *46*(4), 4001-4008. https://doi.org/10.1007/s11033-019-04846-z

Bailey, P., Chang, D. K., Nones, K., Johns, A. L., Patch, A. M., Gingras, M. C., Miller, D. K., Christ, A. N., Bruxner, T. J., Quinn, M. C., Nourse, C., Murtaugh, L. C., Harliwong, I., Idrisoglu, S., Manning, S., Nourbakhsh, E., Wani, S., Fink, L., Holmes, O., Chin, V., Anderson, M. J., Kazakoff, S., Leonard, C., Newell, F., Waddell, N., Wood, S., Xu, Q., Wilson, P. J., Cloonan, N., Kassahn, K. S., Taylor, D., Quek, K., Robertson, A., Pantano, L., Mincarelli, L., Sanchez, L. N., Evers, L., Wu, J., Pinese, M., Cowley, M. J., Jones, M. D., Colvin, E. K., Nagrial, A. M., Humphrey, E. S., Chantrill, L. A., Mawson, A., Humphris, J., Chou, A., Pajic, M., Scarlett, C. J., Pinho, A. V., Giry-Laterriere, M., Rooman, I., Samra, J. S., Kench, J. G., Lovell, J. A., Merrett, N. D., Toon, C. W., Epari, K., Nguyen, N. Q., Barbour, A., Zeps, N., Moran-Jones, K., Jamieson, N. B., Graham, J. S., Duthie, F., Oien, K., Hair, J., Grutzmann, R., Maitra, A., Iacobuzio-Donahue, C. A., Wolfgang, C. L., Morgan, R. A., Lawlor, R. T., Corbo, V., Bassi, C., Rusev, B., Capelli, P., Salvia, R., Tortora, G., Mukhopadhyay, D., Petersen, G. M., Australian Pancreatic Cancer Genome, I., Munzy, D. M., Fisher, W. E., Karim, S. A., Eshleman, J. R., Hruban, R. H., Pilarsky, C., Morton, J. P., Sansom, O. J., Scarpa, A., Musgrove, E. A., Bailey, U. M., Hofmann, O., Sutherland, R. L., Wheeler, D. A., Gill, A. J., Gibbs, R. A., Pearson, J. V., Waddell, N., Biankin, A. V., & Grimmond, S. M. (2016). Genomic analyses identify molecular subtypes of pancreatic cancer. *Nature*, *531*(7592), 47-52. https://doi.org/10.1038/nature16965

Banik, G., Betts, C. B., Liudahl, S. M., Sivagnanam, S., Kawashima, R., Cotechini, T., Larson, W., Goecks, J., Pai, S. I., Clayburgh, D. R., Tsujikawa, T., & Coussens, L. M. (2020). High-dimensional multiplexed immunohistochemical characterization of immune contexture in human cancers. *Methods Enzymol*, *635*, 1-20. https://doi.org/10.1016/bs.mie.2019.05.039

Bardeesy, N., Aguirre, A. J., Chu, G. C., Cheng, K. H., Lopez, L. V., Hezel, A. F., Feng, B., Brennan, C., Weissleder, R., Mahmood, U., Hanahan, D., Redston, M. S., Chin, L., & Depinho, R. A. (2006). Both p16(Ink4a) and the p19(Arf)-p53 pathway constrain progression of pancreatic adenocarcinoma in the mouse. *Proc Natl Acad Sci U S A*, *103*(15), 5947-5952. https://doi.org/10.1073/pnas.0601273103

Bardeesy, N., Cheng, K. H., Berger, J. H., Chu, G. C., Pahler, J., Olson, P., Hezel, A. F., Horner, J., Lauwers, G. Y., Hanahan, D., & DePinho, R. A. (2006). Smad4 is dispensable for normal pancreas development yet critical in progression and tumor biology of pancreas cancer. *Genes Dev*, *20*(22), 3130-3146. https://doi.org/10.1101/gad.1478706

Barry, S., Chelala, C., Lines, K., Sunamura, M., Wang, A., Marelli-Berg, F. M., Brennan, C., Lemoine, N. R., & Crnogorac-Jurcevic, T. (2013). S100P is a metastasis-associated gene that facilitates transendothelial migration of pancreatic cancer cells. *Clin Exp Metastasis*, *30*(3), 251-264. https://doi.org/10.1007/s10585-012-9532-y

Baumann, D., Hägele, T., Mochayedi, J., Drebant, J., Vent, C., Blobner, S., Noll, J. H., Nickel, I., Schumacher, C., Boos, S. L., Daniel, A. S., Wendler, S., Volkmar, M., Strobel, O., & Offringa, R. (2020). Proimmunogenic impact of MEK inhibition synergizes with agonist anti-CD40 immunostimulatory antibodies in tumor therapy. *Nat Commun*, *11*(1), 2176. https://doi.org/10.1038/s41467-020-15979-2

Becheva, Z. R., Gabrovska, K. I., & Godjevargova, T. I. (2018). Comparison between direct and indirect immunofluorescence method for determination of somatic cell count. *Chemical Papers*, *72*, 1861-1867. https://doi.org/10.1007/s11696-018-0445-3

Becht, E., Giraldo, N. A., Lacroix, L., Buttard, B., Elarouci, N., Petitprez, F., Selves, J., Laurent-Puig, P., Sautes-Fridman, C., Fridman, W. H., & de Reynies, A. (2016). Estimating the population abundance of tissue-infiltrating immune and stromal cell populations using gene expression. *Genome Biol*, *17*(1), 218. https://doi.org/10.1186/s13059-016-1070-5

Bhome, R., Al Saihati, H. A., Goh, R. W., Bullock, M. D., Primrose, J. N., Thomas, G. J., Sayan, A. E., & Mirnezami, A. H. (2016). Translational aspects in targeting the stromal tumour microenvironment: from bench to bedside. *New Horiz Transl Med*, *3*(1), 9-21. https://doi.org/10.1016/j.nhtm.2016.03.001

Biankin, A. V., Waddell, N., Kassahn, K. S., Gingras, M. C., Muthuswamy, L. B., Johns, A. L., Miller, D. K., Wilson, P. J., Patch, A. M., Wu, J., Chang, D. K., Cowley, M. J., Gardiner, B. B., Song, S., Harliwong, I., Idrisoglu, S., Nourse, C., Nourbakhsh, E., Manning, S., Wani, S., Gongora, M., Pajic, M., Scarlett, C. J., Gill, A. J., Pinho, A. V., Rooman, I., Anderson, M., Holmes, O., Leonard, C., Taylor, D., Wood, S., Xu, Q., Nones, K., Fink, J. L., Christ, A., Bruxner, T., Cloonan, N., Kolle, G., Newell, F., Pinese, M., Mead, R. S., Humphris, J. L., Kaplan, W., Jones, M. D., Colvin, E. K., Nagrial, A. M., Humphrey, E. S., Chou, A., Chin, V. T., Chantrill, L. A., Mawson, A., Samra, J. S., Kench, J. G., Lovell, J. A., Daly, R. J., Merrett, N. D., Toon, C., Epari, K., Nguyen, N. Q., Barbour, A., Zeps, N., Australian Pancreatic Cancer Genome, I., Kakkar, N., Zhao, F., Wu, Y. Q., Wang, M., Muzny, D. M., Fisher, W. E., Brunicardi, F. C., Hodges, S. E., Reid, J. G., Drummond, J., Chang, K., Han, Y., Lewis, L. R., Dinh, H., Buhay, C. J., Beck, T., Timms, L., Sam, M., Begley, K., Brown, A., Pai, D., Panchal, A., Buchner, N., De Borja, R., Denroche, R. E., Yung, C. K., Serra, S., Onetto, N., Mukhopadhyay, D., Tsao, M. S., Shaw, P. A., Petersen, G. M., Gallinger, S., Hruban, R. H., Maitra, A., Iacobuzio-Donahue, C. A., Schulick, R. D., Wolfgang, C. L., Morgan, R. A., Lawlor, R. T., Capelli, P., Corbo, V., Scardoni, M., Tortora, G., Tempero, M. A., Mann, K. M., Jenkins, N. A., Perez-Mancera, P. A., Adams, D. J., Largaespada, D. A., Wessels, L. F., Rust, A. G., Stein, L. D., Tuveson, D. A., Copeland, N. G., Musgrove, E. A., Scarpa, A., Eshleman, J. R., Hudson, T. J., Sutherland, R. L., Wheeler, D. A., Pearson, J. V., McPherson, J. D., Gibbs, R. A., & Grimmond, S. M. (2012). Pancreatic cancer genomes reveal aberrations in axon guidance pathway genes. *Nature*, *491*(7424), 399-405. https://doi.org/10.1038/nature11547

Blom, S., Paavolainen, L., Bychkov, D., Turkki, R., Maki-Teeri, P., Hemmes, A., Valimaki, K., Lundin, J., Kallioniemi, O., & Pellinen, T. (2017). Systems pathology by multiplexed immunohistochemistry and whole-slide digital image analysis. *Sci Rep*, *7*(1), 15580. https://doi.org/10.1038/s41598-017-15798-4

Bonnans, C., Chou, J., & Werb, Z. (2014). Remodelling the extracellular matrix in development and disease. *Nat Rev Mol Cell Biol*, *15*(12), 786-801. https://doi.org/10.1038/nrm3904

Bonnardel, J., Da Silva, C., Wagner, C., Bonifay, R., Chasson, L., Masse, M., Pollet, E., Dalod, M., Gorvel, J. P., & Lelouard, H. (2017). Distribution, location, and transcriptional profile of Peyer's patch conventional DC subsets at steady state and under TLR7 ligand stimulation. *Mucosal Immunol*, *10*(6), 1412-1430. https://doi.org/10.1038/mi.2017.30

Bos, R., & Sherman, L. A. (2010). CD4+ T-cell help in the tumor milieu is required for recruitment and cytolytic function of CD8+ T lymphocytes. *Cancer Res*, *70*(21), 8368-8377. https://doi.org/10.1158/0008-5472.CAN-10-1322

Boursi, B., Finkelman, B., Giantonio, B. J., Haynes, K., Rustgi, A. K., Rhim, A. D., Mamtani, R., & Yang, Y. X. (2017). A Clinical Prediction Model to Assess Risk for Pancreatic Cancer Among Patients With New-Onset Diabetes. *Gastroenterology*, *152*(4), 840-850 e843. https://doi.org/10.1053/j.gastro.2016.11.046

Bradford, M. M. (1976). A rapid and sensitive method for the quantitation of microgram quantities of protein utilizing the principle of protein-dye binding. *Anal Biochem*, *72*, 248-254. https://doi.org/10.1006/abio.1976.9999

Bruner, H. C., & Derksen, P. W. B. (2018). Loss of E-Cadherin-Dependent Cell-Cell Adhesion and the Development and Progression of Cancer. *Cold Spring Harb Perspect Biol*, *10*(3). https://doi.org/10.1101/cshperspect.a029330

Bryant, K. L., Stalnecker, C. A., Zeitouni, D., Klomp, J. E., Peng, S., Tikunov, A. P., Gunda, V., Pierobon, M., Waters, A. M., George, S. D., Tomar, G., Papke, B., Hobbs, G. A., Yan, L., Hayes, T. K., Diehl, J. N., Goode, G. D., Chaika, N. V., Wang, Y., Zhang, G. F., Witkiewicz, A. K., Knudsen, E. S., Petricoin, E. F., 3rd, Singh, P. K., Macdonald, J. M., Tran, N. L., Lyssiotis, C. A., Ying, H., Kimmelman, A. C., Cox, A. D., & Der, C. J. (2019). Combination of ERK and autophagy inhibition as a treatment approach for pancreatic cancer. *Nat Med*, *25*(4), 628-640. https://doi.org/10.1038/s41591-019-0368-8

Busch, E. L., Hornick, J. L., Umeton, R., Albayrak, A., Lindeman, N. I., MacConaill, L. E., Garcia, E. P., Ducar, M., & Rebbeck, T. R. (2017). Somatic mutations in CDH1 and CTNNB1 in primary carcinomas at 13 anatomic sites. *Oncotarget*, *8*(49), 85680-85691. https://doi.org/10.18632/oncotarget.21115

Cai, D., Chen, S. C., Prasad, M., He, L., Wang, X., Choesmel-Cadamuro, V., Sawyer, J. K., Danuser, G., & Montell, D. J. (2014). Mechanical feedback through E-cadherin promotes direction sensing during collective cell migration. *Cell*, *157*(5), 1146-1159. https://doi.org/10.1016/j.cell.2014.03.045

Carstens, J. L., Correa de Sampaio, P., Yang, D., Barua, S., Wang, H., Rao, A., Allison, J. P., LeBleu, V. S., & Kalluri, R. (2017). Spatial computation of intratumoral T cells correlates with survival of patients with pancreatic cancer. *Nat Commun*, *8*, 15095. https://doi.org/10.1038/ncomms15095

Castino, G. F., Cortese, N., Capretti, G., Serio, S., Di Caro, G., Mineri, R., Magrini, E., Grizzi, F., Cappello, P., Novelli, F., Spaggiari, P., Roncalli, M., Ridolfi, C., Gavazzi, F., Zerbi, A., Allavena, P., & Marchesi, F. (2016). Spatial distribution of B cells predicts prognosis in human pancreatic adenocarcinoma. *Oncoimmunology*, *5*(4), e1085147. https://doi.org/10.1080/2162402X.2015.1085147

Chalhoub, N., & Baker, S. J. (2009). PTEN and the PI3-kinase pathway in cancer. *Annu Rev Pathol*, *4*, 127-150. https://doi.org/10.1146/annurev.pathol.4.110807.092311

Chang, R. B., & Beatty, G. L. (2020). The interplay between innate and adaptive immunity in cancer shapes the productivity of cancer immunosurveillance. *J Leukoc Biol*, *108*(1), 363-376. https://doi.org/10.1002/JLB.3MIR0320-475R

Chen, A., Beetham, H., Black, M. A., Priya, R., Telford, B. J., Guest, J., Wiggins, G. A., Godwin, T. D., Yap, A. S., & Guilford, P. J. (2014). E-cadherin loss alters cytoskeletal organization and adhesion in non-malignant breast cells but is insufficient to induce an epithelial-mesenchymal transition. *BMC Cancer*, *14*, 552. https://doi.org/10.1186/1471-2407-14-552

Chen, J., Tan, Y., Sun, F., Hou, L., Zhang, C., Ge, T., Yu, H., Wu, C., Zhu, Y., Duan, L., Wu, L., Song, N., Zhang, L., Zhang, W., Wang, D., Chen, C., Wu, C., Jiang, G., & Zhang, P. (2020). Single-cell transcriptome and antigen-immunoglobin analysis reveals the diversity of B cells in non-small cell lung cancer. *Genome Biol*, *21*(1), 152. https://doi.org/10.1186/s13059-020-02064-6

Chen, L., Ma, C., Bian, Y., Shao, C., Wang, T., Li, J., Chong, X., Su, L., & Lu, J. (2017). Aberrant expression of STYK1 and E-cadherin confer a poor prognosis for pancreatic cancer patients. *Oncotarget*, *8*(67), 111333-111345. https://doi.org/10.18632/oncotarget.22794

Chen, W., Qin, Y., & Liu, S. (2020). CCL20 Signaling in the Tumor Microenvironment. In C. Springer (Ed.), *In: Birbrair A. (eds) Tumor Microenvironment. Advances in Experimental Medicine and Biology* (Vol. 1231). https://doi.org/10.1007/978-3-030-36667-4_6

Chen, Y., LeBleu, V. S., Carstens, J. L., Sugimoto, H., Zheng, X., Malasi, S., Saur, D., & Kalluri, R. (2018). Dual reporter genetic mouse models of pancreatic cancer identify an epithelial-to-mesenchymal transition-independent metastasis program. *EMBO Mol Med*, *10*(10). https://doi.org/10.15252/emmm.201809085

Cheng, Y., Jutooru, I., Chadalapaka, G., Corton, J. C., & Safe, S. (2015). The long non-coding RNA HOTTIP enhances pancreatic cancer cell proliferation, survival and migration. *Oncotarget*, *6*(13), 10840-10852. https://doi.org/10.18632/oncotarget.3450

Chistiakov, D. A., Killingsworth, M. C., Myasoedova, V. A., Orekhov, A. N., & Bobryshev, Y. V. (2017). CD68/macrosialin: not just a histochemical marker. *Lab Invest*, *97*(1), 4-13. https://doi.org/10.1038/labinvest.2016.116

Clark, C. E., Hingorani, S. R., Mick, R., Combs, C., Tuveson, D. A., & Vonderheide, R. H. (2007). Dynamics of the immune reaction to pancreatic cancer from inception to invasion. *Cancer Res*, *67*(19), 9518-9527. https://doi.org/10.1158/0008-5472.CAN-07-0175

Colamatteo, A., Carbone, F., Bruzzaniti, S., Galgani, M., Fusco, C., Maniscalco, G. T., Di Rella, F., de Candia, P., & De Rosa, V. (2019). Molecular Mechanisms Controlling Foxp3 Expression in Health and Autoimmunity: From Epigenetic to Post-translational Regulation. *Front Immunol*, *10*, 3136. https://doi.org/10.3389/fimmu.2019.03136

Collisson, E. A., Sadanandam, A., Olson, P., Gibb, W. J., Truitt, M., Gu, S., Cooc, J., Weinkle, J., Kim, G. E., Jakkula, L., Feiler, H. S., Ko, A. H., Olshen, A. B., Danenberg, K. L., Tempero, M. A., Spellman, P. T., Hanahan, D., & Gray, J. W. (2011). Subtypes of pancreatic ductal adenocarcinoma and their differing responses to therapy. *Nat Med*, *17*(4), 500-503. https://doi.org/10.1038/nm.2344

Collisson, E. A., Trejo, C. L., Silva, J. M., Gu, S., Korkola, J. E., Heiser, L. M., Charles, R. P., Rabinovich, B. A., Hann, B., Dankort, D., Spellman, P. T., Phillips, W. A., Gray, J. W., & McMahon, M. (2012). A central role for RAF-->MEK-->ERK signaling in the genesis of pancreatic ductal adenocarcinoma. *Cancer Discov*, *2*(8), 685-693. https://doi.org/10.1158/2159-8290.CD-11-0347

Corso, G., Carvalho, J., Marrelli, D., Vindigni, C., Carvalho, B., Seruca, R., Roviello, F., & Oliveira, C. (2013). Somatic mutations and deletions of the E-cadherin gene predict poor survival of patients with gastric cancer. *J Clin Oncol*, *31*(7), 868-875. https://doi.org/10.1200/JCO.2012.44.4612

Cotto-Rios, X. M., Agianian, B., Gitego, N., Zacharioudakis, E., Giricz, O., Wu, Y., Zou, Y., Verma, A., Poulikakos, P. I., & Gavathiotis, E. (2020). Inhibitors of BRAF dimers using an allosteric site. *Nat Commun*, *11*(1), 4370. https://doi.org/10.1038/s41467-020-18123-2

Custódio-Santos, T., Videira, M., & Brito, M. A. (2017). Brain metastasization of breast cancer. *Biochim Biophys Acta Rev Cancer*, *1868*(1), 132-147. https://doi.org/10.1016/j.bbcan.2017.03.004

D'Errico, G., Alonso-Nocelo, M., Vallespinos, M., Hermann, P. C., Alcala, S., Garcia, C. P., Martin-Hijano, L., Valle, S., Earl, J., Cassiano, C., Lombardia, L., Feliu, J., Monti, M. C., Seufferlein, T., Garcia-Bermejo, L., Martinelli, P., Carrato, A., & Sainz, B., Jr. (2019). Tumor-associated macrophage-secreted 14-3-3zeta signals via AXL to promote pancreatic cancer chemoresistance. *Oncogene*, *38*(27), 5469-5485. https://doi.org/10.1038/s41388-019-0803-9

Dauer, P., Zhao, X., Gupta, V. K., Sharma, N., Kesh, K., Gnamlin, P., Dudeja, V., Vickers, S. M., Banerjee, S., & Saluja, A. (2018). Inactivation of Cancer-Associated-Fibroblasts Disrupts Oncogenic Signaling in Pancreatic Cancer Cells and Promotes Its Regression. *Cancer Res*, *78*(5), 1321-1333. https://doi.org/10.1158/0008-5472.CAN-17-2320

Davis, A. S., Richter, A., Becker, S., Moyer, J. E., Sandouk, A., Skinner, J., & Taubenberger, J. K. (2014). Characterizing and Diminishing Autofluorescence in Formalin-fixed Paraffin-embedded Human Respiratory Tissue. *J Histochem Cytochem*, *62*(6), 405-423. https://doi.org/10.1369/0022155414531549

De Gasperi, R., Rocher, A. B., Sosa, M. A., Wearne, S. L., Perez, G. M., Friedrich, V. L., Jr., Hof, P. R., & Elder, G. A. (2008). The IRG mouse: a two-color fluorescent reporter for assessing Cre-mediated recombination and imaging complex cellular relationships in situ. *Genesis*, *46*(6), 308-317. https://doi.org/10.1002/dvg.20400

De Monte, L., Reni, M., Tassi, E., Clavenna, D., Papa, I., Recalde, H., Braga, M., Di Carlo, V., Doglioni, C., & Protti, M. P. (2011). Intratumor T helper type 2 cell infiltrate correlates with cancer-associated fibroblast thymic stromal lymphopoietin production and reduced

survival in pancreatic cancer. *J Exp Med*, *208*(3), 469-478. https://doi.org/10.1084/jem.20101876

De Monte, L., Wormann, S., Brunetto, E., Heltai, S., Magliacane, G., Reni, M., Paganoni, A. M., Recalde, H., Mondino, A., Falconi, M., Aleotti, F., Balzano, G., Algul, H., Doglioni, C., & Protti, M. P. (2016). Basophil Recruitment into Tumor-Draining Lymph Nodes Correlates with Th2 Inflammation and Reduced Survival in Pancreatic Cancer Patients. *Cancer Res*, *76*(7), 1792-1803. https://doi.org/10.1158/0008-5472.CAN-15-1801-T

Delitto, D., Black, B. S., Sorenson, H. L., Knowlton, A. E., Thomas, R. M., Sarosi, G. A., Moldawer, L. L., Behrns, K. E., Liu, C., George, T. J., Trevino, J. G., Wallet, S. M., & Hughes, S. J. (2015). The inflammatory milieu within the pancreatic cancer microenvironment correlates with clinicopathologic parameters, chemoresistance and survival. *BMC Cancer*, *15*, 783. https://doi.org/10.1186/s12885-015-1820-x

Denais, C. M., Gilbert, R. M., Isermann, P., McGregor, A. L., te Lindert, M., Weigelin, B., Davidson, P. M., Friedl, P., Wolf, K., & Lammerding, J. (2016). Nuclear envelope rupture and repair during cancer cell migration. *Science*, *352*(6283), 353-358. https://doi.org/10.1126/science.aad7297

Derksen, P. W., Liu, X., Saridin, F., van der Gulden, H., Zevenhoven, J., Evers, B., van Beijnum, J. R., Griffioen, A. W., Vink, J., Krimpenfort, P., Peterse, J. L., Cardiff, R. D., Berns, A., & Jonkers, J. (2006). Somatic inactivation of E-cadherin and p53 in mice leads to metastatic lobular mammary carcinoma through induction of anoikis resistance and angiogenesis. *Cancer Cell*, *10*(5), 437-449. https://doi.org/10.1016/j.ccr.2006.09.013

Du, M., Wang, G., Barsukov, I. L., Gross, S. R., Smith, R., & Rudland, P. S. (2020). Direct interaction of metastasis-inducing S100P protein with tubulin causes enhanced cell migration without changes in cell adhesion. *Biochem J*, *477*(6), 1159-1178. https://doi.org/10.1042/BCJ20190644

Elyada, E., Bolisetty, M., Laise, P., Flynn, W. F., Courtois, E. T., Burkhart, R. A., Teinor, J. A., Belleau, P., Biffi, G., Lucito, M. S., Sivajothi, S., Armstrong, T. D., Engle, D. D., Yu, K. H., Hao, Y., Wolfgang, C. L., Park, Y., Preall, J., Jaffee, E. M., Califano, A., Robson, P., & Tuveson, D. A. (2019). Cross-Species Single-Cell Analysis of Pancreatic Ductal Adenocarcinoma Reveals Antigen-Presenting Cancer-Associated Fibroblasts. *Cancer Discov*, *9*(8), 1102-1123. https://doi.org/10.1158/2159-8290.CD-19-0094

Eser, S., Reiff, N., Messer, M., Seidler, B., Gottschalk, K., Dobler, M., Hieber, M., Arbeiter, A., Klein, S., Kong, B., Michalski, C. W., Schlitter, A. M., Esposito, I., Kind, A. J., Rad, L., Schnieke, A. E., Baccarini, M., Alessi, D. R., Rad, R., Schmid, R. M., Schneider, G., & Saur, D. (2013). Selective requirement of PI3K/PDK1 signaling for Kras oncogene-driven pancreatic cell plasticity and cancer. *Cancer Cell*, *23*(3), 406-420. https://doi.org/10.1016/j.ccr.2013.01.023

Evans, R. A., Diamond, M. S., Rech, A. J., Chao, T., Richardson, M. W., Lin, J. H., Bajor, D. L., Byrne, K. T., Stanger, B. Z., Riley, J. L., Markosyan, N., Winograd, R., & Vonderheide, R. H. (2016). Lack of immunoediting in murine pancreatic cancer reversed with neoantigen. *JCI Insight*, *1*(14). https://doi.org/10.1172/jci.insight.88328

Fares, J., Fares, M. Y., Khachfe, H. H., Salhab, H. A., & Fares, Y. (2020). Molecular principles of metastasis: a hallmark of cancer revisited. *Signal Transduct Target Ther*, *5*(1), 28. https://doi.org/10.1038/s41392-020-0134-x

Fauskanger, M., Haabeth, O. A. W., Skjeldal, F. M., Bogen, B., & Tveita, A. A. (2018). Tumor Killing by CD4(+) T Cells Is Mediated via Induction of Inducible Nitric Oxide Synthase-Dependent Macrophage Cytotoxicity. *Front Immunol*, *9*, 1684. https://doi.org/10.3389/fimmu.2018.01684

Ferreira, C., Lobo, J., Antunes, L., Lopes, P., Jeronimo, C., & Henrique, R. (2018). Differential expression of E-cadherin and P-cadherin in pT3 prostate cancer: correlation with clinical and pathological features. *Virchows Arch*, *473*(4), 443-452. https://doi.org/10.1007/s00428-018-2406-1

Ferreira, R. M. M., Sancho, R., Messal, H. A., Nye, E., Spencer-Dene, B., Stone, R. K., Stamp, G., Rosewell, I., Quaglia, A., & Behrens, A. (2017). Duct- and Acinar-Derived Pancreatic

Ductal Adenocarcinomas Show Distinct Tumor Progression and Marker Expression. *Cell Rep*, *21*(4), 966-978. https://doi.org/10.1016/j.celrep.2017.09.093

Fridlender, Z. G., Sun, J., Kim, S., Kapoor, V., Cheng, G., Ling, L., Worthen, G. S., & Albelda, S. M. (2009). Polarization of tumor-associated neutrophil phenotype by TGF-beta: "N1" versus "N2" TAN. *Cancer Cell*, *16*(3), 183-194. https://doi.org/10.1016/j.ccr.2009.06.017

Gaida, M. M., Steffen, T. G., Gunther, F., Tschaharganeh, D. F., Felix, K., Bergmann, F., Schirmacher, P., & Hansch, G. M. (2012). Polymorphonuclear neutrophils promote dyshesion of tumor cells and elastase-mediated degradation of E-cadherin in pancreatic tumors. *Eur J Immunol*, *42*(12), 3369-3380. https://doi.org/10.1002/eji.201242628

Gannon, M., Herrera, P. L., & Wright, C. V. (2000). Mosaic Cre-mediated recombination in pancreas using the pdx-1 enhancer/promoter. *Genesis*, *26*(2), 143-144. https://doi.org/10.1002/(sici)1526-968x(200002)26:2<143::aid-gene13>3.0.co;2-l

Gardner, A., & Ruffell, B. (2016). Dendritic Cells and Cancer Immunity. *Trends Immunol*, *37*(12), 855-865. https://doi.org/10.1016/j.it.2016.09.006

Garnelo, M., Tan, A., Her, Z., Yeong, J., Lim, C. J., Chen, J., Lim, K. H., Weber, A., Chow, P., Chung, A., Ooi, L. L., Toh, H. C., Heikenwalder, M., Ng, I. O., Nardin, A., Chen, Q., Abastado, J. P., & Chew, V. (2017). Interaction between tumour-infiltrating B cells and T cells controls the progression of hepatocellular carcinoma. *Gut*, *66*(2), 342-351. https://doi.org/10.1136/gutjnl-2015-310814

Gerdes, M. J., Sevinsky, C. J., Sood, A., Adak, S., Bello, M. O., Bordwell, A., Can, A., Corwin, A., Dinn, S., Filkins, R. J., Hollman, D., Kamath, V., Kaanumalle, S., Kenny, K., Larsen, M., Lazare, M., Li, Q., Lowes, C., McCulloch, C. C., McDonough, E., Montalto, M. C., Pang, Z., Rittscher, J., Santamaria-Pang, A., Sarachan, B. D., Seel, M. L., Seppo, A., Shaikh, K., Sui, Y., Zhang, J., & Ginty, F. (2013). Highly multiplexed single-cell analysis of formalin-fixed, paraffin-embedded cancer tissue. *Proc Natl Acad Sci U S A*, *110*(29), 11982-11987. https://doi.org/10.1073/pnas.1300136110

Gerner, M. Y., Kastenmuller, W., Ifrim, I., Kabat, J., & Germain, R. N. (2012). Histo-cytometry: a method for highly multiplex quantitative tissue imaging analysis applied to dendritic cell subset microanatomy in lymph nodes. *Immunity*, *37*(2), 364-376. https://doi.org/10.1016/j.immuni.2012.07.011

Gitto, S. B., Beardsley, J. M., Nakkina, S. P., Oyer, J. L., Cline, K. A., Litherland, S. A., Copik, A. J., Khaled, A. S., Fanaian, N., Arnoletti, J. P., & Altomare, D. A. (2020). Identification of a novel IL-5 signaling pathway in chronic pancreatitis and crosstalk with pancreatic tumor cells. *Cell Commun Signal*, *18*(1), 95. https://doi.org/10.1186/s12964-020-00594-x

Goebel, L., Grage-Griebenow, E., Gorys, A., Helm, O., Genrich, G., Lenk, L., Wesch, D., Ungefroren, H., Freitag-Wolf, S., Sipos, B., Rocken, C., Schafer, H., & Sebens, S. (2015). CD4(+) T cells potently induce epithelial-mesenchymal-transition in premalignant and malignant pancreatic ductal epithelial cells-novel implications of CD4(+) T cells in pancreatic cancer development. *Oncoimmunology*, *4*(4), e1000083. https://doi.org/10.1080/2162402X.2014.1000083

Golubovskaya, V., & Wu, L. (2016). Different Subsets of T Cells, Memory, Effector Functions, and CAR-T Immunotherapy. *Cancers (Basel)*, *8*(3). https://doi.org/10.3390/cancers8030036

Gorris, M. A. J., Halilovic, A., Rabold, K., van Duffelen, A., Wickramasinghe, I. N., Verweij, D., Wortel, I. M. N., Textor, J. C., de Vries, I. J. M., & Figdor, C. G. (2018). Eight-Color Multiplex Immunohistochemistry for Simultaneous Detection of Multiple Immune Checkpoint Molecules within the Tumor Microenvironment. *J Immunol*, *200*(1), 347-354. https://doi.org/10.4049/jimmunol.1701262

Grant, T. J., Hua, K., & Singh, A. (2016). Molecular Pathogenesis of Pancreatic Cancer. *Prog Mol Biol Transl Sci*, *144*, 241-275. https://doi.org/10.1016/bs.pmbts.2016.09.008

Grünwald, B., Vandooren, J., Gerg, M., Ahomaa, K., Hunger, A., Berchtold, S., Akbareian, S., Schaten, S., Knolle, P., Edwards, D. R., Opdenakker, G., & Kruger, A. (2016). Systemic Ablation of MMP-9 Triggers Invasive Growth and Metastasis of Pancreatic Cancer via Deregulation of IL6 Expression in the Bone Marrow. *Mol Cancer Res*, *14*(11), 1147-1158. https://doi.org/10.1158/1541-7786.MCR-16-0180

Gu, G., Dubauskaite, J., & Melton, D. A. (2002). Direct evidence for the pancreatic lineage: NGN3+ cells are islet progenitors and are distinct from duct progenitors. *Development*, *129*(10), 2447-2457. https://www.ncbi.nlm.nih.gov/pubmed/11973276

Guiducci, C., Vicari, A. P., Sangaletti, S., Trinchieri, G., & Colombo, M. P. (2005). Redirecting in vivo elicited tumor infiltrating macrophages and dendritic cells towards tumor rejection. *Cancer Res*, *65*(8), 3437-3446. https://doi.org/10.1158/0008-5472.CAN-04-4262

Gunderson, A. J., Kaneda, M. M., Tsujikawa, T., Nguyen, A. V., Affara, N. I., Ruffell, B., Gorjestani, S., Liudahl, S. M., Truitt, M., Olson, P., Kim, G., Hanahan, D., Tempero, M. A., Sheppard, B., Irving, B., Chang, B. Y., Varner, J. A., & Coussens, L. M. (2016). Bruton Tyrosine Kinase-Dependent Immune Cell Cross-talk Drives Pancreas Cancer. *Cancer Discov*, *6*(3), 270-285. https://doi.org/10.1158/2159-8290.CD-15-0827

Haas, L., & Obenauf, A. C. (2019). Allies or Enemies-The Multifaceted Role of Myeloid Cells in the Tumor Microenvironment. *Front Immunol*, *10*, 2746. https://doi.org/10.3389/fimmu.2019.02746

Haeberle, L., & Esposito, I. (2019). Pathology of pancreatic cancer. *Transl Gastroenterol Hepatol*, *4*, 50. https://doi.org/10.21037/tgh.2019.06.02

Hanahan, D., & Weinberg, R. A. (2011). Hallmarks of cancer: the next generation. *Cell*, *144*(5), 646-674. https://doi.org/10.1016/j.cell.2011.02.013

Hastings, K. T. (2008). Innate and Adaptive Immune Responses to Cancer. In *Fundamentals of Cancer Prevention*. Springer, Berlin, Heidelberg. https://doi.org/10.1007/978-3-540-68986-7_4

Hausmann, S., Kong, B., Michalski, C., Erkan, M., & Friess, H. (2014). The role of inflammation in pancreatic cancer. *Adv Exp Med Biol*, *816*, 129-151. https://doi.org/10.1007/978-3-0348-0837-8_6

Hegde, S., Krisnawan, V. E., Herzog, B. H., Zuo, C., Breden, M. A., Knolhoff, B. L., Hogg, G. D., Tang, J. P., Baer, J. M., Mpoy, C., Lee, K. B., Alexander, K. A., Rogers, B. E., Murphy, K. M., Hawkins, W. G., Fields, R. C., DeSelm, C. J., Schwarz, J. K., & DeNardo, D. G. (2020). Dendritic Cell Paucity Leads to Dysfunctional Immune Surveillance in Pancreatic Cancer. *Cancer Cell*, *37*(3), 289-307 e289. https://doi.org/10.1016/j.ccell.2020.02.008

Heid, I., Steiger, K., Trajkovic-Arsic, M., Settles, M., Esswein, M. R., Erkan, M., Kleeff, J., Jager, C., Friess, H., Haller, B., Steingotter, A., Schmid, R. M., Schwaiger, M., Rummeny, E. J., Esposito, I., Siveke, J. T., & Braren, R. F. (2017). Co-clinical Assessment of Tumor Cellularity in Pancreatic Cancer. *Clin Cancer Res*, *23*(6), 1461-1470. https://doi.org/10.1158/1078-0432.CCR-15-2432

Helm, O., Held-Feindt, J., Grage-Griebenow, E., Reiling, N., Ungefroren, H., Vogel, I., Kruger, U., Becker, T., Ebsen, M., Rocken, C., Kabelitz, D., Schafer, H., & Sebens, S. (2014). Tumor-associated macrophages exhibit pro- and anti-inflammatory properties by which they impact on pancreatic tumorigenesis. *Int J Cancer*, *135*(4), 843-861. https://doi.org/10.1002/ijc.28736

Helm, O., Mennrich, R., Petrick, D., Goebel, L., Freitag-Wolf, S., Roder, C., Kalthoff, H., Rocken, C., Sipos, B., Kabelitz, D., Schafer, H., Oberg, H. H., Wesch, D., & Sebens, S. (2014). Comparative characterization of stroma cells and ductal epithelium in chronic pancreatitis and pancreatic ductal adenocarcinoma. *PLoS One*, *9*(5), e94357. https://doi.org/10.1371/journal.pone.0094357

Hensel, J. A., Khattar, V., Ashton, R., & Ponnazhagan, S. (2019). Characterization of immune cell subtypes in three commonly used mouse strains reveals gender and strain-specific variations. *Lab Invest*, *99*(1), 93-106. https://doi.org/10.1038/s41374-018-0137-1

Hewitt, S. M., Baskin, D. G., Frevert, C. W., Stahl, W. L., & Rosa-Molinar, E. (2014). Controls for immunohistochemistry: the Histochemical Society's standards of practice for validation of immunohistochemical assays. *J Histochem Cytochem*, *62*(10), 693-697. https://doi.org/10.1369/0022155414545224

Hicks, A. M., Chou, J., Capanu, M., Lowery, M. A., Yu, K. H., & O'Reilly, E. M. (2016). Pancreas Adenocarcinoma: Ascites, Clinical Manifestations, and Management Implications. *Clin Colorectal Cancer*, *15*(4), 360-368. https://doi.org/10.1016/j.clcc.2016.04.014

Hingorani, S. R., Petricoin, E. F., Maitra, A., Rajapakse, V., King, C., Jacobetz, M. A., Ross, S., Conrads, T. P., Veenstra, T. D., Hitt, B. A., Kawaguchi, Y., Johann, D., Liotta, L. A., Crawford, H. C., Putt, M. E., Jacks, T., Wright, C. V., Hruban, R. H., Lowy, A. M., & Tuveson, D. A. (2003). Preinvasive and invasive ductal pancreatic cancer and its early detection in the mouse. *Cancer Cell*, *4*(6), 437-450. https://doi.org/10.1016/s1535-6108(03)00309-x

Hingorani, S. R., Wang, L., Multani, A. S., Combs, C., Deramaudt, T. B., Hruban, R. H., Rustgi, A. K., Chang, S., & Tuveson, D. A. (2005). Trp53R172H and KrasG12D cooperate to promote chromosomal instability and widely metastatic pancreatic ductal adenocarcinoma in mice. *Cancer Cell*, *7*(5), 469-483. https://doi.org/10.1016/j.ccr.2005.04.023

Holokai, L., Chakrabarti, J., Lundy, J., Croagh, D., Adhikary, P., Richards, S. S., Woodson, C., Steele, N., Kuester, R., Scott, A., Khreiss, M., Frankel, T., Merchant, J., Jenkins, B. J., Wang, J., Shroff, R. T., Ahmad, S. A., & Zavros, Y. (2020). Murine- and Human-Derived Autologous Organoid/Immune Cell Co-Cultures as Pre-Clinical Models of Pancreatic Ductal Adenocarcinoma. *Cancers (Basel)*, *12*(12). https://doi.org/10.3390/cancers12123816

Howat, W. J., Lewis, A., Jones, P., Kampf, C., Ponten, F., van der Loos, C. M., Gray, N., Womack, C., & Warford, A. (2014). Antibody validation of immunohistochemistry for biomarker discovery: recommendations of a consortium of academic and pharmaceutical based histopathology researchers. *Methods*, *70*(1), 34-38. https://doi.org/10.1016/j.ymeth.2014.01.018

Hruban, R. H., Maitra, A., & Goggins, M. (2008). Update on pancreatic intraepithelial neoplasia. *Int J Clin Exp Pathol*, *1*(4), 306-316. https://www.ncbi.nlm.nih.gov/pubmed/18787611

Hu, C., Dadon, T., Chenna, V., Yabuuchi, S., Bannerji, R., Booher, R., Strack, P., Azad, N., Nelkin, B. D., & Maitra, A. (2015). Combined Inhibition of Cyclin-Dependent Kinases (Dinaciclib) and AKT (MK-2206) Blocks Pancreatic Tumor Growth and Metastases in Patient-Derived Xenograft Models. *Mol Cancer Ther*, *14*(7), 1532-1539. https://doi.org/10.1158/1535-7163.MCT-15-0028

Hu, Z., Li, Z., Ma, Z., & Curtis, C. (2020). Multi-cancer analysis of clonality and the timing of systemic spread in paired primary tumors and metastases. *Nat Genet*, *52*(7), 701-708. https://doi.org/10.1038/s41588-020-0628-z

Huang, C., Li, N., Li, Z., Chang, A., Chen, Y., Zhao, T., Li, Y., Wang, X., Zhang, W., Wang, Z., Luo, L., Shi, J., Yang, S., Ren, H., & Hao, J. (2017). Tumour-derived Interleukin 35 promotes pancreatic ductal adenocarcinoma cell extravasation and metastasis by inducing ICAM1 expression. *Nat Commun*, *8*, 14035. https://doi.org/10.1038/ncomms14035

Huber, A. H., Stewart, D. B., Laurents, D. V., Nelson, W. J., & Weis, W. I. (2001). The cadherin cytoplasmic domain is unstructured in the absence of beta-catenin. A possible mechanism for regulating cadherin turnover. *J Biol Chem*, *276*(15), 12301-12309. https://doi.org/10.1074/jbc.M010377200

Hunka, J., Riley, J. T., & Debes, G. F. (2020). Approaches to overcome flow cytometry limitations in the analysis of cells from veterinary relevant species. *BMC Vet Res*, *16*(1), 83. https://doi.org/10.1186/s12917-020-02299-2

Hwang, H. J., Oh, M. S., Lee, D. W., & Kuh, H. J. (2019). Multiplex quantitative analysis of stroma-mediated cancer cell invasion, matrix remodeling, and drug response in a 3D co-culture model of pancreatic tumor spheroids and stellate cells. *J Exp Clin Cancer Res*, *38*(1), 258. https://doi.org/10.1186/s13046-019-1225-9

Ichim, G., & Tait, S. W. (2016). A fate worse than death: apoptosis as an oncogenic process. *Nat Rev Cancer*, *16*(8), 539-548. https://doi.org/10.1038/nrc.2016.58

Ischenko, I., Petrenko, O., & Hayman, M. J. (2015). A MEK/PI3K/HDAC inhibitor combination therapy for KRAS mutant pancreatic cancer cells. *Oncotarget*, *6*(18), 15814-15827. https://doi.org/10.18632/oncotarget.4538

Italiani, P., & Boraschi, D. (2014). From Monocytes to M1/M2 Macrophages: Phenotypical vs. Functional Differentiation. *Front Immunol*, *5*, 514. https://doi.org/10.3389/fimmu.2014.00514

Jackson, E. L., Willis, N., Mercer, K., Bronson, R. T., Crowley, D., Montoya, R., Jacks, T., & Tuveson, D. A. (2001). Analysis of lung tumor initiation and progression using conditional expression of oncogenic K-ras. *Genes Dev*, *15*(24), 3243-3248. https://doi.org/10.1101/gad.943001

Jean, S., & Kiger, A. A. (2014). Classes of phosphoinositide 3-kinases at a glance. *J Cell Sci*, *127*(Pt 5), 923-928. https://doi.org/10.1242/jcs.093773

Jonkers, J., Meuwissen, R., van der Gulden, H., Peterse, H., van der Valk, M., & Berns, A. (2001). Synergistic tumor suppressor activity of BRCA2 and p53 in a conditional mouse model for breast cancer. *Nat Genet*, *29*(4), 418-425. https://doi.org/10.1038/ng747

Jun, Y. W., Kim, H. R., Reo, Y. J., Dai, M., & Ahn, K. H. (2017). Addressing the autofluorescence issue in deep tissue imaging by two-photon microscopy: the significance of far-red emitting dyes. *Chem Sci*, *8*(11), 7696-7704. https://doi.org/10.1039/c7sc03362a

Kamentsky, L., Jones, T. R., Fraser, A., Bray, M. A., Logan, D. J., Madden, K. L., Ljosa, V., Rueden, C., Eliceiri, K. W., & Carpenter, A. E. (2011). Improved structure, function and compatibility for CellProfiler: modular high-throughput image analysis software. *Bioinformatics*, *27*(8), 1179-1180. https://doi.org/10.1093/bioinformatics/btr095

Kanda, M., Matthaei, H., Wu, J., Hong, S. M., Yu, J., Borges, M., Hruban, R. H., Maitra, A., Kinzler, K., Vogelstein, B., & Goggins, M. (2012). Presence of somatic mutations in most early-stage pancreatic intraepithelial neoplasia. *Gastroenterology*, *142*(4), 730-733 e739. https://doi.org/10.1053/j.gastro.2011.12.042

Kaneta, Y., Sato, T., Hikiba, Y., Sugimori, M., Sue, S., Kaneko, H., Irie, K., Sasaki, T., Kondo, M., Chuma, M., Shibata, W., & Maeda, S. (2020). Loss of Pancreatic E-Cadherin Causes Pancreatitis-Like Changes and Contributes to Carcinogenesis. *Cell Mol Gastroenterol Hepatol*, *9*(1), 105-119. https://doi.org/10.1016/j.jcmgh.2019.09.001

Kaplon, J., van Dam, L., & Peeper, D. (2015). Two-way communication between the metabolic and cell cycle machineries: the molecular basis. *Cell Cycle*, *14*(13), 2022-2032. https://doi.org/10.1080/15384101.2015.1044172

Karantza, V. (2011). Keratins in health and cancer: more than mere epithelial cell markers. *Oncogene*, *30*(2), 127-138. https://doi.org/10.1038/onc.2010.456

Kennedy, A. L., Morton, J. P., Manoharan, I., Nelson, D. M., Jamieson, N. B., Pawlikowski, J. S., McBryan, T., Doyle, B., McKay, C., Oien, K. A., Enders, G. H., Zhang, R., Sansom, O. J., & Adams, P. D. (2011). Activation of the PIK3CA/AKT pathway suppresses senescence induced by an activated RAS oncogene to promote tumorigenesis. *Mol Cell*, *42*(1), 36-49. https://doi.org/10.1016/j.molcel.2011.02.020

Kessler, D., Gmachl, M., Mantoulidis, A., Martin, L. J., Zoephel, A., Mayer, M., Gollner, A., Covini, D., Fischer, S., Gerstberger, T., Gmaschitz, T., Goodwin, C., Greb, P., Haring, D., Hela, W., Hoffmann, J., Karolyi-Oezguer, J., Knesl, P., Kornigg, S., Koegl, M., Kousek, R., Lamarre, L., Moser, F., Munico-Martinez, S., Peinsipp, C., Phan, J., Rinnenthal, J., Sai, J., Salamon, C., Scherbantin, Y., Schipany, K., Schnitzer, R., Schrenk, A., Sharps, B., Siszler, G., Sun, Q., Waterson, A., Wolkerstorfer, B., Zeeb, M., Pearson, M., Fesik, S. W., & McConnell, D. B. (2019). Drugging an undruggable pocket on KRAS. *Proc Natl Acad Sci U S A*, *116*(32), 15823-15829. https://doi.org/10.1073/pnas.1904529116

Khalili, J. S., Liu, S., Rodriguez-Cruz, T. G., Whittington, M., Wardell, S., Liu, C., Zhang, M., Cooper, Z. A., Frederick, D. T., Li, Y., Zhang, M., Joseph, R. W., Bernatchez, C., Ekmekcioglu, S., Grimm, E., Radvanyi, L. G., Davis, R. E., Davies, M. A., Wargo, J. A., Hwu, P., & Lizee, G. (2012). Oncogenic BRAF(V600E) promotes stromal cell-mediated immunosuppression via induction of interleukin-1 in melanoma. *Clin Cancer Res*, *18*(19), 5329-5340. https://doi.org/10.1158/1078-0432.CCR-12-1632

Khan, M. S., Luong, T. V., Watkins, J., Toumpanakis, C., Caplin, M. E., & Meyer, T. (2013). A comparison of Ki-67 and mitotic count as prognostic markers for metastatic pancreatic and midgut neuroendocrine neoplasms. *Br J Cancer*, *108*(9), 1838-1845. https://doi.org/10.1038/bjc.2013.156

Kleeff, J., Korc, M., Apte, M., La Vecchia, C., Johnson, C. D., Biankin, A. V., Neale, R. E., Tempero, M., Tuveson, D. A., Hruban, R. H., & Neoptolemos, J. P. (2016). Pancreatic cancer. *Nat Rev Dis Primers*, *2*, 16022. https://doi.org/10.1038/nrdp.2016.22

Knudsen, E. S., Vail, P., Balaji, U., Ngo, H., Botros, I. W., Makarov, V., Riaz, N., Balachandran, V., Leach, S., Thompson, D. M., Chan, T. A., & Witkiewicz, A. K. (2017). Stratification of Pancreatic Ductal Adenocarcinoma: Combinatorial Genetic, Stromal, and Immunologic Markers. *Clin Cancer Res*, *23*(15), 4429-4440. https://doi.org/10.1158/1078-0432.CCR-17-0162

Korotkevich, G., Sukhov, V., Budin, N., Shpak, B., Artyomov, M. N., & Sergushichev, A. (2016). Fast gene set enrichment analysis. *Europe PMC*. https://doi.org/10.1101/060012

Krapp, A., Knofler, M., Ledermann, B., Burki, K., Berney, C., Zoerkler, N., Hagenbuchle, O., & Wellauer, P. K. (1998). The bHLH protein PTF1-p48 is essential for the formation of the exocrine and the correct spatial organization of the endocrine pancreas. *Genes Dev*, *12*(23), 3752-3763. https://doi.org/10.1101/gad.12.23.3752

Lachowski, D., Cortes, E., Pink, D., Chronopoulos, A., Karim, S. A., J, P. M., & Del Rio Hernandez, A. E. (2017). Substrate Rigidity Controls Activation and Durotaxis in Pancreatic Stellate Cells. *Sci Rep*, *7*(1), 2506. https://doi.org/10.1038/s41598-017-02689-x

Laemmli, U. K. (1970). Cleavage of structural proteins during the assembly of the head of bacteriophage T4. *Nature*, *227*(5259), 680-685. https://doi.org/10.1038/227680a0

Le Floc'h, A., Jalil, A., Vergnon, I., Le Maux Chansac, B., Lazar, V., Bismuth, G., Chouaib, S., & Mami-Chouaib, F. (2007). Alpha E beta 7 integrin interaction with E-cadherin promotes antitumor CTL activity by triggering lytic granule polarization and exocytosis. *J Exp Med*, *204*(3), 559-570. https://doi.org/10.1084/jem.20061524

LeBien, T. W., & Tedder, T. F. (2008). B lymphocytes: how they develop and function. *Blood*, *112*(5), 1570-1580. https://doi.org/10.1182/blood-2008-02-078071

Lee, C. L., Moding, E. J., Huang, X., Li, Y., Woodlief, L. Z., Rodrigues, R. C., Ma, Y., & Kirsch, D. G. (2012). Generation of primary tumors with Flp recombinase in FRT-flanked p53 mice. *Dis Model Mech*, *5*(3), 397-402. https://doi.org/10.1242/dmm.009084

Lee, J. J., Bernard, V., Semaan, A., Monberg, M. E., Huang, J., Stephens, B. M., Lin, D., Weston, B. R., Bhutani, M. S., Haymaker, C. L., Bernatchez, C., Taniguchi, C. M., Maitra, A., & Guerrero, P. A. (2020). Elucidation of tumor-stromal heterogeneity and the ligand-receptor interactome by single cell transcriptomics in real-world pancreatic cancer biopsies. *bioRxiv*, *2020.07.28.225813*. https://doi.org/10.1101/2020.07.28.225813

Lemstrova, R., Brynychova, V., Hughes, D. J., Hlavac, V., Dvorak, P., Doherty, J. E., Murray, H. A., Crockard, M., Oliverius, M., Hlavsa, J., Honsova, E., Mazanec, J., Kala, Z., Lovecek, M., Havlik, R., Ehrmann, J., Strouhal, O., Soucek, P., Melichar, B., & Mohelnikova-Duchonova, B. (2017). Dysregulation of KRAS signaling in pancreatic cancer is not associated with KRAS mutations and outcome. *Oncol Lett*, *14*(5), 5980-5988. https://doi.org/10.3892/ol.2017.6946

Li, J., Byrne, K. T., Yan, F., Yamazoe, T., Chen, Z., Baslan, T., Richman, L. P., Lin, J. H., Sun, Y. H., Rech, A. J., Balli, D., Hay, C. A., Sela, Y., Merrell, A. J., Liudahl, S. M., Gordon, N., Norgard, R. J., Yuan, S., Yu, S., Chao, T., Ye, S., Eisinger-Mathason, T. S. K., Faryabi, R. B., Tobias, J. W., Lowe, S. W., Coussens, L. M., Wherry, E. J., Vonderheide, R. H., & Stanger, B. Z. (2018). Tumor Cell-Intrinsic Factors Underlie Heterogeneity of Immune Cell Infiltration and Response to Immunotherapy. *Immunity*, *49*(1), 178-193 e177. https://doi.org/10.1016/j.immuni.2018.06.006

Li, M., & Zhang, P. (2009). The function of APC/CCdh1 in cell cycle and beyond. *Cell Div*, *4*, 2. https://doi.org/10.1186/1747-1028-4-2

Li, W., Germain, R. N., & Gerner, M. Y. (2019). High-dimensional cell-level analysis of tissues with Ce3D multiplex volume imaging. *Nat Protoc*, *14*(6), 1708-1733. https://doi.org/10.1038/s41596-019-0156-4

Liberzon, A., Birger, C., Thorvaldsdottir, H., Ghandi, M., Mesirov, J. P., & Tamayo, P. (2015). The Molecular Signatures Database (MSigDB) hallmark gene set collection. *Cell Syst*, *1*(6), 417-425. https://doi.org/10.1016/j.cels.2015.12.004

Lichtman, J. W., & Conchello, J. A. (2005). Fluorescence microscopy. *Nat Methods*, *2*(12), 910-919. https://doi.org/10.1038/nmeth817

Lim, S. A., Kim, J., Jeon, S., Shin, M. H., Kwon, J., Kim, T. J., Im, K., Han, Y., Kwon, W., Kim, S. W., Yee, C., Kim, S. J., Jang, J. Y., & Lee, K. M. (2019). Defective Localization With Impaired Tumor Cytotoxicity Contributes to the Immune Escape of NK Cells in Pancreatic Cancer Patients. *Front Immunol*, *10*, 496. https://doi.org/10.3389/fimmu.2019.00496

Lin, A., & Lore, K. (2017). Granulocytes: New Members of the Antigen-Presenting Cell Family. *Front Immunol*, *8*, 1781. https://doi.org/10.3389/fimmu.2017.01781

Lin, J. R., Izar, B., Wang, S., Yapp, C., Mei, S., Shah, P. M., Santagata, S., & Sorger, P. K. (2018). Highly multiplexed immunofluorescence imaging of human tissues and tumors using t-CyCIF and conventional optical microscopes. *Elife*, *7*. https://doi.org/10.7554/eLife.31657

Liou, G. Y., Doppler, H., Necela, B., Edenfield, B., Zhang, L., Dawson, D. W., & Storz, P. (2015). Mutant KRAS-induced expression of ICAM-1 in pancreatic acinar cells causes attraction of macrophages to expedite the formation of precancerous lesions. *Cancer Discov*, *5*(1), 52-63. https://doi.org/10.1158/2159-8290.CD-14-0474

Liu, P., Wang, Y., & Li, X. (2019). Targeting the untargetable KRAS in cancer therapy. *Acta Pharm Sin B*, *9*(5), 871-879. https://doi.org/10.1016/j.apsb.2019.03.002

Liu, R., Zhang, Y., Ding, Y., Zhang, S., & Pan, L. (2020). Characteristics of TGFBR1-EGFR-CTNNB1-CDH1 Signaling Axis in Wnt-Regulated Invasion and Migration in Lung Cancer. *Cell Transplant*, *29*, 963689720969167. https://doi.org/10.1177/0963689720969167

Liu, X. H., Bauman, W. A., & Cardozo, C. (2015). ANKRD1 modulates inflammatory responses in C2C12 myoblasts through feedback inhibition of NF-kappaB signaling activity. *Biochem Biophys Res Commun*, *464*(1), 208-213. https://doi.org/10.1016/j.bbrc.2015.06.118

Lopes, N., Bergsland, C. H., Bjornslett, M., Pellinen, T., Svindland, A., Nesbakken, A., Almeida, R., Lothe, R. A., David, L., & Bruun, J. (2020). Digital image analysis of multiplex fluorescence IHC in colorectal cancer recognizes the prognostic value of CDX2 and its negative correlation with SOX2. *Lab Invest*, *100*(1), 120-134. https://doi.org/10.1038/s41374-019-0336-4

Love, M. I., Huber, W., & Anders, S. (2014). Moderated estimation of fold change and dispersion for RNA-seq data with DESeq2. *Genome Biol*, *15*(12), 550. https://doi.org/10.1186/s13059-014-0550-8

Lu, M., Marsters, S., Ye, X., Luis, E., Gonzalez, L., & Ashkenazi, A. (2014). E-cadherin couples death receptors to the cytoskeleton to regulate apoptosis. *Mol Cell*, *54*(6), 987-998. https://doi.org/10.1016/j.molcel.2014.04.029

Lyons, Y. A., Wu, S. Y., Overwijk, W. W., Baggerly, K. A., & Sood, A. K. (2017). Immune cell profiling in cancer: molecular approaches to cell-specific identification. *NPJ Precis Oncol*, *1*(1), 26. https://doi.org/10.1038/s41698-017-0031-0

Mace, T. A., Shakya, R., Pitarresi, J. R., Swanson, B., McQuinn, C. W., Loftus, S., Nordquist, E., Cruz-Monserrate, Z., Yu, L., Young, G., Zhong, X., Zimmers, T. A., Ostrowski, M. C., Ludwig, T., Bloomston, M., Bekaii-Saab, T., & Lesinski, G. B. (2018). IL-6 and PD-L1 antibody blockade combination therapy reduces tumour progression in murine models of pancreatic cancer. *Gut*, *67*(2), 320-332. https://doi.org/10.1136/gutjnl-2016-311585

Maddipati, R., & Stanger, B. Z. (2015). Pancreatic Cancer Metastases Harbor Evidence of Polyclonality. *Cancer Discov*, *5*(10), 1086-1097. https://doi.org/10.1158/2159-8290.CD-15-0120

Mahajan, U. M., Langhoff, E., Goni, E., Costello, E., Greenhalf, W., Halloran, C., Ormanns, S., Kruger, S., Boeck, S., Ribback, S., Beyer, G., Dombroswki, F., Weiss, F. U., Neoptolemos, J. P., Werner, J., D'Haese, J. G., Bazhin, A., Peterhansl, J., Pichlmeier, S., Buchler, M. W., Kleeff, J., Ganeh, P., Sendler, M., Palmer, D. H., Kohlmann, T., Rad, R., Regel, I., Lerch, M. M., & Mayerle, J. (2018). Immune Cell and Stromal Signature Associated With Progression-Free Survival of Patients With Resected Pancreatic Ductal Adenocarcinoma. *Gastroenterology*, *155*(5), 1625-1639 e1622. https://doi.org/10.1053/j.gastro.2018.08.009

Matallanas, D., Birtwistle, M., Romano, D., Zebisch, A., Rauch, J., von Kriegsheim, A., & Kolch, W. (2011). Raf family kinases: old dogs have learned new tricks. *Genes Cancer*, *2*(3), 232-260. https://doi.org/10.1177/1947601911407323

Matea, C. T., Mocan, T., Tabaran, F., Pop, T., Mosteanu, O., Puia, C., Iancu, C., & Mocan, L. (2017). Quantum dots in imaging, drug delivery and sensor applications. *Int J Nanomedicine*, *12*, 5421-5431. https://doi.org/10.2147/IJN.S138624

Matthaei, H., Schulick, R. D., Hruban, R. H., & Maitra, A. (2011). Cystic precursors to invasive pancreatic cancer. *Nat Rev Gastroenterol Hepatol*, *8*(3), 141-150. https://doi.org/10.1038/nrgastro.2011.2

Maurer, T., Garrenton, L. S., Oh, A., Pitts, K., Anderson, D. J., Skelton, N. J., Fauber, B. P., Pan, B., Malek, S., Stokoe, D., Ludlam, M. J., Bowman, K. K., Wu, J., Giannetti, A. M., Starovasnik, M. A., Mellman, I., Jackson, P. K., Rudolph, J., Wang, W., & Fang, G. (2012). Small-molecule ligands bind to a distinct pocket in Ras and inhibit SOS-mediated nucleotide exchange activity. *Proc Natl Acad Sci U S A*, *109*(14), 5299-5304. https://doi.org/10.1073/pnas.1116510109

Menyhárd, D. K., Pálfy, G., Orgován, Z., Vida, I., Keserű, G. M., & Perczel, A. (2020). Structural impact of GTP binding on downstream KRAS signaling. *Chemical Science*, *11*, 9272–9289. https://doi.org/https://doi.org/10.1039/D0SC03441J

Mertens, C., Mora, J., Oren, B., Grein, S., Winslow, S., Scholich, K., Weigert, A., Malmstrom, P., Forsare, C., Ferno, M., Schmid, T., Brune, B., & Jung, M. (2018). Macrophage-derived lipocalin-2 transports iron in the tumor microenvironment. *Oncoimmunology*, *7*(3), e1408751. https://doi.org/10.1080/2162402X.2017.1408751

Metzger, P., Kirchleitner, S. V., Kluge, M., Koenig, L. M., Horth, C., Rambuscheck, C. A., Bohmer, D., Ahlfeld, J., Kobold, S., Friedel, C. C., Endres, S., Schnurr, M., & Duewell, P. (2019). Immunostimulatory RNA leads to functional reprogramming of myeloid-derived suppressor cells in pancreatic cancer. *J Immunother Cancer*, *7*(1), 288. https://doi.org/10.1186/s40425-019-0778-7

Meyer, M. A., Baer, J. M., Knolhoff, B. L., Nywening, T. M., Panni, R. Z., Su, X., Weilbaecher, K. N., Hawkins, W. G., Ma, C., Fields, R. C., Linehan, D. C., Challen, G. A., Faccio, R., Aft, R. L., & DeNardo, D. G. (2018). Breast and pancreatic cancer interrupt IRF8-dependent dendritic cell development to overcome immune surveillance. *Nat Commun*, *9*(1), 1250. https://doi.org/10.1038/s41467-018-03600-6

Miao, Y., Lu, M., Yan, Q., Li, S., & Feng, Y. (2016). Inhibition of Proliferation, Migration, and Invasion by Knockdown of Pyruvate Kinase-M2 (PKM2) in Ovarian Cancer SKOV3 and OVCAR3 Cells. *Oncol Res*, *24*(6), 463-475. https://doi.org/10.3727/096504016X14685034103671

Miller-Ocuin, J. L., Liang, X., Boone, B. A., Doerfler, W. R., Singhi, A. D., Tang, D., Kang, R., Lotze, M. T., & Zeh, H. J., 3rd. (2019). DNA released from neutrophil extracellular traps (NETs) activates pancreatic stellate cells and enhances pancreatic tumor growth. *Oncoimmunology*, *8*(9), e1605822. https://doi.org/10.1080/2162402X.2019.1605822

Moffitt, R. A., Marayati, R., Flate, E. L., Volmar, K. E., Loeza, S. G., Hoadley, K. A., Rashid, N. U., Williams, L. A., Eaton, S. C., Chung, A. H., Smyla, J. K., Anderson, J. M., Kim, H. J., Bentrem, D. J., Talamonti, M. S., Iacobuzio-Donahue, C. A., Hollingsworth, M. A., & Yeh, J. J. (2015). Virtual microdissection identifies distinct tumor- and stroma-specific subtypes of pancreatic ductal adenocarcinoma. *Nat Genet*, *47*(10), 1168-1178. https://doi.org/10.1038/ng.3398

Mueller, S., Engleitner, T., Maresch, R., Zukowska, M., Lange, S., Kaltenbacher, T., Konukiewitz, B., Ollinger, R., Zwiebel, M., Strong, A., Yen, H. Y., Banerjee, R., Louzada, S., Fu, B., Seidler, B., Gotzfried, J., Schuck, K., Hassan, Z., Arbeiter, A., Schonhuber, N., Klein, S., Veltkamp, C., Friedrich, M., Rad, L., Barenboim, M., Ziegenhain, C., Hess, J., Dovey, O. M., Eser, S., Parekh, S., Constantino-Casas, F., de la Rosa, J., Sierra, M. I., Fraga, M., Mayerle, J., Kloppel, G., Cadinanos, J., Liu, P., Vassiliou, G., Weichert, W., Steiger, K., Enard, W., Schmid, R. M., Yang, F., Unger, K., Schneider, G., Varela, I., Bradley, A., Saur, D., & Rad, R. (2018). Evolutionary routes and KRAS dosage define pancreatic cancer phenotypes. *Nature*, *554*(7690), 62-68. https://doi.org/10.1038/nature25459

Murciano-Goroff, Y. R., Warner, A. B., & Wolchok, J. D. (2020). The future of cancer immunotherapy: microenvironment-targeting combinations. *Cell Res*, *30*(6), 507-519. https://doi.org/10.1038/s41422-020-0337-2

Muzumdar, M. D., Tasic, B., Miyamichi, K., Li, L., & Luo, L. (2007). A global double-fluorescent Cre reporter mouse. *Genesis*, *45*(9), 593-605. https://doi.org/10.1002/dvg.20335

Neesse, A., Michl, P., Frese, K. K., Feig, C., Cook, N., Jacobetz, M. A., Lolkema, M. P., Buchholz, M., Olive, K. P., Gress, T. M., & Tuveson, D. A. (2011). Stromal biology and therapy in pancreatic cancer. *Gut*, *60*(6), 861-868. https://doi.org/10.1136/gut.2010.226092

Nguyen, A. V., Nyberg, K. D., Scott, M. B., Welsh, A. M., Nguyen, A. H., Wu, N., Hohlbauch, S. V., Geisse, N. A., Gibb, E. A., Robertson, A. G., Donahue, T. R., & Rowat, A. C. (2016). Stiffness of pancreatic cancer cells is associated with increased invasive potential. *Integr Biol (Camb)*, *8*(12), 1232-1245. https://doi.org/10.1039/c6ib00135a

Nguyen, D. T., Lee, E., Alimperti, S., Norgard, R. J., Wong, A., Lee, J. J., Eyckmans, J., Stanger, B. Z., & Chen, C. S. (2019). A biomimetic pancreatic cancer on-chip reveals endothelial ablation via ALK7 signaling. *Sci Adv*, *5*(8), eaav6789. https://doi.org/10.1126/sciadv.aav6789

Nielsen, S. R., Quaranta, V., Linford, A., Emeagi, P., Rainer, C., Santos, A., Ireland, L., Sakai, T., Sakai, K., Kim, Y. S., Engle, D., Campbell, F., Palmer, D., Ko, J. H., Tuveson, D. A., Hirsch, E., Mielgo, A., & Schmid, M. C. (2016). Macrophage-secreted granulin supports pancreatic cancer metastasis by inducing liver fibrosis. *Nat Cell Biol*, *18*(5), 549-560. https://doi.org/10.1038/ncb3340

Noe, M., Niknafs, N., Fischer, C. G., Hackeng, W. M., Beleva Guthrie, V., Hosoda, W., Debeljak, M., Papp, E., Adleff, V., White, J. R., Luchini, C., Pea, A., Scarpa, A., Butturini, G., Zamboni, G., Castelli, P., Hong, S. M., Yachida, S., Hiraoka, N., Gill, A. J., Samra, J. S., Offerhaus, G. J. A., Hoorens, A., Verheij, J., Jansen, C., Adsay, N. V., Jiang, W., Winter, J., Albores-Saavedra, J., Terris, B., Thompson, E. D., Roberts, N. J., Hruban, R. H., Karchin, R., Scharpf, R. B., Brosens, L. A. A., Velculescu, V. E., & Wood, L. D. (2020). Genomic characterization of malignant progression in neoplastic pancreatic cysts. *Nat Commun*, *11*(1), 4085. https://doi.org/10.1038/s41467-020-17917-8

Nones, K., Waddell, N., Song, S., Patch, A. M., Miller, D., Johns, A., Wu, J., Kassahn, K. S., Wood, D., Bailey, P., Fink, L., Manning, S., Christ, A. N., Nourse, C., Kazakoff, S., Taylor, D., Leonard, C., Chang, D. K., Jones, M. D., Thomas, M., Watson, C., Pinese, M., Cowley, M., Rooman, I., Pajic, M., Apgi, Butturini, G., Malpaga, A., Corbo, V., Crippa, S., Falconi, M., Zamboni, G., Castelli, P., Lawlor, R. T., Gill, A. J., Scarpa, A., Pearson, J. V., Biankin, A. V., & Grimmond, S. M. (2014). Genome-wide DNA methylation patterns in pancreatic ductal adenocarcinoma reveal epigenetic deregulation of SLIT-ROBO, ITGA2 and MET signaling. *Int J Cancer*, *135*(5), 1110-1118. https://doi.org/10.1002/ijc.28765

Öhlund, D., Handly-Santana, A., Biffi, G., Elyada, E., Almeida, A. S., Ponz-Sarvise, M., Corbo, V., Oni, T. E., Hearn, S. A., Lee, E. J., Chio, II, Hwang, C. I., Tiriac, H., Baker, L. A., Engle, D. D., Feig, C., Kultti, A., Egeblad, M., Fearon, D. T., Crawford, J. M., Clevers, H., Park, Y., & Tuveson, D. A. (2017). Distinct populations of inflammatory fibroblasts and myofibroblasts in pancreatic cancer. *J Exp Med*, *214*(3), 579-596. https://doi.org/10.1084/jem.20162024

Olive, K. P., Tuveson, D. A., Ruhe, Z. C., Yin, B., Willis, N. A., Bronson, R. T., Crowley, D., & Jacks, T. (2004). Mutant p53 gain of function in two mouse models of Li-Fraumeni syndrome. *Cell*, *119*(6), 847-860. https://doi.org/10.1016/j.cell.2004.11.004

Orozco, C. A., Martinez-Bosch, N., Guerrero, P. E., Vinaixa, J., Dalotto-Moreno, T., Iglesias, M., Moreno, M., Djurec, M., Poirier, F., Gabius, H. J., Fernandez-Zapico, M. E., Hwang, R. F., Guerra, C., Rabinovich, G. A., & Navarro, P. (2018). Targeting galectin-1 inhibits pancreatic cancer progression by modulating tumor-stroma crosstalk. *Proc Natl Acad Sci U S A*, *115*(16), E3769-E3778. https://doi.org/10.1073/pnas.1722434115

Otake, S., Itoh, Y., Omata, C., Saitoh, M., & Miyazawa, K. (2021). ZEB1 and oncogenic Ras constitute a regulatory switch for stimulus-dependent E-cadherin downregulation. *Cancer Sci*, *112*(1), 205-216. https://doi.org/10.1111/cas.14701

Oweira, H., Petrausch, U., Helbling, D., Schmidt, J., Mannhart, M., Mehrabi, A., Schob, O., Giryes, A., Decker, M., & Abdel-Rahman, O. (2017). Prognostic value of site-specific metastases in pancreatic adenocarcinoma: A Surveillance Epidemiology and End Results database analysis. *World J Gastroenterol*, *23*(10), 1872-1880. https://doi.org/10.3748/wjg.v23.i10.1872

Ozkan-Dagliyan, I., Diehl, J. N., George, S. D., Schaefer, A., Papke, B., Klotz-Noack, K., Waters, A. M., Goodwin, C. M., Gautam, P., Pierobon, M., Peng, S., Gilbert, T. S. K., Lin, K. H., Dagliyan, O., Wennerberg, K., Petricoin, E. F., 3rd, Tran, N. L., Bhagwat, S. V., Tiu, R. V., Peng, S. B., Herring, L. E., Graves, L. M., Sers, C., Wood, K. C., Cox, A. D., & Der, C. J. (2020). Low-Dose Vertical Inhibition of the RAF-MEK-ERK Cascade Causes Apoptotic Death of KRAS Mutant Cancers. *Cell Rep*, *31*(11), 107764. https://doi.org/10.1016/j.celrep.2020.107764

Padmanaban, V., Krol, I., Suhail, Y., Szczerba, B. M., Aceto, N., Bader, J. S., & Ewald, A. J. (2019). E-cadherin is required for metastasis in multiple models of breast cancer. *Nature*, *573*(7774), 439-444. https://doi.org/10.1038/s41586-019-1526-3

Paget, S. (1889). The distribution of secondary growths in cancer of the breast. *Lancet*, *133*, 571-573.

Panni, R. Z., Herndon, J. M., Zuo, C., Hegde, S., Hogg, G. D., Knolhoff, B. L., Breden, M. A., Li, X., Krisnawan, V. E., Khan, S. Q., Schwarz, J. K., Rogers, B. E., Fields, R. C., Hawkins, W. G., Gupta, V., & DeNardo, D. G. (2019). Agonism of CD11b reprograms innate immunity to sensitize pancreatic cancer to immunotherapies. *Sci Transl Med*, *11*(499). https://doi.org/10.1126/scitranslmed.aau9240

Parente, P., Parcesepe, P., Covelli, C., Olivieri, N., Remo, A., Pancione, M., Latiano, T. P., Graziano, P., Maiello, E., & Giordano, G. (2018). Crosstalk between the Tumor Microenvironment and Immune System in Pancreatic Ductal Adenocarcinoma: Potential Targets for New Therapeutic Approaches. *Gastroenterol Res Pract*, *2018*, 7530619. https://doi.org/10.1155/2018/7530619

Parra, E. R., Uraoka, N., Jiang, M., Cook, P., Gibbons, D., Forget, M. A., Bernatchez, C., Haymaker, C., Wistuba, II, & Rodriguez-Canales, J. (2017). Validation of multiplex immunofluorescence panels using multispectral microscopy for immune-profiling of formalin-fixed and paraffin-embedded human tumor tissues. *Sci Rep*, *7*(1), 13380. https://doi.org/10.1038/s41598-017-13942-8

Payne, S. N., Maher, M. E., Tran, N. H., Van De Hey, D. R., Foley, T. M., Yueh, A. E., Leystra, A. A., Pasch, C. A., Jeffrey, J. J., Clipson, L., Matkowskyj, K. A., & Deming, D. A. (2015). PIK3CA mutations can initiate pancreatic tumorigenesis and are targetable with PI3K inhibitors. *Oncogenesis*, *4*, e169. https://doi.org/10.1038/oncsis.2015.28

Pein, M., Insua-Rodriguez, J., Hongu, T., Riedel, A., Meier, J., Wiedmann, L., Decker, K., Essers, M. A. G., Sinn, H. P., Spaich, S., Sutterlin, M., Schneeweiss, A., Trumpp, A., & Oskarsson, T. (2020). Metastasis-initiating cells induce and exploit a fibroblast niche to fuel malignant colonization of the lungs. *Nat Commun*, *11*(1), 1494. https://doi.org/10.1038/s41467-020-15188-x

Peranzoni, E., Lemoine, J., Vimeux, L., Feuillet, V., Barrin, S., Kantari-Mimoun, C., Bercovici, N., Guerin, M., Biton, J., Ouakrim, H., Regnier, F., Lupo, A., Alifano, M., Damotte, D., & Donnadieu, E. (2018). Macrophages impede CD8 T cells from reaching tumor cells and limit the efficacy of anti-PD-1 treatment. *Proc Natl Acad Sci U S A*, *115*(17), E4041-E4050. https://doi.org/10.1073/pnas.1720948115

Peterson, V. M., Castro, C. M., Chung, J., Miller, N. C., Ullal, A. V., Castano, M. D., Penson, R. T., Lee, H., Birrer, M. J., & Weissleder, R. (2013). Ascites analysis by a microfluidic chip allows tumor-cell profiling. *Proc Natl Acad Sci U S A*, *110*(51), E4978-4986. https://doi.org/10.1073/pnas.1315370110

Petitprez, F., Sun, C. M., Lacroix, L., Sautes-Fridman, C., de Reynies, A., & Fridman, W. H. (2018). Quantitative Analyses of the Tumor Microenvironment Composition and Orientation in the Era of Precision Medicine. *Front Oncol*, *8*, 390. https://doi.org/10.3389/fonc.2018.00390

Principe, D. R., Narbutis, M., Kumar, S., Park, A., Viswakarma, N., Dorman, M. J., Kamath, S. D., Grippo, P. J., Fishel, M. L., Hwang, R. F., Thummuri, D., Underwood, P. W., Munshi, H. G., Trevino, J. G., & Rana, A. (2020). Long-Term Gemcitabine Treatment Reshapes the Pancreatic Tumor Microenvironment and Sensitizes Murine Carcinoma to Combination Immunotherapy. *Cancer Res*, *80*(15), 3101-3115. https://doi.org/10.1158/0008-5472.CAN-19-2959

Prost, S., Kishen, R. E., Kluth, D. C., & Bellamy, C. O. (2016). Working with Commercially Available Quantum Dots for Immunofluorescence on Tissue Sections. *PLoS One*, *11*(9), e0163856. https://doi.org/10.1371/journal.pone.0163856

Puleo, F., Nicolle, R., Blum, Y., Cros, J., Marisa, L., Demetter, P., Quertinmont, E., Svrcek, M., Elarouci, N., Iovanna, J., Franchimont, D., Verset, L., Galdon, M. G., Deviere, J., de Reynies, A., Laurent-Puig, P., Van Laethem, J. L., Bachet, J. B., & Marechal, R. (2018). Stratification of Pancreatic Ductal Adenocarcinomas Based on Tumor and Microenvironment Features. *Gastroenterology*, *155*(6), 1999-2013 e1993. https://doi.org/10.1053/j.gastro.2018.08.033

Qi, C., Hong, L., Cheng, Z., & Yin, Q. (2016). Identification of metastasis-associated genes in colorectal cancer using metaDE and survival analysis. *Oncol Lett*, *11*(1), 568-574. https://doi.org/10.3892/ol.2015.3956

Quaife, C. J., Pinkert, C. A., Ornitz, D. M., Palmiter, R. D., & Brinster, R. L. (1987). Pancreatic neoplasia induced by ras expression in acinar cells of transgenic mice. *Cell*, *48*(6), 1023-1034. https://doi.org/10.1016/0092-8674(87)90710-0

Racle, J., de Jonge, K., Baumgaertner, P., Speiser, D. E., & Gfeller, D. (2017). Simultaneous enumeration of cancer and immune cell types from bulk tumor gene expression data. *Elife*, *6*. https://doi.org/10.7554/eLife.26476

Rad, R., Cadinanos, J., Rad, L., Varela, I., Strong, A., Kriegl, L., Constantino-Casas, F., Eser, S., Hieber, M., Seidler, B., Price, S., Fraga, M. F., Calvanese, V., Hoffman, G., Ponstingl, H., Schneider, G., Yusa, K., Grove, C., Schmid, R. M., Wang, W., Vassiliou, G., Kirchner, T., McDermott, U., Liu, P., Saur, D., & Bradley, A. (2013). A genetic progression model of Braf(V600E)-induced intestinal tumorigenesis reveals targets for therapeutic intervention. *Cancer Cell*, *24*(1), 15-29. https://doi.org/10.1016/j.ccr.2013.05.014

Radens, C. M., Blake, D., Jewell, P., Barash, Y., & Lynch, K. W. (2019). Meta-Analysis of Transcriptomic Variation in T cell Populations Reveals Novel Signatures of Gene Expression and Splicing. *bioRxiv*. https://doi.org/10.1101/727362

Rahib, L., Smith, B. D., Aizenberg, R., Rosenzweig, A. B., Fleshman, J. M., & Matrisian, L. M. (2014). Projecting cancer incidence and deaths to 2030: the unexpected burden of thyroid, liver, and pancreas cancers in the United States. *Cancer Res*, *74*(11), 2913-2921. https://doi.org/10.1158/0008-5472.CAN-14-0155

Raimondi, S., Maisonneuve, P., Lohr, J. M., & Lowenfels, A. B. (2007). Early onset pancreatic cancer: evidence of a major role for smoking and genetic factors. *Cancer Epidemiol Biomarkers Prev*, *16*(9), 1894-1897. https://doi.org/10.1158/1055-9965.EPI-07-0341

Rawla, P., Sunkara, T., & Gaduputi, V. (2019). Epidemiology of Pancreatic Cancer: Global Trends, Etiology and Risk Factors. *World J Oncol*, *10*(1), 10-27. https://doi.org/10.14740/wjon1166

Reichert, M., Bakir, B., Moreira, L., Pitarresi, J. R., Feldmann, K., Simon, L., Suzuki, K., Maddipati, R., Rhim, A. D., Schlitter, A. M., Kriegsmann, M., Weichert, W., Wirth, M., Schuck, K., Schneider, G., Saur, D., Reynolds, A. B., Klein-Szanto, A. J., Pehlivanoglu, B., Memis,

B., Adsay, N. V., & Rustgi, A. K. (2018). Regulation of Epithelial Plasticity Determines Metastatic Organotropism in Pancreatic Cancer. *Dev Cell*, *45*(6), 696-711 e698. https://doi.org/10.1016/j.devcel.2018.05.025

Reymond, N., d'Agua, B. B., & Ridley, A. J. (2013). Crossing the endothelial barrier during metastasis. *Nat Rev Cancer*, *13*(12), 858-870. https://doi.org/10.1038/nrc3628

Röder, P. V., Wu, B., Liu, Y., & Han, W. (2016). Pancreatic regulation of glucose homeostasis. *Exp Mol Med*, *48*, e219. https://doi.org/10.1038/emm.2016.6

Sadashivaiah, V., Tippani, M., Page, S. C., Kwon, S. H., Bach, S. V., Bharadwaj, R. A., Hyde, T. M., Kleinman, J. E., Jaffe, A. E., & Maynard, K. R. (2021). SUFI: An automated approach to spectral unmixing of fluorescent biological images. *bioRxiv*. https://doi.org/10.1101/2021.01.28.428639

Sakellariou-Thompson, D., Forget, M. A., Creasy, C., Bernard, V., Zhao, L., Kim, Y. U., Hurd, M. W., Uraoka, N., Parra, E. R., Kang, Y., Bristow, C. A., Rodriguez-Canales, J., Fleming, J. B., Varadhachary, G., Javle, M., Overman, M. J., Alvarez, H. A., Heffernan, T. P., Zhang, J., Hwu, P., Maitra, A., Haymaker, C., & Bernatchez, C. (2017). 4-1BB Agonist Focuses CD8(+) Tumor-Infiltrating T-Cell Growth into a Distinct Repertoire Capable of Tumor Recognition in Pancreatic Cancer. *Clin Cancer Res*, *23*(23), 7263-7275. https://doi.org/10.1158/1078-0432.CCR-17-0831

Sarveswaran, K., Kurz, V., Dong, Z., Tanaka, T., Penny, S., & Timp, G. (2016). Synthetic Capillaries to Control Microscopic Blood Flow. *Sci Rep*, *6*, 21885. https://doi.org/10.1038/srep21885

Sato, M., Matsumoto, M., Saiki, Y., Alam, M., Nishizawa, H., Rokugo, M., Brydun, A., Yamada, S., Kaneko, M. K., Funayama, R., Ito, M., Kato, Y., Nakayama, K., Unno, M., & Igarashi, K. (2020). BACH1 Promotes Pancreatic Cancer Metastasis by Repressing Epithelial Genes and Enhancing Epithelial-Mesenchymal Transition. *Cancer Res*, *80*(6), 1279-1292. https://doi.org/10.1158/0008-5472.CAN-18-4099

Schelker, M., Feau, S., Du, J., Ranu, N., Klipp, E., MacBeath, G., Schoeberl, B., & Raue, A. (2017). Estimation of immune cell content in tumour tissue using single-cell RNA-seq data. *Nat Commun*, *8*(1), 2032. https://doi.org/10.1038/s41467-017-02289-3

Schneider, E., Schmid-Kotsas, A., Zhao, J., Weidenbach, H., Schmid, R. M., Menke, A., Adler, G., Waltenberger, J., Grunert, A., & Bachem, M. G. (2001). Identification of mediators stimulating proliferation and matrix synthesis of rat pancreatic stellate cells. *Am J Physiol Cell Physiol*, *281*(2), C532-543. https://doi.org/10.1152/ajpcell.2001.281.2.C532

Schönhuber, N., Seidler, B., Schuck, K., Veltkamp, C., Schachtler, C., Zukowska, M., Eser, S., Feyerabend, T. B., Paul, M. C., Eser, P., Klein, S., Lowy, A. M., Banerjee, R., Yang, F., Lee, C. L., Moding, E. J., Kirsch, D. G., Scheideler, A., Alessi, D. R., Varela, I., Bradley, A., Kind, A., Schnieke, A. E., Rodewald, H. R., Rad, R., Schmid, R. M., Schneider, G., & Saur, D. (2014). A next-generation dual-recombinase system for time- and host-specific targeting of pancreatic cancer. *Nat Med*, *20*(11), 1340-1347. https://doi.org/10.1038/nm.3646

Schonleben, F., Qiu, W., Ciau, N. T., Ho, D. J., Li, X., Allendorf, J. D., Remotti, H. E., & Su, G. H. (2006). PIK3CA mutations in intraductal papillary mucinous neoplasm/carcinoma of the pancreas. *Clin Cancer Res*, *12*(12), 3851-3855. https://doi.org/10.1158/1078-0432.CCR-06-0292

Seidler, B., Schmidt, A., Mayr, U., Nakhai, H., Schmid, R. M., Schneider, G., & Saur, D. (2008). A Cre-loxP-based mouse model for conditional somatic gene expression and knockdown in vivo by using avian retroviral vectors. *Proc Natl Acad Sci U S A*, *105*(29), 10137-10142. https://doi.org/10.1073/pnas.0800487105

Serrill, J. D., Sander, M., & Shih, H. P. (2018). Pancreatic Exocrine Tissue Architecture and Integrity are Maintained by E-cadherin During Postnatal Development. *Sci Rep*, *8*(1), 13451. https://doi.org/10.1038/s41598-018-31603-2

Shamir, E. R., Pappalardo, E., Jorgens, D. M., Coutinho, K., Tsai, W. T., Aziz, K., Auer, M., Tran, P. T., Bader, J. S., & Ewald, A. J. (2014). Twist1-induced dissemination preserves

epithelial identity and requires E-cadherin. *J Cell Biol*, *204*(5), 839-856. https://doi.org/10.1083/jcb.201306088

Shen-Orr, S. S., & Gaujoux, R. (2013). Computational deconvolution: extracting cell type-specific information from heterogeneous samples. *Curr Opin Immunol*, *25*(5), 571-578. https://doi.org/10.1016/j.coi.2013.09.015

Shields, B. D., Koss, B., Taylor, E. M., Storey, A. J., West, K. L., Byrum, S. D., Mackintosh, S. G., Edmondson, R., Mahmoud, F., Shalin, S. C., & Tackett, A. J. (2019). Loss of E-Cadherin Inhibits CD103 Antitumor Activity and Reduces Checkpoint Blockade Responsiveness in Melanoma. *Cancer Res*, *79*(6), 1113-1123. https://doi.org/10.1158/0008-5472.CAN-18-1722

Sinnett-Smith, J., Kisfalvi, K., Kui, R., & Rozengurt, E. (2013). Metformin inhibition of mTORC1 activation, DNA synthesis and proliferation in pancreatic cancer cells: dependence on glucose concentration and role of AMPK. *Biochem Biophys Res Commun*, *430*(1), 352-357. https://doi.org/10.1016/j.bbrc.2012.11.010

Siret, C., Collignon, A., Silvy, F., Robert, S., Cheyrol, T., Andre, P., Rigot, V., Iovanna, J., van de Pavert, S., Lombardo, D., Mas, E., & Martirosyan, A. (2019). Deciphering the Crosstalk Between Myeloid-Derived Suppressor Cells and Regulatory T Cells in Pancreatic Ductal Adenocarcinoma. *Front Immunol*, *10*, 3070. https://doi.org/10.3389/fimmu.2019.03070

Sivakumar, S., Abu-Shah, E., Ahern, D. J., Arbe-Barnes, E. H., Jainarayanan, A. K., Mangal, N., Reddy, S., Rendek, A., Easton, A., Kurz, E., Silva, M., Soonawalla, Z., Heij, L. R., Bashford-Rogers, R., Middleton, M. R., & Dustin, M. L. (2021). Activated regulatory T-cells, dysfunctional and senescent T-cells dominate the microenvironment of pancreatic cancer. *Cancers*, *13*(1176). https://doi.org/10.3390/cancers13081776

Sivaram, N., McLaughlin, P. A., Han, H. V., Petrenko, O., Jiang, Y. P., Ballou, L. M., Pham, K., Liu, C., van der Velden, A. W., & Lin, R. Z. (2019). Tumor-intrinsic PIK3CA represses tumor immunogenecity in a model of pancreatic cancer. *J Clin Invest*, *129*(8), 3264-3276. https://doi.org/10.1172/JCI123540

Smith, M. J., Neel, B. G., & Ikura, M. (2013). NMR-based functional profiling of RASopathies and oncogenic RAS mutations. *Proc Natl Acad Sci U S A*, *110*(12), 4574-4579. https://doi.org/10.1073/pnas.1218173110

Sosa, M. S., Bragado, P., & Aguirre-Ghiso, J. A. (2014). Mechanisms of disseminated cancer cell dormancy: an awakening field. *Nat Rev Cancer*, *14*(9), 611-622. https://doi.org/10.1038/nrc3793

Stamp, L. A., Braxton, D. R., Wu, J., Akopian, V., Hasegawa, K., Chandrasoma, P. T., Hawes, S. M., McLean, C., Petrovic, L. M., Wang, K., & Pera, M. F. (2012). The GCTM-5 epitope associated with the mucin-like glycoprotein FCGBP marks progenitor cells in tissues of endodermal origin. *Stem Cells*, *30*(9), 1999-2009. https://doi.org/10.1002/stem.1167

Steele, N. G., Carpenter, E. S., Kemp, S. B., Sirihorachai, V. R., The, S., Delrosario, L., Lazarus, J., Amir, E. D., Gunchick, V., Espinoza, C., Bell, S., Harris, L., Lima, F., Irizarry-Negron, V., Paglia, D., Macchia, J., Chu, A., Schofield, H., Wamsteker, E., Kwon, R., Schulman, A., Prabhu, A., Law, R., Sondhi, A., Yu, J., Patel, A., Donahue, K., Nathan, H., Cho, C., Anderson, M. A., Sahai, V., Lyssiotis, C. A., Zou, W., Allen, B. L., Rao, A., Crawford, H. C., Bednar, F., Frankel, T. L., & Pasca di Magliano, M. (2020). Multimodal mapping of the tumor and peripheral blood immune landscape in human pancreatic cancer. *Nature Cancer*, *1*, 1097-1112. https://doi.org/10.1038/s43018-020-00121-4

Stodden, G. R., Lindberg, M. E., King, M. L., Paquet, M., MacLean, J. A., Mann, J. L., DeMayo, F. J., Lydon, J. P., & Hayashi, K. (2015). Loss of Cdh1 and Trp53 in the uterus induces chronic inflammation with modification of tumor microenvironment. *Oncogene*, *34*(19), 2471-2482. https://doi.org/10.1038/onc.2014.193

Strell, C., Norberg, K. J., Mezheyeuski, A., Schnittert, J., Kuninty, P. R., Moro, C. F., Paulsson, J., Schultz, N. A., Calatayud, D., Lohr, J. M., Frings, O., Verbeke, C. S., Heuchel, R. L., Prakash, J., Johansen, J. S., & Ostman, A. (2017). Stroma-regulated HMGA2 is an independent prognostic marker in PDAC and AAC. *Br J Cancer*, *117*(1), 65-77. https://doi.org/10.1038/bjc.2017.140

Sturm, G., Finotello, F., Petitprez, F., Zhang, J. D., Baumbach, J., Fridman, W. H., List, M., & Aneichyk, T. (2019). Comprehensive evaluation of transcriptome-based cell-type quantification methods for immuno-oncology. *Bioinformatics*, *35*(14), i436-i445. https://doi.org/10.1093/bioinformatics/btz363

Sumimoto, H., Imabayashi, F., Iwata, T., & Kawakami, Y. (2006). The BRAF-MAPK signaling pathway is essential for cancer-immune evasion in human melanoma cells. *J Exp Med*, *203*(7), 1651-1656. https://doi.org/10.1084/jem.20051848

Sun, Z., Nyberg, R., Wu, Y., Bernard, B., & Redmond, W. L. (2021). Developing an enhanced 7-color multiplex IHC protocol to dissect immune infiltration in human cancers. *PLoS One*, *16*(2), e0247238. https://doi.org/10.1371/journal.pone.0247238

Swift, G. H., Hammer, R. E., MacDonald, R. J., & Brinster, R. L. (1984). Tissue-specific expression of the rat pancreatic elastase I gene in transgenic mice. *Cell*, *38*(3), 639-646. https://doi.org/10.1016/0092-8674(84)90258-7

Szabo, P. A., Levitin, H. M., Miron, M., Snyder, M. E., Senda, T., Yuan, J., Cheng, Y. L., Bush, E. C., Dogra, P., Thapa, P., Farber, D. L., & Sims, P. A. (2019). Single-cell transcriptomics of human T cells reveals tissue and activation signatures in health and disease. *Nat Commun*, *10*(1), 4706. https://doi.org/10.1038/s41467-019-12464-3

Takano, S., Reichert, M., Bakir, B., Das, K. K., Nishida, T., Miyazaki, M., Heeg, S., Collins, M. A., Marchand, B., Hicks, P. D., Maitra, A., & Rustgi, A. K. (2016). Prrx1 isoform switching regulates pancreatic cancer invasion and metastatic colonization. *Genes Dev*, *30*(2), 233-247. https://doi.org/10.1101/gad.263327.115

Tan, W. C. C., Nerurkar, S. N., Cai, H. Y., Ng, H. H. M., Wu, D., Wee, Y. T. F., Lim, J. C. T., Yeong, J., & Lim, T. K. H. (2020). Overview of multiplex immunohistochemistry/immunofluorescence techniques in the era of cancer immunotherapy. *Cancer Commun (Lond)*, *40*(4), 135-153. https://doi.org/10.1002/cac2.12023

Tape, C. J., Ling, S., Dimitriadi, M., McMahon, K. M., Worboys, J. D., Leong, H. S., Norrie, I. C., Miller, C. J., Poulogiannis, G., Lauffenburger, D. A., & Jorgensen, C. (2016). Oncogenic KRAS Regulates Tumor Cell Signaling via Stromal Reciprocation. *Cell*, *165*(4), 910-920. https://doi.org/10.1016/j.cell.2016.03.029

Taube, J. M., Akturk, G., Angelo, M., Engle, E. L., Gnjatic, S., Greenbaum, S., Greenwald, N. F., Hedvat, C. V., Hollmann, T. J., Juco, J., Parra, E. R., Rebelatto, M. C., Rimm, D. L., Rodriguez-Canales, J., Schalper, K. A., Stack, E. C., Ferreira, C. S., Korski, K., Lako, A., Rodig, S. J., Schenck, E., Steele, K. E., Surace, M. J., Tetzlaff, M. T., von Loga, K., Wistuba, II, Bifulco, C. B., & Society for Immunotherapy of Cancer Pathology Task, F. (2020). The Society for Immunotherapy of Cancer statement on best practices for multiplex immunohistochemistry (IHC) and immunofluorescence (IF) staining and validation. *J Immunother Cancer*, *8*(1). https://doi.org/10.1136/jitc-2019-000155

Tekin, C., Aberson, H. L., Waasdorp, C., Hooijer, G. K. J., de Boer, O. J., Dijk, F., Bijlsma, M. F., & Spek, C. A. (2020). Macrophage-secreted MMP9 induces mesenchymal transition in pancreatic cancer cells via PAR1 activation. *Cell Oncol (Dordr)*, *43*(6), 1161-1174. https://doi.org/10.1007/s13402-020-00549-x

Thiery, J. P., Acloque, H., Huang, R. Y., & Nieto, M. A. (2009). Epithelial-mesenchymal transitions in development and disease. *Cell*, *139*(5), 871-890. https://doi.org/10.1016/j.cell.2009.11.007

Thorsson, V., Gibbs, D. L., Brown, S. D., Wolf, D., Bortone, D. S., Ou Yang, T. H., Porta-Pardo, E., Gao, G. F., Plaisier, C. L., Eddy, J. A., Ziv, E., Culhane, A. C., Paull, E. O., Sivakumar, I. K. A., Gentles, A. J., Malhotra, R., Farshidfar, F., Colaprico, A., Parker, J. S., Mose, L. E., Vo, N. S., Liu, J., Liu, Y., Rader, J., Dhankani, V., Reynolds, S. M., Bowlby, R., Califano, A., Cherniack, A. D., Anastassiou, D., Bedognetti, D., Mokrab, Y., Newman, A. M., Rao, A., Chen, K., Krasnitz, A., Hu, H., Malta, T. M., Noushmehr, H., Pedamallu, C. S., Bullman, S., Ojesina, A. I., Lamb, A., Zhou, W., Shen, H., Choueiri, T. K., Weinstein, J. N., Guinney, J., Saltz, J., Holt, R. A., Rabkin, C. S., Cancer Genome Atlas Research, N., Lazar, A. J., Serody, J. S., Demicco, E. G., Disis, M. L., Vincent, B. G., & Shmulevich,

I. (2018). The Immune Landscape of Cancer. *Immunity*, *48*(4), 812-830 e814. https://doi.org/10.1016/j.immuni.2018.03.023

Tian, C., Clauser, K. R., Öhlund, D., Rickelt, S., Huang, Y., Gupta, M., Mani, D. R., Carr, S. A., Tuveson, D. A., & Hynes, R. O. (2019). Proteomic analyses of ECM during pancreatic ductal adenocarcinoma progression reveal different contributions by tumor and stromal cells. *Proc Natl Acad Sci U S A*, *116*(39), 19609-19618. https://doi.org/10.1073/pnas.1908626116

Ting, D. T., Wittner, B. S., Ligorio, M., Vincent Jordan, N., Shah, A. M., Miyamoto, D. T., Aceto, N., Bersani, F., Brannigan, B. W., Xega, K., Ciciliano, J. C., Zhu, H., MacKenzie, O. C., Trautwein, J., Arora, K. S., Shahid, M., Ellis, H. L., Qu, N., Bardeesy, N., Rivera, M. N., Deshpande, V., Ferrone, C. R., Kapur, R., Ramaswamy, S., Shioda, T., Toner, M., Maheswaran, S., & Haber, D. A. (2014). Single-cell RNA sequencing identifies extracellular matrix gene expression by pancreatic circulating tumor cells. *Cell Rep*, *8*(6), 1905-1918. https://doi.org/10.1016/j.celrep.2014.08.029

Torres, C., & Grippo, P. J. (2018). Pancreatic cancer subtypes: a roadmap for precision medicine. *Ann Med*, *50*(4), 277-287. https://doi.org/10.1080/07853890.2018.1453168

Trahey, M., & McCormick, F. (1987). A cytoplasmic protein stimulates normal N-ras p21 GTPase, but does not affect oncogenic mutants. *Science*, *238*(4826), 542-545. https://doi.org/10.1126/science.2821624

Tramacere, I., Scotti, L., Jenab, M., Bagnardi, V., Bellocco, R., Rota, M., Corrao, G., Bravi, F., Boffetta, P., & La Vecchia, C. (2010). Alcohol drinking and pancreatic cancer risk: a meta-analysis of the dose-risk relation. *Int J Cancer*, *126*(6), 1474-1486. https://doi.org/10.1002/ijc.24936

Trowbridge, I. S., & Thomas, M. L. (1994). CD45: an emerging role as a protein tyrosine phosphatase required for lymphocyte activation and development. *Annu Rev Immunol*, *12*, 85-116. https://doi.org/10.1146/annurev.iy.12.040194.000505

Tsujikawa, T., Kumar, S., Borkar, R. N., Azimi, V., Thibault, G., Chang, Y. H., Balter, A., Kawashima, R., Choe, G., Sauer, D., El Rassi, E., Clayburgh, D. R., Kulesz-Martin, M. F., Lutz, E. R., Zheng, L., Jaffee, E. M., Leyshock, P., Margolin, A. A., Mori, M., Gray, J. W., Flint, P. W., & Coussens, L. M. (2017). Quantitative Multiplex Immunohistochemistry Reveals Myeloid-Inflamed Tumor-Immune Complexity Associated with Poor Prognosis. *Cell Rep*, *19*(1), 203-217. https://doi.org/10.1016/j.celrep.2017.03.037

Varga, Z., Li, Q., Jochum, W., Perriard, U., Rau, T., Tille, J. C., Hawle, H., Klingbiel, D., Thuerlimann, B., & Ruhstaller, T. (2019). Ki-67 assessment in early breast cancer: SAKK28/12 validation study on the IBCSG VIII and IBCSG IX cohort. *Sci Rep*, *9*(1), 13534. https://doi.org/10.1038/s41598-019-49638-4

Varricchi, G., Galdiero, M. R., Loffredo, S., Lucarini, V., Marone, G., Mattei, F., Marone, G., & Schiavoni, G. (2018). Eosinophils: The unsung heroes in cancer? *Oncoimmunology*, *7*(2), e1393134. https://doi.org/10.1080/2162402X.2017.1393134

Venkannagari, S., Fiskus, W., Peth, K., Atadja, P., Hidalgo, M., Maitra, A., & Bhalla, K. N. (2012). Superior efficacy of co-treatment with dual PI3K/mTOR inhibitor NVP-BEZ235 and pan-histone deacetylase inhibitor against human pancreatic cancer. *Oncotarget*, *3*(11), 1416-1427. https://doi.org/10.18632/oncotarget.724

von Burstin, J., Eser, S., Paul, M. C., Seidler, B., Brandl, M., Messer, M., von Werder, A., Schmidt, A., Mages, J., Pagel, P., Schnieke, A., Schmid, R. M., Schneider, G., & Saur, D. (2009). E-cadherin regulates metastasis of pancreatic cancer in vivo and is suppressed by a SNAIL/HDAC1/HDAC2 repressor complex. *Gastroenterology*, *137*(1), 361-371, 371 e361-365. https://doi.org/10.1053/j.gastro.2009.04.004

Wan, P. T., Garnett, M. J., Roe, S. M., Lee, S., Niculescu-Duvaz, D., Good, V. M., Jones, C. M., Marshall, C. J., Springer, C. J., Barford, D., Marais, R., & Cancer Genome, P. (2004). Mechanism of activation of the RAF-ERK signaling pathway by oncogenic mutations of B-RAF. *Cell*, *116*(6), 855-867. https://doi.org/10.1016/s0092-8674(04)00215-6

Wang, H. C., Lin, Y. L., Hsu, C. C., Chao, Y. J., Hou, Y. C., Chiu, T. J., Huang, P. H., Tang, M. J., Chen, L. T., & Shan, Y. S. (2019). Pancreatic stellate cells activated by mutant KRAS-

mediated PAI-1 upregulation foster pancreatic cancer progression via IL-8. *Theranostics*, *9*(24), 7168-7183. https://doi.org/10.7150/thno.36830

Wellenstein, M. D., & de Visser, K. E. (2018). Cancer-Cell-Intrinsic Mechanisms Shaping the Tumor Immune Landscape. *Immunity*, *48*(3), 399-416. https://doi.org/10.1016/j.immuni.2018.03.004

Werner, J., Combs, S. E., Springfeld, C., Hartwig, W., Hackert, T., & Buchler, M. W. (2013). Advanced-stage pancreatic cancer: therapy options. *Nat Rev Clin Oncol*, *10*(6), 323-333. https://doi.org/10.1038/nrclinonc.2013.66

Williams, E. D., Gao, D., Redfern, A., & Thompson, E. W. (2019). Controversies around epithelial-mesenchymal plasticity in cancer metastasis. *Nat Rev Cancer*, *19*(12), 716-732. https://doi.org/10.1038/s41568-019-0213-x

Witkiewicz, A. K., McMillan, E. A., Balaji, U., Baek, G., Lin, W. C., Mansour, J., Mollaee, M., Wagner, K. U., Koduru, P., Yopp, A., Choti, M. A., Yeo, C. J., McCue, P., White, M. A., & Knudsen, E. S. (2015). Whole-exome sequencing of pancreatic cancer defines genetic diversity and therapeutic targets. *Nat Commun*, *6*, 6744. https://doi.org/10.1038/ncomms7744

Xu, Z., Vonlaufen, A., Phillips, P. A., Fiala-Beer, E., Zhang, X., Yang, L., Biankin, A. V., Goldstein, D., Pirola, R. C., Wilson, J. S., & Apte, M. V. (2010). Role of pancreatic stellate cells in pancreatic cancer metastasis. *Am J Pathol*, *177*(5), 2585-2596. https://doi.org/10.2353/ajpath.2010.090899

Yang, N., Huang, J., Greshock, J., Liang, S., Barchetti, A., Hasegawa, K., Kim, S., Giannakakis, A., Li, C., O'Brien-Jenkins, A., Katsaros, D., Butzow, R., Coukos, G., & Zhang, L. (2008). Transcriptional regulation of PIK3CA oncogene by NF-kappaB in ovarian cancer microenvironment. *PLoS One*, *3*(3), e1758. https://doi.org/10.1371/journal.pone.0001758

Ye, H., Zhou, Q., Zheng, S., Li, G., Lin, Q., Wei, L., Fu, Z., Zhang, B., Liu, Y., Li, Z., & Chen, R. (2018). Tumor-associated macrophages promote progression and the Warburg effect via CCL18/NF-kB/VCAM-1 pathway in pancreatic ductal adenocarcinoma. *Cell Death Dis*, *9*(5), 453. https://doi.org/10.1038/s41419-018-0486-0

Yu, G., Wang, L. G., Han, Y., & He, Q. Y. (2012). clusterProfiler: an R package for comparing biological themes among gene clusters. *OMICS*, *16*(5), 284-287. https://doi.org/10.1089/omi.2011.0118

Yun, J. H., Chase, R., Parker, M. M., Saferali, A., Castaldi, P. J., Silverman, E. K., & Hersh, C. P. (2019). Peripheral Blood Gene Expression Signatures of Eosinophilic Chronic Obstructive Pulmonary Disease. *Am J Respir Cell Mol Biol*, *61*(3), 398-401. https://doi.org/10.1165/rcmb.2019-0112LE

Zhang, W., Wang, H., Sun, M., Deng, X., Wu, X., Ma, Y., Li, M., Shuoa, S. M., You, Q., & Miao, L. (2020). CXCL5/CXCR2 axis in tumor microenvironment as potential diagnostic biomarker and therapeutic target. *Cancer Commun (Lond)*, *40*(2-3), 69-80. https://doi.org/10.1002/cac2.12010

Zhang, Y., Lazarus, J., Steele, N. G., Yan, W., Lee, H. J., Nwosu, Z. C., Halbrook, C. J., Menjivar, R. E., Kemp, S. B., Sirihorachai, V. R., Velez-Delgado, A., Donahue, K., Carpenter, E. S., Brown, K. L., Irizarry-Negron, V., Nevison, A. C., Vinta, A., Anderson, M. A., Crawford, H. C., Lyssiotis, C. A., Frankel, T. L., Bednar, F., & Pasca di Magliano, M. (2020). Regulatory T-cell Depletion Alters the Tumor Microenvironment and Accelerates Pancreatic Carcinogenesis. *Cancer Discov*, *10*(3), 422-439. https://doi.org/10.1158/2159-8290.CD-19-0958

Zhang, Y., Zhao, J., Yu, H., Li, P., Liang, W., Liu, Z., Lee, G. B., Liu, L., Li, W. J., & Wang, Z. (2020). Detection and isolation of free cancer cells from ascites and peritoneal lavages using optically induced electrokinetics (OEK). *Sci Adv*, *6*(32), eaba9628. https://doi.org/10.1126/sciadv.aba9628

Zhou, P., Li, B., Liu, F., Zhang, M., Wang, Q., Liu, Y., Yao, Y., & Li, D. (2017). The epithelial to mesenchymal transition (EMT) and cancer stem cells: implication for treatment resistance in pancreatic cancer. *Mol Cancer*, *16*(1), 52. https://doi.org/10.1186/s12943-017-0624-9

Zhu, Y., Knolhoff, B. L., Meyer, M. A., Nywening, T. M., West, B. L., Luo, J., Wang-Gillam, A., Goedegebuure, S. P., Linehan, D. C., & DeNardo, D. G. (2014). CSF1/CSF1R blockade reprograms tumor-infiltrating macrophages and improves response to T-cell checkpoint immunotherapy in pancreatic cancer models. *Cancer Res*, *74*(18), 5057-5069. https://doi.org/10.1158/0008-5472.CAN-13-3723

Zilionis, R., Engblom, C., Pfirschke, C., Savova, V., Zemmour, D., Saatcioglu, H. D., Krishnan, I., Maroni, G., Meyerovitz, C. V., Kerwin, C. M., Choi, S., Richards, W. G., De Rienzo, A., Tenen, D. G., Bueno, R., Levantini, E., Pittet, M. J., & Klein, A. M. (2019). Single-Cell Transcriptomics of Human and Mouse Lung Cancers Reveals Conserved Myeloid Populations across Individuals and Species. *Immunity*, *50*(5), 1317-1334 e1310. https://doi.org/10.1016/j.immuni.2019.03.009

Zrazhevskiy, P., & Gao, X. (2013). Quantum dot imaging platform for single-cell molecular profiling. *Nat Commun*, *4*, 1619. https://doi.org/10.1038/ncomms2635